A Portrait of the Sun as a Young Star: Studying Space Weather Around Young Suns in the Optical and Radio

Thesis by
Ivey Davis

In Partial Fulfillment of the Requirements for the
Degree of
Doctor of Philosophy

CALIFORNIA INSTITUTE OF TECHNOLOGY
Pasadena, California

2026
Defended September 3, 2025

Ivey Davis
ORCID: 0000-0001-5397-5969

[I] Have read little and understood less.

James Joyce

A Portrait of the Artist as a Young Man

ACKNOWLEDGEMENTS

First and foremost, I want to thank my family for all of the encouragement and support they have provided over the past five years and over my lifetime. I especially want to thank my parents, without whom I would have never been able to study astronomy and I may not have ever believed that it was a field I could pursue. It means the world to me that while my residence continues to regularly change, I still have a home with you and my siblings.

Thank you to Jean Somalwar and Sam Ponnada for being such incredible friends, all the wonderful conversations, the many weekend breakfasts, and for humoring my lengthy cooking projects. Your companionship, especially as roommates alongside Tony Rodriguez during our first year, made beginning grad school during the height of the pandemic infinitely less lonely. I also want to thank the rest of my cohort for making a year of online classes and the following years survivable. I feel incredibly lucky to have been a part of such an insightful group of astronomers and grad-student community as a whole.

I want to thank the LWA group, especially Kathryn Plant, Yuping Huang, Nikita Kosogorv, Nivedita Mahesh, Ruby Byrne, Casey Law, and Marin Anderson for providing a sense of scientific community to me at Caltech. I also want to thank Greg Taylor for introducing me to this community during my undergraduate at the University of New Mexico, for encouraging me to explore stellar science at low frequencies, and for being the first to extend a research opportunity to me. Thank you also to Jayce Dowell for first showing me how to use the beamformers for the New Mexico LWA stations, continuing to teach me how to use those for the OVRO-LWA, and for repairing them every time I found a new way to break them. This thesis and my appreciation for radio instrumentation would not be what they are without this group. So many thanks are also owed to Stephanie Cha-Ramos and Gita Patel for all of their organizational and administrative work and making sure that the broader Caltech radio astronomy group gets to operate as it does.

I also want to thank the staff at Palomar, especially Jeff Zolkower, Rick Burrus, John Baker, Curt Corcoran, and Carolyn Heffner. I came to Caltech with essentially no hands-on experience with optical instrumentation and you showed me how to make an observatory that works. It is hard to overstate how much I appreciate your patience and insight as I fumbled my way through site selection, learning the

importance of air conditioning, determining the number of outlets an observatory needs, and all of the other details for making a functional observatory. I am also incredibly grateful to Navtej Saini for making Flarescope a remotely-accessible observatory, for teaching me how to build an automated system, and your persistent kindness and encouragement. Thank you so much also to Alex Marlay and Brian Beck for always offering a warm meal and presence for my longer stays at Palomar. In so many ways, Flarescope would not exist without you all.

To the Keck Institute for Space Studies workshop on particle environments—thank you for including me within the space weather community. The conversations and interactions I had during this workshop reminded me why I love astronomy and this particular field so much. I am especially grateful for the conversations I had with Parke Loyd and his encouragement for me to pursue projects outside of my expertise. I am similarly thankful to Joe Lazio for humoring my lofty proposal ideas while also always being willing to make sure my ideas are grounded. Also, many thanks to Bethany Ehlmann, Janet Seid, Harriet Brettle, and others a part of the Keck Institute for making these workshops possible.

Thank you to my extended academic family, especially Sebastian Pineda, Melodie Kao, and Jackie Villadsen for your encouragement and scientific perspective. Thank you also to Harish Vedantham and Joe Callingham for enabling me to study low-frequency stellar astronomy outside of the LWA, for your guidance when I was first beginning in this field, and for your endless kindness over the years. I am incredibly fortunate and excited to work together again.

To the members of the Gender Minorities and Women in PMA, especially Sam Wu, Dee Dunne, Katelyn Horstman, Isabel Sands, Nitika Yadlapalli, and Mia de los Reyes—thank you for inspiring me to take an active role in advocacy for myself and others and spreading education on the intersectionality of our lives within academia. You helped me recognize the capacity we have as individuals and as a group to change our environment into a more inclusive place. I am also incredibly grateful to Nam Ung and Mika Walton for giving us the space and tools to facilitate these changes and for being so active in making the division a better place for everyone. To the broader Caltech astronomy community—thank you so much for making the department such a wonderful environment to be a part of. I especially want to thank Cameron Hummels for all he does for outreach and for including me in those efforts, Rocio Kiman for always being willing to talk to me about stars, and Julie Inglis for being a reliable cat-sitter and even-more reliable friend.

Thank you to Lynne Hillenbrand, Heather Knutson, Jim Fuller, and Vikram Ravi for serving as my thesis committee, for advocating for me, and for helping me course-correct when the instrumentation inevitably ran into the roadblocks you predicted during my candidacy. Special thanks are owed to Lynne Hillenbrand for keeping me in the loop on what is going on in the field of stars and to Vikram Ravi for providing an additional perspective to OVRO-LWA operations.

And, finally, to my advisor Gregg Hallinan. You had more confidence in my ability to do instrumentation than I could have ever mustered for myself and I will always be grateful for the leadership opportunities you offered me in instrumentation and science, all of the communities you introduced me to, and for re-enforcing my conviction in being able to work independently without doing so in isolation. Thank you for your encouragement, your boundless good humor, and love of Nic Cage filmography. *Knowing* (2009) deserves its Rotten Tomatoes score though.

ABSTRACT

The surface and atmospheric chemistry of solar system bodies—including the Earth—are heavily influenced by transient particle events from the Sun like coronal mass ejections (CMEs) and solar energetic particles (SEP). These events, alongside the electromagnetic (EM) radiation of solar flares, comprise what we call space weather. The energy of both the EM and particle events are expected to have been orders of magnitude higher when the Sun was much younger, which raises questions with regards to the evolution of angular momentum, chemistry, and habitability throughout our solar system's history. Studying this history requires we study young stars as proxies for the young Sun, but the particle environment of other stars is notoriously difficult to study and CMEs or SEPs are even more so due to their transience and the multi-wavelength nature of their signatures. Fully characterizing an event thus requires extensive, coordinated monitoring across many instruments.

To address this requirement for studying space weather, I present the beginning of the Space Weather Around Young Suns (SWAYS) program in this thesis. This program includes the Owens Valley Radio Observatory Long Wavelength Array (OVRO-LWA) for identifying stellar analogs of solar type II and III bursts which are associated with bulk plasma motion from the Sun. The SWAYS program also includes Flarescope which I designed and built to detect photometric signatures of flares from solar-type stars with high precision at optical wavelengths. With Flarescope and the OVRO-LWA, I have collected more than 800 hours of simultaneous data on six young, solar-type stars and have developed a framework for analyzing the results of their coordination. This thesis includes a technical overview of Flarescope's design, a summary of its performance with the OVRO-LWA, and the framework for using the two instruments to search for signatures of transient particle flux. I supplement the significance of simultaneous observations of solar-type stars at optical and radio wavelengths with my work with the Very Large Array Sky Survey and *Transiting Exoplanet Survey Satellite* data. In this work, I identify unprecedented stellar radio emission and develop the relationship between such emission and stellar superflares. In all, this thesis illustrates the significance of simultaneous radio and optical observations for constraining stellar space weather and highlights the feasibility of multi-wavelength monitoring.

PUBLISHED CONTENT AND CONTRIBUTIONS

Davis, I., G. Hallinan, C. Ayala, et al. (Aug. 2024). "Detection of Radio Emission from Super-flaring Solar-Type Stars in the VLA Sky Survey." In: *arXiv e-prints*, arXiv:2408.14612, arXiv:2408.14612. DOI: 10.48550/arXiv.2408.14612. arXiv: 2408.14612 [astro-ph.SR].

CONTENTS

LIST OF FIGURES

LIST OF TABLES

Chapter 1

INTRODUCTION: AN OVERVIEW OF STELLAR MAGNETIC ACTIVITY AND SPACE WEATHER

The Sun hosts a menagerie of magnetic phenomena that produce emission across the entire electromagnetic (EM) spectrum. One such phenomenon is magnetic reconnection—the reconfiguration of magnetic field lines—which results in both thermal and non-thermal acceleration of particles. The result of this is commonly observed in the form of flares in soft X-ray (SXR) by, *e.g.*, the Geostationary Operational Environmental Satellite (*GOES*) (Plutino et al., 2023). Enhancement of ionizing EM radiation from flares in the form of ultraviolet (UV) and X-ray emission may play an important role in pre-biotic atmospheric chemistry and retention (Green et al., 2021; Modi et al., 2023), but understanding the acceleration process involved in flares and other magnetic events is also also motivated by a desire to predict *particle* radiation from the solar corona into the interplanetary medium (IPM). Such particles go on to interact with the atmospheres and surfaces of planetary bodies, drive non-thermal chemistry, and facilitate atmospheric escape. Each of these elements could play a key role in abiogenesis and habitability (Luhmann et al., 2007; Jakosky et al., 2015; Airapetian et al., 2016; Airapetian et al., 2020).

Such particle enhancements to the interplanetary environment are associated both with the flare process itself (Cliver and Ling, 2009; Reames, 2021) and with coronal mass ejections (CMEs). These are massive ($\lesssim 10^{16}$ g; Yashiro and Gopalswamy, 2009) eruptions that can coherently expand into colossal magnetic volumes as they propagate (radial size of ≈ 0.2 AU by the time they reach 1 AU, Liu et al., 2005). We do not yet have a full description for the formation and acceleration of CMEs, but there is a strong correlation between highly-energetic flares and CME production; essentially all solar flares with energies $> 10^{30}$ erg leading to a CME (Yashiro et al., 2006). There are additional correlations between flare SXR luminosity and CME masses and velocities (Chen et al., 2006; Yashiro and Gopalswamy, 2009; Aarnio et al., 2011; Moschou et al., 2019).

Although we have observed stellar flares for decades, the particle environments of stars—including both CMEs and the persistent stellar wind—remain largely elusive. Without the ability to make in-situ measurements of the exo-solar system particle

environments or to directly image stellar CMEs (see Figure 1.1 as an illustration of this latter difficulty[1]), we rely largely on what we have observed from the Sun. This may manifest as looking for the stellar equivalents of EM proxies of solar mass escape or relying on scaling laws between solar flares and CME occurrence and characteristics. However, solar scaling laws used for predicting CMEs are likely moot for younger, more active stars. Such stars tend to have magnetic field strengths and topologies distinct from the solar form and likely have different wind strengths, densities, and geometries to match. Additionally, stellar analogs of solar signatures of CMEs (*e.g.*, Doppler-shifted Hα and X-ray dimmings) could also be explained by dynamics consistent with outwardly-accelerated, but still-contained, material (Veronig et al., 2021; Namekata et al., 2021; Otsu et al., 2022). Observing a variety of signatures across multiple wavelengths, and making such observations *simultaneously*, will be critical for minimizing doubt in CME candidates as well as constraining a variety of CME properties. Understanding these events as they occur on other stars will be crucial for understanding the full activity history of the Sun and what that means for the evolution of our solar system.

In this thesis, I present a combined optical and radio perspective for studying flares and the associated particle flux, collectively referred to as space weather, on young solar-type stars. My work highlights how distinct the manifestations of activity on young stars are from how it manifests for the Sun. This work includes leveraging survey data to identify exceptional radio emission from stars that are highly active at optical wavelengths, presented in Chapter 2. It also includes the first iteration of a multi-wavelength monitoring program for studying space weather around young suns (SWAYS). This program currently includes the Owens Valley Radio Observatory (OVRO) Long Wavelength Array (LWA), for which I assisted in commissioning the beamformed observing mode. The OVRO-LWA operate in the 13-87 MHz range, frequencies that should enable identifying stellar equivalents of radio bursts associated with bulk plasma motion in the solar corona and IPM. To supplement the study of space weather with the OVRO-LWA, I have developed the small, optical instrument Flarescope at Palomar observatory. I designed this instrument to reach sub-millimag (mmag) precision on bright stars with the explicit purpose of detecting flares on stars observed by the OVRO-LWA. The operations and performance of the OVRO-LWA and Flarescope are covered in Chapters 3 and 4, respectively. The monitoring program I did with these instruments culminated in $\approx$ 900-hours of

[1]The code I developed to make Figure 1.1 as well as much of the work for this thesis is available here. The CME component makes use of the `FRiED` flux rope modeling code from Isavnin (2016).

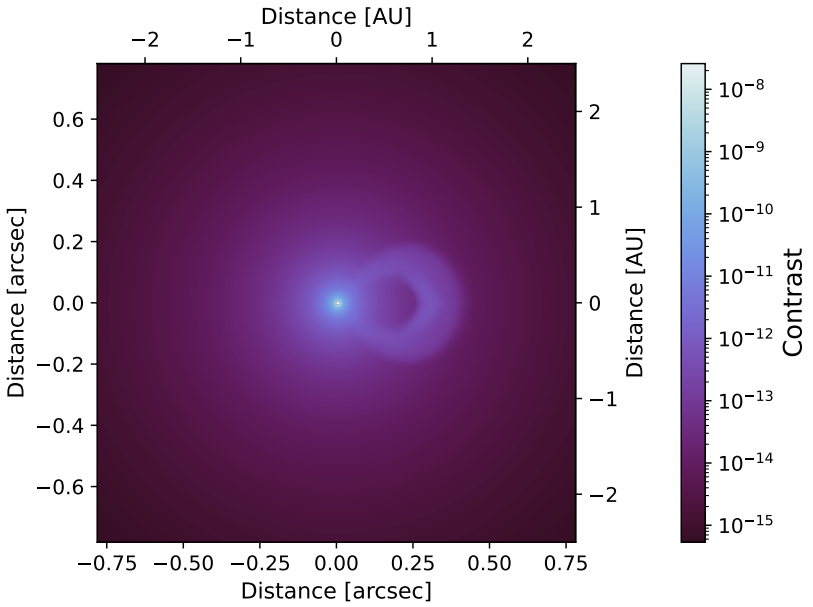

Figure 1.1: The contrast for a simple model of a CME and wind for a star at 3.2 pc. The mass for the CME here is 10^{19} g—a typical mass estimate for stellar CMEs but several orders of magnitude larger than solar CMEs. Notably, the highest contrast represented here is $\approx 10^{-8}$. This is more than an order of magnitude lower than what is achievable by current, high-contrast imaging instrumentation for resolutions represented here, but may be in the realm of detectability for future instrumentation like is planned for the Habitable World Observatory (Allan et al., 2023).

observing dedicated to six young stars, the results of which are presented in Chapter 5. The multi-wavelength—especially for the specific wavelengths explored—and monitoring nature of this program is novel, and afforded unique analysis of the relevant physics for the extreme environments of young stars. I conclude this thesis with a discussion of plans to expand these studies to other instruments, wavelengths, and techniques in Chapter 6. In this chapter, I provide additional context for the significance of studying young stars across the spectrum with a focus on the optical and radio specifically.

1.1 Stellar Evolution and Quiescent Magnetic Environments

Once a star has contracted onto the main sequence, its evolution is largely dictated by angular momentum loss through mass loss, be that loss through transient events like CMEs or through persistent winds. The mass loss facilitates a mechanism commonly referred to as magnetic braking (Mestel, 1968), wherein mass entrained in a star's magnetic field acts as a lever arm torquing the star. When the material

escapes the field, the angular momentum is lost and the star is permanently spun down. As such, for a given spectral type, the rotation rate can be an effective metric for the age of the star (Skumanich, 1972). In the case of binary systems, this is true if the stars are separated enough that they are not tidally interacting ($\approx$ 1 AU, Zahn, 1977; Fleming et al., 2019).

However, the rotation rate plays a significant role in the generation of magnetic fields for stars with convective envelopes (stars F-type and later). This role is commonly explained by invoking a combination of the alpha-omega dynamo and shearing action at the boundary of the convective and radiative regions of the star, called the tachocline (Guerrero et al., 2016). The immediate conclusions this suggests is 1.) the rate of magnetic braking should reduce as the star ages and its field weakens (and, indeed, a regime of weakened magnetic braking has been identified for G and K type stars by Metcalfe et al., 2022) and 2.) younger stars have stronger fields and, by extension, are more magnetically active. The association between youth and activity is how Skumanich (1972) derived the rotation-age relation still referenced today as Skumanich's law.

Notably, our earliest characterizations of activity for stars were based on the properties of the *quiescent* or slowly-varying phase of the star, whereas today most activity discussions note the relationship between the quiescent and transient phases, the latter of which would include distinct flare events. Because of how quiescent properties historically have informed our understanding of activity evolution, the relationship between transient and persistent activity features, and the relevance of quiescent emission in Chapter 2, I first focus on coronal emission and (presumably) associated winds here before talking about flares and their relationship with CMEs and SEPs in Section 1.2.

Continuous Coronal Emissions

The Ca II lines evaluated in Skumanich (1972) and preceding works are, importantly, signatures of *chromospheric* activity. Although such activity is undoubtedly related to coronal activity, there are poorly-constrained dynamics at the transition region between the chromosphere and corona which complicate our understanding of particle transport between the regions (Mariska, 1986; Frogner et al., 2020). Because of this, the innermost boundary of the solar/stellar wind—and, by extension, what that implies for the IPM—is best understood by evaluating the outermost solar/stellar atmosphere, *i.e.*, the corona.

The hot (effective temperature $T > 10^6$ K) nature of coronae lends study of it to the X-ray and EUV. Early solar and stellar X-ray observations made it clear that X-ray-emitting coronae are essentially universal among stars with convective envelopes, with apparently-quiescent fluxes ranging between what we observe during solar activity minima (10^4 erg s^{-1} cm^{-2}) and what we observe from solar flares (10^8 erg s^{-1} cm^{-2}) (Schmitt, 1997). On the surface, this may seem reasonable—stellar activity for solar-type stars seems to span the various activity levels we observe for the Sun. The caveat, of course, is that without spatial resolution, the derived surface flux assumes the X-ray luminosity originates from the entire stellar surface—the 10^8 erg s^{-1} cm^{-2} would imply the entire stellar surface is filled with flaring regions. This has incredible implications both for the global activity and the coronal structure where the X-rays originate.

Spectral-index analyses pointed to these coronae being hotter than the Sun's (Schmitt et al., 1995; Schmitt, 1997), and higher-resolution X-ray spectra reveal that there is both a hot component consistent with the temperature observed for solar flares as well as a cool component which becomes more distinct for younger, more active stars (Güdel et al., 1997). The similarity in temperature between the hot component and flares suggests that the hot component of stellar coronae may be sustained by individual, albeit temporally-unresolved, flare events. This hypothesis seemed to be further supported by the Güdel-Benz Relationship (GBR), an empirical relationship that shows a correlation between thermal SXR emission and incoherent, non-thermal radio emission (Guedel and Benz, 1993; Benz and Guedel, 1994). This relationship holds for both the quiescent phases of stars and generally for the flaring state of the Sun and stars, which would then suggest 1.) that the quiescent and flaring states are related, 2.) that there is some consistent partitioning of energy between thermal and non-thermal particle acceleration, and 3.) stars are constantly flaring at some level. Notably, the GBR does not hold for the quiescent Sun, as it is under luminous in the radio by several orders of magnitude. Taken all together, observations show that young stars have exceptional X-ray emissions that imply incredibly hot, dense coronae. The high thermal and magnetic pressure originating from the corona, taken alongside a likely relationship between reconnection processes and the production of the slow solar wind (Antiochos et al., 2011; Chen et al., 2025), lead to the supposition that young stars should also produce extraordinary winds.

Winds

While stellar coronal emissions often have analogous solar signals, signals associated with material streaming out into the IPM as solar-like winds are a different story. Being orders of magnitude less dense than even coronae make the surface brightness of emission directly from the winds incredibly low. Detecting winds directly then requires both high sensitivity and being able to disentangle light from stellar surface from that of the wind; note, *e.g.*, the low contrast of the wind of the star ϵ Eridani relative to the star in Figure 1.1. Instead, we usually rely on indirect methods of detecting and measuring stellar winds.

The most successful observational technique for winds is through Lyman-α (Ly-α) absorption measurements. This method takes advantage of the fact that the interstellar medium (ISM) that the fully-ionized wind interacts with can be partially neutral. Each of these materials decelerate in the region leading up to the interaction of the wind and ISM, leading to a pile up of the neutral ISM that appears blueshifted relative to the rest frame of the ISM. Thus, enhanced absorption in the blue side of Ly-α can be explained by the stellar wind; the combination of the ISM pressure and level of enhanced absorption can be used to estimate the rate of outflows and the stellar mass loss rate. The results of this suggest that young, main-sequence stars can have mass loss rates upwards of $100\,\dot{M}_\odot$ ($\dot{M}_\odot = 2 \times 10^{-14}\,M_\odot\,\mathrm{yr}^{-1}$). An apparent correlation between mass-loss rate with X-ray flux (Wood et al., 2005) imply that mass-loss does seem to decrease as stars age (or at least as the rotation rate slows), as has been suggested by rotational evolution models (Johnstone et al., 2015b; Johnstone et al., 2015a). All of this said, the stellar wind speed used to estimate the loss rate is assumed to be the same as the slow solar wind, and the previously mentioned models estimate much higher speeds for young stars.

Although the Ly-α technique has been informative, it is also limited due to the requirements that 1.) the ISM around the star actually be neutral, 2.) that we sufficiently understand the properties of the ISM at the star's location in order to appropriately attribute blueshift to the ISM's deceleration at the boundary of the stellar wind, and 3.) the conditions of the ISM (besides ionization state) at a given star's wind boundary are conducive to producing a detectable signal. As such, the sample of stars with winds that have been measured through this technique is relatively small ($\lesssim 100$ stars). However, there are few other techniques with which to confirm or expand upon Ly-α results, and even fewer that would be direct signatures of the wind as opposed to the wind's impact on the ISM. X-ray observations looking

for emission from charge exchange between the wind's heavy ions and the neutral ISM have seen recent success (Kislyakova et al., 2024). This method still depends on the wind's interaction with the ISM, but the signature is coming from the wind's material rather than the ISM's and agree with Ly-α derivations for the same stars within a factor of a few.

One method that does not rely on the ISM interactions at all is direct measurements of thermal emission targeted at radio wavelengths (Lim and White, 1996; Villadsen et al., 2014; Fichtinger et al., 2017; Suresh et al., 2020). The majority of detections of thermal radio emission from solar-type stars has been attributed to chromospheric material with the exception of Suresh et al. (2020)'s detection of coronal gyroresonant emission on ϵ Eridani; the winds themselves remain undetected and the associated mass-loss rates are upper limits. The difficulty in detecting stellar winds poses an interesting problem both with regards to stellar spin-down models as well as with respect to reconciliation of total mass loss when accounting for transient events like CMEs (Cranmer, 2017; Osten and Wolk, 2015).

1.2 Transient Events

Although the full picture of solar and stellar transient events and the sustainment of the quiescent environments is incomplete, each phase is important for contextualizing the other. This was hinted at by the similarity between the temperatures of flares and coronae of active stars, but what does the resulting high-density environment mean for CME propagation—does the CME gather mass, or is it stalled? If the latter case, then do CMEs actually contribute meaningfully to mass loss in young stars? Here, I provide an overview of flare mechanics and their relation to the occurrence and our interpretation of particle events.

Flares

Flares are the EM radiation originating from particles accelerated in the lead-up to, during, and following magnetic reconnection in the solar or stellar corona. As was mentioned previously, flares are a multi-wavelength phenomenon. The increasing temperature in the moments leading up to reconnection causes electrons to evaporate and fill magnetic loops, leading to pre-flare signals in the SXR, UV, and chromospheric lines. This manifests as overall flux enhancements as well as blue-shifted signatures. When reconnection occurs, the proximity to the energy release causes particles in the immediate vicinity of the reconnection point to produce hard X-ray (HXR) emission. Particles from the reconnection point are additionally

non-thermally accelerated along the remaining magnetic field lines—both those that remain as closed, post-flare loops as well as those that were “opened" to the upper atmosphere and IPM—producing a variety of coherent and incoherent radio signals. On their way down the magnetic field of the flare loops, the non-thermal electrons impinge upon denser material that eventually halt them; the sudden braking of the electrons produces an additional, non-thermal HXR signal.

The heating from the impinging particle beam (which may include both electrons and protons, Sadykov et al., 2024), the back radiation from the corona and upper chromosphere, and energy dissipation in the form of Alfvén waves are all expected to contribute to hot spots at the footpoints of the flare loop in the lower atmosphere (Matthews et al., 2003; Hudson et al., 2006; Fletcher and Hudson, 2008; Krucker et al., 2011). This heating is responsible for what is referred to as the white-light (WL) continuum component of flares, representing a 6,000–9,000 K blackbody for the Sun (Kretzschmar, 2011; Namekata et al., 2017), although this temperature may be much higher for younger or more active stars (Berger et al., 2024). The relatively-low filling factor of the footpoints on the solar surface, in addition to the low-temperature contrast between the flare and quiet photosphere, make the WL component a relatively-rare solar flare component to observe from the total solar disk. Although WL flare components are difficult to detect, they represent an exceptional fraction of the flare energy budget—as much as 70% of the total radiated energy (Kretzschmar, 2011). These processes and associated emissions are summarized in Figure 1.2.

Stellar observations rarely have the benefit of a suite of instruments observing an event simultaneously across the EM spectrum; the vast majority of our understanding of transient stellar activity from a multi-wavelength perspective comes from non-contemporaneous observations. For wavelengths from optical to X-rays, light curves of stellar flares often appear rather similar to solar flares; each usually show steep rises indicative of impulsive heating followed by exponential decays as the loop and footpoints cool. That said, the *scale* of the magnetic events for other stars can be orders of magnitude larger than has been observed for the Sun. The stronger magnetic fields on younger stars contain more magnetic energy that can be converted to radiative energy in the flare process. Additionally, the higher densities of the young stellar coronae provide more electrons to contribute to the X-ray signature and may exist at such high densities that flare loops themselves contribute appreciably to the WL component (Namekata et al., 2022a).

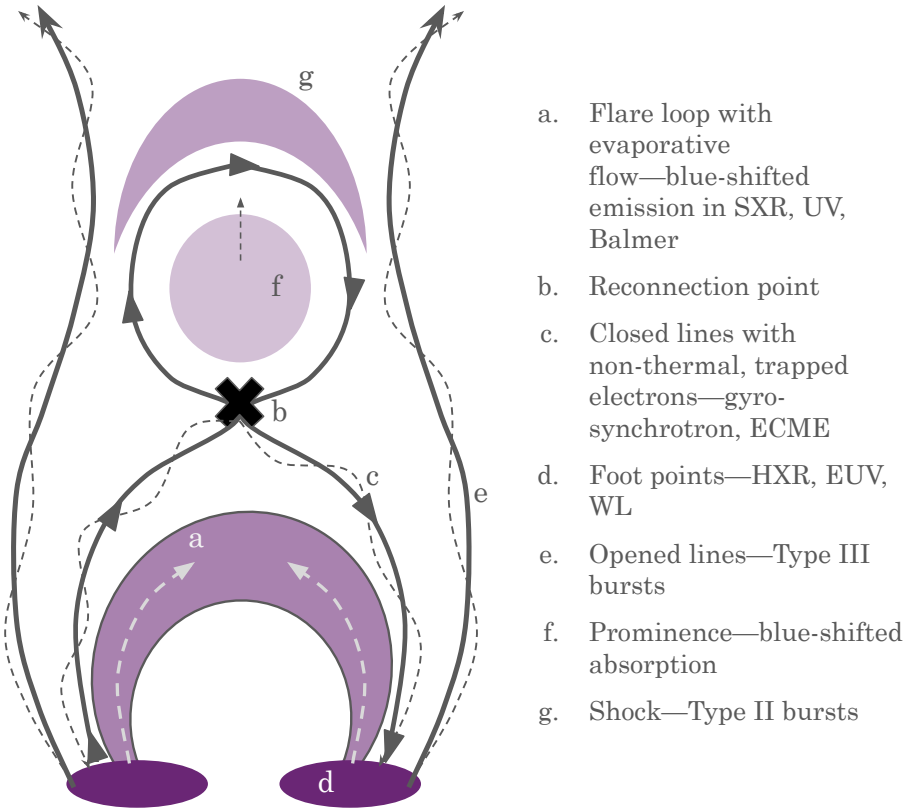

Figure 1.2: A standard model for flare, prominence, and CME geometry and the associated signals; dashed lines indicate particle motion. In this representation, the material indicated as a prominence (labeled f) can erupt as a CME if overlying magnetic field lines (not represented here) do not confine it.

Despite the difference in scales, the similarities between stellar and solar light curves in addition to similarities in the flare-frequency distributions of solar and stellar flares (*e.g.*, Aschwanden et al., 2000; Aschwanden, 2015) suggest that the stellar energy-release process is likely the same reconnection process we observe on the Sun. This is also supported at longer wavelengths, at $\approx$ 1–10 GHz specifically, where we see the GBR. Although some properties of solar and stellar flares—including their correlation with confined particle acceleration—seem to follow the same scaling relation, it is less straight-forward to assert the same for escaping transient particle events.

CMEs and SEPs

Often times following a solar flare—and essentially 100% of the time following a flare with energy $> 10^{30}$ erg—mass and magnetic fields will be expulsed from the corona as a CME. Field lines that are broken through magnetic reconnection and the CME propagating through overlying fields will accelerate particles. Both the CME and the particles tracing the opened fields can manifest as SEPs, with distinct durations, particle species, and energy distributions depending on the origin and duration of the acceleration. Like their quiescent counterpart, transient particle flux from stars other than the Sun is difficult to 1.) detect at all and 2.) attribute to the relevant atmospheric height. More specifically, it is exceptionally difficult to attribute signatures of particle motion to particles that are actually escaping into the IPM as opposed to those contained within flare-loops and non-eruptive prominences.

One common technique is the use of Doppler spectroscopy to identify highly-blueshifted absorption and emission components, either originating from the chromosphere (Vida et al., 2019; Namekata et al., 2021; Namekata et al., 2024a) or the corona (Argiroffi et al., 2019). These observations show line-of-sight (LOS) velocities upwards of 100s to 1000s km/s, but it is difficult to assert that a high speed—even those beyond the gravitational escape velocity of the star—is enough for the material to escape the magnetic potential of the star. Alvarado-Gómez et al. (2022a) has shown that the strong overlying magnetic fields of active stars may substantially decelerate or totally stall plasma motion in stellar atmospheres, preventing mass escape; this has even been observed for the Sun (Peng et al., 2022). There is also a strong dependence on the geometry of the event, which impacts both the morphology of the escaping material and the Doppler-shifted signal it produces. For instance, CMEs with a significant non-radial velocity component are more likely to be contained (Alvarado-Gómez et al., 2022a) and even if a CME manages to erupt, the signal may be highly or entirely red-shifted depending on the projection of the event (Moschou et al., 2019; Otsu et al., 2022). These stalling and projection effects—taken alongside the fact that many solar CMEs have velocities well below the surface gravitational escape velocity—means that blue-shifted signatures alone are not a reliable metric for mass escape, especially if the signature originates from atmospheric heights that could be associated with evaporative flow in the post-flare loop.

The other method that has seen some success is coronal dimming, where the coronal emission will decrease following a flare relative to the pre-flare baseline flux. One

way this signal can be produced is through mass loss; the X-ray or UV flux decreases due to the overall content of the corona decreasing (Veronig et al., 2021). An alternative dimming cause is through obscuration; cool, dense, overlying material blocks flux from the coronal material which could then presumably be associated with material escaping far into the solar atmosphere. This has been observed from the Sun in the microwave and UV (Gopalswamy and Yashiro, 2013; Xu et al., 2024b), but presumably could also manifest in the X-rays. That said, this method runs into a similar problem to Doppler spectroscopy, wherein evidence of mass motion does not necessarily mean mass escape.

There is a smattering of other methods that have been proposed and attempted, some of which have been summarized in Moschou et al. (2019) and Namekata et al. (2022b) and a larger collection of which are discussed in detail in the chapter I led for the Keck Institute for Space Studies' report on stellar particle environments. The difficulty is having a method that is sensitive to the CME (or its effects) when it is at a distance that is unambiguously associated with escape from magnetic containment in the stellar atmosphere. Such disambiguation may be achieved through the employment of exoplanetary signatures (Joseph et al., 2004; Alvarado-Gómez et al., 2022a) which would necessitate that material propagate far to influence the signals. It may also be possible to use future instrumentation like the next-generation Very Large Array (ngVLA) or Habitable Worlds Observatory (HWO) that may enable direct imaging. One method that has seen increasing attention is searching for stellar type II radio bursts, which are associated with CME shocks. I discuss this method in the following section as it relates to my work with the OVRO-LWA in this thesis.

All of this is to say: we understand very little about stellar CMEs and how this relates to the evolution of CMEs across solar history. Even less is known about other transient particle events that can manifest as SEPs. Mass estimates of stellar CMEs suggest that they may have been orders of magnitude more massive and energetic than modern solar CMEs. The frequency of prominence eruption signals on young stars like EK Draconis and AB Doradus suggest that these events may then contribute substantially to the overall mass loss and angular momentum evolution of stars (Aarnio et al., 2011; Xu et al., 2024a), so much so that they may contribute more to the mass loss rate than the winds themselves (Osten and Wolk, 2015; Cranmer, 2017). This then raises the question as to what point you distinguish between transient events and the quasi-steady wind. In the following section, I describe the emission processes I am considering when searching for these transient events.

1.3 Emission Processes

Because I am interested in identifying emission associated with both flares and bulk plasma escape, and because the emission processes for these two phenomena are quite different, I provide more details here on the nature and origin of the emission processes that are relevant for the work in the rest of this thesis. Relevant properties of the emission processes are summarized in Table 1.1.

Flares: Thermal Bremsstrahlung and Non-thermal Gyromagnetic Emission

As mentioned previously, flares play a key role in space weather both through their direct alteration of the environment via ionizing radiation as well as their association with CMEs and SEPs. The two key components of flares that are relevant in this thesis are 1.) the thermal bremsstrahlung that manifests as the WL component and 2.) the non-thermal gyromagnetic emission originating from electrons trapped in flare loops. I have already described the likely mechanisms that contribute to the WL component; here, I will focus on the gyromagnetic emission processes that arise from non-thermal electrons trapped in closed magnetic fields.

This emission is dependent on the magnetic field of the star and thus the spectral properties are related to the gyrofrequency $\nu_{\mathrm{B,\,rel}} = 2.8\,B/\gamma$ MHz where B is the magnetic field strength in Gauss and γ is the Lorentz factor. The actual peak frequency of the emission will occur at harmonics s of the gyrofrequency so that the peak frequency is $\nu_{\mathrm{peak}} \approx 2.8\,B\,\gamma^2$ MHz for large pitch angles between the electron velocity and the magnetic field. In the case that this frequency is much higher than the plasma frequency at the locale of production—and harmonics of the plasma at higher layers—then the emission can escape. It naturally follows then that the observational properties of gyromagnetic emission depends on both the energy of the electrons as well as the field and plasma properties of the emitting region. In the case that the electrons are mildly relativistic ($\gamma \lesssim 3$, electron energies 10–1000 keV), broadband emission known as gyrosynchrotron is produced. This is commonly reported for both solar and stellar flares and is the dominant emission mechanism for the “quiescent" coronae of active stars below $\sim$ 10 GHz (Güdel, 2002). The beaming effects due to relativistic aberration are only mild here, allowing for some preservation of the circular-polarization imprint of the magnetic field—gyrosynchrotron can have circular polarization fractions up to a few 10s of percent at frequencies where it is optically thin (Dulk and Marsh, 1982; Güdel, 2002). Despite a correlation with thermal X-ray emission, gyrosynchrotron (usually) originates from a non-thermal population following power-law energy distributions, with brightness temperatures

on the order of 10^{7-9} K.

In the case that electrons are highly relativistic ($\gamma >> 1$, electron energies $\gtrsim$ 1 MeV), the emission would be synchrotron. The highly-relativistic nature of the acceleration leads to quite significant differences from gyrosynchrotron; extreme aberration of the radiation field leads to any polarization being linear rather than circular, and the maximum brightness temperature is limited to $< 10^{12}$ K by inverse-Compton limitations (Readhead, 1994). The high γ factors paired with the likely strong magnetic field responsible for accelerating electrons to these energies means this emission is less commonly invoked for stellar flares at frequencies $\lesssim$ 10 GHz (although is not unheard of, Lim et al., 1994), and is likely only relevant for solar flares in the sub-mm regime (Nindos, 2020). The question is how to achieve the high-energy electron distribution. Although the reconnection process itself imparts a power-law distribution of electron energy observable in HXR spectra (Reid et al., 2014), electrons trapped in the fields can also be repeatedly reflected due to the magnetic gradient between the loop top and footpoints that can facilitate a high-energy power-law that may be sufficient to produce synchrotron.

Because the magnetic field only responds to the perpendicular velocity component of a charged particle, particles with a large parallel velocity component—or, rather, a small pitch angle—may escape the magnetic field during this reflection process, leading to a distribution of particles with preferentially large pitch angles known as the loss-cone anisotropy. This anisotropy can develop into a significant population inversion that leads to coherent masing in the form of electron cyclotron maser instability emission (ECME) (Wu and Lee, 1979; Hewitt et al., 1982). The resulting emission is inherently brief and narrowband, emitting at a frequency equal to the gyrofrequency at the location of excitation. However, the signal can appear apparently broadband because many regions may emit essentially simultaneously. The specificity of the electron pitch-angle distribution also leads to a unique emission geometry, where emission is originates from the walls of a cone with an opening angle parallel to the field line, and the coherence of the emission allows for exceptionally high polarization (up to 100%) and brightness temperatures (up to 10^{18} K). All of these features make ECME incredibly distinct from the other forms of gyromagnetic emission and allows it to serve as a test of, *e.g.*, field topology as well as put limits on plasma density local to the flare loop (Kavanagh et al., 2024).

On the Sun, ECME is associated with “spike-bursts" (Melrose and Dulk, 1982; Cliver et al., 2011), which are both the most luminous bursts at frequencies $\gtrsim$ 1 GHz

and are associated with strong solar flares (White et al., 2024); this is discussed in more detail in the stellar context in Chapter 2. It is also one of several mechanisms that has been attributed to some solar type IV bursts, a rare type of burst that may sometimes be driven by some element of the CME (Morosan et al., 2019). There have even been some reports of stellar equivalents of type IV bursts by Zic et al. (2020) and Mohan et al. (2024b). However, the unclear nature of type IV bursts' association with CMEs in addition to (or perhaps owed to) their relative rarity, lead to me focusing on ECME as it manifests for flares rather than CMEs.

CMEs and SEPs: Plasma Emission

The critical emission process I am considering with respect to bulk plasma motion is plasma emission. Like ECME, it is a masing process that can reach high intrinsic circular polarizations and brightness temperatures $\approx 10^{18}$ K (Melrose, 1989). However, rather than a loss-cone anisotropy, it derives its energy from the bump-on-tail instability caused by electron beams propagating through an ambient plasma environment (Dulk, 1985; Reid and Ratcliffe, 2014). It is also at minimum a two-step process: after the bump-on-tail instability produces Langmuir waves, they must be converted into transverse waves so that they actually produce EM emission. This is presumably done by scattering off of other waves—either Langmuir or ion sound waves—or by decaying into multiple wave modes. For the Sun, the beams typically manifest as electrons accelerated along field lines at velocities $0.1\,\mathrm{c} \lesssim v \lesssim 0.5$ c or as a CME plasmoid/ prominence core moving $>>$ 100 km/s. Langmuir waves get excited at the plasma frequency $\nu_\mathrm{p} = 9.8\,\mathrm{kHz}\sqrt{n_e}$ of the ambient plasma at the locale of the beam, where n_e is the electron number density with units cm^{-3}. Because of how the frequency scales with plasma density, the beam will excite lower-frequency emission as it propagates to higher parts of the solar atmosphere. As such, plasma emission can serve as a great indicator of bulk plasma motion as well as a diagnostic of the properties of the ambient particle environment of a star—a stellar property that is notoriously difficult to constrain.

The gradual decrease in frequency with time as the beam propagates outwards produces characteristic sweeping structures in a spectrogram or dynamic spectrum (see Figure 1.3). The spatially-broad nature of CMEs allows for the simultaneous excitation of many frequencies and their relatively low speeds causes a slow drift to low frequencies. The result is a slowly-drifting, broadband structure in a dynamic spectrum referred to as a type II burst. Although we do not currently understand all of the conditions required to produce a type II burst, we notably do not observe

type II bursts unless the CME or prominence drives a super-Alfvénic shock (Klein, 2021). Because the magnetic field is stronger at lower atmospheric heights, the Alfvén velocity is higher and thus the material must move much faster to produce the required shock for the type II burst. Being able to move super-Alfvénically may be a limiting factor for type II burst production on young stars with exceptionally strong fields and similarly high Alfvén speeds. That said, we may be able to take advantage of young stars having dense winds—a CME has to travel much further from the star than it would from the Sun to excite a given frequency and would similarly be at height where the Alfvén speed is small, alleviating the super-Alfvénic shock problem. Additionally, type II bursts appearing at frequencies that we would normally associate with shocks in the low solar corona would very likely be at a distance from the star that we can safely say the material has escaped into the star's IPM. This is in incredible contrast to Doppler spectroscopy and coronal dimming that are restricted to low heights in the stellar atmosphere.

On the other hand, if the beam is a group of electrons accelerated along magnetic field lines, the spatial distribution is much narrower (at least low in the corona). The much higher speeds of the beam paired with the small spatial scale produce a narrow, steeply-drifting structure in a dynamic spectrum called a type III burst (right panel in Figure 1.3). These are the most common type of solar radio burst, owed to them requiring low-energy acceleration events compared to type II bursts; essentially all flares produce type III bursts (Bastian et al., 1998). That said, the peak flux density that has been observed for type III bursts is exceptional—on the order of 10^{10} Jy for frequencies $\lesssim$ 200 MHz (Saint-Hilaire et al., 2013) and as high as 10^{11} for frequencies below 100 MHz (Raja et al., 2022). Notably, the distribution of type III flux densities varies throughout the solar magnetic cycle, peaking during solar maximum (Saint-Hilaire et al., 2013). This may be attributed to the increased number of active regions that type III bursts are known to propagate from, which bodes well for stellar expectations; even if there may be physical limits that saturate plasma emission for an individual beam, the presence of many beams may compensate to produce exceptionally luminous stellar type III bursts. Their association with flares rather than CME shocks also perhaps makes them a more likely candidate for detections from other stars since we are more likely to see a flare signature than a CME signature.

Overall, plasma emission as we see it from the Sun has promising applications for understanding stellar environments and transient mass loss rates. That said, there

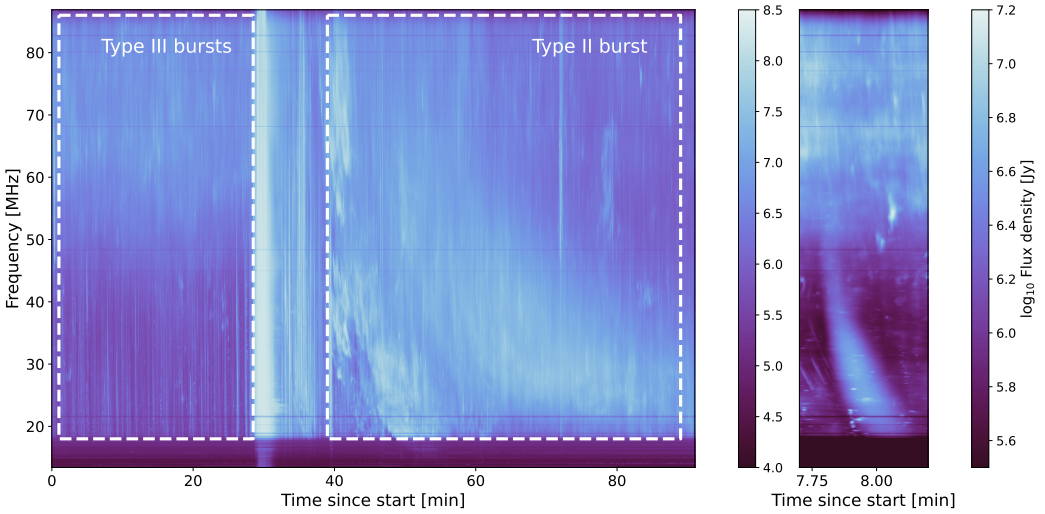

Figure 1.3: A dynamic spectrum of the Sun, collected by the beamforming observing method of the OVRO-LWA (discussed in detail in Section 3.2). In the left panel, there is a collection of type III bursts and a type II burst. A close-up of a single type III burst is shown on the right to show the sweeping structure evident at lower frequencies. Persistent, non-drifting emission above ≈ 50 MHz may be associated with type IV burst continuum emission.

are few if any candidate detections of such emission from any star other than the Sun (Osten and Bastian, 2006). This perhaps could be because of the nature of the stars that have historically been targeted. These have been primarily highly-active M-dwarfs with strong fields that may both inhibit shock development at the relevant frequencies as well as preferentially produce magnetic emission over plasma emission (Villadsen and Hallinan, 2019). As such, our expectations for plasma emission has been informed primarily by the distribution of events we see from the Sun. The validity of these expectations are explored in Chapter 5.

1.4 Summary

The study of stellar space weather, and especially what that means for the habitability of exoplanets, has focused largely on the EM radiation environment. This is owed to the exceptional difficulty of studying stellar particle environments and is exacerbated by the current ambiguity in whether observations of coronal mass motion can be attributed to coronal mass *escape*. The transient nature of CMEs and flares additionally require a substantial amount of time dedicated to individual targets to maximize the likelihood of observing such an event. Taken together with the multi-wavelength nature of both of these phenomena, this science case

Table 1.1: A summary of the various emission processes that are relevant in this thesis. The first four processes are typically associated with the flare loop structure, while plasma emission is associated with material propagating into the IPM. P_C and P_L refer to the level of circular and linear polarization, respectively, although I note here that ECME can may be elliptically polarized, showing significant fractions of both circular and linear polarization. The temperature reported thermal free-free emission is for the flare itself and not the photospheric effective temperature.

Emission process	Characteristic spectral range	Relevant temperatures	Polarization	Relevant chapters
Thermal Free-free	$\approx$ 10–1000 nm	$\approx$ 6–30 kK	–	2, 4, 5
Gyrosynchrotron	$\gamma^2 2.8\,B$ MHz, $\gamma \lesssim 3$	$< 10^{10}$ K	$P_C \lesssim 50\%$	2
Synchrotron	$\gamma^2 2.8\,B$ MHz, $\gamma >> 1$	$<< 10^{12}$ K	$P_L \lesssim 10\%$	2
ECME	$2.8\,B$ MHz	$\lesssim 10^{18}$ K	$P_C \lesssim 100\%$	2
Plasma	$9.8\sqrt{n_{e^-}}$ kHz	$<< 10^{18}$ K	$P_C \approx 10$s%	3, 5

requires a substantial amount of observing time across a variety of instruments in order to robustly constrain not only a single event's properties, but the properties of the distribution of events. With this in mind, my work has been focused on constraining properties of non-thermal particle acceleration in the radio and how they are related to the thermal signature of flares in the optical. This is done both through non-contemporaneous observations which investigate a part of the GBR parameter space previously unaccessed for solar-type stars (Chapter 2) as well as simultaneous monitoring campaigns to search for flares and associated CMEs and SEPs (Chapters 3–5). What will ultimately be illustrated is just how different the behavior of solar-type stars is from the Sun, the considerable power of using the optical and radio in tandem, and the criticality of expanding dedicated observations across the rest of the spectrum.

Chapter 2

A TRANSIENT POPULATION OF SOLAR-TYPE STARS AT GHZ FREQUENCIES

Adapted from

Davis, I., G. Hallinan, C. Ayala, et al. (Aug. 2024). "Detection of Radio Emission from Super-flaring Solar-Type Stars in the VLA Sky Survey." In: *arXiv e-prints*, arXiv:2408.14612, arXiv:2408.14612. DOI: 10.48550/arXiv.2408.14612. arXiv: 2408.14612 [astro-ph.SR].

2.1 Abstract

Solar-type stars have been observed to flare at optical wavelengths to energies much higher than observed for the Sun. To date, no counterparts have been observed at longer wavelengths. I have searched the Very Large Array Sky Survey (VLASS) for radio emission associated with a sample of 150 solar-type that exhibit superflares in the Transiting Exoplanet Survey Satellite (*TESS*) data. Counterparts to six of these stars were present in VLASS as transient or highly-variable radio sources. One of the stars is detected in all three VLASS epochs, exhibiting an unprecedented level of apparently persistent radio emission. The engine for this radio emission is unclear, but may be related to accretion, a binary companion, or the presence of large-scale magnetic fields. Two stars show radio emission with $> 50\%$ circular polarization fraction, indicating a coherent emission process likely being present. We find that the VLASS-detected stars may predominantly emit non-thermal, incoherent emission and tend to have higher flare rates and energies than the rest of our *TESS* sample. This, in addition to the VLASS-detected stars apparently adhering to the Güdel-Benz relation, suggest that the radio emission may be associated with superflares. These results suggest that the superflare phenomenon on solar-type stars extends to radio wavelengths, tracing particle acceleration. These data provide the first window on the luminosity function of radio superflares for solar-type stars and highlights the need for coordinated, multi-wavelength monitoring of such stars to fully illustrate the stellar flare-particle relation.

2.2 Introduction

As discussed in Section 1.2, flares resulting from the release of stored magnetic energy are essentially ubiquitous across main-sequence stars with convective envelopes. While the most energetic flares we see from the Sun are on the order of $\sim 10^{32}$ erg (Woods et al., 2006), other solar-type stars (*i.e.*, stars with temperatures between 5,600-6000 K) have been found to experience superflares– flares in excess of 10^{33} erg. Superflares had been considered exceptionally rare (Schaefer et al., 2000), but the identification of nearly 400 superflares among $\sim$ 150 solar-type stars, including slowly-rotating stars (stars with periods greater than 10 days), in *Kepler* data by Maehara et al., 2012 allowed for the beginning of a rigorous, statistical analysis of the occurrence rate of superflares on solar-type stars and solar analogs. Using a larger set of *Kepler* data, Notsu et al., 2019 and Okamoto et al. (2021) estimate a slowly-rotating, solar-type star may have a 10^{34} erg superflare every few thousand years and that this energy may represent the upper limit of the flare energy that a slowly-rotating star is able to produce. More recently, Vasilyev et al. (2024) has predicted superflare rates on the order of once per century with energies reaching as high as 10^{36} erg. These results are roughly supported first-principles calculations by Shibata et al., 2013. Alternatively, solar-type stars with periods less than a few days can produce flares with orders-of-magnitude higher energy and much more frequently (Davenport, 2016; Tu et al., 2020; Doyle et al., 2020).

These results have important implications when considering possibly-associated particle escape in the form of CMEs and SEP events, especially in the context of habitability and abiogenesis (Airapetian et al., 2016; Airapetian et al., 2020). Although there are no empirical relations for correlating stellar flares with stellar CME occurrence, solar relations lead us to suspect that younger, more active stars with more energetic flares would also have more energetic CMEs and that this may have important implications for both the rotational evolution of the Sun (Skumanich, 1972; Xu et al., 2024a) and the particle environment that a young earth might have been subjected to. Alternatively, relationships between solar flares and CMEs may break down for active stars with stronger, large-scale magnetic fields which may suppress mass escape (Alvarado-Gómez et al., 2022a).

Radio emission at frequencies below a few GHz can provide a window into particle acceleration in stellar coronae. This is supported by the Güdel-Benz relationship (GBR) which shows that the quiescent radio luminosity of binaries and G, K, and M stars have a correlation with their quiescent soft X-ray luminosity, defined in the

$\approx 0.2 - 2$ keV range (Guedel and Benz, 1993). The GBR also holds for flare-related emission both from stars and from the Sun (Benz and Guedel, 1994). Because the dominant radio emission process in the GBR is gyrosynchrotron and thus incoherent, the relationship can break down when the emission process is coherent– either plasma emission or ECME. This occurs on the Sun for a significant fraction of the most extreme radio burst events (solar radio bursts with flux densities $> 10^8$ Jy) at 1 GHz. The distinct spike structure of these bursts in dynamic spectra, high circular polarization fractions ($P_V > 50\%$), and high brightness temperatures ($T_B \gtrsim 10^{12}$ K) preclude an incoherent process. These bursts' association with particularly strong flares may be indicative of a fundamental shift in the conditions and acceleration processes responsible for producing the brightest radio bursts (Gary, 2019; Cliver et al., 2022; White et al., 2024).

Although a broad range of radio emission associated with flare activity has been observed for especially magnetically-active stars like UV Ceti variables (Spangler and Moffett, 1976; Osten et al., 2005; Zic et al., 2020), there has been no observed radio counterpart to the stellar superflare phenomenon on solar-type stars. Because of this, it remains unclear whether the GBR holds for these events, if there is a divorce from the relationship that could be indicative of a transition in emission process from incoherent to coherent for highly-energetic events, and what this might mean for the type of particle acceleration occurring and its impact on the surrounding stellar environment. Addressing this requires dedicated, coordinated observations of solar-type stars at wavelengths sensitive to flares (*i.e.*, optical, ultraviolet, and X-ray) and at radio frequencies to identify for what flares and radio bursts—if any—that the relationship breaks down like it does for extreme solar radio bursts. Although flares are magnetic phenomena and hence associated with active regions, the actual energy release in the flare process is stochastic (Davenport, 2016; Aschwanden et al., 2018; Struminsky et al., 2020). Guaranteeing a detection of a superflare from even an incredibly active star can require days of observing time dedicated to that star. Without dedicated, multi-wavelength monitoring of stars, the detection of the radio analogs to the superflare phenomenon relies on wide-field survey data.

This survey requirement has been partially accommodated by surveys like the Low-Frequency Array (LOFAR) Two-metre Sky Survey (LoTSS) (Shimwell et al., 2017; Yiu et al., 2024), surveys from the Australian Square Kilometer Array Pathfinder (ASKAP) (Pritchard et al., 2021; Pritchard et al., 2024), and the Very Large Array Sky Survey (VLASS) (Lacy et al., 2020). Ayala et al. (in preparation) have

recently identified $\sim$ 80 radio transients associated with stellar counterparts. Two of these stars are young, solar-type stars that produce superflares as observed by the Transiting Exoplanet Survey Satellite (*TESS*, Tu et al., 2020; Doyle et al., 2020). Inspired by these detections, I searched through two VLASS epochs informed by an existing catalog of known *TESS* superflare stars. I used the work of Tu et al. (2020) and Doyle et al. (2020)—both of whom focused on identifying flares from solar-type stars in the first year of *TESS* observations—to build a list of 150 stars to search for radio emission in VLASS as described in Sections 2.3 and 2.4. Of these stars, I find radio emission from four additional stars, bringing the total number of *TESS* super-flaring stars with an identified VLASS counterpart to six. A summary of these stars is provided in Table 2.1.

2.3 Data and Selection

Because I am interested in the radio counterpart to the superflare phenomenon in solar-type stars and investigating whether the radio emission is similarly prevalent, the sample of stars I search for emission in VLASS are those identified to have flares in the catalogs of Tu et al. (2020) and Doyle et al. (2020). Both of these catalogs focus on solar-type stars during the first year of *TESS* data. This search is motivated by the stars that showed up in Ayala et al. (in preparation) that were also present in these catalogs (HD 245567 and HD 156097). A summary of the data and source selection criteria are provided in this section.

VLASS

With a survey speed of $\sim$ 23.83 square degrees per hour to a depth of $\sim$ 120μJy/beam, VLASS presents the 2-4 GHz sky above -40° declination to a sensitivity of 120μ Jy for each of three epochs (Lacy et al., 2020) spaced by $\approx$ 32 months. This survey is being conducted in the B and BnA configurations of the VLA, providing a spatial resolution of $\sim$ 2.5". At the time of this work, VLASS had completed the first two epochs and first half of the third epoch. The combination of spatial resolution, large sky coverage, and multi-epoch nature of VLASS has made it an exemplary resource for looking for radio transients (Dong et al., 2021; Dong and Hallinan, 2023; Somalwar et al., 2025).

The massive scale of VLASS—$\sim 10^{11}$ synthesized beams in each epoch-—makes doing blind transient searches onerous. Because of this, the transient-identification requirements that Ayala et al. (in preparation) chose were stringent and only focused on identifying stellar transients in VLASS epoch 2 (E2); they set a $7\sigma_{2,i}$ threshold

Table 2.1: Information on the six *TESS* super-flaring stars found in VLASS. The associations in the third column have certainties > 70% as calculated by Banyan (Gagné et al., 2018); the full names are Tucana-Horologium association (THA), Columba (COL), and Upper Centaurus Lupus (UCL). Here, TIC is the *TESS* input catalog number, d is the distance to the star, R is the stellar radius reported by Gaia Collaboration et al. (2018) in solar radii, $R_\odot$, and $T_{\rm eff}$ is the effective stellar photospheric temperature as reported by Gaia Collaboration (2022). P is the period we found from the box-least-squares periodogram of the *TESS* data from the `lightkurve` package and the solar rotation period is at the period at the equator. Ro is the Rossby number calculated using equation 11 in Corsaro et al. (2021). The Max Energy is the largest *TESS* flare energy we calculated for the star and $N_{\rm fl}$ is the number of *TESS* flares we identified for a star. The energy, flare number, and flare rate calculations are all described in Appendix A.2. The Median Star row refers to the median value for the sample of 150 *TESS* super-flaring stars. HD 245567 and HD 156097 are the stars identified in Ayala et al. (in preparation)'s blind search for stellar radio emission.

Star	TIC	Association	d	R	$T_{\rm eff}$	P	Ro	Max Energy	$N_{\rm fl}$	Flare rate
			pc	$R_\odot$	K	d		$\log_{10}$(erg)		$\rm yr^{-1}$
HD 22213	93122097	THA	51.378	1.01	5456	1.393	0.0292	34.64	9	77
HD 295290	53417036	COL	60.526	0.98	5554	1.522	0.0295	35.73	26	217
AT Col	144499196	Field	75.802	1.26	5291	2.507	0.0479	36.08	40	159
HD 245567	52588257	Field	106.533	1.53	5362	1.498	0.0301	35.50	14	59
HD 156097	152346470	Field	115.504	1.44	5844	1.976	0.043	35.92	31	246
HD 321958	79358659	UCL	172.765	1.26	5626	1.466	0.0289	36.41	16	130
Median *TESS* Star	—	—	121.759	1.05	5528	2.027	0.0387	35.41	6	56
Sun	—	—	—	1.00	5772[a]	25.67[b]	0.496[c]	—	—	—

[a]Prša et al., 2016
[b]Lang, 2013
[c]Corsaro et al., 2021

for identifying point sources in E2 and that the source *not* be detected ($< 3\sigma_{1,i}$) in VLASS epoch 1 (E1), where $\sigma_{j,i}$ is the noise of the VLASS pointing i containing the star's coordinates in epoch j. A radio source was considered very likely stellar in origin if it was within 1" of the proper-motion-corrected Gaia position of a star. Rather than a blind radio search, I searched for VLASS sources associated with a pre-existing sample of only a few hundred flaring stars. Because of this, my detection threshold is much less strict; I still use the requirement that radio sources are within 1" of the the proper-motion-corrected Gaia position of a star, but the source need only be $\geq 4\sigma_{j,i}$ in *either* epoch (see Section 2.4 for more details). Thus, in principle, my search could also be sensitive to quiescent emission.

Flaring Solar-Type Stars in *TESS*

TESS's photometric precision for bright targets ($\sim$ 70 parts-per-million (ppm) for 1 hr integration in the I_C band), huge field of view ($24^\circ \times 96^\circ$) (Ricker et al., 2014), and persistent observing has made it an exceptional tool to expand our understanding of flares and the kinds of stars that produce them (*e.g.*, Günther et al., 2020; Tu et al., 2020; Doyle et al., 2020; Pietras et al., 2022; Feinstein et al., 2022). *TESS*'s red (600-1000 nm) bandpass was chosen to optimize precision of transits around M-dwarfs. Because flares peak in the bluer part of the spectrum than the stellar surface, and because the photospheres of solar-type stars are larger than M-dwarfs, the contrast of flares on solar-type stars is much lower than for flares on M-dwarfs; generally, *TESS* can only detect extremely high-energy flares on solar-type stars. Although *Kepler*'s bluer bandpass may be sensitive to a broader range of flare energies there is much smaller overlap of the sky covered by VLASS (Koch et al., 2010; Lacy et al., 2020); *TESS* has a much larger sky overlap with VLASS, even from just *TESS*'s first year of observing. Tu et al., 2020 and Doyle et al., 2020 have used the *TESS* 2-minute cadence light curves to analyze flares from solar-type stars observed by *TESS*'s first 13 sectors. From this data, Tu et al. (2020) identified 1216 superflares on 400 stars and Doyle et al. (2020) find 1980 flares from 209 stars.

Of the 400 stars in the Tu et al. (2020) sample, only 112 also show up in the Doyle et al. (2020) collection. The discrepancy in the sources that show up in the catalogs is due to the two studies having slightly different selection criteria for solar-type stars as well as different procedures for flare identification, classification, and reporting. Perhaps most significantly, Tu et al. (2020) only considered superflares specifically– they did not include flares with energies $< 10^{33}$ erg in their analysis while Doyle et al. (2020) consider flares as low-energy as apparently 10^{31} erg. The

energies reported in each catalog are also impacted by differences in their energy calculation; while both catalogs implicitly assume that the flare temperature is the same as the quiescent stellar temperature, Doyle et al. (2020) accounted for the *TESS* band when estimating the bolometric flux from the stars while Tu et al. (2020) estimate flare energies by calculating the bolometric energy from the quiescent stellar temperature. Although the actual stellar flare temperature can be much higher than the $\approx 10,000\,\mathrm{K}$ that is often assumed in flare energy analyses (Berger et al., 2024), excluding any temperature difference between the photosphere and flare leads to underestimating the bolometric energy of the flare. This likely especially affects Tu et al. (2020)'s catalog, which focused specifically on superflares and so required flares be $> 10^{33}$ erg to be included in their catalog. I provide a deeper discussion of this underestimate in Appendix A.1. There are additional discrepancies in the stars that each catalog considered based on different definitions of solar-type as well as Tu et al. (2020)'s attempt to exclude multi-star systems or *TESS* light curves that would have been contaminated by additional bright stars in the TESS point spread function (PSF).

The first year of *TESS*'s operations focused on the southern hemisphere and had a maximum declination of $\approx 15°$. Because VLASS has a minimum declination of $-40°$, only $\approx 55\%$ of the sky covered by VLASS had been covered by *TESS* when Tu et al. (2020) and Doyle et al. (2020) produced their superflare star catalogs. 74 of the 209 flaring stars reported in Doyle et al. (2020) and 146 of the 400 flaring stars reported by Tu et al. (2020) were in a field covered by VLASS. Accounting for stars that showed up in both catalogs, there was a total of 180 stars between the two catalogs that were in fields covered by VLASS.

Addressing Binarity

For isolated, solar-type stars, the spin evolution of the star is driven by magnetic braking, wherein angular momentum is lost to stellar winds and mass ejections interacting with the stellar magnetic field (Skumanich, 1972). In binary systems, tidal interactions can also modify the rotational evolution, resulting in rapid rotation for compact binaries. Gyrochronology is moot as an age tracer in these systems. Examples include RS CVn (Hall, 1976) and some Algol-type systems (Richards, 1992). Because I am interested in stars that may be representative of a young solar system, I want to exclude any systems whose histories or activity may be significantly affected by a stellar companion.

Work by Fleming et al. (2019) suggests that low-mass stars ($M \lesssim M_{\odot}$) can tidally interact out to orbital periods of 100 days. This is roughly consistent with synchronous timescales described in Zahn (1977), assuming a second degree Love number $k_2 \approx 0.5$ (Fleming et al., 2019) and a ratio between the stellar moment of inertia to the moment of inertia of a ring of ≈ 0.07 (Claret and Gimenez, 1989). For binaries composed of solar-mass stars, this then requires that the stars be separated by $\gtrsim 0.5$ AU.

For all 180 stars from Tu et al. (2020) and Doyle et al. (2020)'s catalogs that were covered in a VLASS field, I checked the classification as listed on SIMBAD (Wenger et al., 2000) to identify RS CVns. I also checked the Gaia DR3 non-single star (NSS) catalog (Gaia Collaboration, 2022), the Washington Double Star (WDS) catalog (Mason et al., 2001), and the spectroscopic binary orbit catalog (Pourbaix et al., 2004) in order to identify as many binaries as possible where the orbit may have played a significant role in the rotational properties of the star. Any star that was reported by Gaia Collaboration (2022) or Pourbaix et al. (2004) to have an orbital period < 100 days was flagged as a binary. Additionally, I required that the quality grade provided for the binary in Pourbaix et al. (2004) be 3 or higher[1]. I used the largest angular separation between physical binaries to investigate binarity in the WDS catalog; any angular separation that would correspond to < 1 AU would be flagged as a binary. However, all of the binaries in my sample that were listed in the WDS catalog were > 10 AU.

Of the 180 stars, four were identified as RS CVns: HD 217344, TY Col, AI Lep, and V1198 Ori. An additional 23 stars were identified as having orbital periods < 100 days, for a total of 27 binaries that might be tidally interacting, reducing our sample size to 153 targets. It is worth emphasizing that although this work ruled out several definitive binary stars, it is difficult to definitely rule out binarity and there very well could still be binaries contaminating the sample. The final collection of *TESS* data used in this work can be found in MAST[2].

2.4 Methods and Results

Tu et al. (2020) report the occurrence time and duration of the flares so that I could implement my own energy calculation method for each flare as outlined in Appendix

[1] This refers to the quality of the orbit calculation, ranked from 0 to 5, with 0 being a poor estimate and 5 being definitive. Although Pourbaix et al. (2004) does not give a recommended quality cutoff, grade 3 corresponds roughly to the mean value of available quality assignments as well as the average quality assigned to orbits in catalog (3.45).

[2] [10.17909/8g1x-8945]http://dx.doi.org/10.17909/8g1x-8945

A.1. By contrast, Doyle et al., 2020 do not report information for individual flares. Because of the discrepancies in how the two teams calculated flare energy and reported flare information, and because consistency in flare energy estimation is important for the purposes of my analysis, I produced my own flare-identification and analysis pipeline to run on all 153 assumed single stars that exist in a VLASS field presented by the two catalogs. In this section, I briefly review the flare-identification process as well as my VLASS-source identification method.

TESS Flare Identification and Characterization

My method of identifying flares in *TESS* Science Processing Operations Center (SPOC) light curves closely follows the methodology outlined in Section 3.1 of Jackman et al. (2021). In this method, stellar light curves are iteratively de-trended by applying a median filter to data and flagging points $> 3\sigma$ in order to produce a light curve that has had all flares and eclipses removed. The raw light curve is then divided by this flagged light curve to remove the effects of, *e.g.*, starspots on the flux. Flare candidates are identified in this de-trended light curve and then checked by eye to confirm they are flares. I provide a more in-depth explanation for this method, the flare-energy calculation, and the flare-rate calculation in Appendix A.2. The code I wrote and used for this analysis is available for use on GitHub[3].

Across the 153 stars and all currently completed *TESS* sectors (up to sector 65), the code identified 1,579 flares, 86 of which, I concluded, were not real flares after checking each flare by eye. The total number of flares is then 1,493. The nature of our flare-detection criteria (*i.e.*, that a certain number of consecutive points be three standard deviations above the normalized light curve) resulted in a minimum energy of $\approx 10^{33}$ erg for a flare to be identified for stars of this temperature range and therefore all of the flares qualify as superflares. There were three stars for which the flare-finding code found no flares: TIC 328349131 (TYC 58-209-1), TIC 1258935 (TYC 6027-806-1), and TIC 57719552 (TYC 7216-55-1). For each of these stars, I inspected the entire *TESS* light curve by eye. There is a possible flare for both TIC 328349131 and TIC 1258935, but these flares occur at the very end of a light curve segment I had flagged. For TIC 57719552, there is a flare candidate peaking at 1589.3477 BTJD, but it had an insufficient number of 2.5σ points to be identified as a flare. Although the flare candidates for these stars may very well be actual flares, I did not find it appropriate to find all flares that may have been missed across the other 150 stars. Therefore, I exclude these three stars from my sample. My final

[3] `https://github.com/iveydavis/flare_id/`

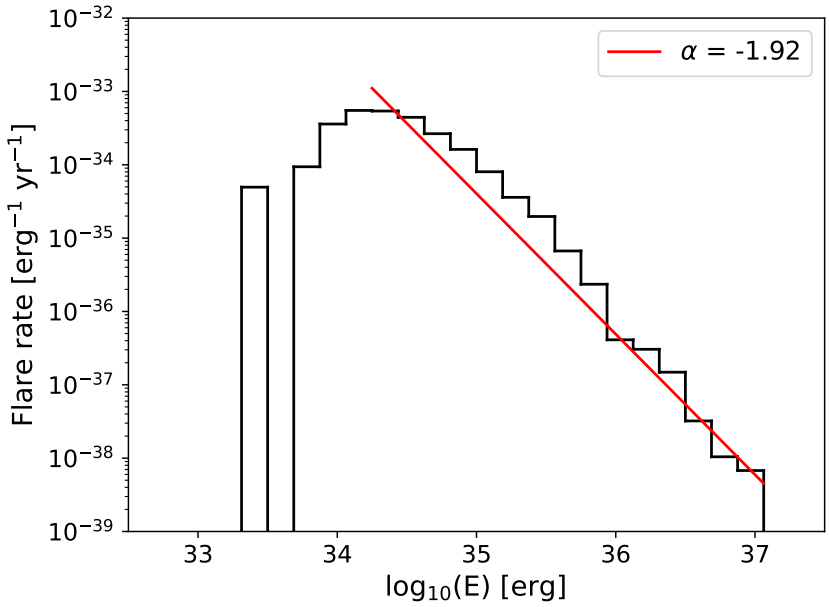

Figure 2.1: The FFD (black) for the 1,493 flares we identified across 150 solar-type stars. The FFD for flares above 10^{34} erg is best fit by a power law index of -1.92 (red).

sample to look for bursts in VLASS is then 150 stars.

As a rudimentary validation of the flare characterization method, I look at the flare frequency distribution (FFD) for the flare energies I calculated (see Figure 2.1). For this FFD, I used thirty bins evenly-spaced in log space between 10^{33} and 10^{38} erg, count the number of flares that are present in each bin, and divide these counts by the total amount of time spent on the 150 stars I identified flares for. I fit a line for the bins in the $10^{34.07-37.17}$ erg bin range using a least-squares method. The lower end represents the “turn-over" point in the FFD, below which the positive power-law index is likely due to detection bias—lower energy flares are still likely more-commonly occurring than higher-energy flares in this positive-power-law range, but they are less likely to be detected due to instrument sensitivity and our flare-identification requirements. The upper energy limit in the FFD fit arises from the last bin that had a non-zero flare count. From this, the slope of the FFD for flares with energies $> 10^{34}$ erg follows a power law index of ≈ -1.9, which is consistent with other studies of superflares from solar-type stars by, *e.g.*, Maehara et al. (2012), Shibata et al. (2013), and Maehara et al. (2015) and is also consistent with the -1.5 to -1.9 value found for solar flares in the 10^{24-32} erg range (Aschwanden et al., 2000).

VLASS Burst Identification

For each of the 150 stars that lie in a VLASS field, I downloaded $2' \times 2'$ cutouts for both VLASS epochs 1 and 2 from the CIRADA Cutout Image Web Service for a total of 300 cutouts to search for stellar radio emission. I identified sources in these cutouts using the `findsources` function in `CASA`[4] version 6.5.2-26 (CASA Team et al., 2022). Sources less than 4σ were excluded, where σ was determined by the root-mean-square (RMS) property of the `statistics` function applied to the CIRADA frame. For each frame, I used the observation date from the CIRADA cutout header and proper motion values from Gaia eDR3 (Gaia Collaboration, 2020) to calculate the proper-motion-corrected position of the star that should be in the frame.

While VLASS has 2.5" spatial resolution, the quick-look images from CIRADA have a pixel size of 1", similar to the survey's maximum positional uncertainty $\approx$ 1" (*e.g.*, VLASS memos 14[5] and 17[6]). Because of this, VLASS sources reported by `findsources` that were $d\theta > 1$" from the star's Gaia position were considered emission not associated with the star. CIRADA frames where there was a source coincident with the star's position were then inspected to confirm convergence of a 2D-gaussian point-source model at the location of the source using `CASA`'s `imfit` function. We expect these sources to have a RMS positional error of $\theta_{\rm RMS} = \theta_{\rm FWHM}{\rm SNR}^{-1}(2\ln 2)^{-1/2}$ where $\theta_{\rm FWHM} = 2.5$" is the beam size and SNR is the signal-to-noise ratio of the source (Condon, 1997). All of my sources have $d\theta < 1.5\sigma_{\rm SNR}$, making me reasonably certain the radio emission is coincident with the associated star's position.

Across the 150 stars and between the two VLASS epochs I searched for radio emission, this method found eight VLASS sources coincident with the position of six stars. Two of these stars (HD 245567 and HD 156097) are the ones identified by Ayala et al. (in preparation). The fields for all VLASS-detected sources are shown in Figure 2.2. Details on these detections are provided in Table 2.2.

Of the six stars, two (HD 156097 and HD 321958) were flagged by Tu et al. (2020) for possibly having an M-dwarf within their *TESS* PSF. While the VLASS beam size makes me confident that the radio emission originated from the solar-type star, there was some risk of the optical flares actually originating from the M-dwarf

[4] https://casa.nrao.edu

[5] `https://library.nrao.edu/public/memos/vla/vlass/VLASS_014.pdf`

[6] `https://library.nrao.edu/public/memos/vla/vlass/VLASS_017.pdf`

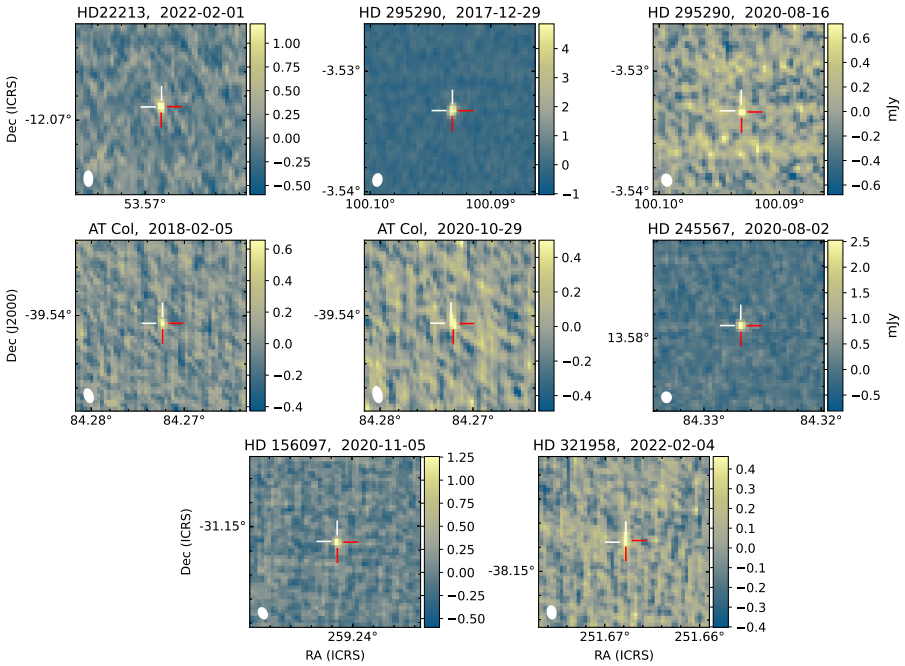

Figure 2.2: The CIRADA Stokes I cutout for each VLASS source associated with a super-flaring star. The white cross-hairs are centered on the proper-motion corrected position of the star from SIMBAD values (Wenger et al., 2000) and the red cross hairs are centered on the position of the source as identified by `CASA`'s `imfit` function. The beam shape is shown as a white ellipse in the bottom left corner of each frame.

because of how large the *TESS* PSF is. However, based on the implied flare energies and associated flux contribution that might be expected from an M-dwarf, it is highly unlikely that an M-dwarf is responsible for the flares; although an M dwarf may be able to produce flares that could account for the lowest-amplitude flares of the HD 156097 *TESS* light curves, it is highly unlikely to reproduce its highest-amplitude flares and similarly unlikely to be responsible for all 31 flares I identified for this star. I provide more details on this analysis in Appendix A.3.

VLASS Polarization

For each of the VLASS sources, Steven Myers re-imaged the field in full polarization. He restored the VLASS observations from the archive using the default VLA Calibration Pipeline for that observation. The sources were imaged in `CASA` using `CASA` version 5.6.1-8. We created a wide-band (1965 - 4013 MHz) multi-frequency synthesis image using a single Taylor expansion term representing the average over

Table 2.2: Details for the VLASS detections of the six stars in E1 (top) and E2 (bottom). In addition to the Stokes I flux density ($S_{\nu,\mathrm{I}}$), we also calculate the radio luminosity $\log_{10} L_{\mathrm{R}}$, the brightness temperature (T_{B}, described in Section 2.5), the offset between the `findsource` source position and the Gaia proper motion corrected position (dθ). We also provide the circularly-polarized flux density, $S_{\nu,\mathrm{V}}$, and the circular polarization fraction, P_{V} ,for sources that were detected in total intensity. For ease of comparison with the Güdel-Benz relation, we also include the quiescent X-ray luminosity $L_{\mathrm{X,quiet}} = 4\pi d^2 F_{\mathrm{X,quiet}}$ as calculated from the presumably quiescent X-ray fluxes $F_{\mathrm{X,quiet}}$ reported in Freund et al. (2022) as well as the average estimated X-ray flare luminosity $L_{\mathrm{X,flare}}$ described in Section 2.5. We also calculate the bolometric luminosity as $L_{\mathrm{bol}} = 4\pi R^2 \sigma_{\mathrm{SB}} T_{\mathrm{eff}}^4$, where σ_{SB} is the Stefan-Boltzmann constant , to provide $L_{\mathrm{X}}/L_{\mathrm{bol}}$ for consideration with regards to activity saturation (discussed in detail in Section 2.5). The signal-to-noise ratios for the flux densities and polarization fractions are reported in parentheses and non-detections are reported as $< 4\sigma$. The row for Median Star refers to the median values of the *TESS* stars that were not detected in VLASS. Note that only 111 of the stars not detected in VLASS have X-ray fluxes in Freund et al. (2022); the L_{X} and $L_{\mathrm{X}}/L_{\mathrm{bol}}$ values reported in the Median Star column are for these 111 stars.

		HD 22213	HD 295290	AT Col	HD 245567	HD 156097	HD 321958	Median Star
E1								
$S_{\nu,\mathrm{I}}$	mJy	<0.88	6.19 (31.6)	0.73 (5.9)	< 0.48	< 0.48	< 0.48	< 0.56
$\log_{10}(L_{\mathrm{R}}/(\mathrm{erg/s/Hz}))$		<15.44	16.43	15.7	<15.81	<15.88	<16.23	<16.00
$T_{\mathrm{B}}/(10^{11}\ \mathrm{K})$		—	1.68	0.19	—	—	—	—
dθ	$''$	—	0.05	0.04	—	—	—	—
$S_{\nu,\mathrm{V}}$	mJy	—	-0.32 (1.7)	-0.37 (3.3)	—	—	—	—
P_{V}		—	-0.05 (1.7)	-0.51 (2.9)	—	—	—	—
E2								
$S_{\nu,\mathrm{I}}$	mJy	1.56 (9.8)	0.85 (4.1)	0.612 (4.3)	3.40 (20.4)	1.57 (10.7)	0.54 (4.5)	< 0.58
$\log_{10}(L_{\mathrm{R}}/(\mathrm{erg/s/Hz}))$		15.69	15.57	15.62	16.67	16.4	16.285	<16.01
$T_{\mathrm{B}}/(10^{11}\ \mathrm{K})$		0.29	0.23	0.16	1.17	0.72	0.72	—
dθ	$''$	0.13	0.35	0.7	0.04	0.23	0.51	—
$S_{\nu,\mathrm{V}}$	mJy	0.43 (2.8)	-0.44 (2.2)	-0.21 (1.4)	2.07 (12.8)	-0.15 (1.0)	0.24 (2.1)	—
P_{V}		0.28 (2.7)	-0.52 (1.9)	-0.34 (1.3)	0.61 (10.8)	-0.10 (1.0)	0.44 (1.9)	—
$\log_{10}(L_{\mathrm{X,flare}}/(\mathrm{erg/s}))$		30.48	30.89	31.02	30.97	31.21	31.43	31.35
$\log_{10}(L_{\mathrm{X,quiet}}/(\mathrm{erg/s}))$		30.12	30.35	30.38	30.67	30.74	30.50	30.24
$(L_{\mathrm{X,quiet}}/L_{\mathrm{bol}})/10^{-4}$		4.20	7.08	5.64	6.94	6.56	5.81	4.69

the band in Stokes I and V. The flux densities in Stokes I for each star is the extremal value in a 5×5 pixel box (2.5" $\times$ 2.5") centered on the position on the source previously identified by `findsources`. The flux densities in Stokes V polarization was extracted at the location of the peak in the Stokes I image, taking the extremal value (positive or negative) in the V image in a 5×5 pixel box around the I peak. Although Stokes Q and U were also imaged, none of the sources identified in Stokes I had a significant ($\geq 4\sigma$) detection in Stokes Q, U, or in total linearly-polarized light $S_{\nu,L} = \sqrt{S^2_{\nu,Q} + S^2_{\nu,U}}$ where $S_{\nu,Q}$ and $S_{\nu,U}$ are the flux densities of the source position in Stokes Q and U, respectively. As such, I only address Stokes I and V.

The values I report in Table 2.2 are those extracted values, with the uncertainties derived using the standard deviation about the mean in the given image calculated in an annulus from 10" to 60" from the source in the image center. The Stokes V data have not been corrected for any systematic effects such as the beam squint between the R and L polarized primary beams of the VLA, or any systematic offset between the R and L antenna based calibrations. The VLASS images are made using data from 128 individual on-the-fly (OTF) pointings surrounding the target and we expect some of these effects to average out. Systematic errors in Stokes V that arise from the uncorrected beam squint are estimated to be 10%, therefore circularly polarized emission above the 10% level are likely believable. The flux densities themselves derived from these Quick-Look Images are also subject to significant uncertainty (VLASS Memo 13[7]) with peak values showing a systematic offset of -15% and scatter of ±8% in flux density for all polarizations.

2.5 Discussion

Because none of the VLASS detections were contemporaneous with *TESS* observations of the respective stars, I cannot unambiguously say that any radio emission is associated with a superflare. Instead, I can investigate the properties of the VLASS-detected stars and how they compare to the properties of the larger sample of super-flaring stars in *TESS* and to the broader population of radio-detected stars. From this, we can explore what that might mean for the likelihood that these bursts are associated with superflares or their correlation with other stellar properties. In particular, I consider what the effects of the observing properties of VLASS, maximum *TESS* flare energy, and the *TESS* flare rate might have on detecting radio emission from these stars. Before discussing my results in the context of the larger *TESS* superflare star sample, I first discuss the relevant emission processes and how

[7] `https://library.nrao.edu/public/memos/vla/vlass/VLASS_013.pdf`

they relate to each of the individual VLASS-detected stars.

Before beginning that discussion, it is worth mentioning that the Rossby number—the ratio between the stellar rotation period and the convective turnover time—is normally included in discussions of activity. This is because of a power-law relation between Ro and activity indicators—such as the X-ray-to-bolometric luminosity ratio $R_{\rm x}$—for Ro greater than a saturating value, $\mathrm{Ro}_{\rm sat}$. Alternatively, for Ro values $<\mathrm{Ro}_{\rm sat}$, the activity indicator value remains essentially constant. Because my stellar sample is so restricted (stars with temperatures between $\sim$ 4900 – 6000 K and rotation periods $\lesssim$ 10 d), I do not expect Ro to be an informative metric. To confirm this, I calculate the Ro values for the sample of 150 stars by using my own period estimations from the *TESS* light curves and using the astroseismological calibration of Corsaro et al. (2021) to estimate the convective turn-over timescales; these values are reported in Table 2.1. The VLASS-detected stars do not have Ro values consistently higher or lower than the median *TESS* superflaring star, although I do find the $R_{\rm X}$ values we calculate for the VLASS-detected stars are generally higher than the median *TESS*-superflaring star, shown in Table 2.2. However, I indeed find there is no correlation between the Rossby number and the flare energies, peak luminosities, or rates of the stars, nor is there any correlation between Ro and the X-ray luminosity for the 111 of these stars that were reported in Freund et al. (2022).

Radio Emission Processes

In addition to the difficulty of associating the radio emission with a potential optical-flare counterpart, the nature of VLASS observations—5 s integrations spaced apart by multiple years—makes it difficult to constrain the process responsible for the radio emission when it is highly variable across the epochs. The primary remaining tools we have available to us in this endeavor are the emission's polarization and brightness temperature $T_B = S_\nu c^2 4\pi d^2 (2k_B \nu^2 A)^{-1}$ where S_ν is the flux density, c is the speed of light, d is the distance to the star, k_B is the Boltzmann constant, ν is the emission frequency, and A is the area of the emitting surface. The non-thermal, incoherent processes we may expect for the stars are synchrotron and gyrosynchrotron (Dulk, 1985; Güdel, 2002; Benz and Güdel, 2010). These processes may present linear and circular polarization, respectively, with the fraction of polarization being less than a few 10s of percent. They are additionally limited to brightness temperatures $<< 10^{12}$ K if synchrotron and $\lesssim 10^{10}$ K if gyrosynchrotron (Dulk and Marsh, 1982; Readhead, 1994). Alternatively, coherent processes like ECME and plasma emission can achieve brightness temperatures well in excess of 10^{12} K and can exhibit high

levels of polarization. These emission properties were summarized in Table 1.1.

The stellar VLASS detections I present here show brightness temperatures on the order 10^{10-11} K, taking $\nu = 3$ GHz (the center of the VLASS band) and assuming the emitting region is the size of the stellar surface (*i.e.*, taking $A = 4\pi R^2$). This assumption is valid if essentially the entire stellar corona is emitting. Thus, this represents an approximate upper limit on the emitting area or *lower* limit on brightness temperature; if we assume the emission originates from smaller regions as we associate with impulsive events like flares, then the brightness temperature could be orders of magnitude higher than what I report in Table 2.2. As such, if the emission is incoherent, it is unlikely that the majority of the emission I report is gyrosynchrotron as it would require a transient acceleration mechanism that fills an area the size of the stellar surface or larger at the highest possible brightness temperature achievable by the process. A process with these properties would not be readily-explainable in the magnetic-activity paradigm. Instead, most of the emission is more easily explained as synchrotron, originating from a relativistic electron population contained in magnetic loops with energies on the order of MeV. This emission process is also consistent with the lack of detectable polarization from most of the stars.

I should note that a lack of polarization and $T_B < 10^{12}$ does not preclude the emission from being coherent. Indeed, if the emitting region is $\lesssim$ 2–20% of the stellar surface area—reasonable limits for the area covered by a flare loop—then the 10^{12} K limit is met and thus would *require* a coherent process. Without more time and spectral information, and especially without a Stokes V detection for most of the sources, synchrotron generally cannot be ruled out. There are two exceptions to this incoherent assertion: AT Col, which had a marginal ($3.3\sigma_V$) detection in Stokes V, and HD 245567, which had a significant Stokes V detection ($12.8\sigma_V$). When paired with the relatively high brightness temperatures, it becomes increasingly likely that the emission from these two stars is coherent. If the emission is ECME, these detections could represent the stellar analog of the transition to coherent processes for the brightest solar radio bursts discussed in Section 2.2. Deeper discussions on the emission mechanism for these two stars are provided in the stars' respective sections.

The VLASS-detected Stars

HD 22213

HD 22213 is one star in the sample that is actually a known binary. However, the orbital separation is on the order of 100 AU (Mason et al., 2001). As such, the companion is not expected to be strongly impacting the rotation evolution of the star or driving magnetic activity. Instead, its high activity is likely related to its young age; its inclusion in the Tucana-Horologium association suggests it is ≈ 45 Myr old (Bell et al., 2015).

HD 22213 was detected in X-ray both by ROSAT in both 1991 (Boller et al., 2016) and eROSITA in 2020 (Merloni et al., 2024). Accounting for the star's distance, the luminosity in the 0.2-2.3 keV eROSITA band was 5.5×10^{30} erg/s. Using the stellar parameters in Table 2.1, this leads to a ratio of X-ray luminosity to bolometric luminosity of $L_X/L_{bol} = 4.2 \times 10^{-4}$, within or near the saturated regime. As mentioned previously, this is to be expected for the stars in our VLASS-detected sample, all of which have Rossby numbers that put them in or near this regime.

HD 295290

HD 295290 is a member of the 40 Myr Columba association (Gagné et al., 2018) and is one of two stars in the sample detected in both VLASS epochs that I search for emission. Its estimated brightness temperature in E1 was the highest of any detection from our sample ($\approx 10^{11}$ K) and, when paired with a lack of polarization, definitively makes synchrotron a more likely emission mechanism than gyrosynchrotron for the E1 detection, although a coherent process cannot be ruled out. When considering the nature of the much weaker E2 emission, it is worth acknowledging that VLASS epoch 3 (E3) data is available for this source. In this epoch, there was an 8σ detection (1.273 ± 0.161 mJy) of the source with no detectable polarized emission (Stokes V flux density = -0.232 ± 0.150 mJy).

HD 295290's E1 radio emission being $\approx 10\times$ higher flux density than the emission in the other epochs makes it more likely that the emission in E1 is burst-related and possibly associated with an event like a flare. It is less certain whether the emission in E2 and E3 are bursts or if they are quiescent in nature. One way to evaluate the likelihood that the emission is a radio burst associated with a flare is to consider the probability of a flare occurring during a VLASS observation. If a flare were only as long as a VLASS exposure time, then the probability of observing a flare would

just be:

$$P = 1 - \exp\left(-f_{\rm fl} \cdot t_{\rm epoch} \cdot N_{\rm epoch}\right) \tag{2.1}$$

where $f_{\rm fl}$ is the flare rate of the star, $t_{\rm epoch}$ is the exposure time per epoch, and $N_{\rm epoch}$ is the number of epochs that we search for a flare during. However, as flares last much longer than 5 s, this would grossly underestimate the probability of observing a flare during a VLASS epoch. Instead, we must scale the argument in the exponent by $t_{\rm fl,avg}/t_{\rm epoch}$, where $t_{\rm fl,avg}$ is the average duration of a flare, such that:

$$P_{\rm flare} = 1 - \exp\left(-f_{\rm fl} \cdot t_{\rm fl,avg} \cdot N_{\rm epoch}\right). \tag{2.2}$$

For HD 295290, the average flare duration is 1657 s and the flare rate is 217 $\rm yr^{-1}$, so that the probability of HD 295290 flaring during a single VLASS observation is only $P_{\rm flare} = 0.011$ and of flaring in all three epochs $P^3_{\rm flare} = 1.45\times10^{-6}$. This is assuming that the *TESS* and VLASS sensitivities are at the same part of the luminosity function for these flares. Instead, it could be that only one of these VLASS detections is a burst associated with a superflare while the other two epochs are showing quiescent emission. Considering that the emission from E1 was 5-7 times stronger than the emission observed in E2 and E3, it could be that E1 is emission associated with a burst while E2 and E3 are quiescent emission.

That said, the flux density of even the lower-intensity E2 emission would be the equivalent of $\approx 10^7$ solar flux unit (SFU) emission at the distance from the Sun. This is an order of magnitude brighter than the brightest burst seen from the Sun at these frequencies (Cliver et al., 2011). Similarly, the radio luminosity of this emission is $\sim 10 - 500\times$ the quiescent emission reported for solar type stars by Gudel et al. (1994), which is already 1000s of times the estimated solar quiescent radio luminosity. The emission is not only luminous, but the brightness temperatures I report here are 1000× the brightness temperatures reported by Gudel et al. (1994) who also assume the emitting surface is the size of the star; for HD 295290's emission to be persistent gyrosynchrotron like has been observed for some other solar-type stars, it would either need to consistently be at the physical limit for the brightness temperature of gyrosynchrotron or be originating from an isotropically-emitting surface extending to several tens of stellar radii. Although the emission reported here is extreme, without better time and spectral data it is difficult to conclude what the emission process is and if it can unambiguously be distinguished between a transient and persistent process. Regardless, the emission is extraordinary.

While this burst probability discussion does assume that the radio emission is associated with a flare, it could be that the emission is associated with an unrelated magnetospheric process as is discussed in Section 2.5. Such strong and consistently-detected emission may also be explained through binary interactions, which are known to be capable of producing bright, persistent, and variable radio emission (Drake et al., 1989). Alternatively, accretion (or ejection) processes are also capable of producing long-lasting and variable radio emission (Skinner and Brown, 1994; Cesaroni et al., 2024). Such events may be reasonable to expect given HD 295290's young age. Because the VLASS observing cadence is so sparse, and especially because HD 295290 is detected in all three epochs, it is essentially impossible to derive a specific radio emission rate that we could compare against its flare rate. Instead I will consider the burst rate of the entire sample as is addressed in Section 2.5. Because of this, the relationship between HD 295290's flare activity and its radio emission remains unclear.

AT Col

AT Col is the other star detected in both E1 and E2 of VLASS. It was most significantly detected in E1 when it also exhibited detectable ($> 3\sigma$) Stokes V emission. The flux density in Stokes I and V suggest a polarization fraction of 0.52 ± 0.18. Such a high circular polarization fraction cannot be explained by synchrotron emission, which is generally much less than 10% (*e.g.*, Melrose (1971) and Sazonov (1972)). This would then suggest that either gyrosynchrotron or a coherent emission process is responsible for the emission in E1.

The brightness temperature of the Stokes I emission, assuming the emitting region is the size of the star ($\approx 2 \times 10^{10}$ K), may be sufficient to rule out transient gyrosynchrotron, which is limited to $\lesssim 10^{10}$ K (Dulk and Marsh, 1982). As I mention in Section 2.5, if we assume the emission is generally persistent with some variability in polarization and thus associated with the quiescent phase of the star, then the emitting surface may be larger than the stellar disk. That said, the emitting area would need to be $\approx 1000\times$ larger, corresponding to distances of about 30 times the stellar radius for an isotropically-emitting region, to reach the $\approx 10^7$ K that has been estimated for the quiescent radio emission for other solar-type stars (estimates which do not assume a surface larger than the stellar disk, Gudel et al., 1994). Thus, if the emission is gyrosynchrotron, either the emitting area (and the length-scale of the accelerator) is extremely large or the brightness temperature would be higher than is

usually estimated for quiescent emission for this spectral type. Alternatively, if the emission is transient, the plausible coherent emission mechanisms can both reach brightness temperatures well in excess of 10^{12}K and circular polarization fractions in excess of 70%, but may have lower polarization fractions due to propagation effects in the stellar atmosphere. Especially because the emission is not strong enough for us to extract a spectrum, we can not conclude whether the emission is an incredible instance of gyrosynchrotron or the result of a coherent process.

Unlike HD 295290, AT Col is not also detected in E3. This might make it more likely that the emission from AT Col is indeed associated with transient phenomena despite the low probability of detecting a flare-associated burst in two epochs ($P^2_{\rm flare} \approx 10^{-5}$). In a similar argument to the case of HD 295290 in Section 2.5, the flux density compared to solar radio bursts at these frequencies may be sufficient on its own to rule out quiescent emission, even for the weaker detection which would have a corresponding flux density of $\approx 10^7$ SFU at 1 AU. As with HD 2959290, considering the luminosity in the context of the Sun might imply that this emission is transient, but it is unclear whether the luminosity of its emission can unambiguously rule out quiescent emission when considered in the stellar context.

It is worth noting that AT Col is consistently detected in X-ray missions, including ROSAT in 1990 (Pye et al., 1995; Mason et al., 1995; Boller et al., 2016) and 2020 (Merloni et al., 2024), Swift between 2009 and 2016 (Evans et al., 2020), and XMM-Newton in 2014 (Freund et al., 2018). Its X-ray flux from ROSAT implies it is in the X-ray saturation regime $L_{\rm X}/L_{\rm bol} \approx 10^{-3}$ (Vilhu, 1984; Wright et al., 2011), which again is indicative of it being a highly active star. It may also have an activity cycle, as suggested by its long-term rotational modulation and brightness variability (Distefano et al., 2017). The persistent X-ray emission paired with the activity cycle might explain the detection in E2 and non-detection in E3; AT Col may have been at a cycle minimum during E3, reducing its possible quiescent radio emission to an undetectable level for VLASS.

HD 245567

HD 245567, a weak-line T Tauri star (Li and Hu, 1998), is one of two stars presented here that was identified in the work of Ayala et al. (in preparation). Because it is a weak-lined T Tauri, it is likely that its inner disk has mostly dissipated and therefore does not play a significant role in its activity. HD 245567 is also one of the two stars in this work that has significantly circularly-polarized radio emission. The high

flux density– the second highest of the sample– made it possible to extract spectra for both Stokes I and V, shown in Figure 2.3. The exceptionally-high polarization fraction– more than 80% in some bands– requires this emission be coherent. I discuss the significance of this in the context of the larger superflare star sample briefly in sections 2.5 and 2.5.

The two main coherent emission mechanisms for stellar radio emission are plasma emission and ECME, both of which can reach polarization fractions up to 100% (*e.g.*, Dulk (1985)). Although plasma emission from the Sun is observed up to several GHz, it is never seen to have such a high polarization fraction above a few hundred MHz. Instead, this emission is more likely to be due to ECME, which has previously been reported for TTSs (Smith et al., 2003; Pritchard et al., 2021; Feeney-Johansson et al., 2021). This is observed from the Sun when electrons are trapped in post-flare loops (Gergely, 1986; Morosan et al., 2019) and is also observed from the magnetized planets. In particular, the cadence and geometry of Jupiter's ECME depends on both the orbital phase of its moons (Goldreich and Lynden-Bell, 1969) and the rotational phase of Jupiter (Zarka et al., 2021). Such periodic emission has also been observed from M dwarfs and brown dwarfs where the observing cadence of the emission is modulated by their rotation (Hallinan et al., 2008; Rose et al., 2023; Bloot et al., 2024). Because of this, it is unclear whether this emission is associated with flaring behavior or if it is rotation-modulated emission, although I should emphasize that rotationally-modulated ECME has never been reported for this spectral type.

The frequency that ECME is observed at depends explicitly on the magnetic field strength of the source with frequency $\nu = s\,2.8\,B\,[\mathrm{MHz}]$ where B is the magnetic field strength in Gauss and s is the harmonic of the emission we are observing. Assuming this emission is ECME at the fundamental, the detection at 3.685 GHz would imply that HD 245567 has a magnetic field $\gtrsim 1,300\,\mathrm{G}$. This field strength is consistent with Zeeman-broadening measurements of T-Tauri magnetic fields reported by, *e.g.*, Yang et al. (2005) and Lavail et al. (2017).

As with the other VLASS-detected stars, HD 245567 is regularly detected in the X-ray, with a luminosity $\approx 4 \times 10^{30}\,\mathrm{erg/s}$ in the 0.1-2 keV band (Voges et al., 1999; Boller et al., 2016; Freund et al., 2022). When paired with its bolometric luminosity, this leads to a $L_X/L_{bol} = 6.94 \times 10^{-4}$, putting it in or near the saturation regime, consistent with this being a highly-active star. Because the emission is likely coherent, we may then expect this star to be radio-luminous relative to the

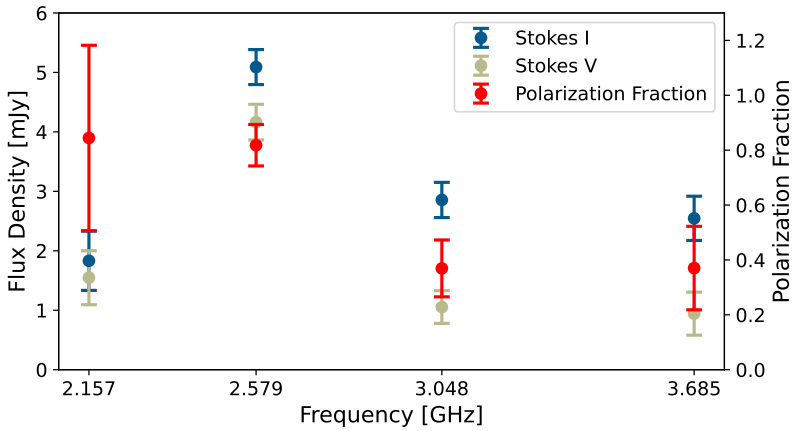

Figure 2.3: The spectra for Stokes I and V (left axis) and the polarization fraction (right axis) for HD 245567 in VLASS E2. At the peak flux density, the polarization fraction is 0.82 ± 0.076. The error bars here represent $\pm 1\sigma$, with the polarization fraction uncertainty being calculated from standard propagation of uncertainty for $S_{\nu,\mathrm{V}}/S_{\nu,\mathrm{I}}$. The frequencies here were selected to be constant fractional bandwidth $\nu_{\mathrm{hi}}/\nu_{\mathrm{low}} = (4013\,\mathrm{MHz}/1965\,\mathrm{MHz})^{1/4} = 1.1954$ where ν_{hi} is the high end of the sub-band, ν_{low} is the low end, and 1965 MHz-4013 MHz is the full frequency range of VLASS.

GBR, discussed in more detail in Section 2.5. However, because the radio emission is transient, the most relevant X-ray luminosity to use to evaluate the emission's position relative to the relationship is the flaring X-ray luminosity, not the quiescent luminosity that is most likely observed by ROSAT. Because we do not know the true X-ray luminosity of this star's flares, we instead estimate the peak X-ray luminosity to be 10% of the peak bolometric luminosity, discussed in more detail in Section 2.5. The mean, estimated X-ray flare luminosity for HD 245567 is 9.37×10^{30} erg/s, which when paired with its radio luminosity of 4.68×10^{16} erg/s/Hz produces a X-ray-to-radio luminosity ratio $L_{\mathrm{X,flare}}/L_{\mathrm{R}} = 10^{14.3}$. This suggests that the radio emission is mildly radio luminous relative to the GBR presented as $L_{\mathrm{X}}/L_{\mathrm{R}} = 10^{15.5\pm0.5}$ by Benz and Guedel (1994), although it is within the error of $10^{14.52\pm1.31}$ reported in Gudel (1992) and Gudel et al. (1993). Without knowing the luminosity of the specific flare that this emission is associated with—or if it even is associated with a flare—it is difficult to use the GBR to estimate the over-luminance of the radio emission and how this relates to the solar paradigm where the brightest solar radio bursts are both associated with strong flares are coherent rather than incoherent (White et al., 2024).

HD 156097

HD 156097 was the VLASS-detected star with the highest flare rate and is one of four stars detected only in VLASS E2. It was one of two stars flagged by Tu et al. (2020) as having an M-dwarf contaminating its *TESS* PSF that may be responsible for the flares in the *TESS* light curves. I address this possible contamination in Appendix A.3 and find that the nearest star with a temperature reported by Gaia DR3 that is within 42" (two pixels on the *TESS* detector) could not reasonably produce flares large enough to account for the flare amplitudes observed from this star.

HD 156097's kinematics lead the `Banyan` moving group association program to classify it as a field star with a probability $\approx$ 74% (Gagné et al., 2018). If this star is indeed a field star, it may be more likely that a companion—rather than a young age—is responsible for its $\approx$ 2 day rotation period. The other possible association is the Upper Centaurus Lupus (UCL) association at 23.5% probability. This association, estimated to have an age between 10-25 Myr (Röser et al., 2018), would be consistent with the $\approx$ 30 Myr age assumed from its Lithium equivalent width (Desidera et al., 2015).

This star has additionally been detected in X-ray in 1990 (Boller et al., 2016), 2007 (Freund et al., 2018), and 2020 (Merloni et al., 2024). Its flux in the eROSITA 0.2-2.3 keV band in 2020 corresponds to a luminosity of 5.50×10^{30} erg/s (Freund et al., 2022). Using the effective temperature and radius for the star reported in Table 2.1 to calculate the bolometric luminosity, this would put it at $L_X/L_{bol} = 6.56 \times 10^{-4} \approx 10^{-3}$, which implies it is in or near the saturated regime, consistent with its extreme activity.

HD 321958

Like HD 156097, HD 321958 was flagged by Tu et al. (2020) to have an M-dwarf in its *TESS* PSF. However, the flare luminosity that would be required from the M-dwarf to reproduce the flares observed in the *TESS* light curve would be orders of magnitude higher than the quiescent luminosity of the M-dwarf, making it a highly-unlikely contaminant in this analysis. This star was marginally detected only in VLASS E2, but has the third-highest radio luminosity and the largest flare energy of the VLASS-detected stars. These details are likely observationally driven as it is the furthest star of the VLASS-detected stars.

HD 321958 is apart of the defining sample for the UCL moving group (Röser et al., 2018), although `Banyan` estimates suggest a 15% probability it is a field star. It was also observed in the X-ray in 1990 by ROSAT (Boller et al., 2016) and in 2020 by eROSITA (Merloni et al., 2024). Its flux in the 0.2-2.3 keV band measured by eROSITA is 9.18×10^{-13}mW/m^2. When paired with the bolometric luminosity estimated from the stellar parameters provided in Table 2.1, this leads to $L_X/L_{bol} = 6.0 \times 10^{-4}$, within the saturated regime as would be expected for a star $\lesssim 30$ Myr old as is estimated for the UCL moving group.

VLASS Detection Limits

If the stars VLASS detected had systematically low radio luminosities due to being especially nearby or in low-noise VLASS fields, it would make sense that we were able to detect them over the other 144 stars in the *TESS* superflare sample. To investigate this possible bias, I calculate how large the radio luminosity from each of the 144 stars would have to be in order to be a 4σ detection in their respective CIRADA frame. This luminosity is taken to be $4\sigma \times (4\pi\, d^2)$, where d is the distance to the star and σ is the RMS value for the CIRADA frame as given by `CASA`'s `statistics` tool. The median value for the minimum required radio luminosity for the *TESS* superflare stars is reported in Table 2.2 along with the actual radio luminosities of the six VLASS-detected stars.

What is immediately obvious is that the radio luminosity of the VLASS-detected stars lie on either side of the median value for the required luminosity for a star to be detected in VLASS. This implies that the majority of the required radio luminosities should not be considered unreasonably large for fast-rotating, solar-type stars and, therefore, the sensitivity of VLASS likely is not an inhibiting factor in this science. That said, it may be that VLASS is only sensitive to bursts associated with the most energetic flares, as is discussed in more detail in Section 2.5.

We can also address this from the perspective of the solar paradigm if we explicitly consider the radio luminosities of the stars detected in VLASS. Five out of six of these stars would have corresponding flux densities of $\approx 10^7$ solar flux units (SFU = 10^4 Jy) at 1 AU. This is only about a factor of 10 brighter than the brightest solar burst observed at similar frequencies (Gary, 2019; Cliver et al., 2011). When considering that young stars tend to have both denser plasmas and stronger magnetic fields—thus providing a larger high-energy electron population for emission—these luminosities seem reasonable in the solar paradigm, granted these exceptionally-

bright solar radio bursts at 1.4 GHz do not behave like typical solar radio bursts (White et al., 2024). The question then is whether there are features of the stars besides their field that might make them more or less likely to be detected in VLASS. This is addressed in the next three subsections.

Flare Luminosity and the Güdel-Benz Relation

Although the GBR had been derived for the steady, quiescent X-ray and radio emission for binaries, M-dwarfs, and solar-type stars, it has been shown to also apply to the X-ray and microwave emission of both solar and stellar flares (Gudel et al., 1993; Benz and Guedel, 1994; Gudel et al., 1994). Because of this relation, we might be able to better constrain whether these bursts are associated with superflares by comparing the radio luminosity of the VLASS bursts to the X-ray luminosities of flares from these stars.

To do this, I take L_x to be 10% of the average peak bolometric luminosity of the superflares of a given star (the bolometric luminosity estimate is described in part in appendices A.1 and A.3). This should be a reasonable order-of-magnitude estimate given that $\sim 70\%$ of the bolometric energy of solar flares is expected to be contained in the white-light component of the flare, the flare component that is measured by *TESS* (Kretzschmar, 2011). This then leaves on order 10% of the energy to be radiated in other parts of the EM spectrum, primarily the X-ray. I calculate $L_{\mathrm{R}} = S_\nu \cdot 4\pi d^2$ from the flux density of the VLASS sources S_ν and distance of the star d.

I plot L_x against L_{R} for each of the six VLASS-detected stars along with three groups of stars that informed the GBR (Gudel, 1992; Gudel et al., 1993; Drake et al., 1989) in Figure 2.4. With the exception of the likely coherently-emitting HD 245567, the VLASS-detected stars follow the $L_x \approx 10^{15.5} \times L_{\mathrm{R}}$ well within error bars, suggesting the radio emission may indeed have a coronal origin associated with a superflare. I also include the population of *TESS* superflaring stars that were not detected in VLASS in this plot, using 10% of the peak luminosity of the brightest flare from each star as L_x and using the required detection luminosity described in Section 2.5 as L_{R}. Interestingly, these values are also consistent with the GBR. This might suggest that should a radio burst associated with a superflare occur on any of the stars in the *TESS* sample, it would have been detectable in VLASS.

In this context, it is worthwhile again to single out the coherently-emitting HD 245567. Because its emission is unambiguously coherent, we should not expect its radio burst

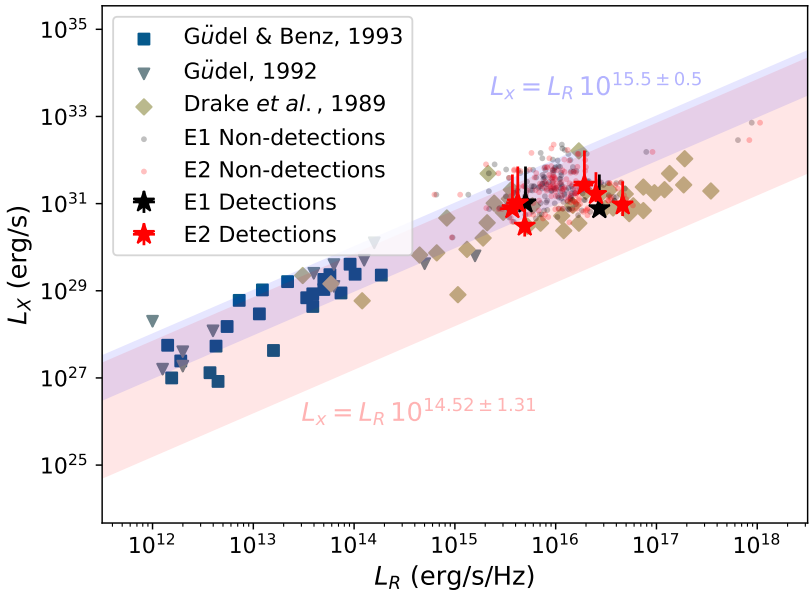

Figure 2.4: Estimated $L_{\rm X}$ plotted against $L_{\rm R}$ for the six VLASS-detected superflaring stars as well as three other populations of stars. The extent of the vertical error bars represent the peak luminosity for the brightest and dimmest flares of the star and the horizontal error bars are calculated from the noise in the CIRADA frame. The minimum required radio luminosity for a 4σ detection vs. the estimated X-ray luminosity for each of the 144 other *TESS* superflaring stars are also included as points. The extent of the GBR from Gudel et al. (1993) is shown in red and the relation from Benz and Guedel (1994) is shown in blue.

luminosity to be correlated with flare luminosity in the GBR framework. Although it is marginally outside the error range of the Benz and Guedel (1994), it is well within the range of Gudel (1992) and Gudel et al. (1993). It could be entirely serendipitous that its estimated X-ray luminosity aligns it so well with the GBR. Alternatively, there have been reports of coherent radio emission—albeit at much lower frequencies—following the GBR (Vedantham et al., 2022). It is also worth emphasizing again the likely high errors associated with my flare luminosity calculation given that we do not actually know the temperature of the flares. Without better constraints on the flare properties or contemporaneous observations of this emission in the radio and X-ray, discussion of what this means for the underlying physics responsible for the empirically-derived GBR is outside of the scope of this work.

Flare Energy

We see that some flare-related phenomena are more likely to occur on the Sun if certain thresholds are exceeded; for instance, Yashiro et al. (2006) report essentially a one-to-one correlation between solar flare energies higher than 10^{30} erg and the occurrence of a CME. This prompts me to investigate whether the the VLASS-detected stars are exceptional in this respect. The flare energy is plotted against the peak luminosity of the flare in Figure 2.5 for all flares we identified in *TESS*.

If we consider the median flare energy for each star, then the VLASS-identified stars do not seem extraordinary; they lie on either side of the median value of the median flare energy for all *TESS* superflaring stars. However, all of the stars detected in VLASS, except for HD 22213, had maximum flare energies higher than the median value for maximum flare energy for the entire *TESS* superflare star sample. This might suggest then that radio bursts detectable by VLASS occur preferentially on stars that can produce more energetic flares. By extension, it may be that such bursts are only detectable in VLASS when they are associated with the most energetic flares. This is consistent with the idea that the radio emission is associated with superflares, but the part of the flare luminosity function sampled by VLASS is different from what is sampled by TESS.

Flare Rate

If the radio emission from these stars is associated with a superflare then it would make sense that the more time the star spends flaring, the more likely we would be to detect it in VLASS (assuming VLASS and *TESS* probe the same part of the flare luminosity function). The flare rates for the 150 stars with superflares in *TESS* are calculated using the method described in Appendix A.2 and the median flare rate, as well as the flare rates for the six VLASS-detected stars, are reported in Table 2.1. All of the VLASS-detected stars have flare rates above the median value of the 150-star sample, consistent with the idea that VLASS may have been able to detect radio emission from them simply because they were flaring more often and thus that the radio emission is flare-related. It is interesting to note that the VLASS-detected star with the lowest flare rate is HD 245567 which, as described in Section 2.5, could be producing radio emission through a mechanism other than flares.

Although the VLASS-detected stars flare more than the typical star in the sample, we have already briefly discussed in Section 2.5 how unlikely it is for a flare from one of the VLASS-detected stars to occur during a VLASS observation. To further

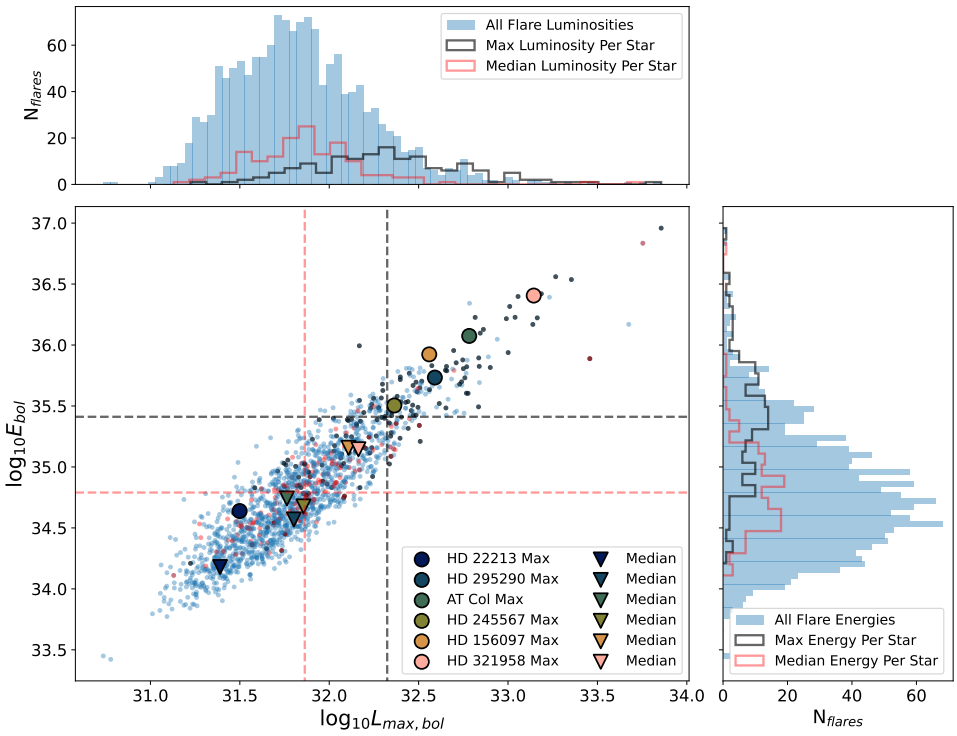

Figure 2.5: The bolometric energy plotted against the peak luminosity for each flare we identified in *TESS* light curves (blue circles). We also include the median flare (red) value and maximum flare values (black) for each star. Histograms for all flares, median flare per star, and peak flare per star are provided in the top and right panels of the figure in the same colors, and the median values are indicated by dashed lines in their respective colors. The max (circles) and median (triangles) flare values for each of the six VLASS-detected stars are also plotted.

consider the role of flare rate in detectability of stars in VLASS, let us consider the VLASS-detected star with the highest flare rate, HD 156097 at 246 flares per year and an average flare duration of 2,492 s. Using these values in equation 2.2, this makes the probability of seeing it in $N_{\rm epoch} = 1$ epoch 0.019, and the probability of seeing it in at least one of $N_{\rm epoch} = 2$ epochs is 0.038. Conversely, the probability of seeing the median star flare during at least one of two VLASS epochs is only 0.006. Because of this, the exceptionally low probability of observing a flare during any single VLASS epoch may be sufficient to explain why only six superflaring stars were observed in VLASS.

Although the VLASS-detected stars were more likely to be flaring during a VLASS observation, the probability of making a radio detection of even our most frequently-flaring star is low. The question then is how this probability compares to the

probability of making a radio detection of a star independent of flare rates. Because the VLASS exposures are so brief and infrequent for any individual source, it is difficult to derive a meaningful radio burst rate for a specific star. Instead, let us consider the ensemble radio burst rate of super-flaring stars observed in *TESS*, $f_{\rm burst}$. This is given as:

$$f_{\rm burst} = \frac{N_{\rm burst}}{N_\star \cdot t_{\rm epoch} \cdot N_{\rm epoch}} \, [\rm burst \cdot star^{-1} \cdot s^{-1}] \tag{2.3}$$

where $N_{\rm burst} = 8$ is the total number of radio bursts found (assuming all radio detections are a burst rather than quiescent emission), $N_\star = 150$ is the number of *TESS* super-flaring stars we looked for radio emission from, $t_{\rm epoch} = 5\,\rm s$ is the exposure time for each star per VLASS epoch, and $N_{\rm epoch} = 2$ is the number of VLASS epochs we searched for emission.

Because we do not know the duration of the bursts, we assume that the duration is the same as $t_{\rm epoch}$ so that we can use $f_{\rm burst}$ in place of $f_{\rm fl}$ in equation 2.1. The probability of any super-flaring star being detected in a single epoch is then 0.026, and of being detected in at least one of $N_{\rm epoch} = 2$ epochs is 0.052. Alternatively, if we acknowledge that the HD 245567 detection is coherent emission possibly not associated with a flare, and that at least one detection of HD 295290 and of AT Col may be attributed to quiescent emission, then $N_{\rm burst} = 5$ and the probability of detecting a burst in a single epoch is $P_{\rm burst} = 0.017$. This is relatively consistent with the probability of detecting a flare from HD 156097 and may indicate that these bursts are indeed associated with superflares.

2.6 Conclusion

In this work, I used catalogs of flaring, solar-type stars from the first year of *TESS* data by Tu et al. (2020) and Doyle et al. (2020) to act as a sample to look for associated radio emission from VLASS epochs 1 and 2. Of the 150 single stars from these catalogs that were covered in a VLASS field, six were found to have radio emission, two of which had radio emission present in multiple epochs. Given the luminosities of the flares from each star and the sensitivity of VLASS, I find that the detectability of radio emission from the rest of the superflare sample likely is not dependent on the required radio luminosity of a burst from a given star—any star capable of producing its respective superflare should be capable of producing the associated radio luminosity. Instead, likely what limited the number of radio detections was the low observing cadence of VLASS, with stars that flare more frequently and to a higher energy being preferentially detected in VLASS. This

dependence on flare rate and energy, as well as apparent an adherence to the GBR by the VLASS-detected stars, suggests that these radio bursts are likely associated with superflares.

There were three VLASS-detected stars that stood out: HD 245567, which had a circular polarization fraction indicative of a coherent emission mechanism; AT Col, which was detected in both epochs and exhibited polarization in one of the epochs; and HD 295290, which was detected in both VLASS epochs systematically searched here in addition to epoch 3 which was incomplete at the time of this work. The coherent emission from HD 245567 is likely ECME, which would imply a magnetic field strength of $\gtrsim$ 1300 G. The fact that this emission places it along the GBR highlights the necessity for simultaneous radio, optical, and X-ray observations of the star in order to understand both the nature of the emission and the GBR.

It is unclear whether all of the VLASS detections of AT Col and HD 295290 are burst related. The high radio luminosities ($>$ 10$\times$ the brightest solar radio burst) may suggest that each detection is associated with impulsive magnetic activity such as a flare in spite of the low probability of a flare occurring during two (and especially three) VLASS epochs. Although this emission is a factor of ten brighter than the brightest solar *bursts*, it is also only 10s-100s times brighter than the *quiescent* emission from active solar-type stars (Gudel et al., 1994). Additionally, although the radio luminosities associated with their weakest detections are the same order of magnitude as those of the stars detected in only a single VLASS epoch, which might then imply that all of the emission observed in VLASS are transient in nature, they are also the weakest of the VLASS detections. That said, for the emission from these stars to be explained by traditional quiescent emission in the stellar activity paradigm, the emission would either need to consistently exist at the brightness temperature threshold of gyrosynchrotron or else extend to tens of stellar radii; neither explanation is consistent with other radio observations of solar-type stars. Follow-up observations of HD 295290 and AT Col in the 2-4 GHz range are needed to both identify the baseline flux density of these sources and the time and spectral structure of any potential bursts in order to conclude whether all of their radio emissions are indeed associated with bursts or if they represent some of the most extraordinary quiescent emission observed from solar-type stars. These radio observations would benefit greatly from simultaneous observations in the optical or higher-energy part of the spectrum in order to identify and characterize potentially-associated flares.

The highly-polarized emission from the TTS HD 245567 is the only emission we can definitively say is not incoherent due to its high circular polarization and was very likely ECME. We see such emission from the Sun during extreme solar bursts as well as sometimes as type IV bursts. However, we also see it from Jupiter and ultra-cool dwarfs due to rotational modulation of a large-scale current sheet, and, in Jupiter's case, due to modulation from Io. There have been previous reports of ECME from TTSs, but the engine for the emission has not been classified; the emission from HD 245567 presented here could either be the stellar analog of the most extreme solar radio bursts or could represent a process that has never been identified for this spectral type. To address this question of HD 245567's emission engine, I have received 60 hr on the VLA in the S-band—the same band as VLASS—to be completed in the 2025B observing semester plus 20 hr for another TTS that has ECME identified by Pritchard et al. (2021) but exhibits no flares. Such a substantial amount of time will be critical for sampling the rotational phase of these stars in order to identify possible rotational modulation of the emission. These observations will happen concurrently with *TESS* observations of the star and, weather permitting, observations with the ground-based, optical photometry instrument that I designed and built (described in Chapter 4). This will be critical for identifying the role—if any—of flares in the emission process.

It is also worth emphasizing that this work was fairly narrow in scope—simply a search for radio emission from fast-rotating, solar-type stars that were known *a priori* to produce superflares from only the first year of *TESS* operations. But as mentioned in the preceding paragraph, there are even exceptionally young stars that produce radio emission without showing flare activity. Although having dedicated monitoring of stars across the spectrum would be ideal for determining emission processes, understanding the full scope of radio emission produced by solar-type stars across various ages would benefit greatly from not biasing the search by the activity level identified in the optical and, of course, expanding the area of sky that we search for radio emission. To this end, I have begun the expansion of this search to all solar-type stars in a VLASS field with a *TESS* and/or *Kepler* light curve, irrespective of flare activity. This search will also be expanded to RACS data which both has significant overlap with the sky observed by VLASS and fills the frequency range from $\approx$ 0.9–2 GHz, which poses the opportunity to better constrain the emission processes of stars that are detected in both surveys.

This work demonstrates the power of VLASS to identify active solar-type stars.

It also exemplifies the necessity of dedicated and multi-wavelength campaigns of such stars in order to clearly associate superflares with radio bursts. Having both time series and higher spectral resolution of bursts from the stars presented here would provide the opportunity to distinguish the emission mechanism as well as possibly derive information on the electron population responsible for the emission. While priority for dedicated follow-up should be given to the six stars identified to have transient radio emission, the sensitivity of VLASS does not seem to be a limiting factor to detectability and I suspect that any of the super-flaring stars investigated in this work would produce a detectable radio burst if enough time were dedicated to accommodate the unpredictability of flare occurrence. Studying the larger superflare star sample—in addition to stars that may not show flare activity—more in-depth across a broader range of frequencies would afford us the ability to constrain the spectral structure and would aid in identifying the relevant emission process. Although much of the emission I present here could be explained by a high-energy, incoherent process like synchrotron, a coherent process cannot be effectively ruled out. In this respect, multi-wavelength observations in, *e.g.*, the optical and X-ray are even more critical to understand whether the emission is actually flare related and how it relates to the GBR and/or the extreme solar radio burst phenomenon. Generally, a broader-spectrum study of the emission to understand is critical for constraining the radio emission processes and may prove instrumental to understanding the particle acceleration process and particle energy distribution for a population meant to represent the young solar environment. Facilitating the necessary coordination of radio and optical monitoring of solar-type stars that this chapter highlighted is explored in the following chapters.

2.7 Acknowledgments

This work was done in collaboration with Dillon Dong, Carlos Ayala, Steven Myers, and Gregg Hallinan and was supported by a grant from the Simons Foundation (668346, JPG). This work is based on data taken with the Very Large Array, operated by the National Radio Astronomy Observatory (NRAO). The NRAO is a facility of the National Science Foundation operated under cooperative agreement by Associated Universities, Inc. This research has made use of the CIRADA cutout service at cutouts.cirada.ca, operated by the Canadian Initiative for Radio Astronomy Data Analysis (CIRADA). CIRADA is funded by a grant from the Canada Foundation for Innovation 2017 Innovation Fund (Project 35999), as well as by the Provinces of Ontario, British Columbia, Alberta, Manitoba and Quebec, in col-

laboration with the National Research Council of Canada, the US National Radio Astronomy Observatory and Australia's Commonwealth Scientific and Industrial Research Organisation. This research made use of APLpy, an open-source plotting package for Python (Robitaille and Bressert, 2012) as well as Lightkurve, a Python package for *Kepler* and *TESS* data analysis (Lightkurve Collaboration et al., 2018).

Chapter 3

SWAYS IN THE RADIO: LEVERAGING MULTIPLE DATA PRODUCTS OF THE OVRO-LWA FOR STELLAR BURST SEARCHES

3.1 Introduction

With the advent of more sensitive instrumentation across all wavelengths, the study of space weather in extra-solar systems has seen significant growth in the past decade, both in the observational (Crosley and Osten, 2018b; MacGregor et al., 2020; Zic et al., 2020; Veronig et al., 2021; Burton et al., 2022; Namekata et al., 2021; Namekata et al., 2022a; Namizaki et al., 2023; Namekata et al., 2024a) and theoretical (Fionnagáin et al., 2022; Alvarado-Gómez et al., 2022a; Kavanagh et al., 2022; Farrish and Garcia-Sage, 2023; Xu et al., 2024a) realms. There has been especially growing focus on low-frequency (LF) radio observations. This is driven largely by 1.) solar type II bursts' association with CMEs (*e.g.*, Lawrance et al., 2024), 2.) SEP events' association with type III bursts during strong flares (Cane and Erickson, 2005; Duffin et al., 2015), and 3.) the dependence these two burst types have on the plasma properties of the solar corona and inter-planetary medium. As suggested in the latter point, type II and III bursts could serve not only as indicators of non-thermal particle acceleration but also give crucial information on the plasma profile of the stars for which such bursts occur, a detail which is poorly constrained in current stellar wind models.

However, despite the important diagnostic and predictive role LF radio plays in solar space-weather, no definitive stellar equivalent of a type II or III burst has ever been reported (Osten and Bastian, 2006; Crosley and Osten, 2018b; Villadsen and Hallinan, 2019; Mohan et al., 2024b). A possible reason for this is that late-type M-dwarfs have traditionally been the focus of targeted, multi-wavelength observations of flares and associated space weather (Crosley and Osten, 2018a; Zic et al., 2020; MacGregor et al., 2021; Zhang et al., 2023; Tristan et al., 2023; Mohan et al., 2024b). This attention has been owed in large part to the high activity levels of such stars driven by kG-scale fields and an observational bias towards being able to detect signs of transient magnetic activity from small, cool stars as opposed to larger, hotter stars. However, the disparity in how M-dwarfs and solar-type stars generate

their magnetic fields, the differing morphologies of these fields, and the orders-of-magnitude difference in the ambient magnetic field strengths likely have important impacts on both stellar wind and transient particle properties. Specifically, stronger fields extend the closed-field region to much larger distances and, by extension, much lower plasma densities. Thus, the plasma emission—with emission frequency that scales with the square-root of the plasma density—may not be observable below the Earth's ionospheric cutoff frequency. The strong fields also increase the Alfvén speed. This makes it more difficult to drive the shocks that are thought necessary to produce type II bursts (Villadsen and Hallinan, 2019; Mullan and Paudel, 2019). Additionally, strong, over-lying fields may contain stellar CMEs from M-dwarfs such that one might only escape from the stellar corona under exceptional circumstances (Alvarado-Gómez et al., 2022a). This is to say that fully-convective stars should not be expected to exhibit the same transient particle properties and associated emission as the Sun.

Instrument limitations likely also are responsible for a lack of detections. Namely, the inadequate sensitivity at low frequencies as well as a lack of coordinated observations with other parts of the EM spectrum make it difficult to look for stellar analogs of solar radio emission and properly attribute the emission to magnetic-reconnection processes. Both of these issues have seen some resolution recently with high-sensitivity, LF surveys like the Low Frequency Array (LOFAR) Two-Metre Sky Survey (LoTSS) (Shimwell et al., 2019; Callingham et al., 2021; Yiu et al., 2024) as well as surveys from the Australian Square Kilometer Array Pathfinder (ASKAP) like the Variable and Slow Transient (VAST) Survey (Murphy et al., 2013) and Rapid ASKAP Continuum Survey (RACS) (McConnell et al., 2020; Pritchard et al., 2021; Pritchard et al., 2024). Surveys at other parts of the spectrum like the Transiting Exoplanet Survey Satellite (*TESS*, Ricker et al., 2014) have also made it easier to accomplish simultaneous, multi-wavelength observations of stellar activity in the radio (Zic et al., 2020; Rigney et al., 2022; Wang et al., 2024). Although there has been movement towards meeting the requirements to unambiguously detect stellar type II and III bursts, with surveys being pivotal in our understanding of stellar radio emission and particle acceleration, the low duty cycle nature of radio surveys compared to dedicated monitoring makes it more difficult to observe phenomena that are transient in nature; there are few multi-wavelength monitoring programs of solar-type stars that include LF radio.

The OVRO-LWA is a recently-upgraded, low-frequency-radio observatory in North

Figure 3.1: A small fraction of the OVRO-LWA antennas.

America (Hallinan et al. in prep, see Figure 3.1). The instrument was inspired by the cross-dipole “fork" design made in collaboration with the United States Naval Research Laboratory for the University of New Mexico (UNM) LWA (Ellingson et al., 2009). It is capable of continuously producing 10 s snapshot images of the entire sky with 24 kHz spectral resolution in the 13-86 MHz range simultaneously with ms-resolution beamformed observations and other data-recording methods. Although the OVRO-LWA facilitates operations for many science cases, many of its performance requirements were driven by the goal of studying exo-solar systems through exoplanet searches and detecting stellar type II and III bursts. To this end, it has infrastructure dedicated to carrying out nightly monitoring of specific stars in addition to an observing mode well suited for general-purpose transient searches, including stellar radio bursts. Here, I discuss the operations and performance of the OVRO-LWA with respect to the SWAYS monitoring program, which will utilize the imaging and beamformed data products. I provide results of my efforts in commissioning the beam-formed observing mode as it informs how I use the beamformer for my science, and evaluate the potential of detecting type III bursts from the six stars of the main SWAYS sample, listed in Table 3.2, based on the results of a 1 hr observation of π^1 UMa (pi UMa).

3.2 Design and Operations

The OVRO-LWA consists of 352 cross-polarization dipoles for a total of 704 signal paths. The array was constructed in three stages: stage I was completed in 2014 and consisted of 251 dipole antennas contained within a 0.2 km diameter; stage II introduced an additional 32 antennas and extended the maximum baseline to 1.5 km (Anderson, 2019; Eastwood, 2019). The recently completed stage III includes 243 core antennas contained within 0.2 km and 109 outrigger antennas that provide a maximum baseline of 2.4 km. This final stage also includes upgraded analog and digital electronics. Analog electronic upgrades include custom optical fiber link boards for transport of signals via radio frequency over fiber (RFOF), as well as a new generation of receiver board with much improved resilience to intermodulation products, improved signal path isolation (80 dB) via shield cans on each signal path and greatly improved reflection coefficients to minimize bandpass ripple. The digital backend was also completely replaced and now facilitates several simultaneous observing modes including full cross-correlation data (704 inputs) at 10 s time resolution and 1% of baselines at 100 ms time resolution, 12 independent total-power beams at 1 ms time resolution, two voltage beams, and voltage buffers.

Here, I focus on the targeted-search capabilities of the OVRO-LWA as they relate to SWAYS; the two observing modes relevant for this work are the 10 s, full-array cross-correlated mode (slow visibilities) for burst-identification and the full-power beams (beamforming) for burst characterization. The full description of these modes will be provided in OVRO-LWA papers that are currently in preparation. I should note that I primarily focus on the observing and analysis method for type III bursts for this discussion. This is because the duration of the two burst types—tens of minutes compared to 10s of seconds for type II and III bursts respectively—pose very different problem spaces. While a type II burst may persist for many integrations in slow visibilities, a type III burst may only be detectable for a single integration. This makes the room for error for burst identification small and also removes the means for spectral analysis in slow visibilities—type III bursts represent the more difficult burst to detect and characterize, burst luminosities aside. The parameter space of solar type III bursts and statistics for brightness are also much better constrained than for type II bursts; it is much easier to make predictions for type III detectability.

Slow Visibilities and Burst Detectability

As mentioned, the slow visibilities (hereafter slow vis) are the cross-correlated data from the OVRO-LWA with 10 s time resolution and a native spectral resolution

of 24 kHz. The nature of the array allows for all-sky imaging via this observing mode with $\approx 5'$ spatial resolution at our highest frequency of 86.87 MHz. When integrated over the full band, a single 10 s snapshot has a theoretical Stokes I (total intensity) thermal noise limit of $\sigma_{\mathrm{I}} \approx 150$ mJy, which may be elevated by confusion noise. This sensitivity, coupled with the capability of mitigating the effects of bright astrophysical sources via peeling (Noordam, 2004; Eastwood, 2017), control the beam shape via weights and tapering (Briggs, 1995; Taylor et al., 1999), and to more easily identify radio-frequency interference (RFI) sources in image space makes the slow-vis observing mode the preferred mode for searching for stellar radio burst candidates.

The coarse time resolution of the slow-vis observing means that, assuming that stellar type III bursts have structures very similar to the solar form, type III bursts are unlikely to be temporally resolved and we should not expect to be able to observe their spectral sweep, irrespective of the array sensitivity. Because I likely will not be able to resolve the spectral structure of the burst, I can integrate in frequency to take advantage of the increase in sensitivity it affords. The data to search for a type III burst would then be a light curve extracted from the location of the star, where a burst signature would appear as a single $> 5\sigma_{\mathrm{I}} \gtrsim 750$ mJy point in a light curve that is otherwise noise centered at 0 mJy for an adequately-subtracted sky. The frequency-integrated, slow-vis images can then be checked to confirm the emission is associated with a point source coincident with the location of the star. Although we cannot resolve type III bursts in this discovery space, we do have the time resolution to resolve them in beamformed data; after verifying the signal in the slow-vis data, I can then use the beamformed data in that time frame to do a burst structure analysis as described in Section 3.2.

It is worth acknowledging that at this sensitivity, the flux density of the burst scaled to a distance of 1 AU would be $3.19 \times 10^{10}\, d_{\mathrm{pc}}^2$ Jy where d_{pc} is the distance of the star in parsec. For the closest star of my sample, ϵ Eri at a distance of 3.21 pc, we would then require a burst equivalent to a 3.27×10^{11} Jy burst from the Sun. This is considered bright for solar type III bursts at the frequencies that the OVRO-LWA operates at (Saint-Hilaire et al., 2013; Krupar et al., 2024), but it is not unreasonable to expect that active stars might produce bursts that are significantly brighter than what we observe from the Sun and do so frequently, especially since solar radio burst occurrence is highly correlated with the solar activity cycle (Saint-Hilaire et al., 2013).

We can additionally estimate how many bursts we might expect to be able to detect with the OVRO-LWA by considering the solar type III burst rates provided by Saint-Hilaire et al., 2013 from data collected by the Nançay Radioheliograph (NRH) (Kerdraon and Delouis, 1997):

$$\frac{dN}{dS_\nu} = 27.7\, S_\nu^{-1.66}\ \mathrm{day}^{-1} \tag{3.1}$$

$$N(>S_\nu) = 51.63\, S_\nu^{-0.69}\ \mathrm{day}^{-1}. \tag{3.2}$$

Here, N is the number of bursts per day with a given flux density S_ν. It is important to note that the coefficients and exponents in the equations were derived from bursts detected at 150 MHz with a 10 s integration time, even though the bursts themselves sweep through the NRH's band in $\sim 1\,s$ (Alvarez and Haddock, 1973; Reid and Ratcliffe, 2014; Vedantham, 2020); some of the burst's flux is being integrated out.

Vedantham (2020) adapted the prior equation into the following to represent the number of bursts as a function of the distance of the star and the bursts' flux density:

$$N(S_{\mathrm{mJy}}) = 0.17 d_{\mathrm{pc}}^{-1.38}\, S_{\mathrm{mJy}}^{-0.69}\ \mathrm{day}^{-1}\ (10\,\mathrm{s\ integration}) \tag{3.3}$$

$$N(S_{\mathrm{mJy}}) = 0.83 d_{\mathrm{pc}}^{-1.38}\, S_{\mathrm{mJy}}^{-0.69}\ \mathrm{day}^{-1}\ (1\,\mathrm{s\ integration}). \tag{3.4}$$

The larger coefficient for equation 3.4 accounts for the fact that bursts only last for $\sim$ 1 s in the LOFAR High-band array (HBA) band (110-250 MHz). In the OVRO-LWA's band though, bursts last $\sim$ 10 s—I can integrate for longer without the risk of integrating out the burst's flux. As such, I assume equation 3.4 to be more representative of the rate for the OVRO-LWA than 3.3. Then, plugging $5\,\sigma_{10\mathrm{s}} \approx 750$ mJy for S_{mJy} in equation 3.4 gives the estimated detectable burst rate for the OVRO-LWA as a function of the distance of the star:

$$N(5\,\sigma_{10\mathrm{s}}) = 0.00886\, d_{\mathrm{pc}}^{-1.38}\ \mathrm{day}^{-1}. \tag{3.5}$$

For ϵ Eri, this amounts to a detection rate of one every ≈ 578 d. Of course, this is using 1.) solar statistics and 2.) flux density estimates from higher frequencies. The association between type III burst and both flares and activity cycles—as well as the likelihood that the more energetic stellar flares would be capable of producing brighter bursts—make this burst rate an underestimate. For instance, although the Sun may only produce a flare with energy on the order of 10^{34} erg once per century (Vasilyev et al., 2024), EK Draconis produces one about once per week (Namekata

Table 3.1: Radio detection expectations for the six main stars apart of the SWAYS sample. f_b is the lower limit for the expected type III burst rate as estimated by equation 3.5, and $S_{\nu,1s,1AU}$ is the flux density that a 5σ detection of a burst would appear at the distance of the Sun in solar-flux units (SFU = 10^4 Jy). Following the discussion in Section 3.2, it is entirely likely that the burst rates could be underestimates by as low as a factor of 5 (accounting flux density differences between 50 MHz and 150 MHz) and several thousand (accounting for flare rate differences between the Sun and highly-active stars).

Star	RA [°]	Dec [°]	d [pc]	$S_{\nu,1s,1AU}$ [SFU]	f_b [d^{-1}]
ϵ Eri	53.23	-9.46	3.21	3.3×10^7	1.7e-3
χ^1 Ori	88.59	+20.28	8.66	2.4×10^8	4.4e-4
κ^1 Ceti	49.84	+3.37	9.14	2.7×10^8	4.1e-4
π^1 UMa	129.80	+65.02	14.4	6.6×10^8	2.2e-4
EK Dra	219.75	+64.29	34.4	3.8×10^9	6.5e-5
V889 Her	278.58	+18.69	35.6	4.0×10^9	6.2e-5

et al., 2021); this might then suggest that the equation could underestimate the type III burst rate of EK Draconis by a factor of several 1000s. Also, type III bursts are brighter at lower frequencies, further exacerbating the under estimation. As such, the burst rates for the SWAYS sample listed in Table 3.2 should be treated as lower limits.

While type II bursts may not be as high of intensity as type III bursts, they last much longer at a given frequency and drift through the OVRO-LWA band much slower due to its accelerator (*i.e.*, a CME shock) moving much slower than the type III accelerator. This affords me the option of integrating in time as well as frequency to increase sensitivity. Integrating up to 10 min would provide $5\sigma_I \approx 65$ mJy, or the equivalent of a 2.83×10^{10} Jy burst from the Sun at the distance of eps Eri. This is again bright (although not unheard of) by solar standards. This also assumes that the star can accelerate a super-Alfvénic shock within a region where the plasma density is conducive for observing plasma emission with the OVRO-LWA ($n_{e^-} \approx 10^6 - 10^8$ cm^{-3}). Although the Alfvén speed should be higher for these young stars with magnetic fields that are stronger than the Sun's, it should not be unreasonable to expect stars with much stronger flares—associated with higher *magnetic* potential energy—to also generally have faster CMEs, which are associated with higher *kinetic* energy. Such an expectation is supported by work by Mohan et al. (2024a), who show that the solar CME radio power are correlated with higher flare X-ray luminosity.

Beamforming

The beamforming mode refers to a power beam; the antennas are weighted based on their position such that when the powers are summed, the array is sensitive to a specified direction. The resulting data product is a dynamic spectrum—the array power as a function of time and frequency. As the data recorder operates currently, there is limited control for shaping the beam; specified antennas can be flagged such that a maximum baseline can be enforced, but baseline-based weighting is not currently possible. Because of this, the incoherently-summed beam shape is complicated when outrigger antennas are included. This is evidenced from drift scans of Cassiopeia A (Cas A), shown in Figure 3.2. For this drift-scan test, I coordinated four beams to record data simultaneously; two beams were calibrated to include contributions from the entire array and two were calibrated to only include the array's core. For each set of calibrations, one of the two beams was tracking Cas A and the other was pointed at the azimuth and elevation that Cas A would be transiting, timed to be half-way through the two-hour observation. The ratio of the stationary and tracking beam then roughly maps the shape of the beam. The beam for the full array shows an underlying Gaussian structure consistent with the shape expected for the core, but it also shows a secondary structure with a full-width half-maximum (FWHM) consistent with the resolution of the full array; the core-only beam is a well-behaved Gaussian structure as expected. For this reason of complex beam structure, outriggers are often excluded from beamformed observations and are excluded from analyses presented here. That said, it is worth noting that even when Cas A is well beyond the primary beam, we can tell it still contributes significantly to the integrated signal of the beam because the effect of scintillation is still apparent even when the tracking beams is $> 10^{\circ}$ from the stationary beam.

The nature of beamforming is such that recorded power includes contribution from sidelobes, which are sensitive to the sky rather than the source. In principle, a second beam could act as an "OFF beam" and be pointed sufficiently far away that the target of interest is not in the beam, while still close enough that the beams can be considered to be observing essentially the same sky. The OFF beam can then be used to subtract the sky from the "ON beam" that is pointed at the science target. In practice, the FWHM of the core beam is several degrees; an OFF beam being far enough to avoid the main lobe of the ON beam would be in a fairly different piece of sky. Similarly, horizon RFI may be in the null of one beam but in the sidelobe of another which can lead to significant disparities in the RFI environment observed by each beam. The results of extreme disparities between two beams are shown in the

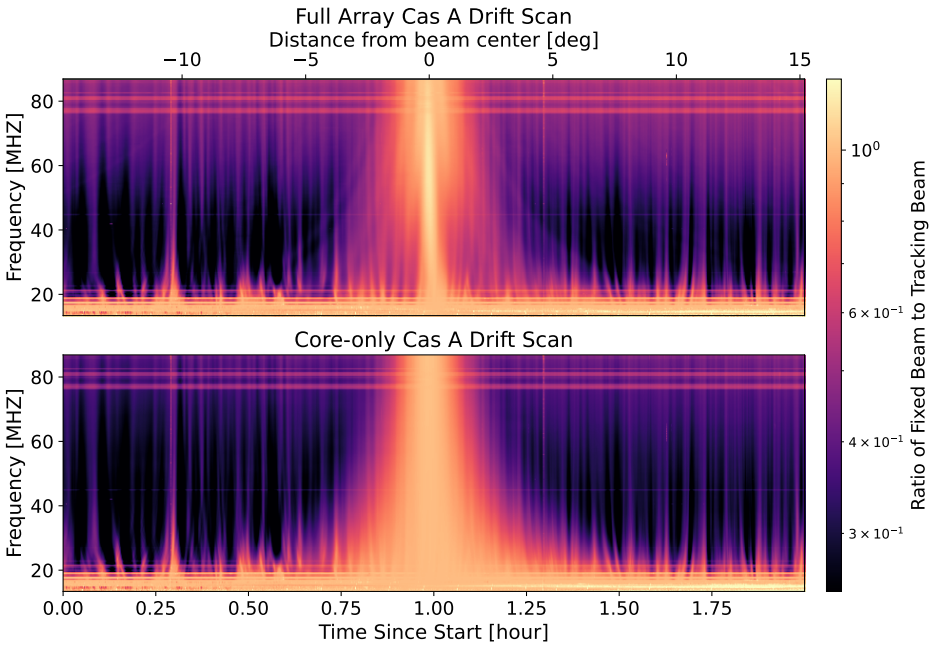

Figure 3.2: The Cas A drift scan for the full array (top panel) and for the core only (bottom panel). The structure of the core-only beam is clearly reflected in the full-array beam, but the full-array beam normalization is dominated by structure from including outriggers. Wispy structures throughout the observation can be attributed to scintillation of Cas A.

ON-OFF beam tests presented in Figure 3.3, where an OFF beam was tracking the sky $\approx 5^\circ$ from a star I was tracking with the ON beam for two different observations. This figure shows the percent difference of the OFF-beam flux density from that of the ON beam; the observing conditions of a highly-disturbed ionosphere—like the top panel shows—or that of a high-RFI environment—like shown in the bottom panel—make the ON-OFF scheme unreliable for background subtraction.

Alternatively, the slow-vis data can be combined to give the equivalent of the beamformed data which can then be used to estimate the sky and RFI to subtract from the beam. The caveat is that the native time resolution of the beamformed data can be set between $0.001 - 1$ s– this is $10 - 10,000\times$ the time resolution of the slow-vis data. Instead, in the work I present here, I perform RFI flagging on a per-channel and per-time-interval basis. This is followed by applying a median filter to the power-beam time series on a per-channel basis in order to estimate the sky background. More details on this process are provided in Section 3.3.

Because the beam does not retain spatial information, it is harder to systematically

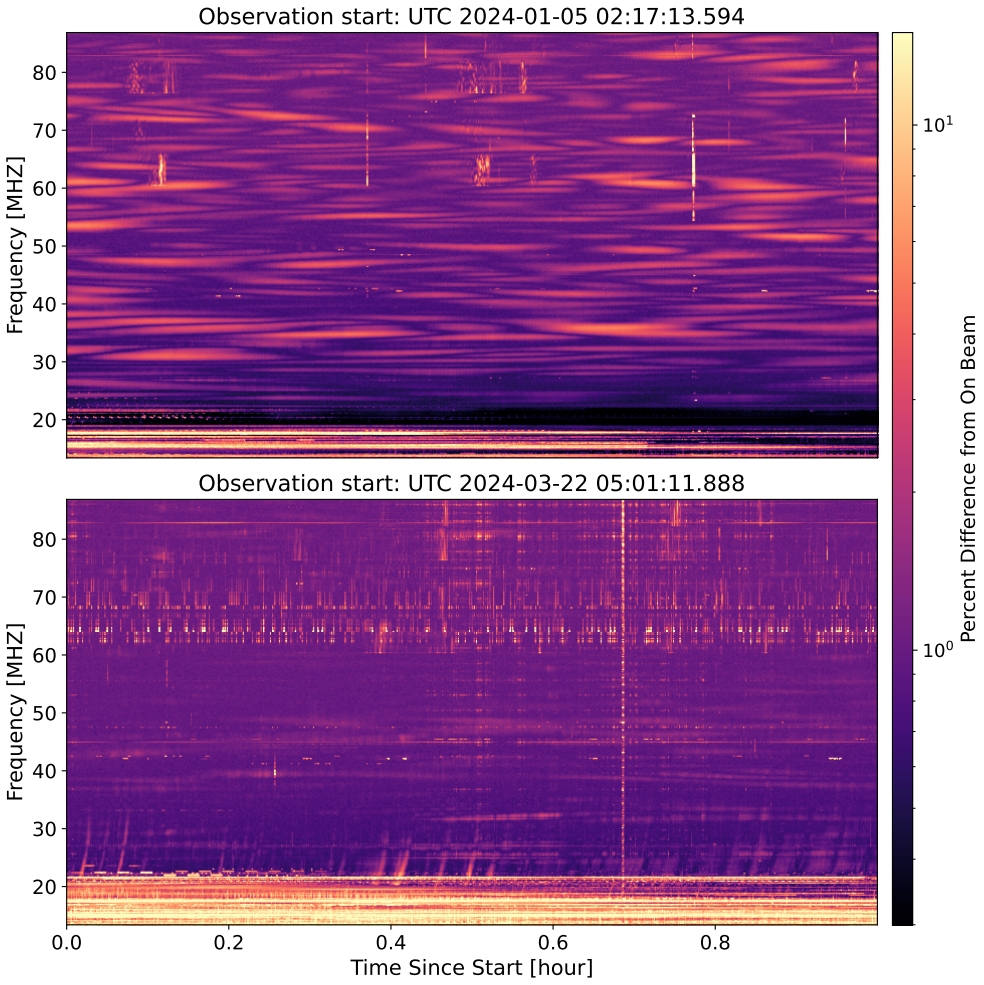

Figure 3.3: The ON-OFF beam test using one hour of data from SWAYS observations in January (top panel) and March (bottom panel) of 2024. The highly variable structure below $\approx$ 20 MHz is largely due to poor calibration solutions for frequencies so close to the ionospheric cutoff. The January observation shows features with strong frequency dependence over $\approx$ 10 min timescales, which is likely due to the ionosphere being highly disturbed. This would then imply that the ionosphere was much more stable during the March observation such that the beams were seeing similar ionospheric patches and could thus be subtracted out. The persistence of various RFI signatures for the March observation however clearly shows that the ON and OFF beams were seeing different RFI environments.

flag RFI than in slow-vis images; in a dynamic spectrum, RFI that is broadband and impulsive resembles a type III burst in many respects. Because the beamformed data are a sum of all antennas' powers, it also means that excising RFI requires flagging data from essentially all signals rather than on a per-antenna basis like cross-correlated data allows. These flagging and spatial information restrictions in addition to the sensitivity are the great motivators for using slow-vis data rather than beamformed data to do initial type III burst *identification*. Once a burst is identified in slow-vis data, the beamformed data—which is collected simultaneously with the slow-vis data—has the time resolution with which to do burst *characterization*. The burst itself is not likely to be detectable in any individual dynamic spectrum pixel, and perhaps is not even detectable without integrating over the entire duration and spectrum of the burst. However, the power of high-resolution, beamformed dynamic spectra for type III burst characterization is in its role of removing the frequency sweep, similar to performing a "de-dispersion" search for pulsars.

For incoherent pulsar de-dispersion searches, various dispersion measures (DMs) are applied to a dynamic spectrum to essentially straighten the sweep of the pulse before integrating over frequency. The DM which maximizes the de-dispersed, integrated signal provides information on the medium the light traveled through and the distance to the pulsar (Ransom, 2011; Stovall et al., 2015; Bassa et al., 2017). The physical principles for a type III burst's spectral sweep is different from that of a a pulsar's pulse, but the principles of the search are the same. Alvarez and Haddock (1973) describe burst drift rate as a function of frequency in the general form $d\nu/dt = -10^{a}\nu^{\alpha}$ MHz/s. For the Sun observed at frequencies between 75 kHz and 550 MHz, Alvarez and Haddock (1973) estimate $a \approx -2$ and $\alpha \approx 1.84$. The actual drift rate will depend both on the speed v of the exciting beam ($0.1c \lesssim v \lesssim 0.5c$ where c is the speed of light (Dulk, 1985)) and the density structure of the stellar atmosphere. For my search, I can vary the values of a and α for de-dispersion to maximize the signal when integrating over frequency. An example of what the dispersed spectra look like for various values of a and α as well as the frequency-averaged light curves are shown in Figure 3.4. As expected, the faster the drift is, the stronger the frequency-averaged signal is, emphasizing the importance of de-dispersing before integrating. Similarly, if the integration time is longer than the duration of the burst as is shown in the middle panels, the intensity of the burst gets integrated out in addition to the structure of the burst being lost.

Having laid out how the two types of OVRO-LWA data sets will be used in the

SWAYS program, I will now focus on the performance of these observing modes in the next section.

3.3 Data Analysis and Performance

The OVRO-LWA has been conducting coordinated observations of stars with Flarescope since November 2023. This coordination started during the commissioning phase of the NSF-funded stage III of the OVRO-LWA. A significant improvement in OVRO-LWA data quality was achieved after February 2024. In this section, I review the data quality and reduction process for one hour of data from a larger observing campaign I conducted for pi UMa. pi UMa is one of the furthest stars in the SWAYS sample and thus demonstrating a performance capable of detecting bursts (and flares, as I demonstrate in Chapter 4) from this star bodes well for being able to detect similar-scale or even weaker events from the other stars of the sample.

Because the goal here is to represent the workflow and resulting data quality, and because processing slow visibility data is so computationally expensive, I only focus on one hour of data rather than the full night or observing campaign. Although the processing is computationally expensive, it should not hinder future SWAYS science as the amount of radio data that I will need to process and evaluate is greatly reduced by using the presence of an optical flare to inform the time frame to search for associated radio emission. The stability of the OVRO-LWA's performance as well as data-processing pipeline development will be addressed in forthcoming OVRO-LWA papers.

The one hour of pi UMa data I evaluate starts at UTC 04:00:00 on April 10, 2024. This time (21:00 local time) was picked so that the data were representative of a time when the ionosphere would have had time to stabilize after the sun set and side-lobe effects due to Cas A and Cyg A—which rise later in the night—were minimal. In this time frame, pi UMa was at an elevation between 58°–62° from the OVRO-LWA's location. As such, the effects of scintillation, atmospheric extinction, and beam projection should be relatively low; we should nominally expect this one hour to be representative of well-behaved observing conditions and some of the highest quality data that the instruments can produce.

Slow Vis

The output of the slow-vis data recorder is a measurement set (MS), a file format used by the Common Astronomy Software Applications (`CASA`) software (CASA Team et al., 2022). There is an MS file for each 10 s integration and for each subband

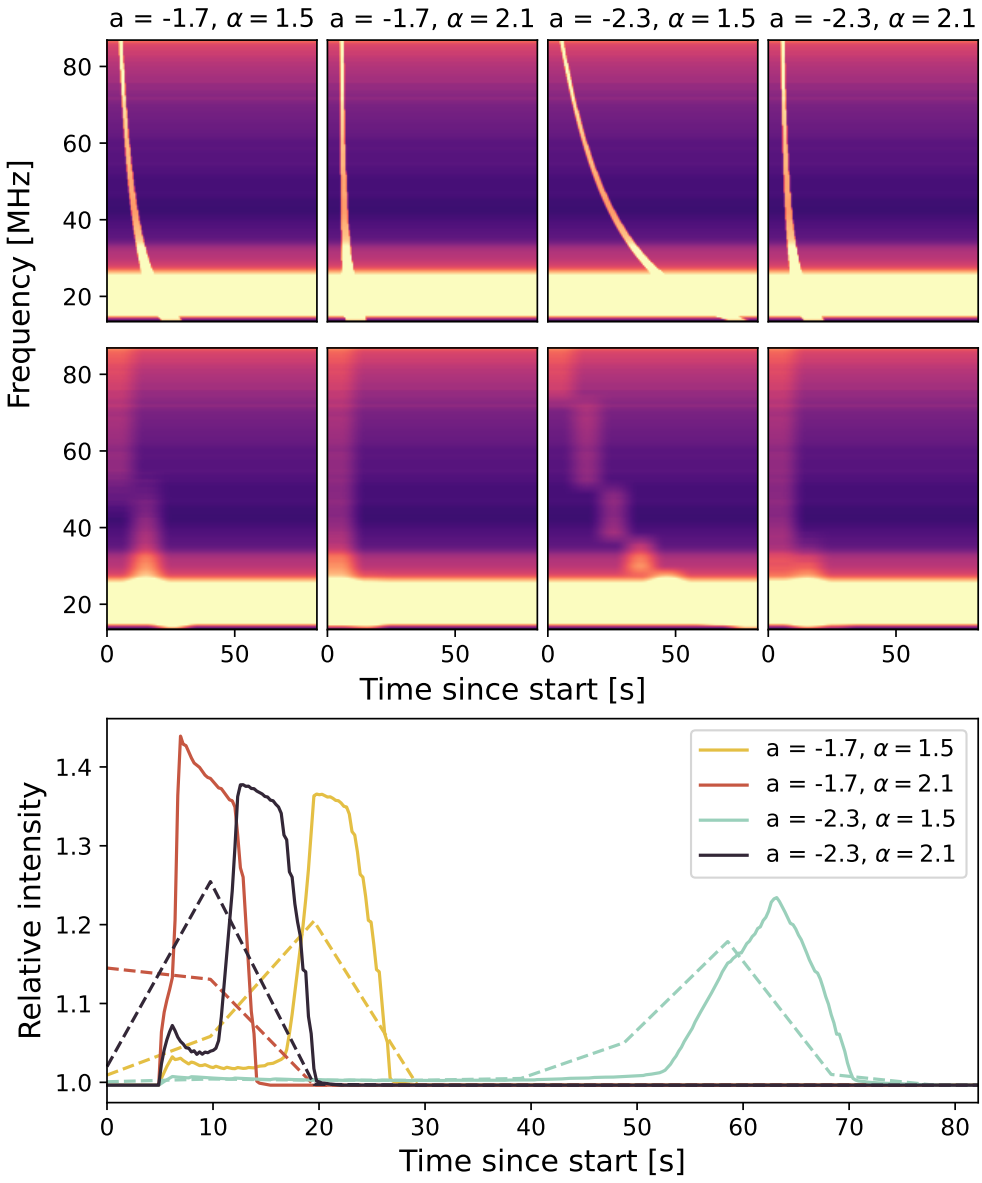

Figure 3.4: Synthetic dynamic spectra for type III bursts with various values of a and α observed at the time and spectral resolution (256 ms, 24 kHz) of the OVRO-LWA SWAYS beam (top panels) and integrated up to the 10 s time resolution of slow-vis data (middle panels). The frequency-averaged light curves for the various beamformed (solid line) and slow-vis (dashed line) dynamic spectra are shown in the bottom panel. These plots are meant to be representative of only the general shape of type III bursts and the effect of the integration time being larger than the duration of the event; the intensity of the burst at each pixel in the 256 ms-resolution data was taken to be 1.5× the background intensity at every frequency channel and is not representative of the actual frequency dependence of burst intensity.

(192 channels per subband for a total of 16 subbands) for a total of 5744 MS files for a one-hour observation. Although there are 16 subbands, here I only focus on the 10 subbands corresponding to frequencies 41–87 MHz since lower frequencies are both often more difficult to calibrate and are not the primary band of interest for the SWAYS science case. The processing of the slow-vis data to produce a light curve for pi UMa is done in three broad steps. The first is the actual data reduction and cleaning performed through `CASA`, `AOFlagger` (Offringa et al., 2012), and, if necessary, peeling (Eastwood, 2017; Williams et al., 2019); this particular step has been consolidated into a pipeline by Nikita Kosogorov and will be discussed in more detail in forthcoming papers. The following steps are imaging the data via `wsclean` (Offringa et al., 2014) and then finally identifying ionosphere-induced changes to source position in order to determine the actual location of the star in the image plane and its associated flux density.

Calibration and Imaging

The first step of reducing the data involves flagging bad antennas. These are identified from auto-correlation data in the 30–80 MHz range where the spectrum should vary smoothly—antennas with anomalous spectral shapes, excessive variability with time, or with a power that is persistently $< 10\%$ the median antenna power are removed from the MS using `flagdata` in `CASA`. `AOFlagger` is then run with default settings to flag RFI in the dynamic spectra of each baseline. After flagging data, we generate a sky model based on the known spectra of the brightest sources in the sky, attenuated by the array-averaged primary beam. For this observation, we used Cassiopeia A (Cas A) and Cygnus A (Cyg A) from data collected seven hours after the pi UMa observation. The model spectra of these sources are based on Baars et al. (1977), with the caveat that Cas A's flux density has changed due to ongoing expansion as a supernova remnant. The overall flux scale is validated through flux extraction to confirm consistency with the model. The models, in the form of a component list, are added to the model column using the `CASA` command `FT`. Then, a bandpass solution is calculated for each antenna; we use baselines greater than 10 wavelengths (λ) to reduce contamination from diffuse sky flux and baselines less than 150λ to avoid resolving sources that are used for calibration.

After application of this bandpass solution, residual calibration errors are present in image data for the brightest sources in the sky, limiting the dynamic range. These typically require an additional step of direction-depedent calibration and source

removal. To facilitate this, we make use of the `TTCAL` software package developed for the OVRO-LWA that makes use of StEFCal (Salvini and Wijnholds, 2014; Eastwood, 2017) to peel bright sources from the data. In the case of the observation presented in this chapter, only one source was above the horizon and bright enough to need this. This source was Cas A which, despite being low elevation, still presented significant direction-dependent effects due to the ionosphere and chromaticity in the antenna beam.

After peeling each time interval and subband, the final step is changing the phase center to pi UMa and imaging with the final frequency integration of 46 MHz and time resolution of 10 s. Because the data have been phase-centered on pi UMa, I can set our image size to be relatively small so that imaging runs faster—I choose a region of 128×128 pix. Paired with a pixel scale of $1.875'$, this region corresponds to a FOV of $4^\circ \times 4^\circ$. I use a gain of 0.85, Briggs robust weighting of 0, and a circular Tukey taper with a minimum baseline length of 30λ to taper the uv plane and remove the diffuse radio sky. The resulting beam size is $\approx 15' \times 11'$. We use the 10 subband MS files per integration as the input MS files for `wsclean`; `wsclean` is run separately for each integration. Two resulting images are shown in the right panels of Figure 3.5.

Source Flux Extraction

Once I have FITS images for all of the time intervals, I can identify sources in the frame in order to distinguish the effects of the ionosphere and determine the true position of pi UMa in the sky. The apparent source positions can be quite different to those reported by, *e.g.*, the VLA Low-frequency Sky Survey Redux (VLSSr) catalogs (Cohen et al., 2007; Lane et al., 2014) due to path length differences introduced by the ionosphere. These differences can manifest as both differences in the bulk ionospheric properties of the different instruments as well as the shorter time-scale variations of the ionosphere and solar wind (*i.e.*, traveling-ionospheric disturbances ((TIDs), Boyde et al., 2022; Loi et al., 2015) and interplanetary scintillation ((IPS), Hewish, 1955; Clarke, 1964), respectively), although IPS variability typically happens on timescales shorter than the time-resolution of slow-vis data. This can make cross-matching sources that show up in our data with catalogs quite difficult.

Instead of cross matching sources in a frame with a pre-exisiting catalog, I use `photutil`'s `DAOStarFinder` (Bradley et al., 2024) class to identify sources in each frame. For this, I use the beam information in the FITS header to build a convolution

kernel; I use the major-axis FWHM for the FWHM input, the beam major and minor axes FWHMs to define the ellipticity ratio, and the beam position angle (BPA) rotated counter-clockwise by 90° as the position angle in `DAOStarFinder`. I look for sources 5σ above the median value in the image. Because the ionosphere can cause extreme position changes on short timescales, I assert that a source found in one image, S_1^i, is the same source found in the next image, $S_2^{i'}$ if 1.) $S_2^{i'}$ is closer to S_1^i than any other S_2^j source and 2.) the separation between S_1^i and $S_2^{i'}$ is less than 0.2° ($\approx$ 6 pix or $\approx$ 1 beam FWHM away). If none of the sources in the second frame satisfy the conditions of being associated with S_1^i, then the source positions are compared against the average position of S^i across the previously evaluated frames to see if any source is close to the average position. If a source in the second frame also cannot be cross-matched to any of the average positions of previously-identified sources then it is considered a new source.

Prioritizing source association based on the locations of the sources in the preceding frame reduces the likelihood of incorrectly cross-matching sources. Allowing for subsequent consideration of the position relative to the average source positions allows for additional flexibility in source association. I confirm the quality of this method by looking at each frame by eye—there are no apparent false associations, and sources that were not identified in every frame were generally excluded because the source's flux was below the detection threshold or the source had moved out of frame. An example of a source being detected in one frame but not another is exemplified by Source 4, indicated by yellow ellipses in the right-hand panels of Figure 3.5; although there is an integration early in the observation when it is not detected (top right panel), it is clearly detected in other integrations (bottom right panel).

There were two source that were detected in all 359 images: VLSSr source J083745.4+651331 (labeled as Source 1 in Figure 3.5) and VLSSr source J085101.0+634342 (labeled as Source 2) which were on average 4′ (*i.e.*, within half a beam width) from the positions of the sources as listed in the VLSSr catalog. Conveniently, Source 1 is also only 15′ from pi UMa, making it likely that pi UMa and the bright source share the same isoplanatic patch (Intema et al., 2009). I can therefore assume differences in Source 1's position from its average position are representative of differences in pi UMa's position as well; I calculate the separation and position angle between Source 1's position in a given frame and its average position and apply these values to pi UMa's true astronomical coordinates to estimate where it would be on the sky

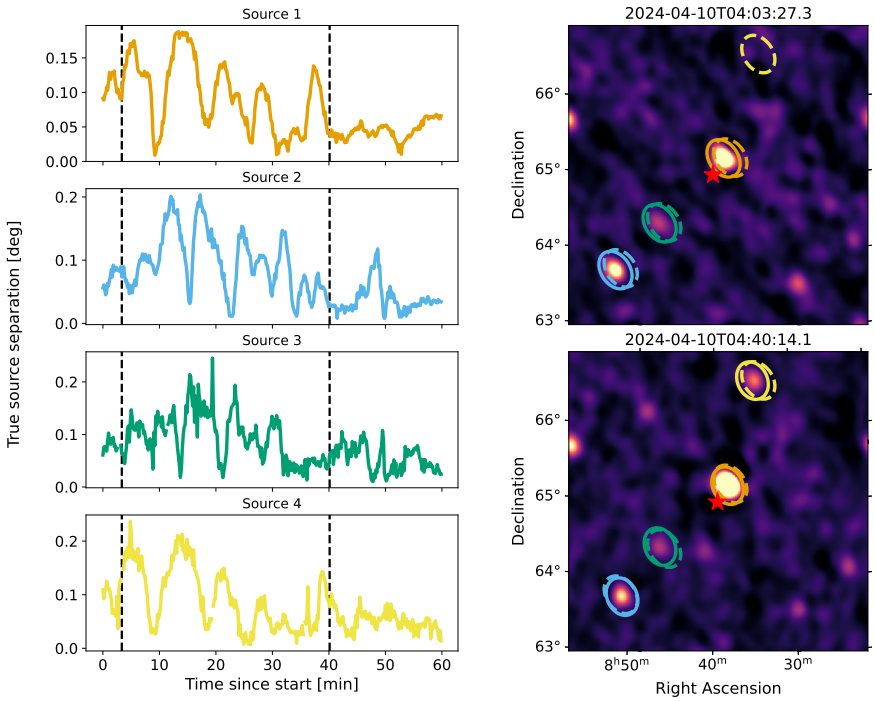

Figure 3.5: The separation between the source position and the average position of the source (left panels) and the corresponding sources in the image plane (right) indicated by ellipses with colors corresponding to their color in the position-change plots. Here, 'True Source' refers to the average position of a source across the one-hour observation. The images are centered on the location of pi UMa and the expected position of pi UMa (based on position changes in Source 1 caused by the ionosphere) that we use for its flux density extraction is indicated by the red star. The source detections in the right panels are indicated by solid-lined ellipses and the average source positions are indicated by dashed-line ellipses; Source 4 was not detected in the top frame and so no solid ellipse is indicated for it in that frame. The timestamps of the images in the right panel correspond to positions of the black dashed lines in the left panels.

as observed by the OVRO-LWA. The flux density for Source 1 and pi UMa are taken to be the value of the pixel where they are positioned (based on `DAOStarFinder` location for Source 1 and the estimation just described for pi UMa). To calculate the RMS for a given frame, I first mask the sources that were identified for that given frame with elliptical apertures, with the ellipse shape defined by beam properties provided in the image's FITS header. The RMS is then calculated from this masked image. The fluxes for Source 1 and pi UMa are shown in the top panel of Figure 3.6[1].

The flux density for Source 1 is highly variable as a function of time. This source is a well-known quasar (Véron-Cetty and Véron, 2006) and so we should not expect variability intrinsic to the source on the timescales that we observe here. To investigate the cause of Source 1's variability, I also consider how the position of Source 1 varied with time, shown in the bottom panel of Figure 3.6 for ease of comparison. What may be immediately apparent is that a sudden or drastic change in Source 1's flux density often has a corresponding rapid change in the position of the source relative to its average position. Because the source position variability is due to ionospheric effects, it is likely that the variability in flux is similarly due to a multi-paths effect in a turbulent ionosphere, causing scintillation.

This effect, while milder, is still somewhat present in the flux density upper limits at the location of pi UMa. This is due largely from the fact that it is so near Source 1 that the flux density recorded at pi UMa's location is impacted by variability in Source 1. The other detriment of pi UMa's proximity to Source 1 is that its location often ends up in a region of over-subtraction from the cleaning and de-convolution. To get around this, we create a 12×12 pix mask around pi UMa's location and then re-run `tclean` in CASA with 10,000 major iterations to create a clean mask that is saved to the model column. This number of iterations was established through simple trial and error, with the goal of removing sufficient sky flux from the dirty image to ensure that the resulting residual image had a peak pixel value less than approximately 3 times the RMS near the center of the image. The goal is to remove the effect of source sidelobes rotating through the image and contaminating the dynamic spectrum at the location of the target. The threshold used is actually very conservative. Due to the exceptional PSF of the OVRO-LWA, with far sidelobes

[1]The code I wrote for source identification, association, position correction, and frame statistics is flexible for any sky images, irrespective of wavelength, so long as they are in FITS format and have world-coordinate system (WCS) information. The code is available at `https://github.com/iveydavis/astro_toolbox/blob/main/vis_lc_extraction.py`.

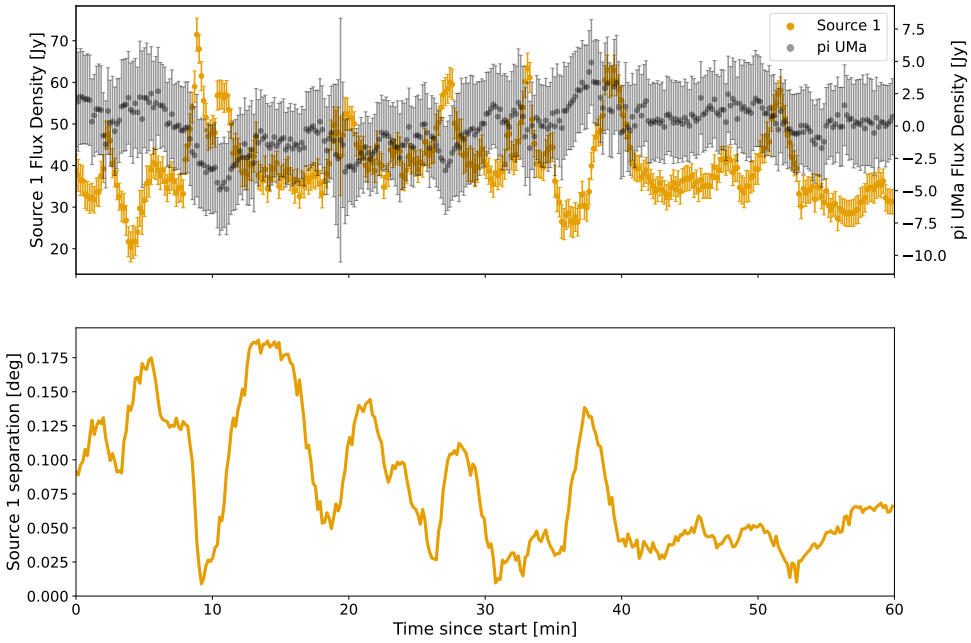

Figure 3.6: Flux density of Source 1 (VLSSr J083745.4+651331) (left axis) and pi UMa (right axis) is shown in the top panel, with error bars representing 3× the RMS of the image after masking sources. The separation between Source 1 and its average position as a function of time (same content as top left panel in Figure 3.5) is shown in the bottom panel. Much of the flux density variability in Source 1 has a corresponding variability in its source position, suggesting that the flux-density variability is an ionospheric or general plasma density variation that is lensing the emission from the source.

$< 10^{-3}$ of the peak PSF for a monochromatic snapshot image, simply removing the bright sources (> 100 Jy) is sufficient to achieve the desirable outcome. We note that the subsequent pipeline to be used in upcoming papers now includes auto-thresholding, calculated for a local RMS in the image.

The results of this cleaning and how it compares to the original peeled image are shown in the top panels of Figure 3.7. The light curve of pi UMa from both versions of the data are shown in the bottom panel of that figure. The RMS of pi UMa's flux in the original, peeled images is 1.70 Jy over the 10 s intrinsic integration time and 41–87 MHz bandwidth; it is 0.96 Jy in the subsequently masked and cleaned data. Similarly, the median background RMS of the original peeled images (with detected sources being masked) is 1.27 Jy while it is only 0.74 Jy in the subsequently

cleaned images. As expected, the flux density as a function of time is more stable and the background RMS is generally lower for the additionally-cleaned data. These results pose an interesting problem for the data reduction pipeline moving forward: a consistently-detected source near the target star is ideal for knowing where exactly on the sky the star is, but its presence impedes reliable flux extraction from the star's location. The correction of image plane distortion by the ionosphere has been studied before (Hurley-Walker and Hancock, 2024) and will be the subject of a forthcoming paper (Huang et al., 2025). That said, I will show in Chapter 5 that the severity of the ionosphere's effects in this observation may not be representative of the typical observing conditions of the OVRO-LWA; the additional masking and cleaning steps taken here to reach reasonable noise levels are not likely to be necessary for most observations.

The measured noise in the image will include both thermal noise and confusion noise, the latter of which is expected to dominate even for short integrations. To investigate this, I attempted to quantify the thermal noise in that data and compare that to the predicted confusion noise. The effective area ($\propto \lambda^2$) and system temperature ($\propto \lambda^{-2.55}$) of the OVRO-LWA varies significantly as a function of wavelength. Therefore, to provide an approximate estimate of thermal noise across the band, I analyzed two channels, one near the high frequency end of the used band and one near the low frequency end. I imaged individual channels in the first time integration of this observation in the 73 MHz and 41 MHz subbands, using the same tapering, weights, and masking as was used for the data with additional cleaning. I then subtract adjacent channel images and find the RMS of the difference of the images. In the 73 MHz subband, this RMS is 16.2 Jy (11.5 Jy per channel); in the 41 MHz subband it is 20.1 Jy (14.4 Jy per channel). These per-channel RMS values approximately corresponds to the thermal noise per channel, as the confusion noise is mostly removed by the subtraction process. Thermal noise should scale inversely with the square root of the number of channels. The number of channels integrated over for this observation was 1920, leading to a thermal noise estimate of $\sigma_{\mathrm{T}} \approx 260$ mJy in the 73 MHz subband and $\sigma_{\mathrm{T}} \approx 320$ mJy in the 41 MHz subband.

Haarlem et al. (2013) estimate confusion noise σ_{c} in their equation 6 as:

$$\sigma_{\mathrm{c}} = 0.03 \left(\frac{\theta}{1''}\right)^{1.54} \left(\frac{\nu}{74\,\mathrm{MHz}}\right)^{-0.7} [\mathrm{mJy\ beam^{-1}}] \tag{3.6}$$

where θ is the full-width-half-maximum of the beam and ν is the frequency. At 74 MHz, $\theta \approx 425''$ for the OVRO-LWA, giving us a confusion noise ≈ 340 mJy.

The total noise would then be $\sqrt{\sigma_{\rm T}^2 + \sigma_{\rm c}^2} \approx 430\,$mJy. Noting that confusion noise is higher at the bottom of the band ($\sigma_c \approx 1300\,$mJy at 41 MHz, for a total noise of 1340 mJy), the difference between the thermal noise floor and the noise we report for this observation can largely be attributed to confusion noise with some contribution from excess thermal noise. There may be additional contribution from side lobe confusion and imperfect peeling that leaves some contamination from bright sources.

At the 0.74 Jy noise level I report here, a 5σ detection of a type III burst at the distance of pi UMa would be the equivalent of a $\approx 3.3 \times 10^{13}$ Jy burst from the Sun–about two orders of magnitude brighter than the brightest solar burst. Although this makes the detectable burst rate a factor of 3 times lower than originally estimated, it may not be unreasonable to expect such large bursts from a star that is also capable of producing flares that are orders of magnitude more energetic than the most energetic observed solar flares (Landini et al., 1986).

Beamforming

Because sources bright enough for beamformer phase and flux calibration are rarely observed simultaneously with the science observations (*e.g.*, Cas A and Cyg A were exceptionally low or below the horizon for the observation of pi UMa), flux calibrations extracted from slow-vis data are applied to the beamformers ahead of the observation. Different aspects of calibration change on different timescales; at a minimum, calibration should occur every two weeks. Smaller effects—like the ionospheric effects presented in the preceding subsection—occur on shorter timescales, but we cannot currently account for calibration errors introduced on, *e.g.*, 1 hr timescales or shorter in the beamformed data. Because of this, and because there is such a narrow time frame between when the ionosphere stabilizes after sunset and when nightly observations begin, the flux calibrations for beamformed observations for SWAYS science are made from slow-vis data collected a minimum of one night in advance. For this particular observation, the slow-vis data for the flux calibrations were made on April 2. Although the time of these solutions is not ideal, the calibrations are stable enough over this time range (variable on the order of a few percent from night to night) for demonstrating the beamformer outputs.

The beamformed observation of pi UMa was conducted at 256 ms time resolution which would provide more-than-adequate time resolution for a “de-dispersion" search as described in Section 3.2. As previously justified, I exclude outriggers for this observation, which leads to a beamwidth $\gtrsim 1^\circ$; at this spatial resolution,

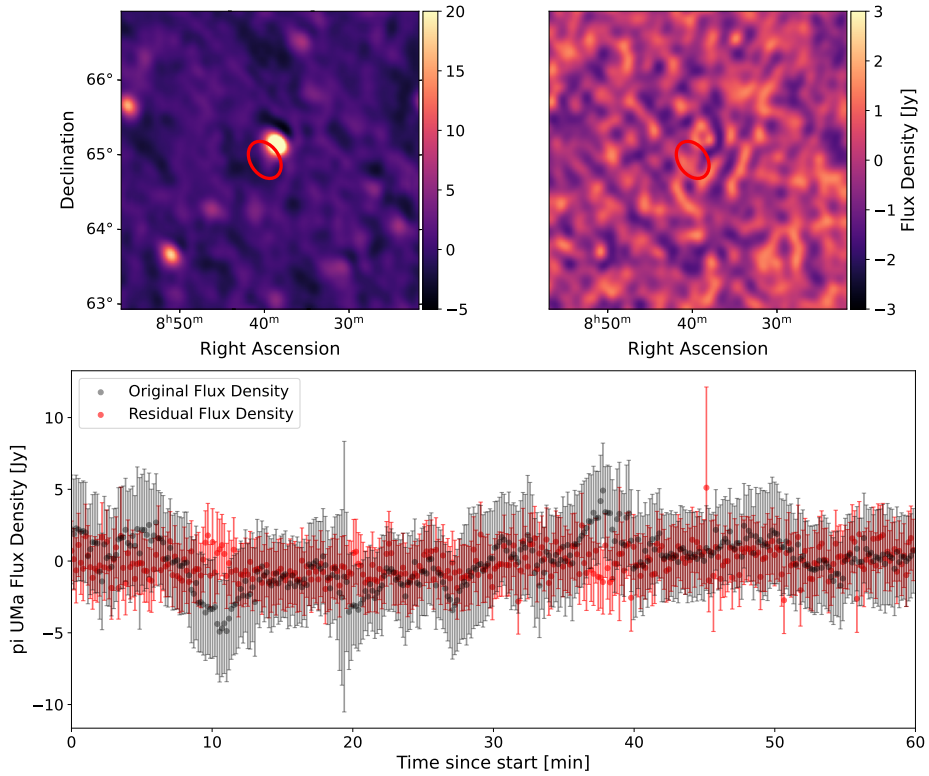

Figure 3.7: The original peeled image (top left) and the image after masking pi UMa to remove bright sources (top right) for the first time integration of the observation. The location of pi UMa is indicated by the red ellipses representing the beam shape, which I extracted the flux density from the center of to produce the light curves shown in the bottom panel. The light curves for pi UMa from these two versions of the data show that the flux from the data with additional cleaning (labeled as Residual Flux Density and indicated with red error bars) is more consistent through the observation than the original peeled image (labeled as Original Flux density and indicated with black error bars). Here, the error bars are 3× the RMS measurement of the respective images. For the Original Flux Density, I mask the identified sources before calculating the RMS.

the ionosphere shifting the apparent source position outside of the beam is not a concern. The cadence for updating the beam pointing was 15 s, which kept the source well within the primary beam. The dynamic spectrum for this observation is shown in Figure 3.8.

Before discussing the data reduction for the beamformed observation, there are a few features worth acknowledging. The first is the mild decline in flux density with time ($\approx$ 3% over the course of the hour) despite the fact that pi UMa was setting and therefore the beam should have been getting bigger and integrating more sky flux with time. This is likely due to the local-sidereal-time (LST) dependence of the system temperature. The decline in flux for this LST range (9.38 to 10.38 hour angle) is consistent with previous measurements with the OVRO-LWA (Eastwood et al., 2019).

Next, the intensity and noise below $\approx$ 30 MHz is anomalously high compared to sky expectations. This is due to poor calibrations from the slow-vis data at these frequencies. As such, frequencies below 30 MHz and above 83 MHz will be excluded before moving forward with the rest of the reduction. Additionally, the bright, broadband emission occurring at $\approx$ 20 min into the observation is a known source of RFI produced by the Los Angeles Department of Water and Power (DWP). This signal lasts $\approx$ 8 s and occurs once an hour. Finally, the various persistent, narrowband emission above $\approx$ 60 MHz are likely associated with digital television (DTV) emission while the sporadic emission between $\sim$ 60 – 70 MHz are likely DTV signals reflected from airplanes. A slowly-varying periodic signal is also evident from the light curve below the dynamic spectrum in Figure 3.8; the $\approx$ 10-minute cadence is consistent with the air conditioning (AC) cycle time. How these signals are addressed is covered in the next subsection.

RFI Flagging and Background Subtraction

RFI is persistent at certain frequencies in the beamformed data. Rigorous flagging via masking needs to be applied before additional analysis can be done. This is done in three steps: I start by flagging bright, persistent, narrowband emission. This is followed by flagging brief, bright, broadband signals. The final flagging step is flagging individual dynamic-spectrum pixels that are anomalously bright. I go into more detail on this process here before discussing background subtraction.

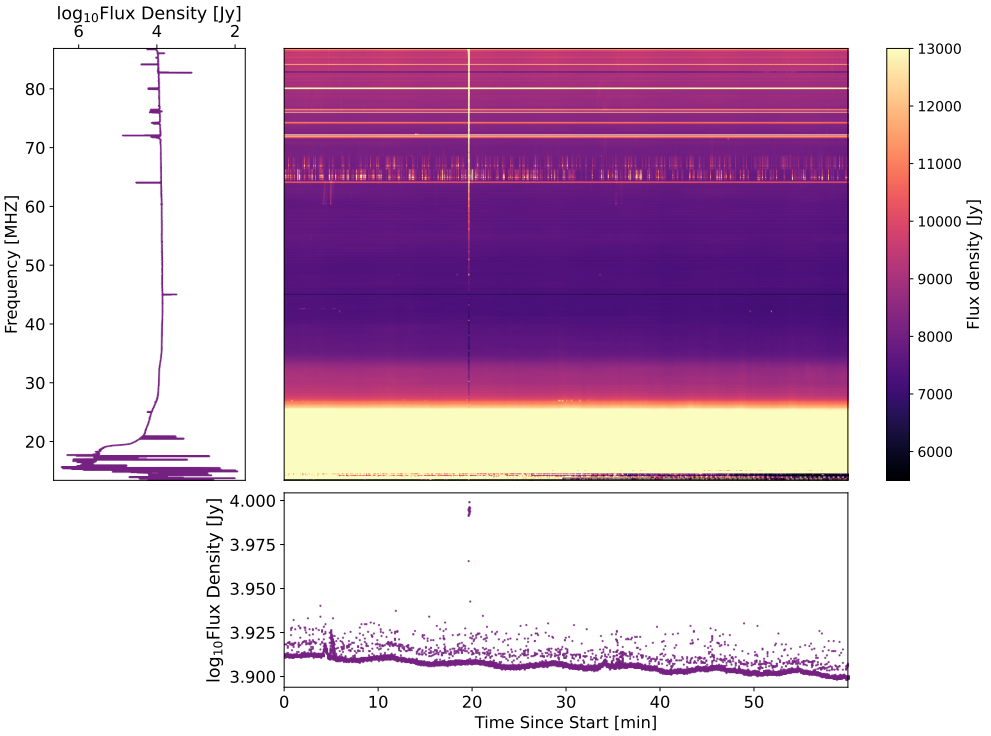

Figure 3.8: The Stokes I dynamic spectrum (top right panel), time-averaged spectrum (left panel) and light curve (bottom panel) from the OVRO-LWA beamformed observation of pi UMa. The increased intensity 20 min into the observation is due to the DWP signal and the sporadic intensity observed in the dynamic spectrum in the $\approx 60 - 70$ MHz range is attributed to reflected DTV.

Narrow-band flagging I start the flagging process with the dynamic spectrum that has been croppped between $30 - 83$ MHz (2216 channels). These data are then sub-divided into eight, equal subbands of 227 channels. For a given subband, I calculate the RMS ($\sigma_{\rm spec}$) and the median value and then go through each channel in the subband to identify channel fluxes that deviate by $> 3\sigma_{\rm spec}$ from the median. I flag these channels in addition to one channel on either side of this channel to account for possible spectral leakage.

Broadband flagging After individual frequency channels have been flagged, I take the median value of the dynamic spectrum along the frequency axis to produce a light curve. I remove slowly-varying emission (*e.g.*, the AC cycle) by taking a median filter of the light curve with `scipy signal`'s `medfilt` function and a window size of 233 time intervals ($\approx$ 1 min of data). I then divide the raw light curve by this median-filtered light curve to produce a "flattened" and normalized

light curve. From this normalized light curve, I take the RMS $\sigma_{\rm lc}$ of the curve and flag intervals where the signal deviates from 1 by $> 5\sigma_{\rm lc}$. For each interval that was flagged, I also flag four intervals ($\approx$ 1 s) on either side

Bright-pixel flagging Finally, to flag the bright pixels, I again evaluate the data on a per-subband basis across eight subbands of 227 channels each. I calculate the RMS σ and median value of a given subband and then flag pixels that deviate by $> 4\sigma$ from the median.

Each of these steps is repeated one more time, with the exception that the flagging threshold is set to $10\,\sigma_{\rm lc}$ and the `medfilt` window size is set to 698 intervals for the second round of broadband flagging. Flagging removes 3.2% of the cropped dataset (2.3% of the full dynamic spectrum). Between the cropping and flagging, $\approx$ 30% of the original data set has been removed. The results of this are shown in the top panels of Figure 3.9. One result that is immediately apparent from the light curve shown in the bottom panel of Figure 3.9 is that the scatter reduces significantly after flagging—from a factor of a few thousand Janskys to a factor of a few hundred. The majority of the scatter that is left can be attributed to the stray reflected DTV signal that was not flagged by this protocol. This flagging method is rudimentary and could perhaps be improved via, *e.g.*, machine-learning methods, although the significant variability in how RFI manifests in dynamic spectra makes it difficult to develop a robust training set without preservation of antenna or baseline-specific information at the timescale the RFI is occurring.

After flagging data we can then subtract the persistent “background" flux. I review multiple background-retrieval methods in Appendix B and conclude that the rolling-median method is the ideal solution both in terms of the results it produces as well as the processing time required to run it. For this method, I retrieve the background flux by applying a rolling median to the light curve of each individual channel with a two-minute (469-interval) window. The resulting light curve of each channel is then shifted back by 235 intervals and the last 235 intervals are flagged (see Appendix B for details on why). The dynamic spectrum with its background subtracted is shown in the middle panel of Figure 3.9.

Two details of the observation and flagging method become apparent from this background-subtracted dynamic spectrum. The first is that there is a significant amount of the reflected DTV signal—especially at frequencies $\gtrsim$ 65 MHz—that

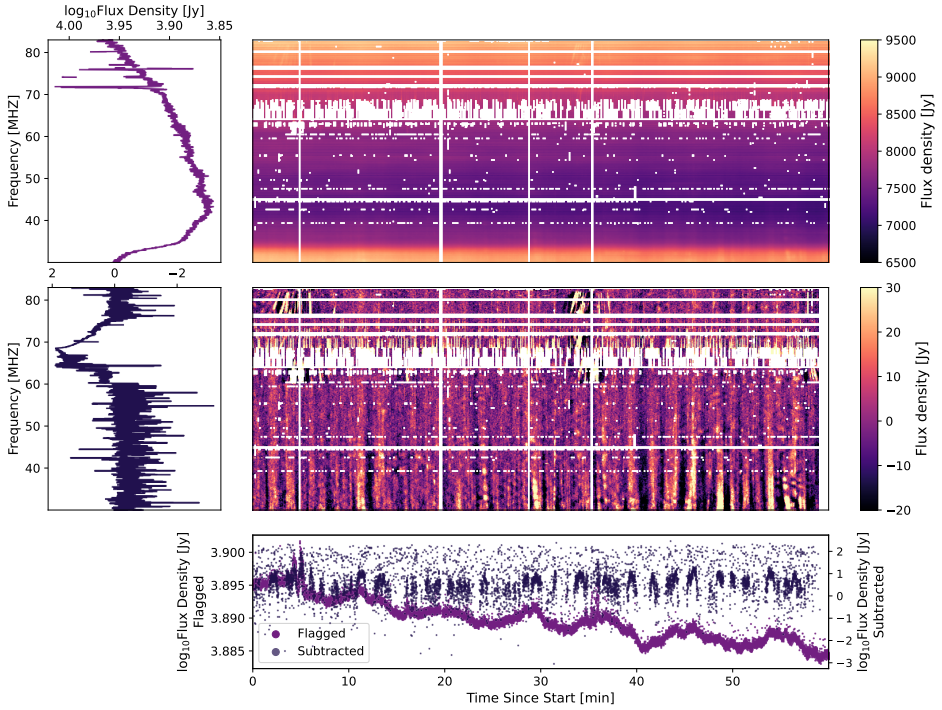

Figure 3.9: The flagged Stokes I dynamic spectrum (top right panel) and its corresponding time-averaged spectrum (top left panel). The background-subtracted dynamic spectrum (center right panel) and its time-averaged spectrum (center left) are also included. The light curves for each of these dynamic spectra are shown in the bottom panel.

was not flagged. This both increases the scatter across the duration of the spectrum-averaged light curve as well as produces the bump at around 65 MHz in the panel to the left of the background-subtracted dynamic spectrum. The second detail is the time-variable structures which last on the order of $\approx$ 1min and span a significant fraction of frequency space. These structures show the emission being stronger and a longer duration at lower frequencies. This is consistent with scintillation due to the ionosphere, and it is also responsible for the arcing structure in the background-subtracted light curve shown in the bottom panel of 3.9. This scintillation effect is prominent when bright sources are in the beam and likely indicates that a bright source—perhaps Cas A on the horizon or Tau A which was at a similar elevation to pi UMa during the observation—was contaminating the side lobes.

Overall, the quality of the beamformed data is dominated by 1.) the RFI environment, over which we have minimal control and 2.) limitations set by the beam shape. Although the primary beam shape produced by only using core antennas is primarily Gaussian, the size of the beam and the nature of integrating so much

of the sky introduces extreme confusion noise. This could perhaps be addressed by implementing antenna-based weighting that is informed by the uv plane so that outriggers can be more effectively utilized, but this functionality is currently unavailable for the OVRO-LWA beamformer data recorder. An alternative solution is to use the visibility data to reproduce the beam that can then be used to subtract the sidelobes and RFI from the beamformed dynamic spectra; the caveat here is that the time resolution of the slow-vis data is much coarser than the beamformed data. Otherwise, I could prioritize observing stars that do not have bright sources in the sky at the time of the observation (which would be similarly beneficial for the slow-vis data reduction by way of mitigating the need for peeling), but this then restricts our ability to produce up-to-date calibration tables for the beams. A re-evaluation of how beam weights are applied—both in terms of shaping and calibration—is likely necessary before beamforming can be effectively utilized for this science beyond providing limits.

3.4 Summary

The OVRO-LWA suffers from standard problems of instrumentation operating at low frequencies, namely large beam sizes (and corresponding high confusion and integrated-sky noise), contamination from bright sources (both astronomical and Earth based), and uncertainty in source position due to the ionosphere. For the slow-vis data, these issues have complicated the ability to extract fluxes from persistently-present sources in the field, let alone fluxes from the expected pi UMa locations. My current method for determining a star's position either requires that a bright source be close enough to the star's location that I can use variations in the source's position as a proxy for the variation in the star's position *or* that there be a sufficient number of consistently-detected sources that a weighted average of position changes can be used to estimate the star's location. While this works well for pi UMa which both has many sources distributed across its field and is also exceptionally close to the brightest source in the field, it is not guaranteed for all of the stars in the SWAYS sample. That said, I will show in Chapter 5 that this particular observation was apparently done while the ionosphere was especially disturbed; the extreme flux and position variability and the rigorous cleaning tasks required to prepare the data are representative of the worst-case scenario and not of all observations. Moving forward, the ideal solution may be making a model of the plasma variations as a function of space and time by taking advantage of a frozen-flow interpretation of the ionosphere (Albert et al., 2020; Laundal et al., 2024); using such a model would

allow estimates of a star's position based on the plasma's dynamics rather than directly on any source's position, even if the dynamics are derived from a collection of sources' positions. Because of the importance of accounting for the way the ionosphere warps the locations and intensities of signals, building a time-dependent model of the ionosphere to de-warp the sky that the OVRO-LWA observes will be invaluable to the data-reduction pipeline of visibility data.

In addition to complications in identifying the source position, the RMS background noise of the radio image data was a factor of a few higher than the thermal noise floor, due largely to confusion noise. This significantly alters the estimates for burst detectability and the rates at which such bursts might occur. That said, those rates are derived from solar statistics and thus are underestimates. Similarly, given the extraordinary energies that stellar flares can reach compared to solar flares, I have no reason to believe that stellar analogs of type II and III bursts could not also be orders of magnitude more intense than solar bursts.

While it is likely still possible to detect candidate bursts with the OVRO-LWA visibility data, being able to do follow-up burst characterization with the beamformed data seems less feasible as the system currently operates. The size of the beam introduces a significant amount of sky noise and the nature of beamformed operations makes it exceptionally difficult to flag RFI, calibrate at the lowest frequencies, and remove the background. Because of this, the beamformed observing mode is likely not currently usable for this science case. Getting the data to a more useful quality would require employing a different antenna weighting scheme that would afford more control of the beam shape as well as possibly introducing an RFI-flagging scheme to the data before summing. Each of these solutions involves altering the data recording architecture for the beams which is outside of the scope of this thesis to investigate further.

In lieu of using the beamformed data or extracting fluxes from the imaged slow-vis data, we may instead extract dynamic spectra directly from the visibility data, following the methodology used by Villadsen and Hallinan (2019). This method benefits from operating faster than imaging as well as not relying on the storage required to do the imaging (and especially the storage required for imaging each time stamp at all 3072 spectral channels). Before being able to effectively use this method, we still need to understand how the ionosphere has affected the source's position and so imaging would still be required for building the plasma-flow model. This model construction will presumably be integrated into the OVRO-LWA reduction

pipeline and so would not manifest as an additional step in this prospective analysis. In the case that a candidate burst is identified, the data can be imaged at that time stamp to more effectively rule out possible contamination. The downside to this is that the slow-vis data likely does not have the time resolution necessary to resolve the structure of a type III burst and so any burst properties would be much less constrained than if a burst was detectable in beamformed data. That said, the extreme environments of young stars may afford slower and longer bursts that makes such a dedispersion search possible, even in slow-vis data. This is explored in more detail in Chapter 5.

Overall, the low-frequency environment poses interesting challenges for data reduction and analysis for transient science. Although the slow-vis data may need more attention than is available in a general reduction pipeline, the quality of the cross-correlated data should be conducive for doing the stellar space weather science that I explore in this thesis.

3.5 Acknowledgements

This material is based in part upon work supported by the National Science Foundation under grant number AST-1828784, the Simons Foundation (668346, JPG), the Wilf Family Foundation and Mt. Cuba Astronomical Foundation. A part of this work was carried out at the Jet Propulsion Laboratory and the California Institute of Technology under a contract with the National Aeronautics and Space Administration and funded through the JPL Researchers on Campus program. This work was done with the support of the OVRO-LWA collaboration, with special support from Gregg Hallinan, Casey Law, Yuping Huang, and Jayce Dowell.

Chapter 4

SWAYS IN THE OPTICAL: DEVELOPING FLARESCOPE FOR HIGH-PRECISION PHOTOMETRIC MONITORING

4.1 Introduction

While the difficulty in determining the emission process at low frequencies is in part due to sensitivity limitations at that part of the spectrum, it is exacerbated by a lack of coordinated observations at other parts of the spectrum that may reveal the *acceleration* process. Although SEPs, CMEs, and their associated low-frequency radio signatures can occur in the absence of flares, solar flares with energies $\gtrsim 10^{30}$ erg are essentially guaranteed to produce CMEs (Yashiro et al., 2006). Similarly, type III bursts are highly associated with solar active regions, with burst frequency distributions tracking the solar cycle (Saint-Hilaire et al., 2013). Although other stars are unlikely to have the same flare-energy threshold as the Sun, the young stars that I am interested in are known to regularly reach flare energies that are orders of magnitude greater than what we observe for the Sun. Beyond the power of other parts of the spectrum for identifying and characterizing radio emission, they are of course also powerful in terms of characterizing the conditions under which certain emission processes are relevant. With respect to the flare-energy threshold for CME production, optical photometry is particularly useful as the white-light (WL) component of flares is estimated to contain the bulk of the bolometric energy of the flare (Kretzschmar, 2011). With this in mind, combined radio and optical detections (or lack there-of) can be used to inform the flare-CME relation for other stars. The new difficulty, however, is detecting solar-scale flares on nearby, solar-type stars.

Solar flares with a WL component were widely considered rare events until relatively recently (Fang et al., 2013). Despite containing the bulk of the bolometric flare energy, a combination of a low filling factor and a relatively low temperature differential between the heated region and the quiet surface ($\sim 6000 - 9000$ K compared to the quiet 5800 K (Kretzschmar, 2011; Watanabe et al., 2013)) made WL flares historically difficult to detect; a typical luminosity of the WL component is only $10^{-6} - 10^{-5}$ $L_\odot$ and typically only last a few to tens of minutes (Namekata et al., 2017; Song et al., 2018). A result of this is that solar-type stars have erroneously

been considered relatively inactive, especially when compared to M-dwarfs which are both cooler and would have a larger flare filling fraction. The significance of the effects from the temperature and filling-factor differences is exemplified in Figure 4.1. This shows a 10,000 K flare for an early-type K-dwarf as observed in the Sloan g' band (400-550 nm) and a flare of the same energy and temperature on an early-type M-dwarf. The flare appears as a 5σ detection for the K-dwarf and is a $> 100\times$ larger signal for the M-dwarf—exceptional precision is needed to detect even energetic flares on solar-type stars.

Space-based, stellar-monitoring missions like *TESS* and *Kepler* have been critical for both achieving the precision and the observing cadence necessary to detect and resolve flares from all spectral types. However, the quality of their data products suffer for stars in the SWAYS sample due to how bright they are; these stars saturate the detectors for these missions in their standard operating modes. As such, monitoring the SWAYS sample in the optical requires a dedicated instrument with high precision and observing capabilities that prevent detector saturation. With these requirements in mind, I designed Flarescope. This instrument now exists and operates at Palomar mountain, performing observations of the SWAYS sample simultaneously with the OVRO-LWA. In this chapter, I review the design of Flarescope in Section 4.2, its data reduction process in Section 4.3, and its performance in the context of accomplishing SWAYS science goals in Section 4.4.

4.2 Design

Flarescope, shown in Figure 4.2, is a 0.5 m aperture telescope on Palomar mountain. Its initial construction was completed in December 2022, after which it underwent commissioning and was incorporated into an automated-observing framework before beginning regular science operations in November 2023. Flarescope's concept arises directly from the need for a dedicated, optical, monitoring instrument for identifying the flare counterpart of stellar radio emission observed by the OVRO-LWA. As such, I use Flarescope to observe stars simultaneously with one of the OVRO-LWA power beams in addition to the OVRO-LWA all-sky imaging. I have designed Flarescope's optical train to allow for sub-mmag photometric precision on the order of 10 min integration times with off-the-shelf (OTS) equipment. This level of precision is crucial for detecting flares on solar-type stars due to the low contrast between the quiescent photosphere and the flare itself, as I described previously. Because the sensitivity of the OVRO-LWA leads to prioritizing targets within ~ 10 pc, my sample of stars are relatively bright (apparent Sloan g' magnitude $m_{g'} < 8$).

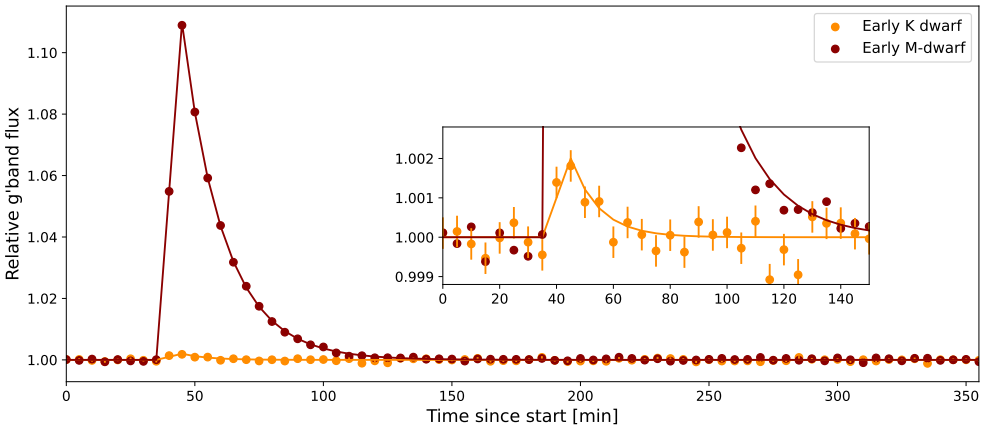

Figure 4.1: A 10,000 K flare as it appears on an early K-dwarf ($T_{\rm eff}$ = 5200, R = 0.75 $R_\odot$) and an early M-dwarf ($T_{\rm eff}$ = 3500, R = 0.4 $R_\odot$) when observed in the Sloan g' band. For this simple representation, I take the flare temperature to be persistent, leading to an flare energy of $\approx 3 \times 10^{33}$ erg when integrated over the light curve. An inset of the light curves is provided to better illustrate the flare on the K-dwarf. The error bars represent 0.4 mmag precision, which is representative of the precision that Flarescope can achieve on 5 min timescales.

This made avoiding detector saturation another major design driver. Here, I review the full design of Flarescope, including repairs that led to substantial improvements in performance.

Detector

Flarescope's detector is an Andor iXon3 888[1] electron-multiplying (EM) charged-coupling device (CCD) that has been repurposed from its time as a spare camera for the Caltech HIgh-speed Multi-color CamERA (CHIMERA, Harding et al., 2016) instrument. This camera is 2048 by 1024 pixels; only 1024 by 1024 of these pixels are active to support a frame-transfer mode, allowing for simultaneous exposure and read-out of the preceding exposure. While this allows for higher imaging cadence, it also determines the minimum exposure time for frames, as it is limited by how quickly the stored frame can be read out. The detector has an EM-amplifying mode that can be used to reduce the relative contribution of read noise at the expense of reducing the dynamic range and introducing excess noise (Hynecek and Nishiwaki, 2003). Instead, to minimize the impact of read noise, I use the conventional read-out mode with 1× gain (no amplification) and the slowest read-

[1] https://www.morrellonline.com/uploads/2/7/0/1/27013482/andor_ixon3_emccd_brochure.pdf

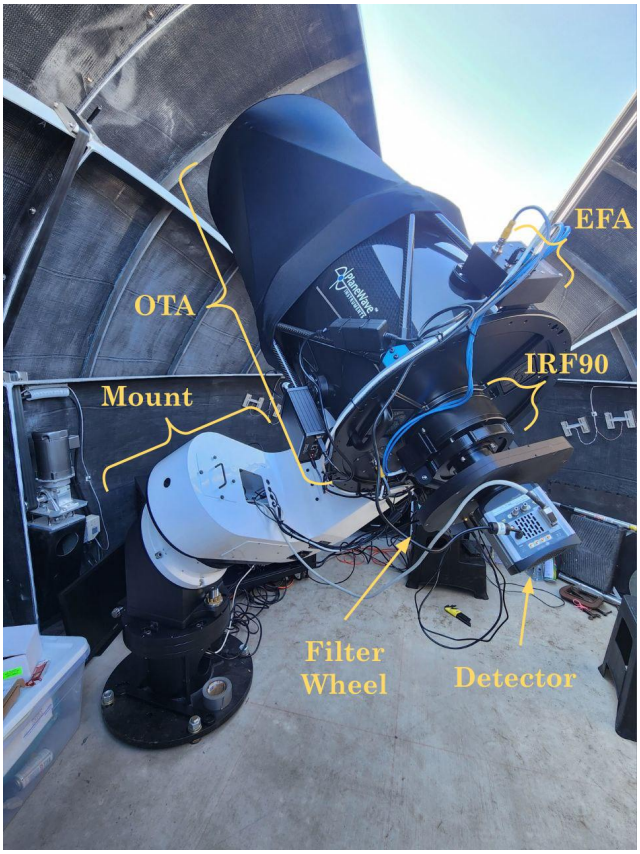

Figure 4.2: Flarescope as it currently exists at Palomar observatory. Several pieces of hardware that I describe in Section 4.2 are labeled here.

out rate of 1 MHz, or $\approx$ 1 frame per second for the 1-Megapixel detector. With a vertical shift speed of 6 μs, this puts the exposure and kinetic cycle time (KCT) at 1.11 s. A summary of the detector's properties are provided in Table 4.1. The camera is thermoelectrically cooled to -20° C for observations; although it can cool down to -70° C, the thermalization time is significantly longer for such temperatures and -20°C produces $\lesssim$ 10 electrons across the entire detector, which I consider acceptable dark noise.

Optical Tube Assembly

As a small, ground-based telescope looking at bright targets, we should expect scintillation to dominate the noise budget. For a given star, such noise scales relative to the star's flux like:

$$\sigma_S = 1.5 \times 0.09\, D^{-2/3} \chi^{1.75}\, (2\, t_{\rm int})^{-1/2} \exp(-h/h_0) \tag{4.1}$$

Table 4.1: Details for the Andor iXon3 888 EMCCD used in Flarescope.

Property	Value
Dimensions (Active)	1024 px×1024 px
Pixel size	$13 \times 13 \mu m^2$
Read noise (1 MHz)	$6e^-$
Full well depth	$90{,}000e^-$
KCT (1 MHz frame-transfer)	1.11 s
Operating temperature	-20°C
Quantum efficiency (> 400 nm)	> 90%

where D is the diameter of the telescope in cm, $t_{\rm int}$ is the integration time in seconds, χ is the observing airmass, h is the elevation of the observatory in meters, and h_0 is 8000 m. More details on this can be found in Stefansson et al., 2017 and Osborn et al., 2015.

For Flarescope's location on Palomar mountain, h = 800 m and χ varies throughout the observation. This left D and $t_{\rm int}$ to our discretion. All else held equal, smaller apertures would mean lower signal-to-noise (SNR) with the benefits of allowing for longer exposure times without saturating the detector as well as providing a larger field of view (FOV) with which to include stars for photometric calibration. Larger apertures reduce both the scintillation and photon noise, but at the expense of having a smaller FOV and saturating the detector faster. With this in mind, we decided on the PlaneWave (PW) Corrected Dall-Kirkham (CDK) 20" (0.508 m) optical tube assembly (OTA) (hereafter called the CDK20). This aperture has a smaller FOV and lower expected stellar and scintillation noise than the 17" OTA also available through PW. Similarly, it has a larger FOV and higher expected stellar and scintillation noise than the larger, 24" PW OTA aperture.

Having a smaller field than the 17" aperture is accommodated by using the PW rotational focuser (IRF90) which allows for use of the detector's diagonal dimension to maximize allowable distance between the science target and a photometric standard star. Although the 24" aperture would have 12% lower scintillation noise than the CDK20, the cost scaled significantly faster than between the 17" and 20" apertures while still having a smaller FOV than the 20". A summary of the relevant features of the CDK20 is included in Table 4.2.

The IRF90, mirror temperatures, and backplate temperature are maintained by the PW Electronic Focuser Accessory (EFA), which is controlled using the PlaneWave Interface 3 (PWI3) software. The EFA includes both a fan and a dew heater for

Table 4.2: Details on the observing properties of the CDK20 + Andor iXon3 888 EMCCD system. The range in the maximum distance between the science target and the photometric companion comes from the difference in the size of the PSF for different diffusers (*e.g.*, if the target and companion were separated by 17.34′ but with the 2° diffuser, the stars would extend off of the detector.

Property	Value
Effective diameter	0.508 m
F#	6.8
Per-mirror throughput	96%
Lens-group throughput	99.5%
Primary-mirror central obstruction	0.39 diameter
Plate scale	0.72″/px
FOV	$12.28' \times 12.28'$
Max companion distance	16.25′-17.34′

maintaining consistent temperatures throughout observations.

Mount

Flarescope's CDK20 OTA is mounted on a PW L500 direct-drive mount (the combined system called CDK500). This mount was designed to maintain 0.3″ (sub-pixel) RMS tracking over 5 minutes. The mount is nominally alt-az, but has been installed on an equatorial wedge to remove the need to de-rotate the field. Both of these features should in principle aid in stabilizing the source position on the detector, which in turn aids in aperture photometry. However, the manufacturer's mount performance tests were done in the alt-az orientation; we witnessed a marked degradation in tracking over time that eventually led to complete failure of the altitude axis of the mount. This failure resulted from the equatorial orientation applying excess pressure to the coil plate which facilitates the current and associated field for the direct-drive motor control, eventually causing it to short circuit. The altitude motor was redesigned to better accommodate the equatorial orientation and the mount motors were fully replaced in August 2023. The mount has maintained high-quality tracking since these repairs.

The tracking quality prior to and post mount repairs is shown in the panels of Figure 4.3, which shows the position of the star eps Eri across two, $\approx$ 5 hr observations without guiding. The overall drift in the position of the source across 5 hr is about $\approx 4\times$ better after the repairs and the general stability is also substantially better; the median, 5-minute RMS for the source position prior to the repairs was 0.6″ (nearly

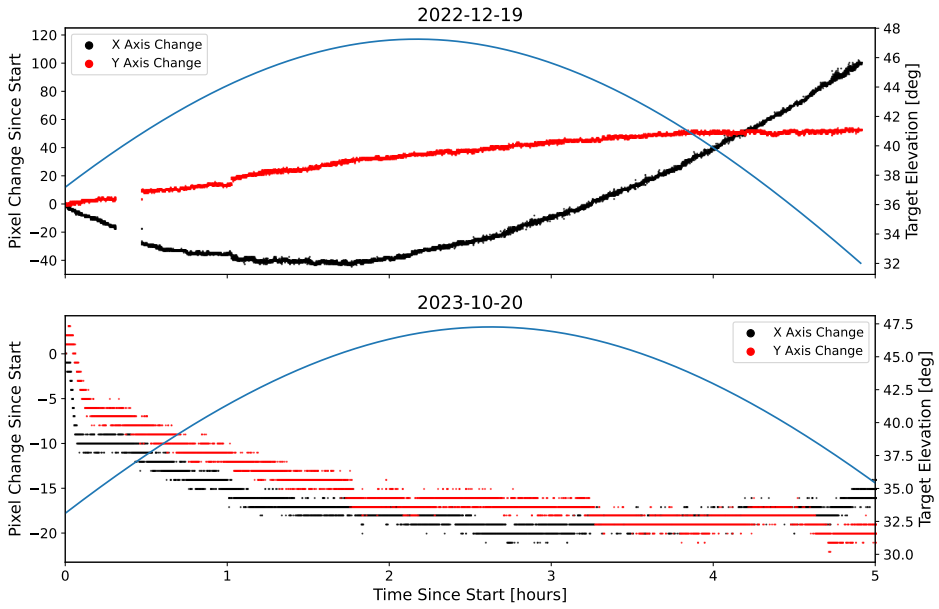

Figure 4.3: Change in eps Eri's position on the detector (red and black dots) and its elevation (blue line) over the course of five-hour-long observations. The top plot represents an observation prior to mount repairs and the bottom plot is an observation after mount repairs. The repairs led to substantial improvement in the tracking quality. Post-repairs, the tracking appears to become increasingly stable towards the peak of the target's transit.

1 pixel). This was reduced to 0.38″ after the repairs. This final tracking RMS is still about 0.12 pixel worse worse than the expected tracking quality reported by PlaneWave, although it is worth noting that weather conditions can also impact the tracking quality. I also note that the rate of change of the tracking quality reaches a minimum at ≈ 3 hr into the observation, which is aligned with the time when the target is near its transit peak. This may suggest that the tracking quality may also be a function of pointing elevation or, alternatively, a function of the rate in change of the target's altitude and azimuth position. A more in-depth exploration of tracking as a function of altitude, azimuth, and transit is needed in order to conclude which dominates the tracking quality. Overall, based on the tracking demonstrated here after the repairs, the quality is consistent with expectations. The L500 mount is mounted on the PW 12" steel pier to both extend the available viewing range and to prevent the optical tube from slewing into the concrete pad that the equipment is installed on.

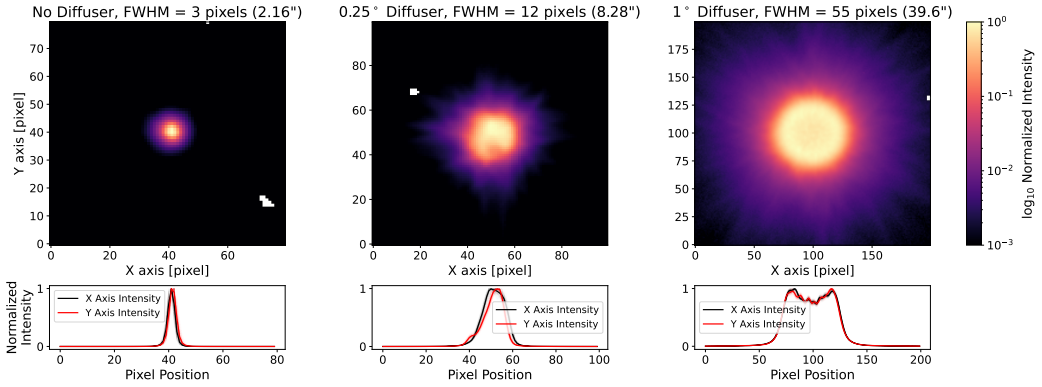

Figure 4.4: Log-scale, time-series-averaged images of the PSF (top) and the X and Y-axis cross sections of the PSF for each individual image (bottom). The PSF with no diffuser (left), the 0.25° diffuser (center), and the 1° diffuser (right) are shown here. The full-width half maxima (FWHMs) are indicated in the titles and reported in Table 4.3. White pixels are where either hot pixels, dead pixels, or high-RMS pixels were flagged as determined from dark images. 50 frames were used for each of the averaged images.

Diffusers

With the detector and aperture decided, my targets now dominate the remaining design decisions. The brightest target of the SWAYS sample is ϵ Eridani (eps Eri) with a g' magnitude of $m_{g'} = 4.1$; this would saturate the detector in ~ 1 ms. Defocusing the telescope has been successfully implemented by, *e.g.*, Southworth et al. (2009), Mann et al., 2011, and Fukui et al. (2016), but doing this can introduce position-dependent aberrations in the PSF (Stefansson et al., 2017) with the benefit of maintaining throughput by avoiding additional optical components.

Instead of defocusing, I use engineered diffusers from RPC Photonics. These particular diffusers provide a top-hat PSF which will be helpful in doing aperture photometry. Flarescope has three different diffusers (0.25°, 1°, and 2° opening angles), summarized in Table 4.3. The optical path has been designed such that eps Eri only half-fills the detector pixels during the KCT of the slowest read-out rate (1 MHz, 0.9 fps) of the CCD when using the 1° diffuser; this requires that the diffusers be 3.56 cm from the detector. This is achieved using a custom adapter machined by the company PreciseParts[2] which connects the filter wheel to the IRF90. The PSFs of the system with no diffuser, the 0.25° diffuser, and 1° diffuser are shown in Figure 4.4.

[2]https://www.preciseparts.com/

Table 4.3: Details on the expected and measured observing quality of the various diffusing modes. Here, I include the total number of pixels that light is diffused across as well as the radius that this corresponds to in parentheses. We also include the full-width half maximum (FWHM). The magnitude at which the detector saturates for a given diffuser is calculated by assuming the detector pixels are only half filled to ensure we stay within the linear-response regime of the detector. Here, the limiting mag refers to the highest magnitude that has mmag sensitivity for 272, 1.1 s co-added frames (5 min integration).

Diffuser	# pixels [Expected]	# pixels [Measured]	FWHM $''$	Saturating g' magnitude	Limiting mag
No diffuser	7	7	2.16	≈ 10	11.5
0.25°	114	114	8.28	≈ 7	9.5
1°	1725	2376	39.6	≈ 4	8.0
2°	6903	–	–	≈ 2.5	7.5

Filters and Filter Wheel

Sloan filters have larger bandwidths than Johnson filters; the larger number of photons that this provides lead me to use Sloan filters for this science. Because the quiescent photosphere of the stars of interest are $\approx 5000 - 6000$ K while the flares themselves are generally modeled as $\sim 10,000$ K, the photometric contrasts will be enhanced when observing in blue bands. This would suggest that the primary science band be the Sloan u'. However, while the u' filter is expected to provide the highest contrast, light in this wavelength range is highly absorbed by atmospheric ozone (Huggins and Huggins, 1890) and the detector has a lower quantum efficiency at these wavelengths than at longer wavelengths. This leads me to favor the g' band as the primary science band, although the Sloan u', r', and i' filters are also available for other science cases. The filters are the 2" × 2" (50 mm × 50 mm) square filters manufactured by Baader Planetarium[3]. See Table 4.4 for a summary of the available filters, where the contrast factor for eps Eri has been calculated using the following expression for contrast:

$$\frac{L_{\text{flare,band}}}{L_{\text{quiet,band}}} = \frac{L_{\text{flare, bol}}}{4\pi R_\star^2 \sigma_{\text{SB}} T_{\text{flare}}^4} \frac{\int_{\text{band}} B_\lambda(\lambda, T_{\text{flare}}) d\lambda}{\int_{\text{band}} B_\lambda(\lambda, T_{\text{quiet}}) d\lambda} \tag{4.2}$$

[3]https://www.baader-planetarium.com/

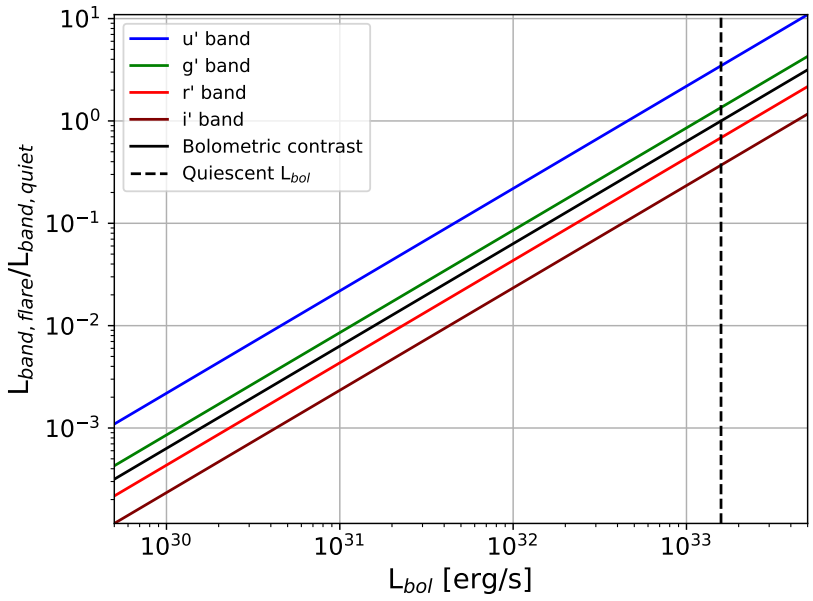

Figure 4.5: The ratio of flare luminosity to quiescent photosphere luminosity (*i.e.*, the contrast) for various bandpasses as a function of different bolometric flare luminosities. This assumes that the flare is 10,000 K and that the star is eps Eri (effective photospheric temperature of 5002 K and radius of 0.83 $R_\odot$). The black, dashed line indicates where the bolometric flare luminosity would be the same luminosity as eps Eri's quiescent photosphere. Observing in the Sloan g' band increases the contrast of the flare by a factor of ~ 2 relative to no filter; observing in redder filters decreases the contrast relative to no filter.

where $L_{\text{flare,band}}$ is the luminosity of the flare in the band, $L_{\text{quiet,band}}$ is the quiescent photospheric luminosity of the star, $L_{\text{flare, bol}}$ is the bolometric luminosity of the flare, $R_\star$ is the stellar radius, T_{flare} is the temperature of the flare, T_{quiet} is the quiescent photospheric temperature of the star, σ_{SB} is the Stefan-Boltzmann constant, and $B_\lambda(\lambda, T)$ is the Planck function for blackbody radiation. The expected contrast for a 10,000 K flare on eps Eri for the various filters is shown in Figure 4.5.

Because these observations require the use of filters and diffusers simultaneously, I am using a two-carousel filter wheel. The wheel is the Finger Lakes Instrumentation (FLI) Centerline (CL) 1-10 filter wheel which has two carousels with 5, 50 mm square slots each. Since we have three diffusers and 4 filters, there are two configurations of the filter wheel with no filter or diffuser.

Table 4.4: Information on the various filters available to Flarescope. The magnitudes for eps Eri are calculated from the expressions for the Sloan filters as a function of the Johnson filter magnitudes from Fukugita et al. (1996). The saturation time is calculated assuming 1725 px diffusion size (*i.e.*, 1° diffuser) and that eps Eri is the source being observed. The contrast factor is calculated from equation 4.2 assuming a flare temperature of 10,000 K and bolometric luminosity equal to the quiescent photosphere of eps Eri.

Filter	Wavelength range [nm]	Transmission	Contrast factor	eps Eri mag	Saturation time
None	–	–	×1	3.58	–
u'	320-385	$\lesssim$ 80%	×3.39	6.04	20.7 s
g'	401-550	$\approx$ 90%	×1.44	4.10	1.12 s
r'	562-695	$\gtrsim$ 95%	×0.79	3.41	0.76 s
i'	695-844	$\gtrsim$ 95%	×0.45	3.19	0.68 s

Dome and Weather

The observatory-control computer, data storage and analysis computer, network management, and the Flarescope optical path are all stored in a 12.5′-diameter (3.8 m) AstroHaven dome. The dome is operated through the DomeProU-c controller[4] from Astrometrics which provides both a graphical user interface for easier manual control and introduces Astronomy Common Object Model (ASCOM) drivers to control the dome for easier integration into an automated observing system. During power outages, the connection to the Astrometrics controller is disrupted, requiring a serial connection directly to the AstroHaven dome to facilitate restarts and re-establish connection with the Astrometrics controller. The dome is belt-driven, with magnetic limit switches for identifying the open/close status. Because of this, mechanical obstructions that prevent limit switches from ever meeting can lead the belts to unspool to such extremes that catastrophic failure modes can occur (*e.g.*, the dome shutters being capable of free falling or an “open" command in software triggering a “close" mechanical operation). To avoid such failure modes, we incorporate time-out commands for reaching limit switches in our automation code, described in more detail in Appendix C.

The clamshell design of the dome allows for fast thermal equilibration between the observatory and the surrounding environment and also removes the need for coordinating the telescope’s pointing with the dome’s shutter position. This is at

[4] https://www.astrometric.com/products/dome_control/domeprou_c_dome_controller/

the expense of increased exposure to possibly harmful environmental conditions. To identify such conditions, weather data is pulled from the Wide-field Infrared Transient Explorer (WINTER) observatory's weather station on Palomar mountain, accessible through the WINTER control server (Lourie et al., 2020). This station provides information on relative humidity, atmospheric pressure, dew point, and wind speed among other details. Although it does not report whether there is precipitation, this is acceptable as we want to preemptively close the dome before there is precipitation. Flarescope only operates when the dew-point depression is higher than 2° C, the humidity is less than 85%, and the wind speed is less than 3.5 m/s. Observing does not occur unless communication with the weather station can be established.

Control Software and Automation

The SWAYS program aspires to deliver 1000s of hours on each of several G-dwarf targets which leads to a heavy human-resource requirement in a human-in-the-loop operation mode. To minimize this burden, all Flarescope operations for the camera, focuser, filter wheel, mount, and dome are being automated. This automation system checks the weather before operations begin and then continuously every three minutes throughout the night. If unsafe weather conditions are detected, or if communication with the weather station is lost, the dome closes and the observatory returns to its inactive state (mount parked, camera and its cooler off, and EFA off). While the automation is being completed, I have been managing remote operations through virtual network computing with the observatory control computer.

Softwares for observatory automation, like ACP Observatory control[5], are available for integrating other OTS equipment. However, the unique readout mode and requirements of the camera, the way that the weather data is sourced, and the need to communicate with the dome through both the DomeProU-c controller and the direct serial connection necessitated a custom automation code. This code is written in Python and takes advantage of the ASCOM drivers available for all of the astronomical equipment (with the exception of the native dome controller). In addition to more effectively meeting the observing needs, custom control code also allows for more flexibility for observations by, *e.g.*, allowing for power cycling equipment and universal serial bus (USB) connections, higher customization of Flexible Image Transport System (FITS) headers, and fine-tuned control for startup

[5] `http://acp.dc3.com/index2.html`

and shutdown protocol. More details on the automation schema is provided in Appendix C.

Anticipated Noise Budget

At the operating temperature of -20°C of the detector, the noise associated with dark current is essentially negligible. The noise sources per exposure are then the stellar noise $\sigma_\star$ (eq. 4.3), the sky noise $\sigma_{\rm sky}$ (eq. 4.4), the read noise $\sigma_{\rm RN}$ (eq. 4.5), and the scintillation noise, already introduced in equation 4.1. In these equations, ϕ_0 is the zero-point flux of the band, D is the diameter of the aperture, ϵ is the effective efficiency of the optical train for a given band, $t_{\rm exp}$ is the exposure time of a single frame, $\Delta\lambda$ is the bandwidth of the filter, m is the magnitude of the star, m_s is the sky magnitude, p is the plate scale of the system, and $n_{\rm pix}$ is the number of pixels that are being diffused across for a given source.

$$\sigma_\star = \sqrt{\phi_\star} = \left(\phi_0 \pi \left(\frac{D}{2}\right)^2 \epsilon\, t_{\rm exp} \Delta\lambda\, 10^{-m/2.5}\right)^{1/2} \tag{4.3}$$

$$\sigma_{\rm sky} = \sqrt{\phi_{\rm sky}} = \left(\phi_0 \pi \left(\frac{D}{2}\right)^2 \epsilon\, t_{\rm exp} \Delta\lambda\, 10^{-m_{\rm sky}\, p^2/2.5}\right)^{1/2} \tag{4.4}$$

$$\sigma_{\rm RN} = \text{Read Noise}\sqrt{n_{\rm pix}} \tag{4.5}$$

The total photometric noise per frame excluding scintillation, $\sigma_{\rm phot,pf}$, is then:

$$\sigma_{\rm phot,pf} = \sqrt{\sigma_\star^2 + \sigma_{\rm sky}^2 + \sigma_{\rm RN}^2}. \tag{4.6}$$

And the total noise including scintillation noise for $n_{\rm frames}$ coadded together and normalized to ppm is:

$$\sigma_{\rm ppm} = 10^3 \sqrt{\frac{\sigma_{\rm phot,pf}^2}{n_{\rm frames}\, \phi_\star} + \frac{\sigma_{\rm S}^2}{n_{\rm frames}}} \tag{4.7}$$

where $\sigma_{\rm S}$ is the scintillation noise (expressed in equation 4.1) evaluated at $t_{\rm int} = t_{\rm exp}$. Examples of the expected noise for the various diffusers with the Sloan g' band ($m_{\rm sky} \approx 22.2$ mag/arcsec^2[6]), 1.1 s exposure time, airmass of 1.5, and 272 co-added

[6]https://sites.astro.caltech.edu/palomar/observer/200inchResources/lfc/lfcpick.html

frames (300 s integration time) are shown in Figure 4.6. It is important to note that although these plots show noise as a function of source magnitude, not all targets would be observed at the minimum KCT of 1.1s; those with longer exposure times would have have a higher photometric precision for the same total co-added time.

Due to Flarescope's limited FOV and the SWAYS program's focus on exceptionally bright stars that require diffusers, other stars in Flarescope's field cannot effectively be used in order to do differential photometry in the standard operation mode; any star with a magnitude $\gtrsim 9$ will not afford us our target precision for detecting and resolving flares when using the 1° diffuser. Instead, the Flarescope data reduction will primarily be direct photometry of the target star, with photometry of other stars in the field being used to inform how I interpret variability, but not utilized in *deriving* the target star's light curve and associated variability. I discuss the photometry process in detail in Section 4.3.

I note here that although Flarescope was designed to search for the optical flare counterpart to the type II and III bursts sought by the OVRO-LWA, its photometric capabilities and access to a variety of diffuser and filter modes makes it capable of a variety of science cases. It is also worth noting that Flarescope is a part of a larger movement towards utilizing small, ground-based apertures for high-precision science. The DEdicated MONitor of EXotransits and Transients (DEMONEXT) instrument also uses a CDK20 aperture and has managed to achieve comparable precision to what is described in this section (Villanueva Jr. et al., 2018). The MINiature Exoplanet Radial Velocity Array (MINERVA) also utilizes PW instrumentation; it couples four, 0.7 m apertures which emulates an effective collecting area of a 1.4 m aperture for a fraction of the cost of a single aperture of that size (Swift et al., 2015). As hardware performances (*e.g.*, mount tracking and detector read noise) improve, the cost-effectiveness, scalability, and relatively-easy customization that small-aperture observatories afford will make them an increasingly-enticing solution, especially for science that relies on dedicated observing programs.

4.3 Data Reduction

As in Chapter 3, I evaluate the performance of the instrument based primarily on a 1-hour observation of pi UMa that began on UTC 04:00:00 on April 10, 2024. In this time frame, pi UMa was at an elevation between 54°–58° from Flarescope's location. As such, the effects of scintillation and atmospheric extinction should be relatively low. pi UMa is 5.50 mag in g' band and thus required that I use the

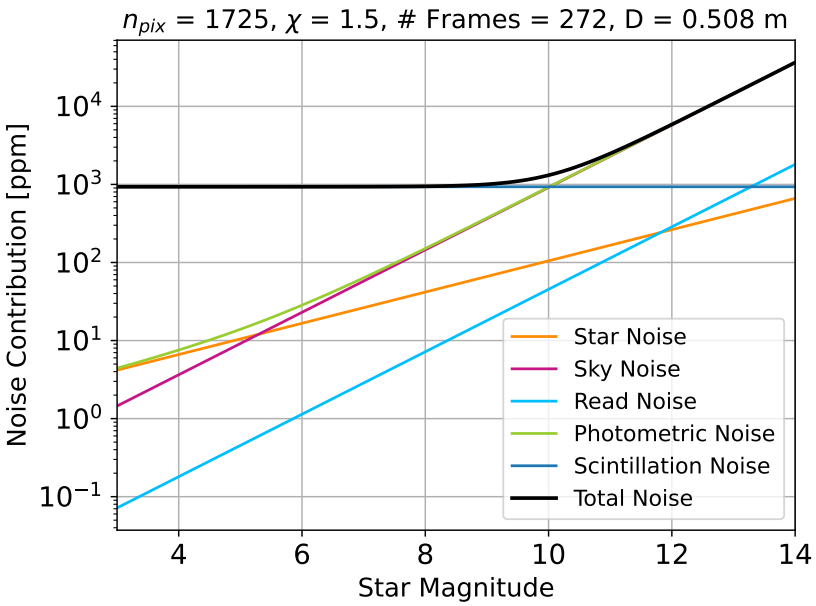

Figure 4.6: The estimated noise contributions to the total noise budget assuming a 1° diffuser (1,725 px), 1.1 s exposure time (1 MHz read out), 5 min integration time (272 frames), and g' band efficiency and sky noise. We assume an airmass of 1.5 for estimating the scintillation noise.

1° diffuser to avoid detector saturation, with each exposure being 3.0 s. Using the equations outlined in Section 4.2 and taking the airmass to be 1.2 (corresponding to $\approx 55°$ elevation), we would then expect that photometry for pi UMa would have ≈ 6 mmag precision on the 3 s exposure timescale and ≈ 0.6 mmag when integrated to 5 min.

pi UMa is orders of magnitude brighter than any other star in its field (see Figure 4.7). The three stars that were detected in addition to pi UMa—TYC 4133-1453-1, TYC 4133-532-1, and Gaia DR3 1092545573075703680, listed in descending order of brightness—are all 11.3 mag or dimmer in the g' band. Additionally, although the FWHM of the PSF with the 1° diffuser is 39.6″, the intensity of pi UMa leads to diffuser-scattered photon contributions at levels on the order of the same photon contribution of the dimmer stars. This extends to distances up to $\approx 2'$ from pi UMa's center. As such, I cannot effectively use other stars in the field to do differential photometry, especially to achieve sub-mmag precision on few-minutes integration time. Instead, the photometry I describe in this section is derived directly from pi UMa. This is possible due to the remarkable stability of the observing conditions for this particular observation, which I discuss in more detail in this section. I note

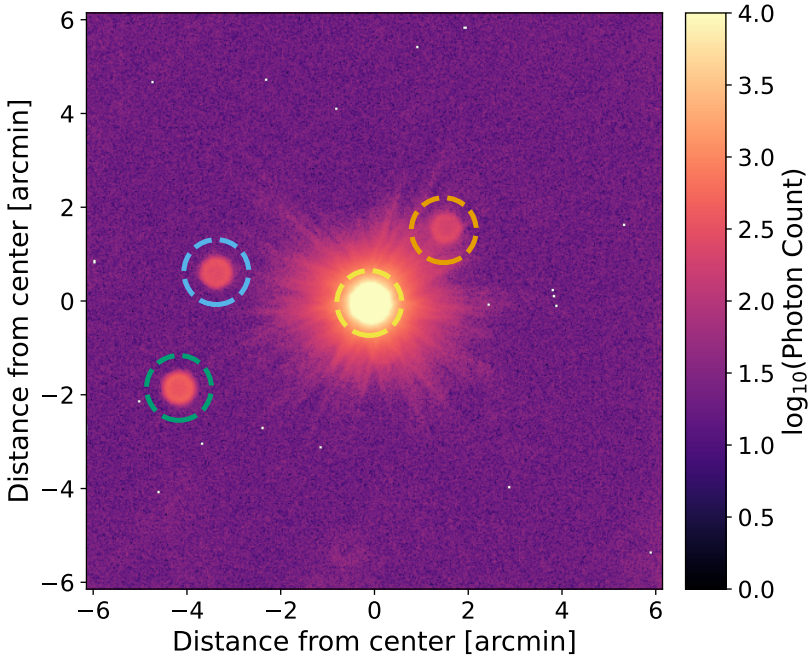

Figure 4.7: A calibrated image of a single exposure for pi UMa's field, with pi UMa in the center and indicated by the yellow dashed circle. White dots in the image indicate where hot or dead pixels were masked. The other stars are TYC 4133-1453-1 (green circle, 11.39 mag), TYC 4133-532-1 (blue circle, 12.12 mag), and Gaia DR3 1092545573075703680 (orange circle, 12.40 mag). Light from pi UMa scattered up to $\approx 2'$ from its center; the intensity of the scattered light within this region is on the same order of magnitude of the other stars in the field. It is worth emphasizing here that 3C 204, which contaminates pi UMa's field in slow-visibility data discussed in Chapter 3, is beyond Flarescope's FOV.

again here that my interpretation of any transient or variable phenomena I observe from pi UMa and the other stars in the SWAYS sample will still be informed by the photometry of the other stars in the field.

Image Reduction and Photometry

The data reduction for Flarescope can be described in four broad steps: 1.) calibration, 2.) source centering/image repositioning and co-adding, 3.) background subtraction and aperture photometry, and 4.) airmass correction. I describe each step here before discussing the results in Section 4.4.

Calibration Each image was calibrated using a standard method of subtracting a master dark frame and dividing by a master sky flat frame. These master calibration frames were produced using the same observing conditions (g' filter, 1° diffuser, and 3 s exposure time). The master dark frame was used to identify dead pixels (pixels with 0 counts) and hot pixels (pixels with counts $> 10\sigma$ above the median value of the frame). The dark frames used to produce the master dark were also used to create an RMS map of the detector; pixels in this map that were 4× higher than the mean value of the map were considered noisy or high-variance pixels. The hot, dead, and noisy pixels were used to create a bad-pixel mask for the master dark frame, where bad pixels were set to NaN values.

Because Flarescope's observatory does not support dome flats, sky flats were taken close to dusk at an altitude $\approx 50°$. The master dark is subtracted from these frames before they are individually normalized. Normalization on an individual-frame basis is required before taking the median of all flats due to the sky flux changing substantially over the course of collecting the frames. Because stars are visible in these flat images, I take the median of all flat frames to be the master flat.

Image Repositioning and Co-adding Because Flarescope's tracking is not perfect, we cannot co-add images before ensuring all sources are in the same position in each frame. In order to align sources in all frames, I start by identifying stars in the first image. This is done using `photutil`'s `DAOStarFinder` class with a custom PSF kernel that accounts for the diffuser's impact on the PSF. The information on these sources is saved for the aperture photometry described in the next step, but are not actually used in the frame-alignment process. Instead, each subsequent image is cross correlated with this first frame using the `correlate` function from `scipy`'s `signal` submodule (Virtanen et al., 2020a). The position of the maximum value of the cross correlation relative to the center pixel indicates the integer number of pixels that the sources have moved relative to the first frame.

Note that this method does not return phase information and thus does not indicate how much the sky has rotated in the detector; because Flarescope is on an equatorial mount, rotation should not be a problem except for sources close to zenith, which does not apply for this observation. Once the shifts are determined for each image, they are then shifted using `numpy`'s `roll` function so that all sources are in the same position as they are in the first image. These shifted frames can then be summed; for this observation, I co-added 5, 20, and 100 frames for 15 s, 60 s, and 300 s final

time resolutions, respectively.

Background subtraction and photometry After the images are repositioned and co-added, I use the `SigmaClip` class from `astropy`'s `stats` package to remove sources from the co-added image so that `photutil`'s `Background2D` class can be used to identify the background of the co-added image. This background is then subtracted from the image. Once the background is subtracted, I use `photutil`'s `aperture_photometry` function to extract fluxes from each frame using the aperture positions identified in the previous step. For this observation, an aperture radius of 40 pixels was used; this is the equivalent of the PSF half-width at about 5% of the maximum flux. Using an aperture larger than the half-width at half max more completely integrates the light from the star.

Airmass Correction Once we have the light curves from the photometry performed in the previous step, the final reduction step is to account for airmass extinction which causes the source to have a lower flux at lower elevation. For this correction, I take the true flux F_t to be related to the measured flux F_m like $F_\mathrm{t} = F_\mathrm{m} \exp(c \cdot \chi)$ where c is a unitless, constant value. For this observation, I take $c = -0.12$. It is worth noting that pi UMa's flux due to rotational modulation changes by $\approx 0.5\%$ (a few mmag) in *TESS*'s band and this one-hour observation covers $\approx 0.5\%$ of pi UMa's rotational period. Because of this, Flarescope is sensitive to pi UMa's rotational modulation, but the sampling of the rotation phase makes it difficult to differentiate between flux variance due to poor airmass correction as opposed to star-spot effects. Because of this, I apply a median filter to the time-series data using the `medfilt` function from `scipy`'s `signal` submodule. This ensures that slow (relative to a possible flare's duration) flux variance not intrinsic to the optical path or observing conditions is not included in the photometric precision analysis discussed in the next section.

4.4 Photometric Performance Results

The light curves produced following the method outlined in the previous section are shown in the bottom panel of Figure 4.8. The precision at the 3 s exposure time is 2.65 mmag—more than a factor of two better than was expected for the assumed observing conditions. By 60 s of integration time, the precision is sub-mmag ($\approx$ 0.7 mmag) and the precision is $\approx$ 0.4 mmag by 5 min of integration; the precision scales roughly $\propto \sqrt{t_\mathrm{int}}$ as should be expected. To better evaluate the

precision of Flarescope, we also consider the full, 6-hour observation that this one-hour dataset is a part of in order to calculate the Allan deviation (Allan, 1966). This is helpful for identifying regimes of integration time where noise does not scale like white noise and is used to evaluate system stability. This deviation is defined as

$$\sigma_A(\tau) = \sqrt{0.5\langle(\bar{y}_{i+1} - \bar{y}_i)^2\rangle}, \tag{4.8}$$

where $\bar{y}_i$ is the flux averaged over a time τ (which we use to distinguish from $t_{\rm int}$ that describes the co-addition or integration time) at the $i^{\rm th}$ index.

The Allan deviation for the 6-hour observation for τ ranging from 3 s to 1,500 s is shown in Figure 4.9 along with indications of white noise and random-walk frequency-modulation (RWFM) noise. This shows that the noise begins to deviate from white-noise expectations for $\tau \gtrsim 60$ s and that noise no longer decreases with increasing τ for $\tau \gtrsim 400$ s as the noise becomes dominated by contribution from RWFM. This implies a noise floor of ≈ 0.4 mmag for pi UMa. Considering that we would not want to integrate much longer than 5 minutes so that we can identify the temporal structure of flares, the timescale of the photometric stability of Flarescope is conducive for the SWAYS science. It is also worth noting that the RMS of the light curves from the co-added data is slightly lower than the Allan deviation of the averaged light curve. It may be that the observing conditions were particularly good for the data collection during the one-hour subset of data evaluated throughout the rest of this section. This is supported by the apparent convergence of the noise calculation to the larger Allan-deviation trend for longer co-adding times. For a star as bright as pi UMa, scintillation is by far the dominant contributor to white noise. As such, the higher-than-expected precision achieved by Flarescope in the white-noise regime may be explained by anomalously-good environmental conditions.

Using pi UMa's temperature (5711 K) and radius ($0.98\,R_\odot$) and assuming a flare temperature of 10,000 K, a 5σ detection of a flare at the 300 s integration time would have a corresponding bolometric luminosity of 5.93×10^{30} erg/s (energy of 1.78×10^{33} erg for a single 300 s integration) in Flarescope's g' band. The bolometric luminosity and energy may be a factor of a few times this depending on the flare's temperature. This minimum energy detection threshold is promising considering pi UMa is expected to produce several flares per day in excess of 10^{32} erg (Leitzinger et al., 2020). I show an example of what a 5σ detection of a flare's peak and its corresponding profile would look like in pi UMa's light curve in Figure 4.10.

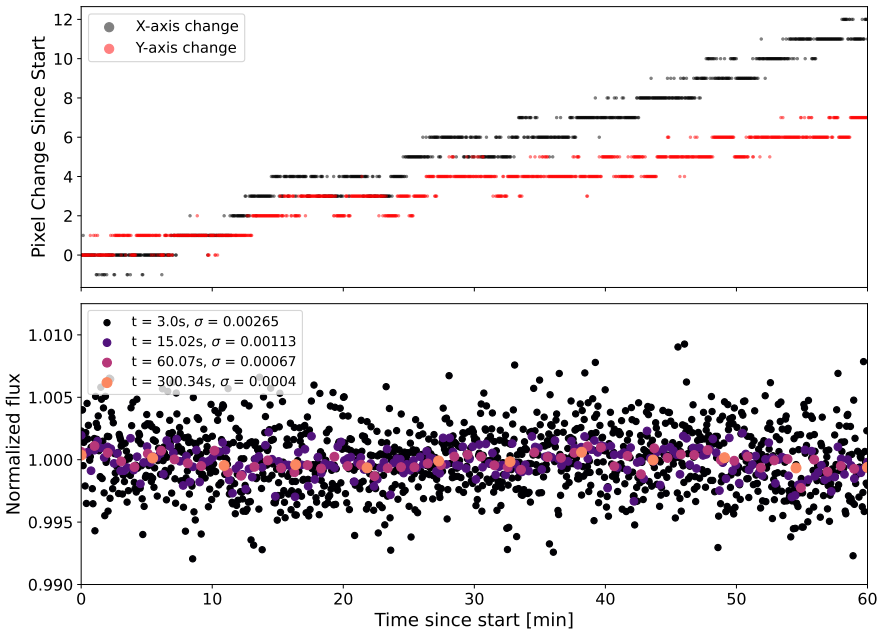

Figure 4.8: pi UMa's position on the detector relative to the start of the observation (top) and pi UMa's normalized flux for various integration times (bottom).

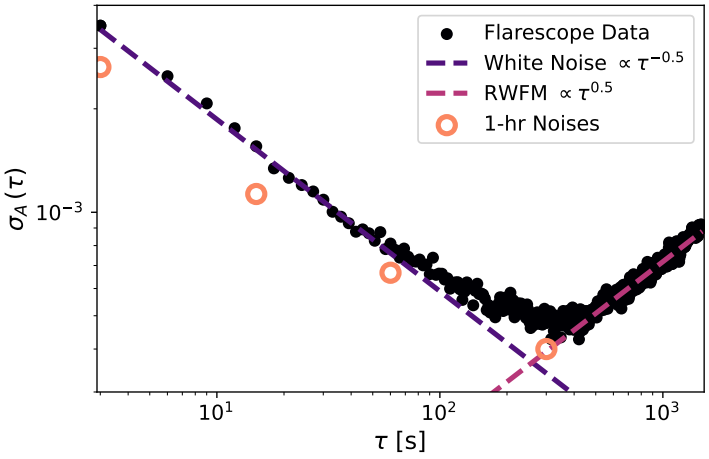

Figure 4.9: The Allan deviation, $\sigma_A(\tau)$ (defined in equation 4.8), derived from the airmass-corrected, normalized, 3 s-cadence light curve for the full, 6-hour observation of pi UMa. Noise expectations for white noise and random-walk frequency modulation (RWFM) are indicated as dashed lines. Here, τ is the time that the original, 3 s-cadence light curve is averaged over. The noises derived from the light curves produced from co-added images (shown in Figure 4.8) are plotted as open circles here. The noise from the 1-hour time frame that I consider in the rest of Section 4.4 is lower than the Allan variance from the full observation. This suggests that Flarescope (or at least its observing conditions) was particularly well behaved during the hour I evaluate in this section.

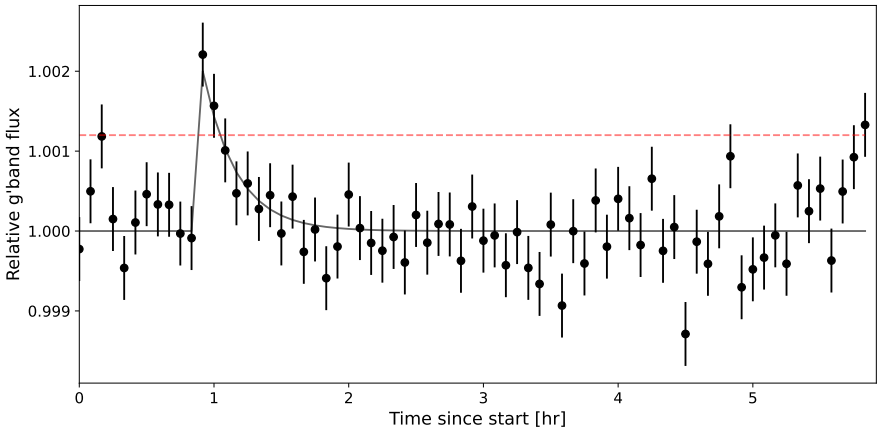

Figure 4.10: The entire, 6-hour pi UMa light curve (starting at UTC 03:00:00 on April 10, 2024) at 5 min integration time with $1\sigma \approx 0.4$ mmag error bars. The 3σ threshold is indicated by the dashed red line. A flare—modeled simply as a steep, linear rise and exponential decay with an e-folding time of 15 minutes—with a peak of 5σ was injected and is indicated by the solid line. The integration corresponding to the peak of this "flare" would correspond to an energy of $\approx 10^{33}$ erg, although the entire integrated profile (conservatively assuming a persistent flare temperature of 10,000 K) would correspond to an energy of 7.6×10^{33} erg.

4.5 Summary and Future

Flarescope was designed to detect the optical-flare counterpart to the radio emission I hope to observe with the OVRO-LWA. The stars I am focused on are nearby to accommodate the sensitivity of the OVRO-LWA; that said, the radio emission detectable by the OVRO-LWA would still correspond to bursts orders of magnitude more intense than the bursts we observe from the Sun. This would then suggest that Flarescope would need to be able to, at a minimum, detect flares a similar factor more energetic than the typical flares we observe from the Sun. Although many instruments can achieve the few-hundred ppm precision necessary to resolve flares of such an energy on solar-type stars, there is difficulty in achieving this for the nearby stars of the SWAYS sample that risk saturating detectors on short ($<<$ 1 s) timescales. Flarescope manages to achieve this precision for bright targets by taking advantage of engineered diffusers.

I have demonstrated in this chapter that for good observing conditions, Flarescope can indeed reach the sub-mmag precision I designed it to achieve. This is made possible both by the native sensitivity for each exposure afforded by the high-efficiency optical train as well as the stability of the system that allow for meaningful integration up to $\approx$ 6 min. At the 0.4 mmag precision that Flarescope achieves at

5 min integration times, a 5σ detection of a flare peak from pi UMa would be $\approx 10^{33}$ erg, or about $10\times$ the energy of the most energetic solar flares. As one of the furthest and hottest stars of the SWAYS sample, pi UMa represents one of the most difficult cases for the SWAYS science. The fact that Flarescope should be able to detect flares from pi UMa that have reasonable energies by stellar standards is encouraging for its capacity to do high quality science for the sample as a whole. It is worth noting that Flarescope is sensitive to flares energies within a factor of a few of the energies that *TESS* is able to detect; this is a great demonstration of both the precision of OTS instrumentation as well as the opportunity for Flarescope to do coordinated observations with *TESS* to better characterize flares.

It is worth re-emphasizing that Flarescope's performance was characterized based on its observations using the 1° diffuser as it will be the standard diffuser for most of the SWAYS sample. Without the use of diffusers, Flarescope is capable of 10σ detections for 16.5 mag stars on the 6 min integration timescales that it is stable over. This makes it an exceptional tool for doing M-dwarf science during downtime in the sparse SWAYS sample, especially given the significance of M-dwarf flare signatures in Flarescope's primary science band (shown in Figure 4.1). Flarescope's stability—and by extension its limiting magnitude—may be improved upon in the future through the introduction of closed-loop guiding through real-time image reduction and analysis to provide feedback to the mount on a target star's position. As Flarescope enters the final stages of automation for its continued coordination with the OVRO-LWA, the inclusion of such a guiding system is of great interest to expand the scientific capacity of Flarescope.

4.6 Acknowledgments

This material is based in part upon work supported by the National Science Foundation under grant number AST-1828784, the Simons Foundation (668346, JPG), the Wilf Family Foundation and Mt. Cuba Astronomical Foundation. A part of this work was carried out at the Jet Propulsion Laboratory and the California Institute of Technology under a contract with the National Aeronautics and Space Administration and funded through the JPL Researchers on Campus program. I would also like to specifically acknowledge Navtej Saini who provided a tremendous amount of help and guidance with acquiring and setting up the hardware that have made remote and automated operations possible. The staff at Palomar, especially Jeff Zolkower, Rick Burruss, John Baker, Carolyn Heffner, and Curt Corcoran, have also been invaluable to Flarescope and its operations; in addition to their assistance

with installing most elements of the Flarescope observatory, their attention to the facility has made diagnosing and solving problems efficient. Finally, I would like to acknowledge Eric Blackhurst and Cameron Vittiglio of PlaneWave who helped with the installation of the Flarescope mount and OTA and facilitated the mount repairs. Their responsiveness was critical to Flarescope's operations and the quality of its performance.

Chapter 5

THE FIRST YEAR OF SWAYS OBSERVATIONS: CME AND SEP CONSTRAINTS FOLLOWING A SUPERFLARE

The SWAYS program, currently consisting of the OVRO-LWA and Flarescope discussed in Chapters 3 and 4, respectively, began regular operations in November of 2023 and continued until July 2024. In that time, Flarescope completed 500 hours of observing across six young, solar-type stars with 388 hours of complementary beamformed data (see Figure 5.1 and Table 5.1). This constitutes the longest monitoring program for such stars < 100 MHz and the longest radio monitoring program with complementary optical data. The goal of these observations was to use signatures of flares from Flarescope's optical photometry (a relatively small computational expense) to inform which radio datasets to search for associated signals—a much more computationally-expensive task. In this chapter, I review the properties of the stars I collected nearly 900 hr of data for and the results of those observations. These results include a superflare from EK Draconis with an energy that has been associated with eruptive prominences based on chromospheric signals; I find no escape signatures for distances beyond the corona. Data below 100 MHz are rarely, if ever, collected contemporaneously with detections of flares at other parts of the EM spectrum; the novelty of this observation allows me the unique opportunity to conjecture as to possible limitations of the plasma emission process for young, solar-type stars.

5.1 Targets

As motivated throughout this thesis, the targets of the SWAYS program are young, solar-type stars; these are stars between 5000–6000 K between 50–800 Myr. The stars I have selected are additionally unlikely, or at least not known, to have a nearby stellar companion. This is to avoid stars whose rotation and activity would have been significantly impacted by tidal and magnetic interactions with a stellar companion and thus would not be representative of the Sun's history. Most of the stars in this particular collection are a re-occurring sample in the literature, driven in part by the intent of constructing a timeline for the Sun's activity evolution, with each star representing a possible snapshot of the Sun at that age (Dorren and Guinan, 1994; Ribas et al., 2005; Fichtinger et al., 2017). With the exception of EK Draconis

(EK Dra) and V889 Herculis (V889 Her), all of these stars are within 15 pc to accommodate the sensitivity of the OVRO-LWA. I make an exception for EK Dra and V889 Her due to their exceptionally high levels of activity and recent reports of a CME candidate from EK Dra (Namekata et al., 2021; Namekata et al., 2024a). The stars that were observed on a given night were determined primarily by their elevation at Palomar; I required that a star be $> 20^\circ$ elevation for at least an hour. Because my sample is sparse and distributed substantially in right ascension (RA, see Table 5.1), there was little scheduling conflict. In the case that two stars meet the observing criteria, stars were prioritized based on whether they are (in descending level of importance) 1.) near the end of their observing season, 2.) at an elevation $> 20^\circ$ for the longest duration, and/or 3.) were the most nearby system. Each of the six stars are described below and their properties are summarized in Table 5.1.

ϵ Eridani (eps Eri) eps Eri is the main target of interest for the SWAYS program. It is a K2 dwarf at 3.2 pc, making it the nearest and coolest star of this sample, as well as the nearest solar-type star with an exoplanet (Mawet et al., 2019). Its magnetic field supports both a 13 yr and 3 yr chromospheric cycle (Metcalfe et al., 2013; Coffaro et al., 2020), and it should have been near the maximum of its 3 yr cycle during the observations I conducted for it between November 2023–January 2024. Compared to the other stars in the sample, eps Eri is relatively inactive in terms of flare rate; this is perhaps because it is also the oldest star in the sample. However, it has exhibited flares with evidence of CME production in the far UV (Loyd et al., 2022) and was the first solar-type star found with transient sub-mm emission (Burton et al., 2022). Both quiescent (Suresh et al., 2020) and transient (Bastian et al., 2018) radio emission has been detected in the 2–4 GHz range and Fionnagáin et al. (2022) predicts that eps Eri would produce type II bursts that are detectable at lower frequencies, making it a promising optical-radio target.

χ^1 Orionis (chi Ori) chi Ori does actually have a stellar companion determined from spectroscopic observations (Pourbaix et al., 2004). However, its orbital period is > 5000 days, corresponding to a separation of ~ 7 AU. At this separation, tidal and magnetic interactions between the components of the binary are likely negligible in the scheme of stellar evolution (Fleming et al., 2019). chi Ori itself has not been detected at GHz frequencies, but its companion—a late M-dwarf—has (Fichtinger et al., 2017). Neither Flarecope nor the OVRO-LWA will be able to resolve the two stars in chi Ori's system. However, in the case that a flare is detected, we

can make reasonable energetic arguments to associate the emission with chi Ori rather than its companion. More specifically, chi Ori's quiescent, photospheric flux is expected to be $\approx 6000\times$ greater than its M-dwarf companion in Flarescope's primary science band (401-550 nm); for the M-dwarf to produce a detectable ($\geq 5\sigma$) flare in a Flarescope light curve, the flare would need a bolometric luminosity that exceeds the M-dwarf's entire photospheric luminosity. Although this is not unheard of (Chang et al., 2018), it is rather uncommon. I will make any future analysis of transient emission from chi Ori with this caveat in mind.

κ^1 Ceti (kappa Cet) kappa Cet is one of the least active stars in the sample. Despite this, stellar wind simulations informed by broad-spectrum analysis of the star suggest a mass loss rate $\gtrsim 50\times$ the solar mass-loss rate (do Nascimento Jr. et al., 2016). Along with this wind, it has a ~ 400 G field with a 10 yr cycle (Kochukhov et al., 2020) as well as 3 yr and 6 yr chromospheric cycles (Saikia et al., 2022). A super-flare from kappa Cet was observed by Robinson and Bopp (1987) with an estimated energy of 10^{34} erg (Schaefer et al., 2000). Such an event was possibly comparable in scale to the Carrington event (Cliver and Dietrich, 2013) and likely capable of releasing a CME (Lynch et al., 2019).

π^1 UMa (pi UMa) pi UMa is a peculiar 200-600 Myr G-dwarf (King et al., 2003; Mamajek and Hillenbrand, 2008) in that measurements of its astrosphere suggest a mass loss rate less than the Sun's (Wood et al., 2014). Despite this peculiarity, pi UMa has an active chromosphere (Gaidos, 1998) and is expected to experience on the order of 10 EUV flares per day (Leitzinger et al., 2020). It was first observed to flare in 1986, when it released a 10^{33} erg flare in the 0.1-10keV band of EXOSAT (Landini et al., 1986). X-ray flares detected by XMM-Newton in 2015 had similar energies (Pandey, 2015). This bodes well for detectability in the optical, and a weak wind may better facilitate the shock development required for type II burst production at low frequencies.

EK Draconis (EK Dra) EK Dra is the second youngest and most active main-sequence star of the sample. It has an anticipated flare rate of more than 50 flares per day exceeding 10^{32} erg (Leitzinger et al., 2020), and one flare every ten days that exceeds 10^{34} erg (Namekata et al., 2022a). EK Dra has been consistently detected at GHz frequencies (Guedel et al., 1995; Fichtinger et al., 2017), and other coronal measurements suggest an extreme environment. Even so, there only exists

extreme upper limits to its mass-loss rate—on the order of $10^{-10} M_{\odot}\,\mathrm{yr}^{-1}$, or about 4 orders of magnitude higher than the current solar mass loss rate (Fichtinger et al., 2017). Although I prioritized stars within 15 pc for the rest of our sample, I made an exception for EK Dra due to its higher activity in addition to its candidate prominence eruptions that may have evolved into a CME (Namekata et al., 2021; Namekata et al., 2024a).

V889 Herculis (V889 Her) V889 Her is the youngest star of the sample; if EK Dra represents the Sun just after it has turned onto the main sequence, then V889 Her would represent it right *before* the main sequence. It is an exceptionally active star, with its *TESS* light curves suggesting it has a higher flare rate and flare energies than EK Dra[1], although there are no studies evaluating its flares in detail like there are for the other stars of the SWAYS sample. V889 Her's magnetic field has been a topic of major interest since its exceptionally short rotation period ($\lesssim$ 1.4 days) allows for robust phase coverage of its star spots and field geometry. Doppler imaging and spectropolarimetry have revealed a large spot/spot group at V889 Her's pole that seems to persist for many years (Strassmeier et al., 2003), accompanied by a concentration of azimuthal field strength at high latitudes (Marsden et al., 2006). While there has not been substantial discussion of V889 Her in the context of space weather, it represents the earliest form of the Sun in this sample and any space weather signatures found through the SWAYS program will benefit from the pre-established framework for evaluating this star's magnetic environment.

5.2 Flare Search

To look for flares, I follow the data-reduction process outlined in Chapter 4 to produce light curves. All observations were conducted in the Sloan g' band with either the 1° or 0.25° diffuser. Although exposure time varied with the particular source (maximum of 5 s for V889 Her and minimum time of 1.1 s for eps Eri), I co-add all data to 90 s integration times for the flare search. Such an integration time produced sub-mmag precision for pi UMa and, because of the dominance of scintillation in the noise budget for stars dimmer than $\approx$ 9 mag, we should expect similar precision even for stars like EK Dra and V889 Her that are $\approx$ 2 mag dimmer than pi UMa.

[1] I use the same flare identification and characterization code that I used in Chapter 2 to estimate a flare rate of 100 flares/yr for EK Dra and 145 flares/yr for V889 Her. The highest flare energy was 1.4×10^{35} for EK Dra and was 6.0×10^{35} for V889 Her.

Table 5.1: Properties and completed observing time for the six main stars apart of the SWAYS sample. Radii $R_\star$ come from Gaia Collaboration et al. (2018) and distances d come from Gaia Collaboration (2022). All observations were conducted in the Sloan g' band with either a 1° or 0.25° diffuser on Flarescope and with a 256 ms integration time for the OVRO-LWA beamformer. The OVRO-LWA time is calculated based on the number of hours spent on each star with the beamformer; there is some additional overlap to be accounted for from the slow-vis data.

Star	RA [°]	Dec [°]	d [pc]	Age [Myr]	T [K]	$R_\star$ [$R_\odot$]	Flarescope hours	OVRO-LWA hours	Overlap
ϵ Eri	53.23	-9.46	3.21	800^{MH}	5002^{G22}	0.83	153	97	51%
χ^1 Ori	88.59	+20.28	8.66	$300\text{-}400^{R05}$	5808^{G22}	1.5	19	20	70%
κ^1 Ceti	49.84	+3.37	9.14	$400\text{-}800^{R10}$	5694^{H}	0.96	2	4	44%
π^1 UMa	129.80	+65.02	14.4	$200\text{-}600^{K}$	5711^{G22}	0.98	95	69	71%
EK Dra	219.75	+64.29	34.4	$\lesssim 100^{R05}$	5423^{G22}	1.01	189	168	76%
V889 Her	278.58	+18.69	35.6	$\lesssim 50^{S}$	5516^{G22}	1.06	42	30	71%

(MH) Mamajek and Hillenbrand (2008); (K) King et al. (2003); (R10) Ribas et al. (2010); (R05) Ribas et al. (2005); (S) Strassmeier et al., 2003; (G22)Gaia Collaboration (2022);(H)Pal et al. (2023); (G) Gudel et al., 1998; (V) Vidotto et al., 2014; (P) Petit et al., 2021; (R) Rosén et al., 2016; (W) Waite et al., 2017

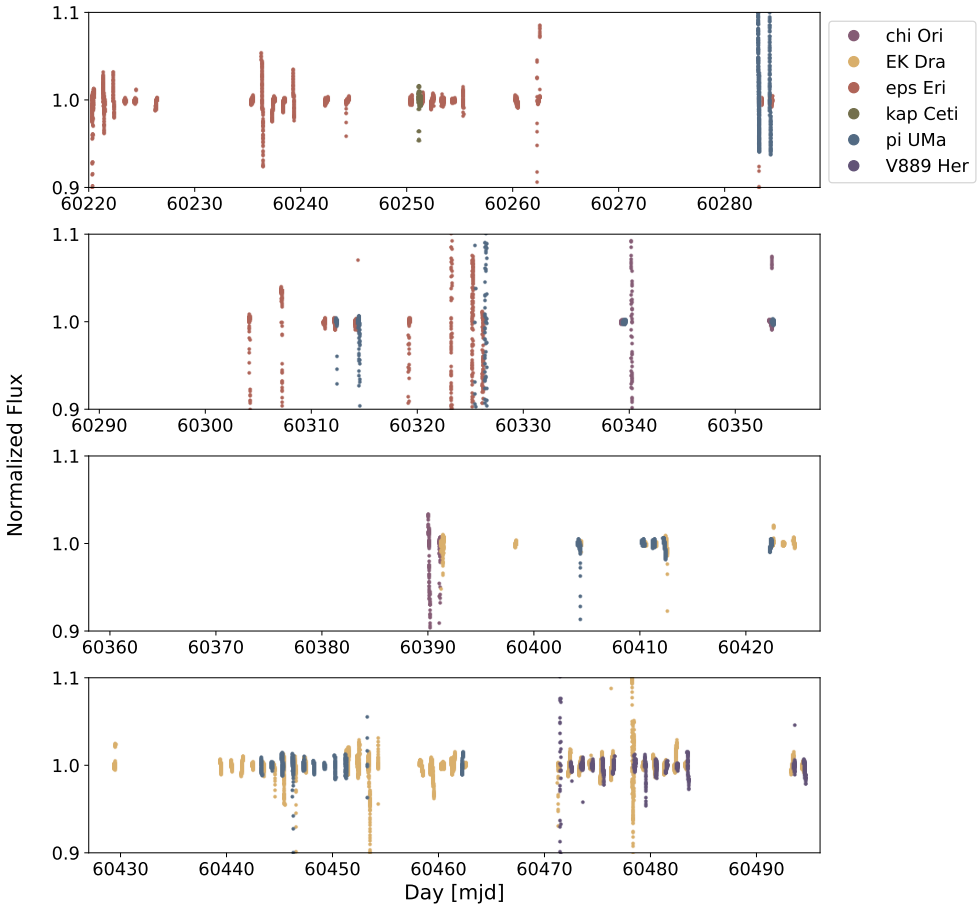

Figure 5.1: The airmass-corrected, normalized Flarescope light curves for the six stars apart of the SWAYS program.

I demonstrated in Chapter 4 that Flarescope's precision can reach a factor of a few better than anticipated, and I attributed this precision excess to the quality of the observing conditions that the performance was based on. Looking at the other ≈ 500 hr of data, this conclusion seems apt. Many of the observations show extreme variability in the light curves that could not be attributed meaningfully to intrinsic stellar variability. Although I do not show every individual light curve in detail, the effects of poor observing conditions are obvious in the composite light curves shown in Figure 5.1; scatter on the order of 10% of the stellar flux are apparent for many observations, especially for those taking place during the winter season (modified Julian date (mjd) $\approx$ 60280-60390), which is notoriously a time of high precipitation at Palomar[2].

[2]Confirmed by data archived by the Western Regional Climate Center.

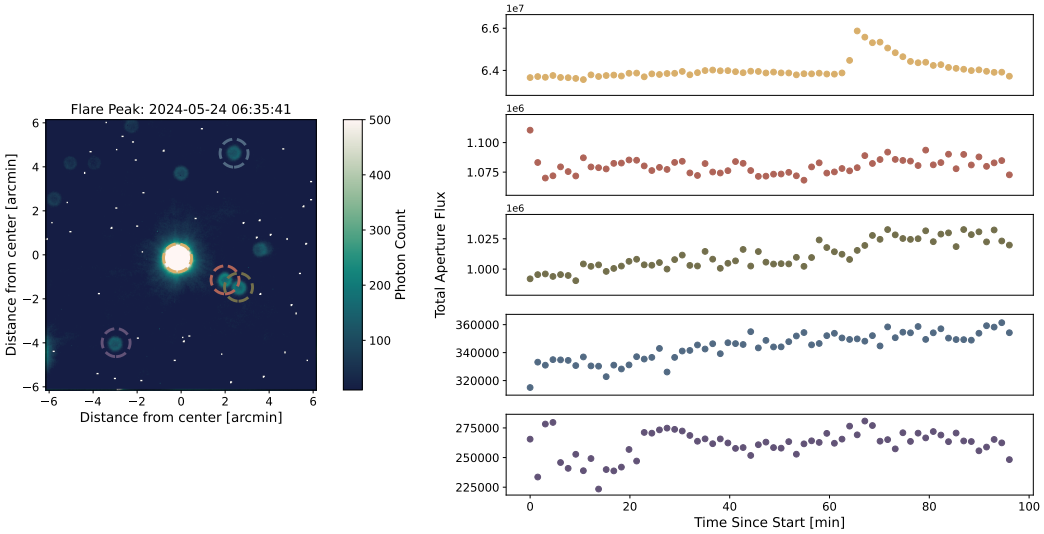

Figure 5.2: The FOV for EK Dra (left) and the 90 s-integrated light curves for EK Dra and the four other brightest stars in the FOV (right panels); the light curves' colors correspond to the color of the dashed-line aperture in the field. The distinctive steep rise and exponential decay of a flare is apparent in EK Dra's light curve (top most panel) and is absent from the light curves of the other stars, suggesting this flare is unique to EK Dra and is not the result of, *e.g.*, weather contamination. Note that the data here are not airmass corrected—the subtle trend for the all objects' fluxes to increase may be attributed to the airmass increasing throughout the observation.

Although I look through all of the data for flares, the April–June is the window of time with the most consistently-reliable weather and data quality. The three stars targeted during this window of good weather were pi UMa, EK Dra, and V889 Her—notably, and unfortunately, the furthest stars of the SWAYS sample and thus likely the most difficult to detect in the radio. From this search, there were a few marginal ($< 4\sigma$) flare candidates and one very-likely flare ($\approx 26\sigma$ detection at flare peak). This flare occurred on EK Dra and is the focus for the rest of this chapter.

Flare Validation

The candidate flare on EK Dra occurred on May 24, 2024, peaking around UTC 06:34:00. The light curve for EK Dra (top panel of Figure 5.2) around the time of the flare ($\approx$ 60 min into the start of the observation) follows the typical steep rise and exponential decay over $\approx$ 20 min. However, the observation stopped soon after the decay of the flare due to dangerous observing conditions—in this case, high humidity that suggested imminent rain. The first question then is whether the flare profile is a weather-based effect due to, *e.g.*, clouds. Looking directly at

the integrated images themselves, there is no apparent cloud coverage or change thereof. I should also note that EK Dra is the brightest star in its field by at least an order of magnitude in total flux—for an environmental factor to increase its flux so substantially, the corresponding signal in the light curves of the other stars in the field would be, at minimum, an order-of-magnitude increase in their total aperture fluxes. Such a signal is not observed at any point in any of the light curves of the other stars in the field (see the bottom four light curves of Figure 5.2) and so the signal is likely unrelated to weather conditions.

Alternatively, a satellite or plane could in principle affect only EK Dra's derived flux. However, the duration of the effect cannot be explained by these as they pass through Flarescope's FOV over the course of a few seconds, not minutes. To be certain that the flare profile is not the effect of a satellite, I checked single-integration images (5 s exposures) as the shorter integration time would be more sensitive to the signal at a given position. I indeed find no streaks indicative of a satellite passing through the field at the time of the apparent flare. The distinctive shape and duration of the flare candidate in addition to the lack of an analogous signal on the other stars make me reasonably confident this is a genuine flare from EK Dra.

Checking the single-integration images prompted me to produce a light curve at the cadence of the native 5 s exposure time, shown in Figure 5.3. Doing this revealed two phenomenal features: the first is that some subtle, complex structure in the decay phase of the flare is confirmed to be the result of a secondary peak and, by extension, a secondary reconnection event perhaps triggered by the first event. The second extraordinary feature is a 3.8σ detection of the peak of another flare candidate that precedes the original by about 30 min. The profile for this second candidate is not nearly as distinct as the larger flare and so it is more difficult to definitively say it is a flare. That said, as with the original flare, this profile does not have an equivalent signal in the light curves of the other stars, which may suggest this is indeed a second flare that precedes the originally-identified flare. The strength of this signal in the high-noise but high time-resolution data compared to the lack of a detection ($\lesssim 1\sigma$) in the lower-noise, lower time-resolution data is incredibly informative for both Flarescope searches and similar searches with other instruments. It is worth revisiting these datasets at a higher time resolution to identify lower-energy flare candidates and will be the focus of later work. For now, I focus on the qualities of this large flare and what that could mean for an associated CME or SEP.

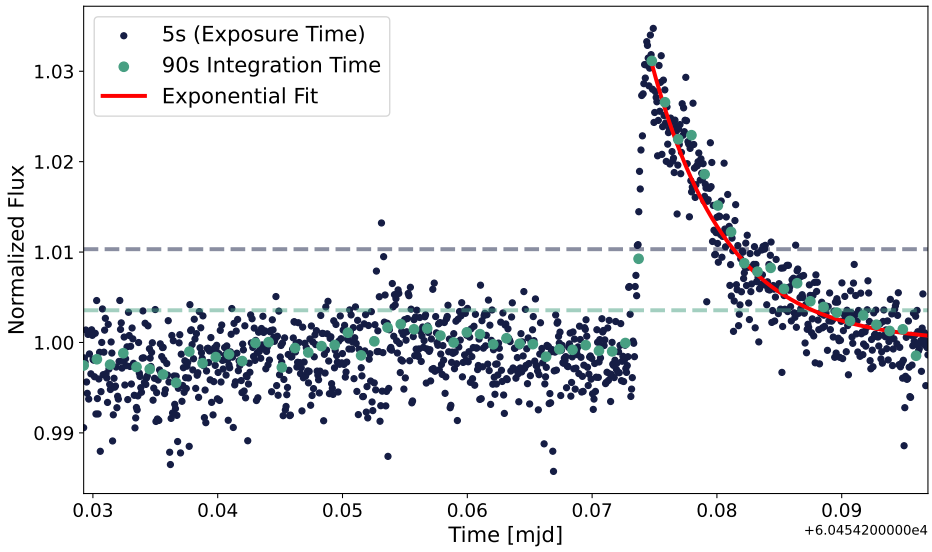

Figure 5.3: The EK Dra light curve at the native 5 s integration time (dark blue) and the light curve at 90 s integration time (teal). The 3σ limits for these two light curves are based on the first 30 minutes of data when there are no flare candidates and are indicated by the dashed lines for the datasets of the respective colors.

Flare Characterization and Particle Acceleration Estimates

Although the large flare has some complex structure, its overall profile is dominated by the primary flare, as indicated by the exponential decay fit shown in red in Figure 5.3. This best fit for this profile, estimated using `curve_fit` from `scipy`'s `optimize` module, has an amplitude of 0.0311 relative to the median flux and an e-folding time $\tau_{\rm decay}$ of 8.59 min. I use this profile and assume a constant flare temperature of 10,000 K in order to estimate the bolometric energy of the flare. Using equation A.5, a flare with this profile in Flarescope's band would have a bolometric energy $E_{\rm flare} = 4 \times 10^{34}$ erg; this may vary by a factor of a few depending on the temperature used. This energy is consistent with superflares observed from EK Dra, including those associated with massive prominence eruptions (Namekata et al., 2021; Namekata et al., 2022a; Namekata et al., 2024a). It is also worth noting from these works that a flare $> 10^{34}$ erg is expected to occur on EK Dra about once every seven days, or once every 168 hours—this is consistent with Flarescope only detecting one flare of this scale in the 189 hours it spent on EK Dra. The major question is then: what can this flare tell us about possibly-accompanying particle flux and its detectability in the radio?

Namekata et al. (2024a) find that the kinetic energy of eruptive prominences, $E_{\rm kin}$,

from EK Dra can be 0.02–3 $E_{\rm flare}$, with masses ranging from 3×10^{17}–10^{19} g. The caveat here is that Namekata et al. (2024a) derived the kinetic energy based on the line-of-sight projected velocity of the prominence—their velocities and energies are likely underestimates. More energetic prominences were associated with both higher speeds and larger masses; this is also generally true for solar CMEs (Moschou et al., 2019). Given this, we might expect an associated prominence to have an energy between 8×10^{32}–1.2×10^{35} erg and velocities between 515–1,092 km/s. For estimates in the rest of this section, I will take $v_{\rm CME} = 1000$ km/s for ease.

For a prominence or CME to produce a type II burst, it will need to produce a super-Alfvénic shock, *i.e.*, we need the difference between the CME velocity and ambient wind velocity to be $v_{\rm CME} - v_{\rm SW} > v_{\rm A}$, where $v_{\rm A} = B/\sqrt{4\pi\rho}$, B is the magnetic field strength, and ρ is the ambient mass density at the location of mass propagation. If we assume that the corona is entirely ionized Hydrogen, then $v_{\rm A} = B/\sqrt{4\pi\, n_{\rm e^-} m_{\rm p}}$ where $m_{\rm p}$ is the proton mass and $n_{\rm e^-}$ is the electron number density. We can now re-frame the problem in terms of instrumentation restrictions, namely that the plasma density is low enough that the plasma frequency $\nu_{\rm p} = 9.8\,{\rm kHz}\sqrt{n_{\rm e^-}}$ is in the OVRO-LWA's band (< 87 MHz). This then requires that $n_{\rm e^-} \leq 7.9 \times 10^7\,{\rm cm^{-3}}$. Plugging this value into the expression for $v_{\rm A}$, we then get that the ambient magnetic field must be $\lesssim 2.5$ G for a shock to form if the stellar wind velocity is the solar value of 400 km/s (as is often assumed for mass-loss estimates, Wood et al., 2005; Fichtinger et al., 2017).

To determine whether such a field strength is reasonable to expect, let us consider the coronal density limits estimated by Guedel et al. (1995) who found that EK Dra's corona should be $\gtrsim 4 \times 10^{10}\,{\rm cm^{-3}}$. I will take this value to be the base coronal density. Assuming then that the density profile is $\propto R^{-2}$ where R is the distance from the stellar surface, then we get that the plasma density requirement is met at $22.5 R_\star$. Assuming, generously, that the magnetic field is still closed at this distance, then the dipolar component of the magnetic field should be dominant and scales $\propto R^{-3}$. For the field to be 2.5 G at $22.5 R_\star$, it would require a 28.5 kG *global* field at the surface of EK Dra. Such a field strength is unheard of for main-sequence stars and is indeed inconsistent with field estimates for EK Dra from Zeeman-Doppler imaging which find average field strengths on the order of 100 G (Waite et al., 2017; Namekata et al., 2024b) or at most 1.4 kG (Kochukhov et al., 2020).Thus, it is reasonable to expect that the ambient conditions needed for detecting plasma emission in the OVRO-LWA's band is also conducive to the shock formation required to produce a

type II burst.

A scaling relation between CME properties and type II properties have been identified for the first time by Mohan et al. (2024a). More specifically, they find that the power of the CME can be associated with the radio luminosity of the accompanying type II burst. They relate the type II luminosity $L_{\rm R}$ and CME velocity to the SXR luminosity of the flare $L_{\rm x}$ like:

$$\log(L_{\rm X}) \approx 1.12 \log_{10}(\sqrt{L_{\rm R}\, v_{\rm CME}^2}) + 9.5 \tag{5.1}$$

where all values are in centimeter-gram-second units. As in Chapter 2, I will take the X-ray luminosity to be 10% of the bolometric luminosity estimated from the white-light light curve; the peak X-ray luminosity would then be 7.9×10^{30} erg/s. Using equation 5.1, the peak radio luminosity would then be 1.6×10^{22} erg s^{-1} Hz^{-1}, or the equivalent of a signal more than 11 kJy. It is worth noting that Mohan et al. (2024a)'s expression comes from a fit of radio data at 3-7 MHz; it is entirely plausible that type II bursts are less luminous in the OVRO-LWA band, although probably not by much more than an order of magnitude. All of this leads to the expectation that a type II burst should be detectable should it arrive to the OVRO-LWA's band within the timeframe that I have data for. The flare properties and associated CME estimates are summarized in Table 5.2

We are less constrained by arrival time to the OVRO-LWA band when it comes to detecting type III bursts since the relevant particles move more than an order of magnitude faster than CMEs. The question then is whether a type III burst will be bright enough to detect. Vedantham (2020) uses a simple linear scaling between flare energy and type III flux density that is normalized by the most energetic solar flares (10^{32} erg) and brightest type III bursts (10^{11} Jy). Their equation 4 suggests that the 4×10^{34} erg flare from EK Dra would produce a 0.85 Jy signal. However, this signal is for 150 MHz—type III bursts should be brighter by about a factor of 5 in the OVRO-LWA band, suggesting a 4.2 Jy signal. This would be a $\gtrsim 5\sigma$ detection at the sensitivity of the OVRO-LWA when integrated $41 - 87$ MHz; the prospects of detecting a type III burst are promising in this simple estimation. It is worth noting that this estimate may be a factor of a few larger than what is physically possible based on brightness temperature limitations for the plasma emission process. That said, the complex structure of EK Dra's flare, which is indicative of multiple reconnection events, may negate this saturation limit as there could be multiple contributing plasma beams. This is discussed in more detail in Section 5.5; the search for radio signatures is the focus of the following sections.

Table 5.2: The flare properties assuming a flare temperature of 10,000 K and the estimates for the associated CME depending on whether very little (second from left column) or very much (left-most column) of the magnetic energy is partitioned to the CME. Notably, if the CME is low energy and slow, it will not arrive to the OVRO-LWA band within the timeframe we have data for (UTC hours 05-12).

Flare properties		**CME Estimates**	Minimum Energy	Maximum Energy
Start time (UTC)	2024-05-24 06:32:38	$E_{\rm Kin}$ [erg]	8×10^{32}	1×10^{35}
$\tau_{\rm decay}$ [min]	8.59	$v_{\rm CME}$ [km/s]	515	1,093
Peak Amplitude	0.0311	Arrival time to band (UTC)	~2024-05-24 13:40:00	~2024-05-24 09:56:00
Peak $L_{\rm bol}$ [erg/s]	7.87×10^{31}	$L_{\rm R}$ [erg s^{-1} Hz^{-1}]	6.1×10^{22}	1.35×10^{22}
Total Energy [erg]	3.98×10^{34}	Peak flux density [Jy]	42,900	9,540

5.3 OVRO-LWA Data Reduction

I established in Chapter 3 that the search for type III bursts is best suited by slow-vis (cross-correlated) data as opposed to beamformed data. This is true even more so for type II bursts, which should persist in the OVRO-LWA band for many time integrations. As such, I only focus on the slow-vis data here. The ultimate goal is to derive a coarse dynamic spectrum for EK Dra from the images produced from slow-vis data. Type III bursts can happen essentially any time relative to the flare event while type II bursts should occur some time after the flare. More specifically, if we assume that a CME launched during the reconnection process of the flare in fact travels at 1000 km/s, then it would take about 4 hr for the CME to reach 22.5 $R_\star$ where the density should be low enough for us to observe it in the OVRO-LWA's band (see Figure 5.4); the significance of the difference between such an environment and the Sun's for observing frequency is demonstrated in Figure 5.5. As such, I evaluate data ranging from UTC hours 05–12 (hours 21–05 local time, ≈ -1.5–5.5 hours relative to the flare peak) across 10 subbands ranging from 41–87 MHz (4.6 MHz bandwidth per subband).

The observing environment for this observation was incredibly different from the pi UMa observation that the original data reduction and analysis were based on. More specifically, the ionosphere was much better behaved in the EK Dra observation, and the nearest bright source that could be used to estimate the ionosphere-shifted position of EK Dra is $\gtrsim 1^\circ$ away from EK Dra; this is in stark contrast to

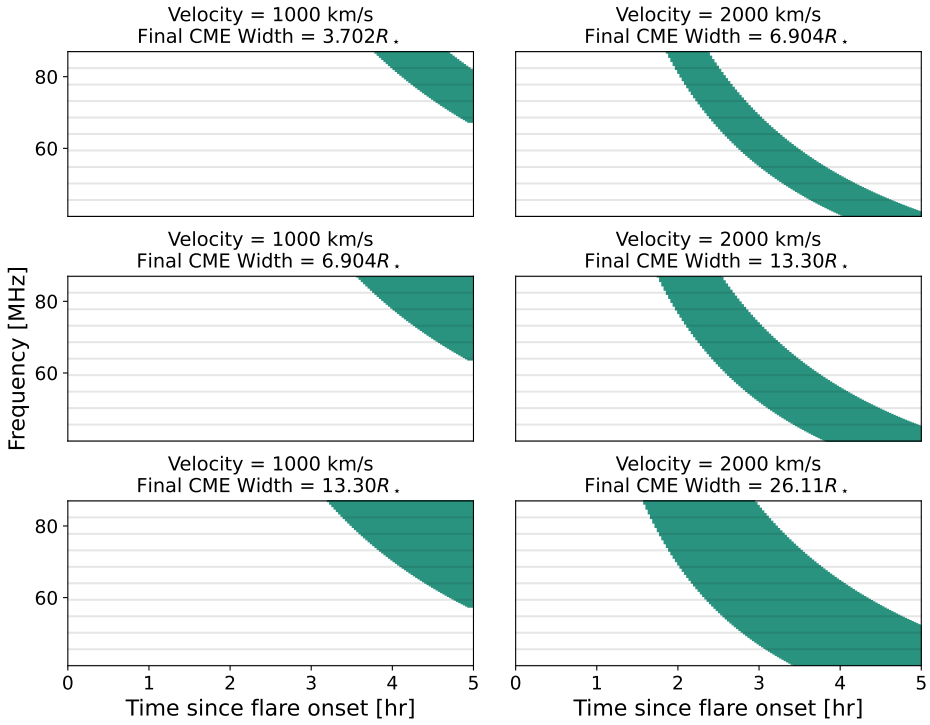

Figure 5.4: Estimates for the type II burst profiles in the OVRO-LWA band assuming various propagation speeds and expansion rates, that the base coronal density is 4×10^{10} cm^{-3}, and that the density decreases with the inverse-squared distance from the stellar surface. The extent of the 10 subbands are indicated by gray lines.

the huge impact that the ionosphere had on source position and flux density and the $\lesssim 15'$ distance between pi UMa and 3C 204. These differing observing conditions, plus my intent to search for type II bursts in addition to type III bursts, has led to a fairly different reduction and analysis process here.

Data Preparation

The data were calibrated in three stages: delay calibration, bandpass calibration, and per-snapshot imaging. The pipeline for this calibration was developed by Yuping Huang and adapted by Nikita Kosogorov and will be discussed in detail in forthcoming papers, but I will summarize the steps here as they were adapted for this dataset.

Delay calibration For each subband in the 41–87 MHz range, the pipeline identifies the MS integration with an LST closest to Cyg A's meridian transit; these MSs are concatenated into a single MS that represents the full 41–87 MHz range and are

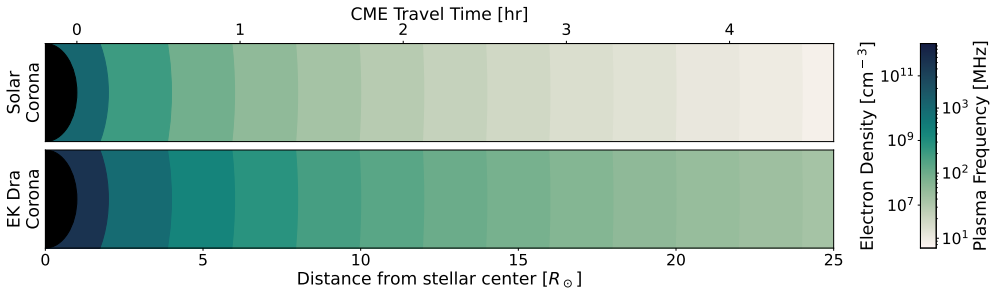

Figure 5.5: A schematic of the coronal density profile and associated plasma frequency for the Sun (top panel) and of EK Dra (bottom panel). The travel time to reach the associated distance is also provided assuming a CME velocity of 1,000 km/s. This demonstrates that a CME launched from the Sun would produce a type II burst within the OVRO-LWA band within a few solar radii and << 1 hr while it would take about an order of magnitude longer for it to do so for EK Dra.

regridded using `CASA`'s `mstransform` function so that the delay solver will see the full instantaneous bandwidth. We flagged bad antennas based on the same stability standards described in Chapter 3.3—this led to 46 of the 352 antennas being flagged alongside additional baseline flagging from `AOFlagger` run with default parameters. A beam-weighted model of Cyg A is Fourier-transformed into the data column of the MS and `gaincal` is run in the K-delay mode across baselines 10-125 λ to solve for the antenna delays. The quality of the delay calibration is confirmed by eye.

Bandpass calibration Bandpass calibrations are derived from MS files spanning four minutes nearest Cyg A's transit. A sky model is made which includes all bright sources above the horizon; for this observation, the dominant bright sources are Cyg A and Cas A. The phase center is shifted to zenith of the middle snapshot so that all scans share the same direction-independent gains. After applying flags, `CASA`'s `bandpass` task solves for amplitude- and phase-versus-frequency using the delay table derived in the previous step. These bandpass and delay solutions are applied to all integration times using `applycal`.

Imaging Because there were no exceptionally-bright sources near EK Dra, we did not need to clean the data nearly as aggressively; Cyg and Cas A being low on the horizon posed the biggest limitation to producing high-quality data. We did relatively shallow peeling (maximum of five major iterations) with `ttcal`'s `zest` functionality in an attempt to remove the effects of sidelobes from these

sources without leading to the peeling algorithm diverging due to the sources' low elevations. Stokes I and V images were produced for each integration time in each subband using 20,000 cleaning iterations and using the same `wsclean` imaging parameters as in Section 3.3, an inner tukey taper of 30 wavelengths, a Briggs weighting of 0, horizon mask of 10°, and a pixel resolution of 1.875′ as inputs for `wsclean`.

Some of the subbands were missing timestamps, possibly due to the data recorder failing on some intervals, that led to the loss of a total of 291 integrations, or about 1.2% of the data. The amount of flagged or unavailable data increases to 6% after flagging data during the DWP beacon signals. After the entire sky is imaged, I crop the images to $256 \times 256\,\mathrm{pix} \approx 8^\circ \times 8^\circ$ centered on EK Dra, as shown in the left panels of Figure 5.6. To compare the quality of this data to that of the pi UMa observation, I average over all subbands and subtract out sources so that what is left is the background. The median background noise across the seven hours is 0.64 Jy—10–20% better than the noise in the pi UMa observation.

Position Estimates

As discussed in detail in Chapter 3, being able to reliably identify emission from the star requires we account for the ionosphere's effects on the apparent position of the source in the sky. The radio sky in the vicinity of EK Dra is sparse compared to pi UMa's sky; there is only one source that is consistently detected in the individual subbands. This is concerning as we saw in Section 3.3 that sources' positional offsets can vary as functions of both time and intrinsic location. Additionally, we should expect that the severity of the source displacement from its true position will increase inversely with frequency. Therefore, understanding how the sky varies as a function of position *and* frequency requires that 1.) we integrate over multiple subbands to achieve the necessary sensitivity to reliably detect more than one source to determine position dependence and 2.) we maintain some level of spectral resolution to evaluate the variability as a function of frequency. I compromise by integrating over the lower 23 MHz (41–64 MHz, hereafter LB) and upper 23 MHz (64–87 MHz, hereafter HB) to achieve the necessary sensitivity to detect multiple sources while maintaining some spectral information.

I use the same framework for estimating source-position evolution that I describe in Section 3.3 and cross-match the persistently-detected sources detected in the LB and HB based on their average positions in each band. The results for the LB

and HB source positions are shown in Figure 5.6, including how the positions of sources evolve relative to their average position as well as how their position changes relative to bright source that is detectable in all subbands. Remarkably, perturbations in source position seem to be coherent across source location—a stark contrast to the coherent *flow* that manifested in a strong location and time dependence for the perturbation magnitude in the pi UMa observation. One apparent outlier is the source indicated by the yellow ellipses and in the yellow position curves of Figure 5.6, which shows substantial variability compared to the other detected sources. This can likely be explained by its low SNR, making accurate centroid fitting more difficult compared to the other sources and thus making it non-representative of the behavior of the ionosphere. The general stability of source positions suggests that the ionosphere's isoplanatic patch is on the order of several degrees for this observation and, as such, I am reasonably satisfied with using the positional offset of the singular bright source that is detectable in all of the subbands—identified as the Seyfert II galaxy IC 1065 (3C 305)—to estimate the change in position of EK Dra. The ionospheric stability assertion is also supported by the stability of the flux density extracted for 3C 305, shown in Figure 5.7; while the flux density of 3C 204 could vary between 20-60 Jy during the pi UMa observation, 3C 305's variability is ≈5–8 Jy depending on the subband, consistent with the noise expected from a source of this flux density.

There was one additional change made to the position estimation described in Section 3.3 before using 3C 305 to determine EK Dra's position on the sky. This is related to the accuracy of the OVRO-LWA's world-coordinates system (WCS) and what that means for derived positions. More specifically, the position of 3C 305 in the OVRO-LWA observation relative to its actual position as reported by NVSS increases to as much as 15′. I therefore use the location of 3C 305 reported in NVSS instead of its average position in the OVRO-LWA observation in order to understand both the short-timescale and bulk change in the position of sources due to the ionosphere. The extraction of the flux density at the location of EK Dra in each sub-band then follows basically the same procedure as the flux-density extraction for pi UMa; the resulting dynamic spectrum and light curve is shown in Figure 5.8.

5.4 Radio Results and Burst Search

At the 10 s native integration time, there is no apparent type II or III signal in EK Dra's dynamic spectrum. It is entirely likely that the noise– on average 1.73 Jy in the highest (82–87 MHz) subband and 2.29 Jy in the lowest (41–46 MHz) subband—

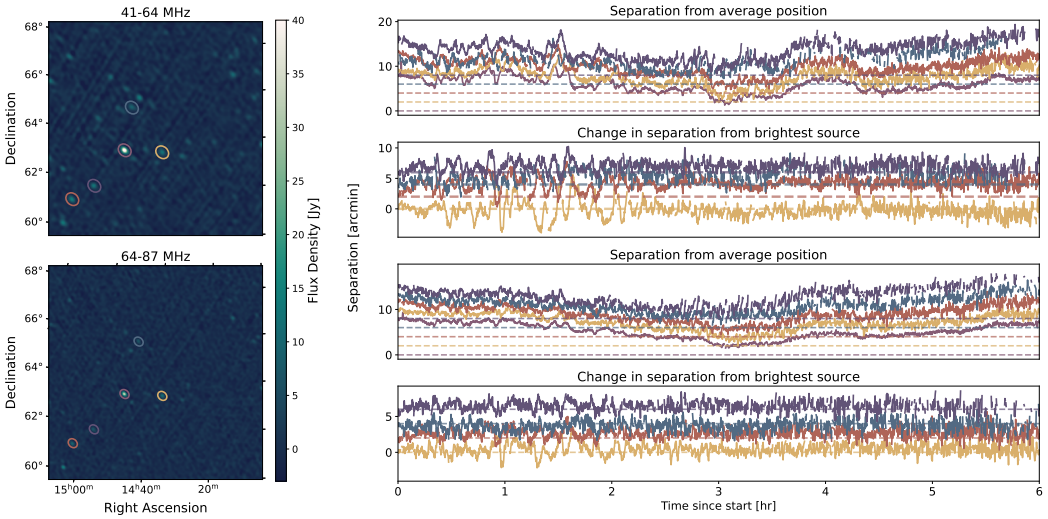

Figure 5.6: An LB (top left) and HB (bottom left) image of the OVRO-LWA field centered on EK Dra at UTC 2024-05-24 05:59:40. The separation between each source and its average position are shown in the first and third panels for the LB and HB, respectively; the separation between each source and 3C 305 is shown in the second and fourth panels. That sources seem to experience the same magnitude of motion nearly simultaneously suggests that the ionosphere is well-behaved and that the motion of one source can reasonably be used to estimate the motion of another.

is too high in any given subband to observe the burst. After I average across frequency to produce the light curve (bottom most panel of Figure 5.8), there are a few integrations that suggest a signal; checking these integrations by eye in the image plane make it clear there were disturbances during those integrations and it is not originating from EK Dra.

In Chapter 3, I asserted that a type III burst would likely not benefit from a de-dispersion search in slow-vis data because the minimum integration time is on the order of the duration and integrated drift rate of solar bursts at these frequencies. However, the extreme conditions of EK Dra's corona may benefit us in the type III search. More specifically, the drift rate scales inversely with the scale height of the atmosphere (Crosley and Osten, 2018a), which itself scales with temperature. Because EK Dra's corona is so hot—consisting of a "cool" 2 MK and hot 10 MK component (Guedel et al., 1995)—compared to the Sun, we might expect that the drift rate in EK Dra's atmosphere is shallower than for solar type III bursts at these frequencies. Similarly, the velocity dispersion of the electron beam exciter elongates the beam as a function of distance—the further a beam travels, the longer the excitation lasts at the corresponding frequency (Reid and Ratcliffe, 2014). Because

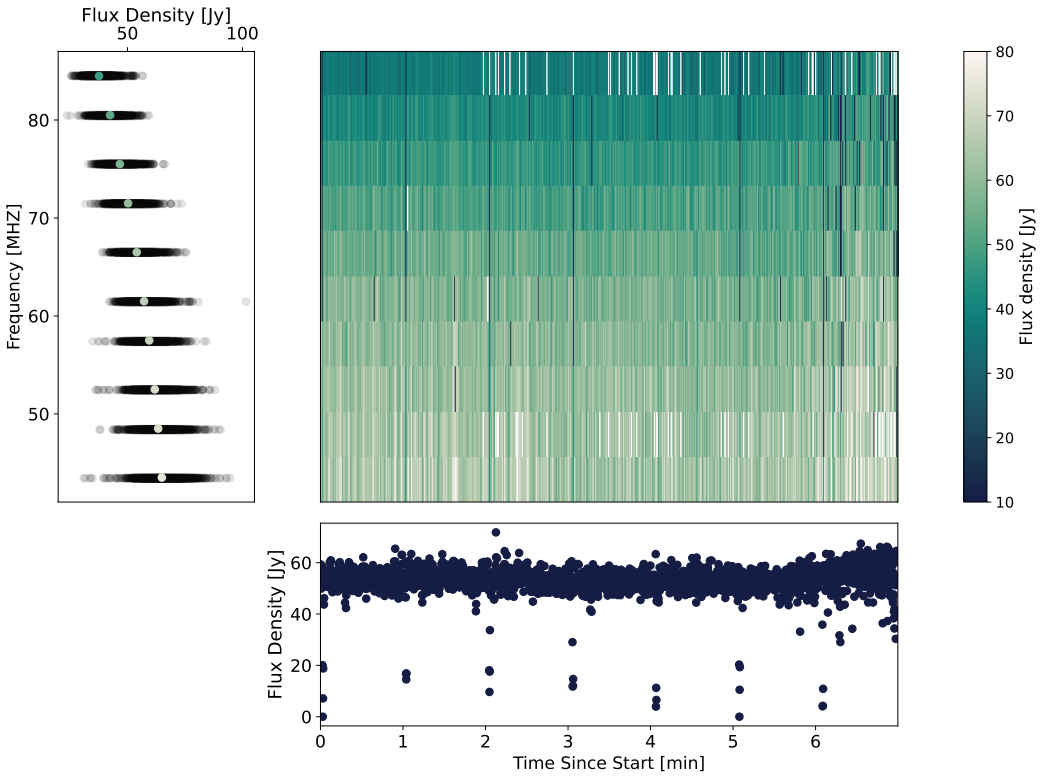

Figure 5.7: 3C 305's dynamic spectrum (top right), the per-integration (black points) and time-averaged (colored points) spectrum (top left), and frequency-averaged light curve (bottom panel) derived from the slow-vis data. The periodic drop outs in flux density apparent in the light curve are the result of non-linearity during the time of the LA DWP beacon pulses.

the beam would need to travel $\approx 10\times$ further to excite the OVRO-LWA frequencies than a beam from the Sun (see Figure 5.5), we might expect then that the burst lasts $\approx 10\times$ longer than a solar type III burst at these frequencies. If this is the case, bursts would last on the order of minutes instead of ≈ 10 s, enabling me to bin in time without the risk of losing signal. This all suggests that the corona of EK Dra may be conducive to conducting the type III de-dispersion search I had originally only considered feasible in the high-time-resolution beamformed data.

Before starting the search, I mask the data at the timestamps and 20 s around the times of the DWP signal, as identified in the dynamic spectrum of 3C 305. Then, as described in Section 3.2, I estimate the delay in frequencies using the expression provided by Alvarez and Haddock (1973):

$$d\nu/dt = -10^{a}\nu^{\alpha} \rightarrow \Delta t = -10^{-a}(1-\alpha)(\nu_{i+1}^{(1-\alpha)} - \nu_{i}^{(1-\alpha)})\,\text{MHz s}^{-1}, \tag{5.2}$$

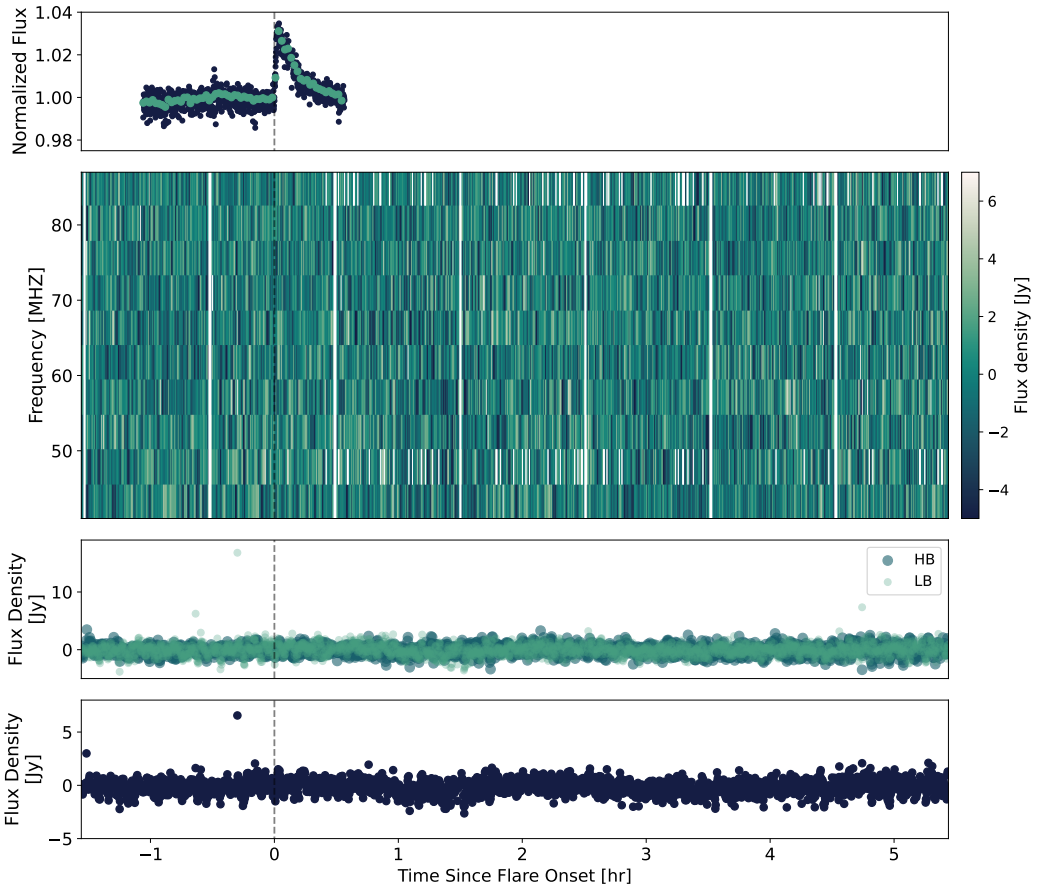

Figure 5.8: The dynamic spectrum for EK Dra, along with the light curves extracted from the HB and LB images (second panel from bottom) and from averaging over the entire dynamic spectrum (bottom-most panel). The Flarescope light curve is included in the top-most panel to indicate when the flare occurred relative to the rest of the observation.

where ν_i is a lower frequency and ν_{i+1} is the frequency immediately above it. Because I expect the drift rate to be slower than for the Sun, I prioritize evaluating a and α values smaller than the solar estimate ($a = -2$, $\alpha = 1.84$); I take $-5 < a < -1$ and $0 < \alpha < 3$. For each a and α value, I integrate over frequency at the native integration time, after binning up to 1 min (six integrations), and after binning up to 2 min. Because binning can reduce the signal if the bin includes a substantial amount of the background, I also evaluate the light curves produced from doing a bulk shift of the de-dispersed dynamic spectrum curve by 30 s intervals. This search did not reveal any signal that could not be explained by a contaminating, poor-quality integration; there is no detectable type III burst at the $5\sigma = 3.2$ Jy threshold.

The type II burst search was conducted using a similar method with two meaningful

differences. The first is that there is no standard dispersion relation for type II bursts because of the dependence on both the environment that the CME propagates through as well as the speed and geometry of the CME; although the beams of type III bursts have a (relatively) narrow spatial spread and velocity distribution, CMEs show substantial variability in their shapes, expansions, and speeds. As such, I do not attempt to de-disperse the signal as the parameter space is so unconstrained and because a type II search can benefit from much longer integration times. I bin in time to 2, 5, and 10 min time resolutions and again shift the binnings by various intervals to account for possible signal loss due to excessive background inclusion. The second major change is that because I did not de-disperse the signal, I perform various frequency integrations, including integrating 2 (9.2 MHz), 3 (13.8 MHz), 5 (23 MHz), and 10 (46 MHz, the full band) subbands. I look for a signature of a type II burst in these extra-coarse dynamic spectra and light curve. Again, there is no emission that can be attributed to the star; EK Dra produced no radio emission in the 5.5 hr following its flare that satisfies expectations based on scaling relations from the Sun.

5.5 Discussion

As I have mentioned, EK Dra has had several flares with signatures of bulk plasma motion with LOS velocities on the order of several hundred kilometers per second; by virtue of the measurement, these velocities are likely under estimates. The energy for the flare presented here is comparable to, or more energetic than, the flares producing such prominences, thus we may expect a similar mass acceleration in this case. Additionally, the magnetic field strength at the distance where the plasma frequency is within the OVRO-LWA's band should be conducive to a CME driving a super-Alfvénic shock. The question then is whether the lack of a type II or III detection is a function of the stellar properties, the CME/plasma beam properties, or related to the fundamental mechanics of type II and III bursts. Here, I present the different conditions that could lead to us not detecting a type II or III burst associated with this flare.

Type III Non-detection

It is worth re-emphasizing here that type III bursts are the most common burst on the Sun—essentially all solar flares produce them and they even occur in the absence of X-ray flares. The reconnection process intrinsically opens magnetic field lines—there are almost certainly beams of electrons being produced during this EK Dra

flare, and the simultaneity of the Flarescope and OVRO-LWA observation allows us to investigate observational and physical limitations in a way that has never before been afforded to LF-radio analyses. We may not see a type III burst if 1.) the beam velocity is insufficient to develop the bump-on-tail distribution, 2.) the instability growth rate is insufficient to facilitate the effective conversion to Langmuir waves, 3.) the magnetic field line leading the beam does not extend out to the distance where the density is conducive to being observed by the OVRO-LWA, or 4.) the burst brightness is limited by the saturation limit of the plasma emission mechanism. I will consider each of these possibilities here.

Beam velocity and instability development: The bump-on-tail instability requires that the velocity of the propagating beam $v_{\rm b}$ is higher than the background thermal speed of electrons $v_{\rm th} = \sqrt{k_{\rm B} T\, m_{\rm e^-}^{-1}}$ where $k_{\rm B}$ is the Boltzmann constant and $m_{\rm e^-}$ is the electron mass. EK Dra's coronal temperatures of 2–10 MK are $\approx$ 1–10$\times$ the quiescent solar temperature and require that $v_{\rm b} \gtrsim 0.04\,c$ where c is the speed of light. In actuality, we see for solar bursts that $v_{\rm b}/v_{\rm th} \approx$ 10–50 (Dulk, 1985). This may then imply that we need a beam with velocity $v_{\rm b} >> 0.4\,c$ to develop the anisotropy. This exceptionally-high speed requirement is relaxed if we assume the temperature at 10s of stellar radii is much lower than the coronal temperature; this assumption is consistent with what we observe for the Sun and that has been estimated for TTSs (Johns-Krull and Herczeg, 2007). It is thus likely that a beam reaching 10s of stellar radii would be capable of reaching a speed sufficient to develop the instability needed to excite Langmuir waves. The development of the instability also requires that its growth rate is much larger than the diffusion rate. However, both of these rates depend on quantities that are not reasonable to speculate for EK Dra, especially as the beam evolves throughout the stellar atmosphere; I will assume that if the beam moves fast enough to initiate the anisotropy then it is also capable of facilitating the instability and wave growth.

Beam directionality Although solar type III bursts are most commonly observed as consistently propagating to lower frequencies/densities, there are a few records of type III bursts (and, presumably, their driving beam) changing direction (Maxwell and Swarup, 1958). Such bursts—called type U or J bursts due to the shape that the reversal produces in dynamic spectra—are associated with fields confined in the solar corona. Given the extreme distances that EK Dra's beam needs to travel to excite the necessary frequencies for the observation, it is not unreasonable that even

an opened field line kinks in such a way that the beam does not reach the relevant densities for the OVRO-LWA. Observing at higher frequencies may then reveal type III bursts, although the low altitudes and corresponding high temperatures probed by such frequencies may then reintroduce the velocity distribution problem I mentioned previously. Discussion would normally also involve the domination of the magnetic field and thus magnetic emission processes at such low altitudes. However, even when assuming a base magnetic field strength of 1.4 kG like Kochukhov et al. (2020) suggest EK Dra produces, the plasma frequency is larger than the cyclotron frequency for distances $\gtrsim 0.4\,R_\star$ above the stellar surface; radio emission from EK Dra that is detected $\lesssim$ 1300 MHz is not likely to be cyclotron emission. As of this thesis, this is by far the lowest-frequency dedicated observation reported for EK Dra—follow-up observations in the 300-1400 MHz range may be more sensitive to type III bursts if directionality of the beam is a limiting factor at low frequencies.

Brightness limitations Finally, it may be that any burst EK Dra could produce just may not be bright enough to be observed by the OVRO-LWA. To evaluate this possibility, let us consider the brightness temperature and source size to estimate what the flux density would be. The brightness temperature of plasma emission is limited by the energy density of Langmuir waves and their associated temperature, which in turn is limited by the thermal electron temperature. For a thermal plasma with temperature 10^6 K—which we will assume is representative of the temperature of EK Dra's atmosphere where the burst originates even though the corona is much hotter—Melrose (1989) estimates the limiting brightness temperature of plasma emission to be $\approx 10^{17-18}$ K. The median source size of type III bursts at 150 MHz is 5.3′ when observed at a distance of $\sim$ 1 AU (Saint-Hilaire et al., 2013); I will conservatively estimate the source size to be 15′ in the OVRO-LWA band. Thus, if the type III burst is emitting at the brightness temperature limit for plasma emission, the burst would have a flux density of $\approx$ 30 Jy. Vedantham, 2020 reduces this quantity by a factor of 100 based on solid angle broadening; this would reduce our estimate to 0.3 Jy, below the sensitivity threshold of the OVRO-LWA. This might suggest that based on physical limitations of the plasma emission process, type III bursts from the distance of EK Dra would be undetectable by the OVRO-LWA. That said, the propagation requirements for EK Dra may again work in our favor; it would be reasonable to expect that the type III burst source size would be much larger due to how much further the beam would need to travel, both addressing the flux density limit as well as the saturation extremity. This is to say that it should not be

unreasonable for detectable emission to be produced within the physical limits of plasma emission, but that a detectable burst just may not have occurred during this observation either for this reason of saturation or due to beam confinement to low altitudes.

Type II Non-detection

Although type II bursts are also the result of plasma emission, the conditions of their production are very different from—and much less well constrained than—type III bursts. Assuming a CME was actually produced, at minimum we can assume that it would need to be able drive a shock at $\approx 22.5\,R_\star$ within 5.5 hr of the flare. If it were capable of doing this, then we can put limits on an associated type II luminosity and evaluate it relative to solar scaling laws.

CME Velocity: Band arrival time and shock development Assuming that this flare has an associated CME, a simple explanation is that the CME did not travel fast enough to 1.) reach a distance within EK Dra's corona or wind where the density is conducive to producing plasma emission within the OVRO-LWA band and/or 2.) drive a super-Alfvénic shock. To consider the plausibility that a late time of arrival (TOA) is responsible, let us again take the density profile of the wind to evolve like $n_\mathrm{b}(R/R_\star)^{-2}$ where n_b is the density at the base of the corona. For simplicity, let us also ignore that the CME is expanding—all other properties held equal, this leads us to over-estimate the TOA. The expression for the TOA at the top of the OVRO-LWA band is then:

$$\mathrm{TOA} = 0.69 \left(\frac{n_\mathrm{b}}{10^9\,\mathrm{cm}^{-3}}\right)^{1/2} \cdot \left(\frac{v_\mathrm{CME}}{1000\,\mathrm{km\,s}^{-1}}\right)^{-1} \cdot \left(\frac{R_\star}{R_\odot}\right) \mathrm{hr}. \tag{5.3}$$

To visualize this, I take $10^9 < n_\mathrm{b} < 10^{12}$, the lower limit of which is representative of the solar corona and the upper limit of which is an order of magnitude lower than the high-end of stellar coronal densities (Güdel, 2004). Similarly, I take that $100 < v_\mathrm{CME} < 2100\,\mathrm{km/s}$. This parameter space is represented in Figure 5.9, where I have also represented the lower-limit estimate for EK Dra's coronal density ($4 \times 10^{10}\mathrm{cm}^{-3}$) and the upper limit of TOAs for the type II to have arrived within the observing timeframe. Taking the lower limit on the base density, we get that the speed would need to be at least 880 km/s for the CME to show up in the band within five hours of the flare onset; for densities $\gtrsim 5\times$ this lower limit, the CME needs to move faster than 2,100 km/s to appear in the band. All of these speeds are higher than the LOS velocities that have been reported for EK Dra, but that discrepancy can

be explained at least somewhat by projection effects; assuming equipartition of flare and CME kinetic energy, the CME could be moving anywhere 850–5150 km/s when considering the mass range of prominences for EK Dra ($\sim 10^{17-19}$ g). Although strong fields in principle could slow a CME, reports of velocities for CME candidates on other highly active stars have achieved these speeds. This is to say that it is not unreasonable for a CME to move fast enough to show up in the OVRO-LWA's band, but also a "low" speed could very easily explain why we did not see a type II signal.

Even if the CME is fast enough to have a reasonable TOA, we may not observe a type II burst if it was unable to drive a shock. This depends on both the Alfvén and wind velocities at the location of the CME. Although the Alfvén speed would be $\lesssim$ 10 km/s at the distances with observationally-conducive densities and thus should not be a limiting factor, we do not have reasonable means to measure wind speeds of other stars; often times in mass-loss-rates estimates the wind speed is simply assumed to be at or near the solar value. Attempts to model the equivalent of the slow solar wind and extrapolate to younger stars produce results that vary by orders of magnitude—as high as 1000s km/s to speeds even lower than the solar wind depending on the assumptions for the base coronal values, coupling between material and fields, and consideration of pressure sources (Vidotto et al., 2010; Johnstone et al., 2015a; Farrish et al., 2019; Evensberget et al., 2021; Fionnagáin et al., 2022). Assuming the solar value, any CME that would have arrived to the OVRO-LWA band in time would have been able to drive a shock, but we cannot rule out that EK Dra may have have a fast "slow" wind—and even faster fast wind—that could easily inhibit shock development.

It is worth noting that this issue of CME TOA is an unexplored complement to what is often cited as the reason for why we do not observe type II bursts from late-type, active M-dwarfs, namely that strong magnetic fields inhibit super-Alfvénic shock development until far distances where the density may be too low to observe the plasma emission from the ground due to the ionosphere (Villadsen and Hallinan, 2019; Alvarado-Gómez et al., 2022b). The moderate field strengths—and consequently lower Alfvén speeds—of young, solar-type stars made them promising targets for avoiding this problem. But, as laid out here, dense coronae that further reduce the Alfvén velocity and alleviate the shock-development problem then require we observe at higher frequencies or else consider low-frequency radio data many hours after the flare occurrence. This poses a new consideration for how multi-instrument coordination should be handled in the future.

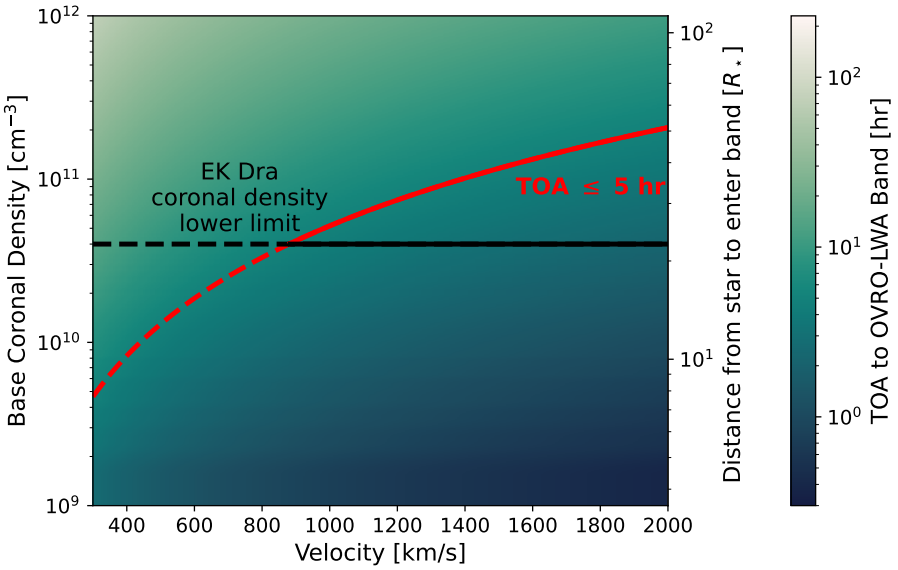

Figure 5.9: Type II TOA estimates for various CME velocity and base coronal densities, using equation 5.3. This assumes that the density profile evolves like R^{-2} from the stellar surface and shows that there exists a narrow range of reasonable base densities ($n > 4 \times 10^{10}\,\mathrm{cm}^{-3}$, indicated by the black line) that would also allow for a CME to arrive within the OVRO-LWA's observing time frame (indicated by the red line).

Under-luminosity If the CME was actually fast enough to satisfy both the TOA and shock conditions, then an alternative explanation is that the type II burst simply was not bright enough to detect. If this is the case, let us revisit Mohan et al. (2024a)'s scaling relation between CME velocity, X-ray luminosity, and radio luminosity (equation 5.1). In my original consideration, I found that the flux density would be on the order of 10^4 Jy—certainly within the realm of detectability. Here, I consider velocities ranging from the minimum velocity for a CME to reach the OVRO-LWA band (880 km/s) to 5× this value, which happens to be close to the upper limit of CME velocities in the energy-equipartition estimation. I let the X-ray luminosity of the flare range between 1–50% of the peak bolometric flare luminosity and, because Mohan et al. (2024a)'s scaling relation come from frequencies outside of the OVRO-LWA band and thus may be more luminous than in our band, I reduce my anticipated flux densities by a factor of 10 to produce Figure 5.10.

Even with this reduction to anticipated flux density, the resulting type II burst should have produced a $\gtrsim 5\sigma$ signal so long as the X-ray luminosity was $\gtrsim 4\%$ of the bolometric luminosity—such an X-ray contribution is entirely reasonable given

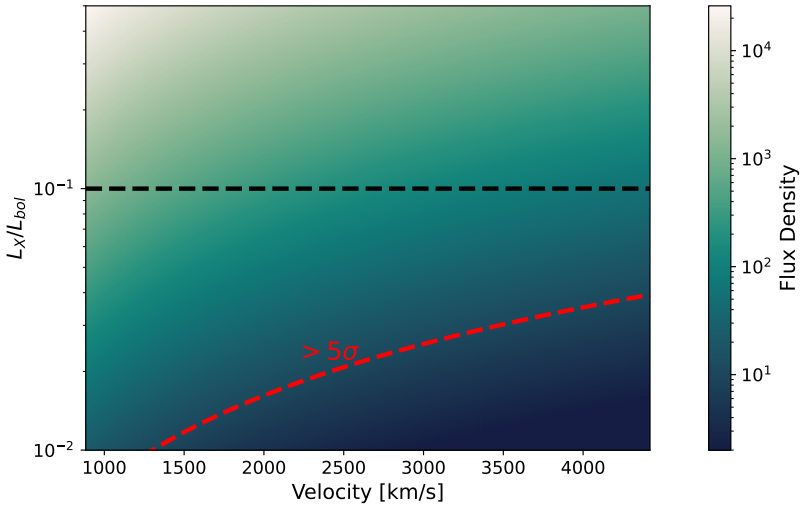

Figure 5.10: The anticipated flux density of EK Dra, calculated from equation 5.1 for CME velocities that would have allowed a type II burst to show up in the OVRO-LWA band within 5 hr after the flare and for a broad range of fractional X-ray luminosities of the flare. An X-ray luminosity that is 10% of the bolometric flare luminosity is indicated by a black dashed line, as this is the typical partitioning of energy expected of flares. The red indicates flux densities above which a burst would have been a $5\sigma \approx 10$ Jy detection in any 4.6 MHz-wide subband. Clearly, any reasonable partitioning of the bolometric flare luminosity to the X-ray would have produced a detectable burst if type II bursts follow the same scaling relation as the Sun.

typical estimates that it makes up $\approx$ 10% of the bolometric flare energy (Osten and Wolk, 2015). This is to say that assuming the CME was fast enough and that stellar bursts follow solar scaling laws then it definitely should have been luminous enough to observe. This latter caveat is, of course, a major limitation to our ability to determine detectability. Although there are several stellar-flare scaling laws that follow solar ones, solar CME scaling laws seem to over-estimate our limited sample of stellar CME properties (Moschou et al., 2019). Without any previously-reported detections of stellar type II bursts, being able to justify this extrapolation from solar to stellar quantities is even more dubious, especially considering the importance of shock formation on type II production and the incredibly different conditions that EK Dra presents for shock formation. Although it would be useful to use flux density estimates to put constraints on the CME velocity, the solar scaling law may, in fact, only be credible for the Sun.

Table 5.3: A summary of the quantities used to estimate the CME pressure $P_{\rm CME}$ and magnetic pressure P_B.

L	V [cm^3]	$E_{\rm Kin}$ [erg]	$P_{\rm CME}$ [erg cm^{-3}]	B_0 [G]	P_B [erg cm^{-3}]	$P_{\rm CME}/P_B$
$0.4\,R_\star$	7×10^{30}	8×10^{32}	114	200	211	0.54
		8×10^{32}	114	1400	10,360	0.01
		1×10^{35}	14,350	200	211	68.01
		1×10^{35}	14,350	1400	10,360	1.39

Confinement In the previous non-detection discussions, I had assumed that there had actually been a CME to detect. However, the ever-present problem of stellar CME studies is being able to conclusively say that material escaped. As an order-of-magnitude estimate, we may say that a CME would be confined if pressure from the overlying magnetic field is greater than the outward pressure of the CME. I will estimate the CME pressure as its energy divided by its volume. I use the flare loop volume of 7×10^{30} cm^3 that I calculate in Appendix D and the energies I estimated in Section 5.2. The magnetic pressure is simply $B^2/8\pi$ where $B = B_0(R/R_\star)^{-3}$ and B_0 is the surface magnetic field strength. ZDI imaging and modeling reported in Namekata et al. (2024b) found maximal global field strengths > 200 G. At the distance of the top of the flare loop ($\approx 0.4\,R_\star$ above the stellar surface) the magnetic field would be ≈ 73 G. The ratio of the CME kinetic pressure to the magnetic field pressure would then be $\approx$ 0.5–70 using the lower and upper estimates of CME energy, where a ratio < 1 implies the magnetic pressure dominates over the CME pressure and thus inhibits escape. I replicate these calculations using the field strength estiamte of 1.4 kG from Kochukhov et al. (2020) and get ratios of 0.01–1.39, implying, as we would expect, that confinement is much more likely; relevant quantities and their resulting pressure ratios are reported in Table 5.3.

This rough estimate suggests that there is a range of CME energies where overlying magnetic fields can reasonably prevent the CME from actually escaping. When considering additional complications introduced by, *e.g.*, ejection geometry and fragmentation (Alvarado-Gómez et al., 2018; Alvarado-Gómez et al., 2022a), it becomes easy to imagine that this could have been a scenario where there was a failed eruption—material would have never gone further than a couple stellar radii, let alone 20. In this case, it is worth again noting the exceptional energy of the flare, which was on the same scale or larger than flares from EK Dra that have produced fast, massive prominences. Although a lack of a CME at this flare energy

does not necessarily mean a CME could *never* occur at this energy or lower, it could suggest, for instance, that mass loss through CMEs does not contribute nearly as much to overall mass loss rates as has been suggested (Osten and Wolk, 2015; Cranmer, 2017). That said, the prediction for CME confinement presented here is far from rigorous; this discussion would benefit greatly from similar wind and CME modeling done in Alvarado-Gómez et al. (2018) and Alvarado-Gómez et al. (2022a) when accounting for EK Dra's exceptional coronal environment.

5.6 Conclusion and Future

In this chapter, I presented the first season of of the SWAYS program which included 500 hr of optical photometry; 66% of these observations had complementary data < 87 MHz, making this the most extensive coordinated observing program for solar-type stars in the radio and optical and the largest dedicated program to solar-type stars below 100 MHz where we frequnetly see signatures of bulk plasma motion from the Sun. At the 90 s integration time that I performed my flare search at in the Flarescope data, I identified one unambiguous flare. This originated from EK Dra and had an energy consistent with superflares reported for the star in previous works. Previous reports of mass motion in EK Dra's chromosphere associated with flares of this energy had been considered possibly eruptive, but I found no signatures of material escaping into EK Dra's upper atmosphere. This could imply that even these highly energetic flares are indeed not always accompanied by CMEs—this is in contrast to the Sun always having a CME for flares four orders of magnitude less energetic than EK Dra's flare—which would in turn suggests that CMEs may not contribute as substantially to the bulk mass and angular momentum loss of stars as has been suggested. Alternatively, there are a variety of conditions specific to EK Dra's atmosphere that could inhibit type II burst production; it is difficult to extrapolate solar expectations to stellar contexts without a better understanding of both the environment of EK Dra and the conditions under which type II bursts occur for the Sun. What is clear is that this analysis would benefit from models of EK Dra's corona and wind to understand 1.) the requirements for shock development, 2.) expectations for a CME being able to meet those requirements, and 3.) what this means for, *e.g.*, the dynamic pressure contribution of CMEs relative to the wind. This is especially important to evaluate at the distance of the Alfvén radius that acts as the lever arm for angular momentum loss as well as at the distance of exoplanets in the habitable zone for this spectral type.

Evaluating more events is necessary to better understand the significance of the non-

detections presented here, especially the type III non-detection, which may represent a saturation or limiting mechanic of plasma emission that does not have an observed solar equivalent. A novel outcome of the analysis here is the identification of the limitations that high densities impose on low-frequency science, especially when done in coordination with other parts of the spectrum. Although simultaneous data may be helpful for identifying potential type III bursts, this work has addressed for the first time that type II bursts may not develop for hours at frequencies for which we see solar type II bursts develop within minutes. Thus, looking for type II bursts from stars with coronae like EK Dra's may benefit more from non-contemporaneous observations. This will be addressed in future work where I analyze OVRO-LWA data that was collected > 6 hr after flares identified in *TESS* data. It is worth noting here that while the coordination of Flarescope and the OVRO-LWA is not likely to lead to type II detections for EK Dra, the other stars apart of the SWAYS program have coronae that are more likely to be akin to the solar corona and thus would still benefit from the coordination for type II searches. All of the stars benefit from the coordination for type III searches.

The other element mentioned here that will be addressed in future work is the impact that integration time has on flare detectability. The 90 s integration time was originally chosen to achieve a high sensitivity that would also be conducive to resolving flare structure. However, we saw that it can substantially reduce potential flare signals; a flare candidate that peaked at 3.8σ in the 5 s time-resolution light curve was completely absent at 90 s. I have re-processed all Flarescope light curves to 5–6 s time resolution and will be re-doing the flare search to look for lower-energy flare candidates and, when possible, investigating complementary radio data. Despite the non-detection of radio bursts, the search presented in this chapter has addressed a gap in the multi-wavelength analysis of stellar space weather and introduced a novel framework for non-detection analysis. The secondary flare search will afford the possibility of building statistics around radio signatures of space weather.

5.7 Acknowledgments

I would like to thank Yuping Huang and Nikita Kosogorov for their work in developing the OVRO-LWA calibration and imaging pipeline which produced the radio images used in this chapter. I would also like to thank Gregg Hallinan for developing the calibration protocol and for feedback on peeling limitations, Kosuke Namekata for recommending that I include V889 Her in the SWAYS sample, and

Júlian Alvarado-Gómez for his feedback on my flare-loop and CME-confinement math.

Chapter 6

FUTURE AND CONCLUSIONS

This thesis was prompted by a growing interest in the particle component of stellar space weather and especially how it may inform our understanding of the history of the Sun and its impact on the solar system. It is notoriously difficult to constrain the properties of even the persistent state of the particle environment, largely because the particle signatures we are sensitive to are contained in the corona or lower atmospheres of a star—material in the interplanetary medium has low surface brightness across the spectrum that makes it difficult to detect and characterize. Transient mass escape into the IPM is even more difficult to constrain, largely due to the difficulty in disentangling signatures of the flare from those of allegedly-escaping material. This is exacerbated by the unpredictability of occurrence that is inherent to the transience, which then requires an immense amount of dedicated observing to witness such events. This is further coupled with the difficulty of needing simultaneous, multi-wavelength observing to corroborate candidate mass ejection signals. In all, this has led to a limited understanding of the evolution of solar space weather, especially in the transient form of coronal mass ejections and energetic particle events.

The work I presented in this thesis was dedicated to tying non-thermal particle acceleration to thermal signatures of flares. This included taking advantage of survey data from *TESS* and VLASS that, while non-contemporaneous, hinted for the first time at the radio counterpart to superflares from solar-type stars. This work suggests that solar-type stars are more active in the radio than is typically assumed and the high brightness temperatures I reported could point to radio emission being the stellar analog of the highly-luminous, coherent solar radio bursts that we see at GHz frequencies. Unambiguous ECME from one *TESS*/VLASS star inspired conversations with individuals at the Commonwealth Scientific and Industrial Research Organisation (CSIRO) who identified ECME from a young solar-type star in RACS. This other ECME-producing star was also detected in a single VLASS epoch just eight days after its detection in RACS. This not only confirms the high activity of young solar-type stars in the radio, but the capacity for collaboration between instruments in different hemispheres for this science. I have received time on the VLA to re-observe the two ECME-producing stars in order to constrain whether the

emission is originating from a large-scale magnetospheric current sheet—the first this would be identified for this type of star—or if it is indeed related to superflares. Regarding this latter point, the HD 245567 observation in particular will benefit from additional *TESS* observations of it that will be occurring simultaneously, allowing us to possibly confirm the flare-ECME phenomenon on a solar-type star other than the Sun. HD 245567 will also be observable at night by Flarescope during this time; because Flarescope and *TESS* are sensitive to similar flare energies, simultaneous observations of a flare in the *TESS* and Flarescope bands can help estimate the flare temperature to better estimate the flare energy and possibly identify the stellar flare-energy thresholds for producing ECME.

The significant sky overlap between VLASS and RACS ($-40°$– $+40°$ in declination) also poses the opportunity to investigate stellar emission and variability from $\approx$ 900–4000 MHz for a massive population of stars. Using the flare-identification and radio-source-finding frameworks that I have already developed for this thesis, I will be expanding my search for—and characterization of—radio emission from solar-type stars. This search will be done in collaboration with individuals at CSIRO and the University of Sydney (USYD). Others have successfully implemented my `flare_id` code for all solar-type stars with a *TESS* light curve and a declination $> -40°$, and the RACS expertise of those at CSIRO and USYD will be critical both for evaluating the validity of RACS detections and extracting dynamic spectra from RACS MSs. By avoiding the Stokes V or distance restrictions that blind stellar radio searches often impose, I hope that this work will greatly expand our understanding of the types of stars that are radio-active and the nature of their radio emission.

My work with the *TESS* and VLASS datasets was done while I was designing, building, and automating Flarescope and commissioning the OVRO-LWA beamformer for simultaneous optical and LF radio monitoring of nearby stars. The goal was to use flare signatures identified from Flarescope's light curves to inform which timestamps in the OVRO-LWA data to look for plasma emission associated with CMEs or SEPs. I demonstrated that Flarescope is capable of exceptional photometric precision that should allow for the detection of superflares on solar-type stars. It accomplishes this even for nearby, bright stars that saturate detectors like those of *TESS* through the implementation of engineered diffusers. In 500 hours of observing dedicated to six stars, this revealed one unambiguous flare. The relatively-low detection rate may be attributed to doing the search at too high of an integration time; the worse precision at short integration times is compensated by the strength

of the signal when it is not integrated with non-flare emission. A follow-up flare search will be conducted at a higher time resolution to see if it reveals additional flares like it did for EK Dra in Chapter 5.

For the flare on EK Dra that was detected, a rigorous search in the complementary OVRO-LWA visibility data did not reveal any signatures of plasma emission. Because there are no reports of stellar equivalents of type II or III bursts, it is difficult to attribute the non-detection to physical limitations of the plasma emission process as opposed to the specific properties of EK Dra's corona. That said, it is reasonable to conclude that extrapolations of solar scaling laws are not informative for non-solar observations, even for stars considered young solar analogs. Although this search did not lead to the detection of stellar plasma emission, it did highlight the possible necessity of low-frequency radio observations to be conducted many hours after flare detections in order to observe type II bursts from very young stars with dense coronae; this is a previously unevaluated condition for looking for this sort of emission. With this in mind, I will take advantage of *TESS* observations of EK Dra that show flares within $\approx$ 6–12 hours of OVRO-LWA observations to give adequate time for any shock to have reached the necessary heights in EK Dra's atmosphere to produce emission in the OVRO-LWA band. By increasing the number of observations I search for associated radio emission—and the time between the radio and optical observations—I will be able to better constrain whether it was the conditions of EK Dra's environment that inhibited the radio detection during this observation.

This search for bursts informed by flares in *TESS* data can reasonably be extended to a huge swath of stars due to the all-sky, all-night nature of the OVRO-LWA slow visibilities. Flares identified from any of the stars observed during a *TESS* sector at declinations $\gtrsim -10^\circ$ and within the OVRO-LWA's two-week buffer are essentially guaranteed to have complementary radio data. It should be relatively straight forward to combine the frameworks of the flare-identification pipeline I developed for *TESS* data and the dynamic-spectrum/de-dispersion pipelines I developed for the OVRO-LWA into a single, robust flare and burst pipeline. In addition to the OVRO-LWA-*TESS* synergistic pipeline, I will be finalizing a similar pipeline for the combined operations of targeted observations between Flarescope and OVRO-LWA visibilities and beamforming. Through funding provided by the JPL President's and Director's Research and Development Fund, Flarescope will receive the expertise it needs to finalize its automation so that it can operate as the fully autonomous, optical complement to the OVRO-LWA that I designed it to be.

My thesis has been focused on the elements of stellar space weather that can be studied through optical photometry and radio wavelengths, but fully understanding space weather is ultimately a full-spectrum endeavor. In this respect, I am incredibly fortunate to have been introduced to the broader space-weather community through the Keck Institute for Space Studies (KISS). Through the guidance of experts in this group, I am looking forward to expanding my experience to Doppler spectroscopy by taking advantage of the observational overlap between the OVRO-LWA and the Solar Calibrator (SOCAL, Rubenzahl et al., 2023) on Keck, which collects Sun-as-a-star spectra daily, in order to investigate possible relations between Doppler signatures of CMEs and type II bursts. This would be especially informative in discussions with respect to the (relative) abundance of stellar Doppler signatures of CMEs but dearth of type II bursts. Similarly, developing a framework for characterizing CMEs based on the combination of these signals will be invaluable in the case that we make detections of stellar Doppler signatures associated with apparent type II emissions.

Discussions I had as a part of this group also highlighted the lack of literature on the possibility of directly imaging stellar CMEs. It is generally assumed we would be unable to achieve the contrast necessary to successfully image a CME, but there has not been rigorous investigation into how the extreme masses or potentially-unique morphologies of stellar CMEs may facilitate sufficient levels of Thomson-scattered flux to be detectable in white light. I am working with members of this group to incorporate wind and CME models into coronagraph models by Lin (2024) to identify the limits of directly imaging both CMEs and winds. The efforts of the KISS stellar particle group—including evaluations of the future of multi-wavelength monitoring for transient events and a preliminary discussion of direct imaging—have been summarized in a forth-coming report.

The instrumentation and observing foundation I developed for coordinated radio and optical monitoring, as well as the frameworks for analysis between these parts of the spectrum, has coalesced into a considerable amount of groundwork for understanding space weather and activity for solar-type stars. The tool sets that I have developed will see substantial use and expansion through its continued and evolving implementation for the OVRO-LWA, Flarescope, and *TESS* as well as its application to other instruments and data sets. I am especially excited to be extending my de-dispersion search for bursts to higher frequencies with LOFAR dynamic spectra where we might be more sensitive to particle events occurring in dense coronae. As radio surveys persist and improve, dedicated observing expands to other parts of

the spectrum, and observational and theoretical realms develop their relationship, I suspect we will see massive improvements in our understanding of the Sun and the history of habitability in the next few years.

BIBLIOGRAPHY

Aarnio, A. N., K. G. Stassun, W. J. Hughes, et al. (Jan. 2011). "Solar Flares and Coronal Mass Ejections: A Statistically Determined Flare Flux - CME Mass Correlation." In: *Solar Physics* 268.1, pp. 195–212. DOI: 10.1007/s11207-010-9672-7. arXiv: 1011.0424 [astro-ph.SR].

Airapetian, V. S., R. Barnes, O. Cohen, et al. (Apr. 2020). "Impact of space weather on climate and habitability of terrestrial-type exoplanets." In: *International Journal of Astrobiology* 19.2, pp. 136–194. DOI: 10.1017/S1473550419000132. arXiv: 1905.05093 [astro-ph.EP].

Airapetian, V. S., A. Glocer, G. Gronoff, et al. (June 2016). "Prebiotic chemistry and atmospheric warming of early Earth by an active young Sun." In: *Nature Geoscience* 9.6, pp. 452–455. DOI: 10.1038/ngeo2719.

Albert, J. G., R. J. van Weeren, H. T. Intema, et al. (Mar. 2020). "Probabilistic direction-dependent ionospheric calibration for LOFAR-HBA." In: *Astronomy and Astrophysics* 635, A147, A147. DOI: 10.1051/0004-6361/201937424. arXiv: 2002.00127 [astro-ph.IM].

Allan, D. W. (Feb. 1966). "Statistics of atomic frequency standards." In: *Proceedings of the Institute of Electrical and Electronics Engineers* 54, pp. 221–230. DOI: 10.1109/PROC.1966.4634.

Allan, G., G. Ruane, A. B. Walter, et al. (Oct. 2023). "Demonstration of coronagraph technology for high-contrast point spectroscopy of ExoEarths." In: *Society of Photo-Optical Instrumentation Engineers (SPIE) Conference Series*. Vol. 12680. Society of Photo-Optical Instrumentation Engineers (SPIE) Conference Series, 1268019, p. 1268019. DOI: 10.1117/12.2676876.

Alvarado-Gómez, J. D., O. Cohen, J. J. Drake, et al. (Apr. 2022a). "Simulating the Space Weather in the AU Mic System: Stellar Winds and Extreme Coronal Mass Ejections." In: *The Astrophysical Journal* 928.2, 147, p. 147. DOI: 10.3847/1538-4357/ac54b8. arXiv: 2202.07949 [astro-ph.SR].

Alvarado-Gómez, J. D., J. J. Drake, O. Cohen, et al. (Aug. 2018). "Suppression of Coronal Mass Ejections in Active Stars by an Overlying Large-scale Magnetic Field: A Numerical Study." In: *The Astrophysical Journal* 862.2, 93, p. 93. DOI: 10.3847/1538-4357/aacb7f. arXiv: 1806.02828 [astro-ph.SR].

Alvarado-Gómez, J. D., J. J. Drake, O. Cohen, et al. (May 2022b). "Coronal mass ejections and exoplanets: A numerical perspective." In: *Astronomische Nachrichten* 343.4, e10100, e10100. DOI: 10.1002/asna.20210100. arXiv: 2111.09704 [astro-ph.SR].

Alvarez, H. and F. T. Haddock (Mar. 1973). "Solar Wind Density Model from km-Wave Type III Bursts." In: *Solar Physics* 29.1, pp. 197–209. DOI: 10.1007/BF00153449.

Anderson, M. M. (Jan. 2019). "Adventures Through Time and Phase Space: Characterizing the Dynamic Radio Sky, from MHz to GHz, from Seconds to Years." PhD thesis. California Institute of Technology.

Antiochos, S. K., Z. Mikić, V. S. Titov, et al. (Apr. 2011). "A Model for the Sources of the Slow Solar Wind." In: *The Astrophysical Journal* 731.2, 112, p. 112. DOI: 10.1088/0004-637X/731/2/112. arXiv: 1102.3704 [astro-ph.SR].

Argiroffi, C., F. Reale, J. J. Drake, et al. (May 2019). "A stellar flare-coronal mass ejection event revealed by X-ray plasma motions." In: *Nature Astronomy* 3, pp. 742–748. DOI: 10.1038/s41550-019-0781-4. arXiv: 1905.11325 [astro-ph.SR].

Aschwanden, M. J. (Nov. 2015). "Thresholded Power law Size Distributions of Instabilities in Astrophysics." In: *The Astrophysical Journal* 814.1, 19, p. 19. DOI: 10.1088/0004-637X/814/1/19. arXiv: 1510.01987 [astro-ph.SR].

Aschwanden, M. J., F. Scholkmann, W. Béthune, et al. (Mar. 2018). "Order out of Randomness: Self-Organization Processes in Astrophysics." In: *Space Science Reviews* 214.2, 55, p. 55. DOI: 10.1007/s11214-018-0489-2. arXiv: 1708.03394 [astro-ph.SR].

Aschwanden, M. J., T. D. Tarbell, R. W. Nightingale, et al. (June 2000). "Time Variability of the "Quiet" Sun Observed with TRACE. II. Physical Parameters, Temperature Evolution, and Energetics of Extreme-Ultraviolet Nanoflares." In: *The Astrophysical Journal* 535.2, pp. 1047–1065. DOI: 10.1086/308867.

Baars, J. W. M., R. Genzel, I. I. K. Pauliny-Toth, et al. (Oct. 1977). "The absolute spectrum of Cas A: an accurate flux density scale and a set of secondary calibrators." In: *Astronomy and Astrophysics* 61, pp. 99–106.

Bassa, C. G., Z. Pleunis, and J. W. T. Hessels (Jan. 2017). "Enabling pulsar and fast transient searches using coherent dedispersion." In: *Astronomy and Computing* 18, pp. 40–46. DOI: 10.1016/j.ascom.2017.01.004. arXiv: 1607.00909 [astro-ph.IM].

Bastian, T. S., A. O. Benz, and D. E. Gary (Jan. 1998). "Radio Emission from Solar Flares." In: *Annual Review of Astronomy and Astrophysics* 36, pp. 131–188. DOI: 10.1146/annurev.astro.36.1.131.

Bastian, T. S., J. Villadsen, A. Maps, et al. (Apr. 2018). "Radio Emission from the Exoplanetary System Eridani." In: *The Astrophysical Journal* 857.2, 133, p. 133. DOI: 10.3847/1538-4357/aab3cb. arXiv: 1706.07012 [astro-ph.SR].

Bell, C. P. M., E. E. Mamajek, and T. Naylor (Nov. 2015). "A self-consistent, absolute isochronal age scale for young moving groups in the solar neighbourhood." In: *Monthly Notices of the Royal Astronomical Society* 454.1, pp. 593–614. DOI: 10.1093/mnras/stv1981. arXiv: 1508.05955 [astro-ph.SR].

Benz, A. O. and M. Guedel (May 1994). "X-ray/microwave ratio of flares and coronae." In: *Astronomy and Astrophysics* 285, pp. 621–630.

Benz, A. O. and M. Güdel (Sept. 2010). "Physical Processes in Magnetically Driven Flares on the Sun, Stars, and Young Stellar Objects." In: *Annual Review of Astronomy and Astrophysics* 48, pp. 241–287. DOI: 10.1146/annurev-astro-082708-101757.

Berger, V. L., J. T. Hinkle, M. A. Tucker, et al. (Aug. 2024). "Stellar flares are far-ultraviolet luminous." In: *Monthly Notices of the Royal Astronomical Society* 532.4, pp. 4436–4445. DOI: 10.1093/mnras/stae1648. arXiv: 2312.12511 [astro-ph.SR].

Bloot, S., J. R. Callingham, H. K. Vedantham, et al. (Feb. 2024). "Phenomenology and periodicity of radio emission from the stellar system AU Microscopii." In: *Astronomy and Astrophysics* 682, A170, A170. DOI: 10.1051/0004-6361/202348065. arXiv: 2312.09071 [astro-ph.SR].

Boller, T., M. J. Freyberg, J. Trümper, et al. (Apr. 2016). "Second ROSAT all-sky survey (2RXS) source catalogue." In: *Astronomy and Astrophysics* 588, A103, A103. DOI: 10.1051/0004-6361/201525648. arXiv: 1609.09244 [astro-ph.HE].

Boyde, B., A. Wood, G. Dorrian, et al. (Aug. 2022). "Lensing from small-scale travelling ionospheric disturbances observed using LOFAR." In: *Journal of Space Weather and Space Climate* 12, 34, p. 34. DOI: 10.1051/swsc/2022030.

Bradley, L., B. Sipőcz, T. Robitaille, et al. (Apr. 2024). *astropy/photutils: 1.12.0*. Version 1.12.0. DOI: 10.5281/zenodo.10967176. URL: https://doi.org/10.5281/zenodo.10967176.

Briggs, D. S. (Jan. 1995). "High fidelity deconvolution of moderately resolved sources." PhD thesis. New Mexico Institute of Mining and Technology.

Burton, K., M. A. MacGregor, and R. A. Osten (Nov. 2022). "First Millimeter Flares Detected from Eridani with the Atacama Large Millimeter/submillimeter Array." In: *The Astrophysical Journal Letters* 939.1, L6, p. L6. DOI: 10.3847/2041-8213/ac9973. arXiv: 2210.10818 [astro-ph.SR].

Callingham, J. R., H. K. Vedantham, T. W. Shimwell, et al. (Dec. 2021). "The population of M dwarfs observed at low radio frequencies." In: *Nature Astronomy* 5, pp. 1233–1239. DOI: 10.1038/s41550-021-01483-0. arXiv: 2110.03713 [astro-ph.SR].

Cane, H. V. and W. C. Erickson (Dec. 2005). "Studies of Space Weather Using Solar Radio Bursts." In: *From Clark Lake to the Long Wavelength Array: Bill Erickson's Radio Science*. Ed. by N. Kassim, M. Perez, W. Junor, et al. Vol. 345. Astronomical Society of the Pacific Conference Series, p. 133.

CASA Team, B. Bean, S. Bhatnagar, et al. (Nov. 2022). "CASA, the Common Astronomy Software Applications for Radio Astronomy." In: *Publications of the Astronomical Society of the Pacific* 134.1041, 114501, p. 114501. DOI: 10.1088/1538-3873/ac9642. arXiv: 2210.02276 [astro-ph.IM].

Cesaroni, R., L. Moscadelli, A. C. o Garatti, et al. (Mar. 2024). "Radio outburst from a massive (proto)star. III. Unveiling the bipolarity of the radio jet from S255IR NIRS 3." In: *Astronomy and Astrophysics* 683, L15, p. L15. DOI: 10.1051/0004-6361/202449288. arXiv: 2403.02999 [astro-ph.SR].

Chang, H. .-., C. .-. Lin, W. .-. Ip, et al. (Nov. 2018). "Hyperflares of M Dwarfs." In: *The Astrophysical Journal* 867.1, 78, p. 78. DOI: 10.3847/1538-4357/aae2bc.

Chen, A. Q., P. F. Chen, and C. Fang (Sept. 2006). "On the CME velocity distribution." In: *Astronomy and Astrophysics* 456.3, pp. 1153–1158. DOI: 10.1051/0004-6361:20065378.

Chen, B., D. Gary, S. Mondal, et al. (Jan. 2025). "Early Solar Science with the Long Wavelength Array at the Owens Valley Radio Observatory." In: *American Astronomical Society Meeting Abstracts #245*. Vol. 245. American Astronomical Society Meeting Abstracts, 105.13, p. 105.13.

Claret, A. and A. Gimenez (Nov. 1989). "The moment of inertia of main sequence stars." In: *Astronomy and Astrophysics Supplement Series* 81.1, pp. 37–45.

Clarke, M. E. (Jan. 1964). "The determination of the positions of 88 radio sources." In: *Monthly Notices of the Royal Astronomical Society* 127, p. 405. DOI: 10.1093/mnras/127.5.405.

Cliver, E. W. and A. G. Ling (Jan. 2009). "Low-Frequency Type III Bursts and Solar Energetic Particle Events." In: *The Astrophysical Journal* 690.1, pp. 598–609. DOI: 10.1088/0004-637X/690/1/598.

Cliver, E. W., S. M. White, and K. S. Balasubramaniam (Dec. 2011). "The Solar Decimetric Spike Burst of 2006 December 6: Possible Evidence for Field-aligned Potential Drops in Post-eruption Loops." In: *The Astrophysical Journal* 743.2, 145, p. 145. DOI: 10.1088/0004-637X/743/2/145.

Cliver, E. W. and W. F. Dietrich (Oct. 2013). "The 1859 space weather event revisited: limits of extreme activity." In: *Journal of Space Weather and Space Climate* 3, A31, A31. DOI: 10.1051/swsc/2013053.

Cliver, E. W., C. J. Schrijver, K. Shibata, et al. (Dec. 2022). "Extreme solar events." In: *Living Reviews in Solar Physics* 19.1, 2, p. 2. DOI: 10.1007/s41116-022-00033-8. arXiv: 2205.09265 [astro-ph.SR].

Coffaro, M., B. Stelzer, S. Orlando, et al. (Apr. 2020). "An X-ray activity cycle on the young solar-like star Eridani." In: *Astronomy and Astrophysics* 636, A49, A49. DOI: 10.1051/0004-6361/201936479. arXiv: 2002.11009 [astro-ph.SR].

Cohen, A. S., W. M. Lane, W. D. Cotton, et al. (Sept. 2007). "The VLA Low-Frequency Sky Survey." In: *The Astronomical Journal* 134.3, pp. 1245–1262. DOI: 10.1086/520719. arXiv: 0706.1191 [astro-ph].

Condon, J. J. (Feb. 1997). "Errors in Elliptical Gaussian Fits." In: *Publications of the Astronomical Society of the Pacific* 109, pp. 166–172. DOI: 10.1086/133871.

Corsaro, E., A. Bonanno, S. Mathur, et al. (Aug. 2021). "A calibration of the Rossby number from asteroseismology." In: *Astronomy and Astrophysics* 652, L2, p. L2. DOI: 10.1051/0004-6361/202141395. arXiv: 2107.08551 [astro-ph.SR].

Cranmer, S. R. (May 2017). "Mass-loss Rates from Coronal Mass Ejections: A Predictive Theoretical Model for Solar-type Stars." In: *The Astrophysical Journal* 840.2, 114, p. 114. DOI: 10.3847/1538-4357/aa6f0e. arXiv: 1704.06689 [astro-ph.SR].

Crosley, M. K. and R. A. Osten (Mar. 2018a). "Constraining Stellar Coronal Mass Ejections through Multi-wavelength Analysis of the Active M Dwarf EQ Peg." In: *The Astrophysical Journal* 856.1, 39, p. 39. DOI: 10.3847/1538-4357/aaaec2. arXiv: 1802.03440 [astro-ph.SR].

– (Aug. 2018b). "Low-frequency Radio Transients on the Active M-dwarf EQ Peg and the Search for Coronal Mass Ejections." In: *The Astrophysical Journal* 862.2, 113, p. 113. DOI: 10.3847/1538-4357/aacf02.

Davenport, J. R. A. (Sept. 2016). "The Kepler Catalog of Stellar Flares." In: *The Astrophysical Journal* 829.1, 23, p. 23. DOI: 10.3847/0004-637X/829/1/23. arXiv: 1607.03494 [astro-ph.SR].

Desidera, S., E. Covino, S. Messina, et al. (Jan. 2015). "The VLT/NaCo large program to probe the occurrence of exoplanets and brown dwarfs in wide orbits. I. Sample definition and characterization." In: *Astronomy and Astrophysics* 573, A126, A126. DOI: 10.1051/0004-6361/201323168. arXiv: 1405.1559 [astro-ph.EP].

Distefano, E., A. C. Lanzafame, A. F. Lanza, et al. (Oct. 2017). "Activity cycles in members of young loose stellar associations." In: *Astronomy and Astrophysics* 606, A58, A58. DOI: 10.1051/0004-6361/201730967. arXiv: 1706.07938 [astro-ph.SR].

do Nascimento Jr., J. .-., A. A. Vidotto, P. Petit, et al. (Mar. 2016). "Magnetic Field and Wind of Kappa Ceti: Toward the Planetary Habitability of the Young Sun When Life Arose on Earth." In: *The Astrophysical Journal Letters* 820.1, L15, p. L15. DOI: 10.3847/2041-8205/820/1/L15. arXiv: 1603.03937 [astro-ph.SR].

Dong, D. Z., G. Hallinan, E. Nakar, et al. (Sept. 2021). "A transient radio source consistent with a merger-triggered core collapse supernova." In: *Science* 373.6559, pp. 1125–1129. DOI: 10.1126/science.abg6037. arXiv: 2109.01752 [astro-ph.HE].

Dong, D. Z. and G. Hallinan (May 2023). "A Flat-spectrum Radio Transient at 122 Mpc Consistent with an Emerging Pulsar Wind Nebula." In: *The Astrophysical Journal* 948.2, 119, p. 119. DOI: 10.3847/1538-4357/acc06c. arXiv: 2206.11911 [astro-ph.HE].

Dorren, J. D. and E. F. Guinan (June 1994). "HD 129333: The Sun in Its Infancy." In: *The Astrophysical Journal* 428, p. 805. DOI: 10.1086/174289.

Doyle, L., G. Ramsay, and J. G. Doyle (May 2020). "Superflares and variability in solar-type stars with TESS in the Southern hemisphere." In: *Monthly Notices of the Royal Astronomical Society* 494.3, pp. 3596–3610. DOI: 10.1093/mnras/staa923. arXiv: 2003.14410 [astro-ph.SR].

Drake, S. A., T. Simon, and J. L. Linsky (Dec. 1989). "A Survey of the Radio Continuum Emission of RS Canum Venaticorum and Related Active Binary Systems." In: *The Astrophysical Journal Supplement Series* 71, p. 905. DOI: 10.1086/191402.

Duffin, R. T., S. M. White, P. S. Ray, et al. (Sept. 2015). "Type III-L Solar Radio Bursts and Solar Energetic Particle Events." In: *Journal of Physics Conference Series*. Vol. 642. Journal of Physics Conference Series. IOP, 012006, p. 012006. DOI: 10.1088/1742-6596/642/1/012006.

Dulk, G. A. (Jan. 1985). "Radio emission from the sun and stars." In: *Annual Review of Astronomy and Astrophysics* 23, pp. 169–224. DOI: 10.1146/annurev.aa.23.090185.001125.

Dulk, G. A. and K. A. Marsh (Aug. 1982). "Simplified expressions for the gyrosynchrotron radiation from mildly relativistic, nonthermal and thermal electrons." In: *The Astrophysical Journal* 259, pp. 350–358. DOI: 10.1086/160171.

Eastwood, M. W. (Nov. 2017). *TTCal*. Version 0.3.0. DOI: 10.5281/zenodo.1049160. URL: https://doi.org/10.5281/zenodo.1049160.

Eastwood, M. W., M. M. Anderson, R. M. Monroe, et al. (Aug. 2019). "The 21 cm Power Spectrum from the Cosmic Dawn: First Results from the OVRO-LWA." In: *The Astronomical Journal* 158.2, 84, p. 84. DOI: 10.3847/1538-3881/ab2629. arXiv: 1906.08943 [astro-ph.CO].

Eastwood, M. W. (Jan. 2019). "Searching for the Cosmic Dawn with the Hyperfine Structure Transition of Hydrogen." PhD thesis. California Institute of Technology, Division of Physics, Mathematics and Astronomy.

Ellingson, S. W., T. E. Clarke, A. Cohen, et al. (Aug. 2009). "The Long Wavelength Array." In: *Proceedings of the Institute of Electrical and Electronics Engineers* 97.8, pp. 1421–1430. DOI: 10.1109/JPROC.2009.2015683.

Evans, P. A., K. L. Page, J. P. Osborne, et al. (Apr. 2020). "2SXPS: An Improved and Expanded Swift X-Ray Telescope Point-source Catalog." In: *The Astrophysical Journal Supplement Series* 247.2, 54, p. 54. DOI: 10.3847/1538-4365/ab7db9. arXiv: 1911.11710 [astro-ph.IM].

Evensberget, D., B. D. Carter, S. C. Marsden, et al. (Sept. 2021). "The winds of young Solar-type stars in the Hyades." In: *Monthly Notices of the Royal Astronomical Society* 506.2, pp. 2309–2335. DOI: 10.1093/mnras/stab1696. arXiv: 2106.04937 [astro-ph.SR].

Fang, C., P.-F. Chen, Z. Li, et al. (Dec. 2013). "A new multi-wavelength solar telescope: Optical and Near-infrared Solar Eruption Tracer (ONSET)." In: *Research in Astronomy and Astrophysics* 13.12, 1509-1517, pp. 1509–1517. DOI: 10.1088/1674-4527/13/12/011. arXiv: 1307.4533 [astro-ph.SR].

Farrish, A. and K. Garcia-Sage (Oct. 2023). "Modeling Stellar Winds and Coronal Emission of Young Solar Analogues." In: *54th Meeting of the Solar Physics Division*. Vol. 55. AAS/Solar Physics Division Meeting, 202.05, p. 202.05.

Farrish, A. O., D. Alexander, M. Maruo, et al. (Nov. 2019). "Characterizing the Magnetic Environment of Exoplanet Stellar Systems." In: *The Astrophysical Journal* 885.1, 51, p. 51. DOI: 10.3847/1538-4357/ab4652.

Feeney-Johansson, A., S. J. D. Purser, T. P. Ray, et al. (Sept. 2021). "Detection of coherent low-frequency radio bursts from weak-line T Tauri stars." In: *Astronomy and Astrophysics* 653, A101, A101. DOI: 10.1051/0004-6361/202140849. arXiv: 2106.15445 [astro-ph.SR].

Feinstein, A. D., D. Z. Seligman, M. N. Günther, et al. (Jan. 2022). "Testing Self-organized Criticality across the Main Sequence Using Stellar Flares from TESS." In: *The Astrophysical Journal Letters* 925.1, L9, p. L9. DOI: 10.3847/2041-8213/ac4b5e. arXiv: 2109.07011 [astro-ph.SR].

Fichtinger, B., M. Güdel, R. L. Mutel, et al. (Mar. 2017). "Radio emission and mass loss rate limits of four young solar-type stars." In: *Astronomy and Astrophysics* 599, A127, A127. DOI: 10.1051/0004-6361/201629886. arXiv: 1702.08393 [astro-ph.SR].

Fionnagáin, D. Ó., R. D. Kavanagh, A. A. Vidotto, et al. (Jan. 2022). "Coronal Mass Ejections and Type II Radio Emission Variability during a Magnetic Cycle on the Solar-type Star Eridani." In: *The Astrophysical Journal* 924.2, 115, p. 115. DOI: 10.3847/1538-4357/ac35de. arXiv: 2111.02284 [astro-ph.SR].

Fleming, D. P., R. Barnes, J. R. A. Davenport, et al. (Aug. 2019). "Rotation Period Evolution in Low-mass Binary Stars: The Impact of Tidal Torques and Magnetic Braking." In: *The Astrophysical Journal* 881.2, 88, p. 88. DOI: 10.3847/1538-4357/ab2ed2. arXiv: 1903.05686 [astro-ph.SR].

Fletcher, L. and H. S. Hudson (Mar. 2008). "Impulsive Phase Flare Energy Transport by Large-Scale Alfvén Waves and the Electron Acceleration Problem." In: *The Astrophysical Journal* 675.2, pp. 1645–1655. DOI: 10.1086/527044. arXiv: 0712.3452 [astro-ph].

Freund, S., S. Czesla, J. Robrade, et al. (Aug. 2022). "The stellar content of the ROSAT all-sky survey." In: *Astronomy and Astrophysics* 664, A105, A105. DOI: 10.1051/0004-6361/202142573. arXiv: 2205.12874 [astro-ph.SR].

Freund, S., J. Robrade, P. C. Schneider, et al. (June 2018). "The stellar content of the XMM-Newton slew survey." In: *Astronomy and Astrophysics* 614, A125, A125. DOI: 10.1051/0004-6361/201732009. arXiv: 1712.07410 [astro-ph.SR].

Frogner, L., B. V. Gudiksen, and H. Bakke (Nov. 2020). "Accelerated particle beams in a 3D simulation of the quiet Sun." In: *Astronomy and Astrophysics* 643, A27, A27. DOI: 10.1051/0004-6361/202038529. arXiv: 2005.14483 [astro-ph.SR].

Fukugita, M., T. Ichikawa, J. E. Gunn, et al. (Apr. 1996). "The Sloan Digital Sky Survey Photometric System." In: *The Astronomical Journal* 111, p. 1748. DOI: 10.1086/117915.

Fukui, A., N. Narita, Y. Kawashima, et al. (Mar. 2016). "Demonstrating High-precision, Multiband Transit Photometry with MuSCAT: A Case for HAT-P-14b." In: *The Astrophysical Journal* 819.1, 27, p. 27. DOI: 10.3847/0004-637X/819/1/27. arXiv: 1510.03997 [astro-ph.EP].

Gagné, J., E. E. Mamajek, L. Malo, et al. (Mar. 2018). "BANYAN. XI. The BANYAN Σ Multivariate Bayesian Algorithm to Identify Members of Young Associations with 150 pc." In: *The Astrophysical Journal* 856.1, 23, p. 23. DOI: 10.3847/1538-4357/aaae09. arXiv: 1801.09051 [astro-ph.SR].

Gaia Collaboration (Nov. 2020). "VizieR Online Data Catalog: Gaia EDR3 (Gaia Collaboration, 2020)." In: *VizieR Online Data Catalog*, I/350, pp. I/350.

– (May 2022). "VizieR Online Data Catalog: Gaia DR3 Part 3. Non-single stars (Gaia Collaboration, 2022)." In: *VizieR Online Data Catalog*, I/357, pp. I/357.

Gaia Collaboration, A. G. A. Brown, A. Vallenari, et al. (Aug. 2018). "Gaia Data Release 2. Summary of the contents and survey properties." In: *Astronomy and Astrophysics* 616, A1, A1. DOI: 10.1051/0004-6361/201833051. arXiv: 1804.09365 [astro-ph.GA].

Gaidos, E. J. (Nov. 1998). "Nearby Young Solar Analogs. I. Catalog and Stellar Characteristics." In: *Publications of the Astronomical Society of the Pacific* 110.753, pp. 1259–1276. DOI: 10.1086/316251.

Gary, D. E. (Jan. 2019). "Cause and Extent of the Extreme Radio Flux Density Reached by the Solar Flare of 2006 December 06." In: *arXiv e-prints*, arXiv:1901.09262, arXiv:1901.09262. DOI: 10.48550/arXiv.1901.09262. arXiv: 1901.09262 [astro-ph.SR].

Gergely, T. E. (Mar. 1986). "Type-Iv Bursts and Coronal Mass Ejections." In: *Solar Physics* 104.1, pp. 175–178. DOI: 10.1007/BF00159959.

Goldreich, P. and D. Lynden-Bell (Apr. 1969). "Io, a jovian unipolar inductor." In: *The Astrophysical Journal* 156, pp. 59–78. DOI: 10.1086/149947.

Gopalswamy, N. and S. Yashiro (Dec. 2013). "Obscuration of Flare Emission by an Eruptive Prominence." In: *Publications of the Astronomical Society of Japan* 65, S11, S11. DOI: 10.1093/pasj/65.sp1.S11. arXiv: 1309.2046 [astro-ph.SR].

Green, N. J., J. Xu, and J. D. Sutherland (2021). "Illuminating Life's Origins: UV Photochemistry in Abiotic Synthesis of Biomolecules." In: *Journal of the American Chemical Society* 143.19. PMID: 33880920, pp. 7219–7236. DOI: 10.1021/jacs.1c01839. eprint: https://doi.org/10.1021/jacs.1c01839. URL: https://doi.org/10.1021/jacs.1c01839.

Gudel, M. (Oct. 1992). "Radio and X-ray emission from main-sequence K stars." In: *Astronomy and Astrophysics* 264, pp. L31–L34.

Gudel, M., E. F. Guinan, and S. L. Skinner (Jan. 1998). "The X-Ray and Radio Sun in Time: Coronal Evolution of Solar-Type Stars with Different Ages." In: *Cool Stars, Stellar Systems, and the Sun*. Ed. by R. A. Donahue and J. A. Bookbinder. Vol. 154. Astronomical Society of the Pacific Conference Series, p. 1041.

Gudel, M., J. H. M. M. Schmitt, J. A. Bookbinder, et al. (Sept. 1993). "A Tight Correlation between Radio and X-Ray Luminosities of M Dwarfs." In: *The Astrophysical Journal* 415, p. 236. DOI: 10.1086/173158.

Gudel, M., J. H. M. M. Schmitt, and A. O. Benz (Aug. 1994). "Discovery of Microwave Emission from Four Nearby Solar-Type G Stars." In: *Science* 265.5174, pp. 933–935. DOI: 10.1126/science.265.5174.933.

Güdel, M. (Jan. 2002). "Stellar Radio Astronomy: Probing Stellar Atmospheres from Protostars to Giants." In: *Annual Review of Astronomy and Astrophysics* 40, pp. 217–261. DOI: 10.1146/annurev.astro.40.060401.093806. arXiv: astro-ph/0206436 [astro-ph].

– (Sept. 2004). "X-ray astronomy of stellar coronae." In: *Astronomy and Astrophysics Reviews* 12.2-3, pp. 71–237. DOI: 10.1007/s00159-004-0023-2. arXiv: astro-ph/0406661 [astro-ph].

Güdel, M., E. F. Guinan, and S. L. Skinner (July 1997). "The X-Ray Sun in Time: A Study of the Long-Term Evolution of Coronae of Solar-Type Stars." In: *The Astrophysical Journal* 483.2, pp. 947–960. DOI: 10.1086/304264.

Guedel, M., J. H. M. M. Schmitt, A. O. Benz, et al. (Sept. 1995). "The corona of the young solar analog EK Draconis." In: *Astronomy and Astrophysics* 301, p. 201.

Guedel, M. and A. O. Benz (Mar. 1993). "X-Ray/Microwave Relation of Different Types of Active Stars." In: *The Astrophysical Journal Letters* 405, p. L63. DOI: 10.1086/186766.

Guerrero, G., P. K. Smolarkiewicz, E. M. de Gouveia Dal Pino, et al. (Mar. 2016). "On the Role of Tachoclines in Solar and Stellar Dynamos." In: *The Astrophysical Journal* 819.2, 104, p. 104. DOI: 10.3847/0004-637X/819/2/104. arXiv: 1507.04434 [astro-ph.SR].

Günther, M. N., Z. Zhan, S. Seager, et al. (Feb. 2020). "Stellar Flares from the First TESS Data Release: Exploring a New Sample of M Dwarfs." In: *The Astronomical Journal* 159.2, 60, p. 60. DOI: 10.3847/1538-3881/ab5d3a. arXiv: 1901.00443 [astro-ph.EP].

Haarlem, M. P. van, M. W. Wise, A. W. Gunst, et al. (Aug. 2013). "LOFAR: The LOw-Frequency ARray." In: *Astronomy and Astrophysics* 556, A2, A2. DOI: 10.1051/0004-6361/201220873. arXiv: 1305.3550 [astro-ph.IM].

Hall, D. S. (Jan. 1976). "The RS CVn Binaries and Binaries with Similar PROPERTIÉS." In: *IAU Colloq. 29: Multiple Periodic Variable Stars*. Ed. by W. S. Fitch. Vol. 60. Astrophysics and Space Science Library, p. 287. DOI: 10.1007/978-94-010-1175-4_15.

Hallinan, G., A. Antonova, J. G. Doyle, et al. (Sept. 2008). "Confirmation of the Electron Cyclotron Maser Instability as the Dominant Source of Radio Emission from Very Low Mass Stars and Brown Dwarfs." In: *The Astrophysical Journal* 684.1, pp. 644–653. DOI: 10.1086/590360. arXiv: 0805.4010 [astro-ph].

Harding, L. K., G. Hallinan, J. Milburn, et al. (Apr. 2016). "CHIMERA: a wide-field, multi-colour, high-speed photometer at the prime focus of the Hale telescope." In: *Monthly Notices of the Royal Astronomical Society* 457.3, pp. 3036–3049. DOI: 10.1093/mnras/stw094. arXiv: 1601.03104 [astro-ph.IM].

Hawley, S. L., J. C. Allred, C. M. Johns-Krull, et al. (Nov. 2003). "Multiwavelength Observations of Flares on AD Leonis." In: *The Astrophysical Journal* 597.1, pp. 535–554. DOI: 10.1086/378351.

Hewish, A. (Jan. 1955). "The scintillation of radio stars." In: *Vistas in Astronomy* 1.1, pp. 599–606. DOI: 10.1016/0083-6656(55)90073-8.

Hewitt, R. G., D. B. Melrose, and K. G. Ronnmark (Jan. 1982). "The loss-cone driven electron-cyclotron maser." In: *Australian Journal of Physics* 35.4, pp. 447–471. DOI: 10.1071/PH820447.

Huang, Z., C. Law, G. Hallinan, et al. (Jan. 2025). "Studying and Correcting for Ionospheric Effects in OVRO-LWA Images." In: *American Astronomical Society Meeting Abstracts*. Vol. 245. American Astronomical Society Meeting Abstracts, 407.04, p. 407.04.

Hudson, H. S., C. J. Wolfson, and T. R. Metcalf (Mar. 2006). "White-Light Flares: A TRACE/RHESSI Overview." In: *Solar Physics* 234.1, pp. 79–93. DOI: 10.1007/s11207-006-0056-y.

Huggins, W. and M. L. Huggins (Aug. 1890). "On a New Group of Lines in the Photographic Spectrum of Sirius." In: *Sidereal Messenger* 9, pp. 318–319.

Hurley-Walker, N. and P. Hancock (Nov. 2024). *fits_warp: Warp catalogs and images to dedistort the effects of the ionosphere*. Astrophysics Source Code Library, record ascl:2411.016.

Hynecek, J. and T. Nishiwaki (Jan. 2003). "Excess noise and other important characteristics of low light level imaging using charge multiplying CCDs." In: *Institute of Electrical and Electronics Engineers Transactions on Electron Devices* 50.1, pp. 239–245. DOI: 10.1109/TED.2002.806962.

Intema, H. T., S. van der Tol, W. D. Cotton, et al. (July 2009). "Ionospheric calibration of low frequency radio interferometric observations using the peeling scheme. I. Method description and first results." In: *Astronomy and Astrophysics* 501.3, pp. 1185–1205. DOI: 10.1051/0004-6361/200811094. arXiv: 0904.3975 [astro-ph.IM].

Isavnin, A. (Dec. 2016). "FRiED: A Novel Three-dimensional Model of Coronal Mass Ejections." In: *The Astrophysical Journal* 833.2, 267, p. 267. DOI: 10.3847/1538-4357/833/2/267. arXiv: 1703.01659 [physics.space-ph].

Jackman, J. A. G., E. Shkolnik, and R. O. P. Loyd (Apr. 2021). "Stellar flares from blended and neighbouring stars in Kepler short cadence observations." In: *Monthly Notices of the Royal Astronomical Society* 502.2, pp. 2033–2042. DOI: 10.1093/mnras/stab166. arXiv: 2101.07269 [astro-ph.SR].

Jakosky, B. M., R. P. Lin, J. M. Grebowsky, et al. (Dec. 2015). "The Mars Atmosphere and Volatile Evolution (MAVEN) Mission." In: *Space Science Reviews* 195.1-4, pp. 3–48. DOI: 10.1007/s11214-015-0139-x.

Johns-Krull, C. M. and G. J. Herczeg (Jan. 2007). "How Hot is the Wind from TW Hydrae?" In: *The Astrophysical Journal* 655.1, pp. 345–350. DOI: 10.1086/508770. arXiv: astro-ph/0609239 [astro-ph].

Johnstone, C. P., M. Güdel, I. Brott, et al. (May 2015a). "Stellar winds on the main-sequence. II. The evolution of rotation and winds." In: *Astronomy and Astrophysics* 577, A28, A28. DOI: 10.1051/0004-6361/201425301. arXiv: 1503.07494 [astro-ph.SR].

Johnstone, C. P., M. Güdel, T. Lüftinger, et al. (May 2015b). "Stellar winds on the main-sequence. I. Wind model." In: *Astronomy and Astrophysics* 577, A27, A27. DOI: 10.1051/0004-6361/201425300. arXiv: 1503.06669 [astro-ph.SR].

Joseph, W. L. T., W. M. Farrell, J. Dietrick, et al. (Sept. 2004). "The Radiometric Bode's Law and Extrasolar Planets." In: *The Astrophysical Journal* 612.1, pp. 511–518. DOI: 10.1086/422449.

Kavanagh, R. D., H. K. Vedantham, K. Rose, et al. (Dec. 2024). "Unravelling substellar magnetospheres." In: *Astronomy and Astrophysics* 692, A66, A66. DOI: 10.1051/0004-6361/202452094. arXiv: 2410.18073 [astro-ph.EP].

Kavanagh, R. D., A. A. Vidotto, H. K. Vedantham, et al. (July 2022). "Radio masers on WX UMa: hints of a Neptune-sized planet, or magnetospheric reconnection?" In: *Monthly Notices of the Royal Astronomical Society* 514.1, pp. 675–688. DOI: 10.1093/mnras/stac1264. arXiv: 2205.01661 [astro-ph.SR].

Kerdraon, A. and J.-M. Delouis (1997). "The Nançay Radioheliograph." In: *Coronal Physics from Radio and Space Observations*. Ed. by G. Trottet. Vol. 483, p. 192. DOI: 10.1007/BFb0106458.

King, J. R., A. R. Villarreal, D. R. Soderblom, et al. (Apr. 2003). "Stellar Kinematic Groups. II. A Reexamination of the Membership, Activity, and Age of the Ursa Major Group." In: *The Astronomical Journal* 125.4, pp. 1980–2017. DOI: 10.1086/368241.

Kislyakova, K. G., M. Güdel, D. Koutroumpa, et al. (May 2024). "X-ray detection of astrospheres around three main-sequence stars and their mass-loss rates." In: *Nature Astronomy* 8, pp. 596–605. DOI: 10.1038/s41550-024-02222-x. arXiv: 2404.14980 [astro-ph.SR].

Klein, K.-L. (Mar. 2021). "Radio astronomical tools for the study of solar energetic particles II.Time-extended acceleration at subrelativistic and relativistic energies." In: *Frontiers in Astronomy and Space Sciences* 7, 93, p. 93. DOI: 10.3389/fspas.2020.580445.

Koch, D. G., W. J. Borucki, G. Basri, et al. (Apr. 2010). "Kepler Mission Design, Realized Photometric Performance, and Early Science." In: *The Astrophysical Journal Letters* 713.2, pp. L79–L86. DOI: 10.1088/2041-8205/713/2/L79. arXiv: 1001.0268 [astro-ph.EP].

Kochukhov, O., T. Hackman, J. J. Lehtinen, et al. (Mar. 2020). "Hidden magnetic fields of young suns." In: *Astronomy and Astrophysics* 635, A142, A142. DOI: 10.1051/0004-6361/201937185. arXiv: 2002.10469 [astro-ph.SR].

Kowalski, A., S. L. Hawley, J. A. Holtzman, et al. (Jan. 2010). "A White Light Megaflare on the dM4.5e Star YZ CMi." In: *American Astronomical Society Meeting Abstracts #215*. Vol. 215. American Astronomical Society Meeting Abstracts, 424.11, p. 424.11.

Kretzschmar, M. (June 2011). "The Sun as a star: observations of white-light flares." In: *Astronomy and Astrophysics* 530, A84, A84. DOI: 10.1051/0004-6361/201015930. arXiv: 1103.3125 [astro-ph.SR].

Krucker, S., H. S. Hudson, N. L. S. Jeffrey, et al. (Oct. 2011). "High-resolution Imaging of Solar Flare Ribbons and Its Implication on the Thick-target Beam Model." In: *The Astrophysical Journal* 739.2, 96, p. 96. DOI: 10.1088/0004-637X/739/2/96.

Krupar, V., O. Kruparova, A. Szabo, et al. (Jan. 2024). "Comparative Analysis of Type III Radio Bursts and Solar Flares: Spatial Localization and Correlation with Solar Flare Intensity." In: *The Astrophysical Journal* 961.1, 88, p. 88. DOI: 10.3847/1538-4357/ad12ba.

Lacy, M., S. A. Baum, C. J. Chandler, et al. (Mar. 2020). "The Karl G. Jansky Very Large Array Sky Survey (VLASS). Science Case and Survey Design." In: *Publications of the Astronomical Society of the Pacific* 132.1009, 035001, p. 035001. DOI: 10.1088/1538-3873/ab63eb. arXiv: 1907.01981 [astro-ph.IM].

Landini, M., B. C. M. Fossi, R. Pallavicini, et al. (Mar. 1986). "EXOSAT detection of an X-ray flare from the solar type star pi 1 UMa." In: *Astronomy and Astrophysics* 157, pp. 217–222.

Lane, W. M., W. D. Cotton, S. van Velzen, et al. (May 2014). "The Very Large Array Low-frequency Sky Survey Redux (VLSSr)." In: *Monthly Notices of the Royal Astronomical Society* 440.1, pp. 327–338. DOI: 10.1093/mnras/stu256. arXiv: 1404.0694 [astro-ph.IM].

Lang, K. R. (2013). *Essential Astrophysics*. DOI: 10.1007/978-3-642-35963-7.

Laundal, K. M., S. M. Hatch, J. P. Reistad, et al. (June 2024). "How the Ionosphere Responds Dynamically to Magnetospheric Forcing." In: *Geophysical Research Letters* 51.11, e2024GL108695, e2024GL108695. DOI: 10.1029/2024GL108695.

Lavail, A., O. Kochukhov, G. A. J. Hussain, et al. (Dec. 2017). "Magnetic fields of intermediate mass T Tauri stars." In: *Astronomy and Astrophysics* 608, A77, A77. DOI: 10.1051/0004-6361/201731889. arXiv: 1711.05143 [astro-ph.SR].

Lawrance, B., P. Devi, R. Chandra, et al. (June 2024). "A Catalog of Metric Type II Radio Bursts Detected by RSTN During Solar Cycle 24." In: *Solar Physics* 299.6, 75, p. 75. DOI: 10.1007/s11207-024-02317-8.

Leitzinger, M., P. Odert, R. Greimel, et al. (Apr. 2020). "A census of coronal mass ejections on solar-like stars." In: *Monthly Notices of the Royal Astronomical Society* 493.3, pp. 4570–4589. DOI: 10.1093/mnras/staa504. arXiv: 2002.04430 [astro-ph.SR].

Li, J. Z. and J. Y. Hu (Oct. 1998). "Newly discovered candidate weak-line T Tauri stars in the surrounding area of the Taurus-Auriga region." In: *Astronomy and Astrophysics Supplement Series* 132, pp. 173–179. DOI: 10.1051/aas:1998288.

Lightkurve Collaboration, J. V. d. M. Cardoso, C. Hedges, et al. (Dec. 2018). *Lightkurve: Kepler and TESS time series analysis in Python*. Astrophysics Source Code Library. ascl: 1812.013.

Lim, J. and S. M. White (May 1996). "Limits to Mass Outflows from Late-Type Dwarf Stars." In: *The Astrophysical Journal Letters* 462, p. L91. DOI: 10.1086/310038.

Lim, J., S. M. White, G. J. Nelson, et al. (July 1994). "Directivity of the Radio Emission from the K1 Dwarf Star AB Doradus." In: *The Astrophysical Journal* 430, p. 332. DOI: 10.1086/174408.

Lin, Y.-C. (Sept. 2024). "Unveiling habitable planets: Toy coronagraph tackles the exozodiacal dust challenge." In: *arXiv e-prints*, arXiv:2409.05797, arXiv:2409.05797. DOI: 10.48550/arXiv.2409.05797. arXiv: 2409.05797 [astro-ph.IM].

Liu, Y., J. D. Richardson, and J. W. Belcher (Jan. 2005). "A statistical study of the properties of interplanetary coronal mass ejections from 0.3 to 5.4 AU." In: *Planetary Space Science* 53.1-3, pp. 3–17. DOI: 10.1016/j.pss.2004.09.023.

Loi, S. T., T. Murphy, I. H. Cairns, et al. (May 2015). "Real-time imaging of density ducts between the plasmasphere and ionosphere." In: *Geophysical Research Letters* 42.10, pp. 3707–3714. DOI: 10.1002/2015GL063699. arXiv: 1504.06470 [physics.space-ph].

Lourie, N. P., J. W. Baker, R. S. Burruss, et al. (Dec. 2020). "The wide-field infrared transient explorer (WINTER)." In: *Ground-based and Airborne Instrumentation for Astronomy VIII*. Ed. by C. J. Evans, J. J. Bryant, and K. Motohara. Vol. 11447. Society of Photo-Optical Instrumentation Engineers (SPIE) Conference Series, 114479K, 114479K. DOI: 10.1117/12.2561210. arXiv: 2102.01109 [astro-ph.IM].

Loyd, R. O. P., J. P. Mason, M. Jin, et al. (Sept. 2022). "Constraining the Physical Properties of Stellar Coronal Mass Ejections with Coronal Dimming: Application to Far-ultraviolet Data of Eridani." In: *The Astrophysical Journal* 936.2, 170, p. 170. DOI: 10.3847/1538-4357/ac80c1. arXiv: 2207.05115 [astro-ph.SR].

Luhmann, J. G., W. T. Kasprzak, and C. T. Russell (Apr. 2007). "Space weather at Venus and its potential consequences for atmosphere evolution." In: *Journal of Geophysical Research (Planets)* 112.E4, E04S10, E04S10. DOI: 10.1029/2006JE002820.

Lynch, B. J., V. S. Airapetian, C. R. DeVore, et al. (Aug. 2019). "Modeling a Carrington-scale Stellar Superflare and Coronal Mass Ejection from {}{\hat{1}}{Cet}." In: *The Astrophysical Journal* 880.2, 97, p. 97. DOI: 10.3847/1538-4357/ab287e. arXiv: 1906.03189 [astro-ph.SR].

MacGregor, M. A., R. A. Osten, and A. M. Hughes (Jan. 2020). "Properties of M Dwarf Flares at Millimeter Wavelengths." In: *arXiv e-prints*, arXiv:2001.10546, arXiv:2001.10546. DOI: 10.48550/arXiv.2001.10546. arXiv: 2001.10546 [astro-ph.SR].

MacGregor, M. A., A. J. Weinberger, R. O. P. Loyd, et al. (Apr. 2021). "Discovery of an Extremely Short Duration Flare from Proxima Centauri Using Millimeter through Far-ultraviolet Observations." In: *The Astrophysical Journal Letters* 911.2, L25, p. L25. DOI: 10.3847/2041-8213/abf14c. arXiv: 2104.09519 [astro-ph.SR].

Maehara, H., T. Shibayama, S. Notsu, et al. (May 2012). "Superflares on solar-type stars." In: *Nature* 485.7399, pp. 478–481. DOI: 10.1038/nature11063.

Maehara, H., T. Shibayama, Y. Notsu, et al. (Apr. 2015). "Statistical properties of superflares on solar-type stars based on 1-min cadence data." In: *Earth, Planets and Space* 67, 59, p. 59. DOI: 10.1186/s40623-015-0217-z. arXiv: 1504.00074 [astro-ph.SR].

Mamajek, E. E. and L. A. Hillenbrand (Nov. 2008). "Improved Age Estimation for Solar-Type Dwarfs Using Activity-Rotation Diagnostics." In: *The Astrophysical Journal* 687.2, pp. 1264–1293. DOI: 10.1086/591785. arXiv: 0807.1686 [astro-ph].

Mann, A. W., E. Gaidos, and G. Aldering (Nov. 2011). "Ground-Based Submillimagnitude CCD Photometry of Bright Stars Using Snapshot Observations." In: *Publications of the Astronomical Society of the Pacific* 123.909, p. 1273. DOI: 10.1086/662640. arXiv: 1109.1358 [astro-ph.EP].

Mariska, J. T. (Jan. 1986). "The quiet solar transition region." In: *Annual Review of Astronomy and Astrophysics* 24, pp. 23–48. DOI: 10.1146/annurev.aa.24.090186.000323.

Marsden, S. C., J. .-. Donati, M. Semel, et al. (July 2006). "Surface differential rotation and photospheric magnetic field of the young solar-type star HD 171488 (V889 Her)." In: *Monthly Notices of the Royal Astronomical Society* 370.1, pp. 468–476. DOI: 10.1111/j.1365-2966.2006.10503.x.

Mason, B. D., G. L. Wycoff, W. I. Hartkopf, et al. (Dec. 2001). "The 2001 US Naval Observatory Double Star CD-ROM. I. The Washington Double Star Catalog." In: *The Astronomical Journal* 122.6, pp. 3466–3471. DOI: 10.1086/323920.

Mason, K. O., B. J. M. Hassall, G. E. Bromage, et al. (June 1995). "Optical identification of EUV sources from the ROSAT Wide Field Camera all-sky survey." In: *Monthly Notices of the Royal Astronomical Society* 274.4, pp. 1194–1218. DOI: 10.1093/mnras/274.4.1194.

Matthews, S. A., L. van Driel-Gesztelyi, H. S. Hudson, et al. (Oct. 2003). "A catalogue of white-light flares observed by Yohkoh." In: *Astronomy and Astrophysics* 409, pp. 1107–1125. DOI: 10.1051/0004-6361:20031187.

Mawet, D., L. Hirsch, E. J. Lee, et al. (Jan. 2019). "Deep Exploration of Eridani with Keck Ms-band Vortex Coronagraphy and Radial Velocities: Mass and Orbital Parameters of the Giant Exoplanet." In: *The Astronomical Journal* 157.1, 33, p. 33. DOI: 10.3847/1538-3881/aaef8a. arXiv: 1810.03794 [astro-ph.EP].

Maxwell, A. and G. Swarup (Jan. 1958). "A New Spectral Characteristic in Solar Radio Emission." In: *Nature* 181.4601, pp. 36–38. DOI: 10.1038/181036a0.

McConnell, D., C. L. Hale, E. Lenc, et al. (Nov. 2020). "The Rapid ASKAP Continuum Survey I: Design and first results." In: *Publications of the Astronomical Society of Australia* 37, e048, e048. DOI: 10.1017/pasa.2020.41. arXiv: 2012.00747 [astro-ph.IM].

Melrose, D. B. (July 1971). "On the Degree of Circular Polarization of Synchrotron Radiation." In: *Astrophysics and Space Science* 12.1, pp. 172–192. DOI: 10.1007/BF00656148.

– (Sept. 1989). "The Brightness Temperatures of Solar Type-Iii Bursts." In: *Solar Physics* 120.2, pp. 369–381. DOI: 10.1007/BF00159885.

Melrose, D. B. and G. A. Dulk (Aug. 1982). "Electron-cyclotron masers as the source of certain solar and stellar radio bursts." In: *The Astrophysical Journal* 259, pp. 844–858. DOI: 10.1086/160219.

Merloni, A., G. Lamer, T. Liu, et al. (Feb. 2024). "The SRG/eROSITA all-sky survey. First X-ray catalogues and data release of the western Galactic hemisphere." In: *Astronomy and Astrophysics* 682, A34, A34. DOI: 10.1051/0004-6361/202347165. arXiv: 2401.17274 [astro-ph.HE].

Mestel, L. (Jan. 1968). "Magnetic braking by a stellar wind-I." In: *Monthly Notices of the Royal Astronomical Society* 138, p. 359. DOI: 10.1093/mnras/138.3.359.

Metcalfe, T. S., A. P. Buccino, B. P. Brown, et al. (Feb. 2013). "Magnetic Activity Cycles in the Exoplanet Host Star epsilon Eridani." In: *The Astrophysical Journal Letters* 763.2, L26, p. L26. DOI: 10.1088/2041-8205/763/2/L26. arXiv: 1212.4425 [astro-ph.SR].

Metcalfe, T. S., A. J. Finley, O. Kochukhov, et al. (July 2022). "The Origin of Weakened Magnetic Braking in Old Solar Analogs." In: *The Astrophysical Journal Letters* 933.1, L17, p. L17. DOI: 10.3847/2041-8213/ac794d. arXiv: 2206.08540 [astro-ph.SR].

Modi, A., R. Estrela, and A. Valio (Nov. 2023). "Impact of M-dwarf stellar wind and photoevaporation on the atmospheric evolution of small planets." In: *Monthly Notices of the Royal Astronomical Society* 525.4, pp. 5168–5179. DOI: 10.1093/mnras/stad2557. arXiv: 2309.10942 [astro-ph.EP].

Mohan, A., N. Gopalswamy, H. Raju, et al. (Nov. 2024a). "Novel scaling laws to derive spatially resolved flare and CME parameters from sun-as-a-star observables." In: *Astronomy and Astrophysics* 691, L8, p. L8. DOI: 10.1051/0004-6361/202451072. arXiv: 2409.19145 [astro-ph.SR].

Mohan, A., S. Mondal, S. Wedemeyer, et al. (June 2024b). "Energetic particle activity in AD Leo: Detection of a solar-like type-IV burst." In: *Astronomy and Astrophysics* 686, A51, A51. DOI: 10.1051/0004-6361/202347924. arXiv: 2402.00185 [astro-ph.SR].

Morosan, D. E., E. K. J. Kilpua, E. P. Carley, et al. (Mar. 2019). "Variable emission mechanism of a Type IV radio burst." In: *Astronomy and Astrophysics* 623, A63, A63. DOI: 10.1051/0004-6361/201834510. arXiv: 1902.01140 [astro-ph.SR].

Moschou, S.-P., J. J. Drake, O. Cohen, et al. (June 2019). "The Stellar CME-Flare Relation: What Do Historic Observations Reveal?" In: *The Astrophysical Journal* 877.2, 105, p. 105. DOI: 10.3847/1538-4357/ab1b37. arXiv: 1904.09598 [astro-ph.SR].

Mullan, D. J. and R. R. Paudel (Mar. 2019). "Origin of Radio-quiet Coronal Mass Ejections in Flare Stars." In: *The Astrophysical Journal* 873.1, 1, p. 1. DOI: 10.3847/1538-4357/ab041b. arXiv: 1902.00810 [astro-ph.SR].

Murphy, T., S. Chatterjee, D. L. Kaplan, et al. (Feb. 2013). "VAST: An ASKAP Survey for Variables and Slow Transients." In: *Publications of the Astronomical Society of Australia* 30, e006, e006. DOI: 10.1017/pasa.2012.006. arXiv: 1207.1528 [astro-ph.IM].

Namekata, K., V. S. Airapetian, P. Petit, et al. (Jan. 2024a). "Multiwavelength Campaign Observations of a Young Solar-type Star, EK Draconis. I. Discovery of Prominence Eruptions Associated with Superflares." In: *The Astrophysical Journal* 961.1, 23, p. 23. DOI: 10.3847/1538-4357/ad0b7c. arXiv: 2311.07380 [astro-ph.SR].

Namekata, K., K. Ikuta, P. Petit, et al. (Dec. 2024b). "Multiwavelength Campaign Observations of a Young Solar-type Star, EK Draconis. II. Understanding Prominence Eruption through Data-driven Modeling and Observed Magnetic Environment." In: *The Astrophysical Journal* 976.2, 255, p. 255. DOI: 10.3847/1538-4357/ad85df. arXiv: 2410.05523 [astro-ph.SR].

Namekata, K., H. Maehara, S. Honda, et al. (Dec. 2021). "Probable detection of an eruptive filament from a superflare on a solar-type star." In: *Nature Astronomy* 6, pp. 241–248. DOI: 10.1038/s41550-021-01532-8. arXiv: 2112.04808 [astro-ph.SR].

Namekata, K., H. Maehara, S. Honda, et al. (Feb. 2022a). "Discovery of a Long-duration Superflare on a Young Solar-type Star EK Draconis with Nearly Similar Time Evolution for Hα and White-light Emissions." In: *The Astrophysical Journal Letters* 926.1, L5, p. L5. DOI: 10.3847/2041-8213/ac4df0. arXiv: 2201.09416 [astro-ph.SR].

Namekata, K., H. Maehara, S. Honda, et al. (Nov. 2022b). "Hunting for stellar coronal mass ejections." In: *arXiv e-prints*, arXiv:2211.05506, arXiv:2211.05506. DOI: 10.48550/arXiv.2211.05506. arXiv: 2211.05506 [astro-ph.SR].

Namekata, K., T. Sakaue, K. Watanabe, et al. (Dec. 2017). "Statistical Studies of Solar White-light Flares and Comparisons with Superflares on Solar-type Stars." In: *The Astrophysical Journal* 851.2, 91, p. 91. DOI: 10.3847/1538-4357/aa9b34. arXiv: 1710.11325 [astro-ph.SR].

Namizaki, K., K. Namekata, H. Maehara, et al. (Mar. 2023). "A Superflare on YZ Canis Minoris Observed by the Seimei Telescope and TESS: Red Asymmetry of Hα Emission Associated with White-light Emission." In: *The Astrophysical*

Journal 945.1, 61, p. 61. DOI: 10.3847/1538-4357/acb928. arXiv: 2302.03007 [astro-ph.SR].

Nindos, A. (Nov. 2020). "Incoherent Solar Radio Emission." In: *Frontiers in Astronomy and Space Sciences* 7, 57, p. 57. DOI: 10.3389/fspas.2020.00057. arXiv: 2007.14888 [astro-ph.SR].

Noordam, J. E. (Oct. 2004). "LOFAR calibration challenges." In: *Ground-based Telescopes*. Ed. by J. Oschmann Jacobus M. Vol. 5489. Society of Photo-Optical Instrumentation Engineers (SPIE) Conference Series, pp. 817–825. DOI: 10.1117/12.544262.

Notsu, Y., H. Maehara, S. Honda, et al. (May 2019). "Do Kepler Superflare Stars Really Include Slowly Rotating Sun-like Stars?—Results Using APO 3.5 m Telescope Spectroscopic Observations and Gaia-DR2 Data." In: *The Astrophysical Journal* 876.1, 58, p. 58. DOI: 10.3847/1538-4357/ab14e6. arXiv: 1904.00142 [astro-ph.SR].

Offringa, A. R., J. J. van de Gronde, and J. B. T. M. Roerdink (Mar. 2012). "A morphological algorithm for improving radio-frequency interference detection." In: *Astronomy and Astrophysics* 539, A95, A95. DOI: 10.1051/0004-6361/201118497. arXiv: 1201.3364 [astro-ph.IM].

Offringa, A. R., B. McKinley, Hurley-Walker, et al. (2014). "WSClean: an implementation of a fast, generic wide-field imager for radio astronomy." In: *Monthly Notices of the Royal Astronomical Society* 444.1, pp. 606–619. DOI: 10.1093/mnras/stu1368.

Okamoto, S., Y. Notsu, H. Maehara, et al. (Jan. 2021). "Statistical Properties of Superflares on Solar-type Stars: Results Using All of the Kepler Primary Mission Data." In: *The Astrophysical Journal* 906.2, 72, p. 72. DOI: 10.3847/1538-4357/abc8f5. arXiv: 2011.02117 [astro-ph.SR].

Osborn, J., D. Föhring, V. S. Dhillon, et al. (Sept. 2015). "Atmospheric scintillation in astronomical photometry." In: *Monthly Notices of the Royal Astronomical Society* 452.2, pp. 1707–1716. DOI: 10.1093/mnras/stv1400. arXiv: 1506.06921 [astro-ph.IM].

Osten, R. A. and T. S. Bastian (Feb. 2006). "Wide-Band Spectroscopy of Two Radio Bursts on AD Leonis." In: *The Astrophysical Journal* 637.2, pp. 1016–1024. DOI: 10.1086/498410. arXiv: astro-ph/0509815 [astro-ph].

Osten, R. A., S. L. Hawley, J. C. Allred, et al. (Mar. 2005). "From Radio to X-Ray: Flares on the dMe Flare Star EV Lacertae." In: *The Astrophysical Journal* 621.1, pp. 398–416. DOI: 10.1086/427275. arXiv: astro-ph/0411236 [astro-ph].

Osten, R. A. and S. J. Wolk (Aug. 2015). "Connecting Flares and Transient Mass-loss Events in Magnetically Active Stars." In: *The Astrophysical Journal* 809.1, 79, p. 79. DOI: 10.1088/0004-637X/809/1/79. arXiv: 1506.04994 [astro-ph.SR].

Otsu, T., A. Asai, K. Ichimoto, et al. (Nov. 2022). "Sun-as-a-star Analyses of Various Solar Active Events Using Hα Spectral Images Taken by SMART/SDDI." In: *The Astrophysical Journal* 939.2, 98, p. 98. DOI: 10.3847/1538-4357/ac9730. arXiv: 2210.02819 [astro-ph.SR].

Pal, T., I. Khan, G. Worthey, et al. (June 2023). "HST Low-resolution Stellar Library." In: *The Astrophysical Journal Suplement Series* 266.2, 41, p. 41. DOI: 10.3847/1538-4365/accea7. arXiv: 2301.05335 [astro-ph.SR].

Pandey, J. C. (Apr. 2015). "Observations of X-ray Flares on π^1 UMa." In: *Physics and Evolution of Magnetic and Related Stars*. Ed. by Y. Y. Balega, I. I. Romanyuk, and D. O. Kudryavtsev. Vol. 494. Astronomical Society of the Pacific Conference Series, p. 203.

Peng, Z., J. Chaowei, W. Juntao, et al. (Apr. 2022). "Mechanism of the Failed Eruption of an Intermediate Solar Filament." In: *The Astrophysical Journal* 928.2, 160, p. 160. DOI: 10.3847/1538-4357/ac581f.

Petit, P., C. P. Folsom, J. .-. Donati, et al. (Apr. 2021). "Multi-instrumental view of magnetic fields and activity of Eridani with SPIRou, NARVAL, and TESS." In: *Astronomy and Astrophysics* 648, A55, A55. DOI: 10.1051/0004-6361/202040027. arXiv: 2101.02643 [astro-ph.SR].

Pietras, M., R. Falewicz, M. Siarkowski, et al. (Aug. 2022). "Statistical Analysis of Stellar Flares from the First Three Years of TESS Observations." In: *The Astrophysical Journal* 935.2, 143, p. 143. DOI: 10.3847/1538-4357/ac8352. arXiv: 2207.11039 [astro-ph.SR].

Plutino, N., F. Berrilli, D. D. Moro, et al. (Feb. 2023). "A new catalogue of solar flare events from soft X-ray GOES signal in the period 1986-2020." In: *Advances in Space Research* 71.4, pp. 2048–2058. DOI: 10.1016/j.asr.2022.11.020. arXiv: 2211.10189 [astro-ph.SR].

Pourbaix, D., A. A. Tokovinin, A. H. Batten, et al. (Sept. 2004). "S_{B^9}: The ninth catalogue of spectroscopic binary orbits." In: *Astronomy and Astrophysics* 424, pp. 727–732. DOI: 10.1051/0004-6361:20041213. arXiv: astro-ph/0406573 [astro-ph].

Pritchard, J., T. Murphy, G. Heald, et al. (Apr. 2024). "Multi-epoch sampling of the radio star population with the Australian SKA Pathfinder." In: *Monthly Notices of the Royal Astronomical Society* 529.2, pp. 1258–1270. DOI: 10.1093/mnras/stae127. arXiv: 2312.11031 [astro-ph.SR].

Pritchard, J., T. Murphy, A. Zic, et al. (Apr. 2021). "A circular polarization survey for radio stars with the Australian SKA Pathfinder." In: *Monthly Notices of the Royal Astronomical Society* 502.4, pp. 5438–5454. DOI: 10.1093/mnras/stab299. arXiv: 2102.01801 [astro-ph.SR].

Prša, A., P. Harmanec, G. Torres, et al. (Aug. 2016). "Nominal Values for Selected Solar and Planetary Quantities: IAU 2015 Resolution B3." In: *The Astronomical Journal* 152.2, 41, p. 41. DOI: 10.3847/0004-6256/152/2/41. arXiv: 1605.09788 [astro-ph.SR].

Pye, J. P., P. A. McGale, D. J. Allan, et al. (June 1995). "The ROSAT Wide Field Camera all-sky survey of extreme-ultraviolet sources - II. The 2RE Source Catalogue." In: *Monthly Notices of the Royal Astronomical Society* 274.4, pp. 1165–1193. DOI: 10.1093/mnras/274.4.1165.

Raja, K. S., M. Maksimovic, E. P. Kontar, et al. (Jan. 2022). "Spectral Analysis of Solar Radio Type III Bursts from 20 kHz to 410 MHz." In: *The Astrophysical Journal* 924.2, 58, p. 58. DOI: 10.3847/1538-4357/ac34ed. arXiv: 2110.10935 [astro-ph.SR].

Ransom, S. (July 2011). *PRESTO: PulsaR Exploration and Search TOolkit*. Astrophysics Source Code Library, record ascl:1107.017.

Readhead, A. C. S. (May 1994). "Equipartition Brightness Temperature and the Inverse Compton Catastrophe." In: *The Astrophysical Journal* 426, p. 51. DOI: 10.1086/174038.

Reames, D. V. (2021). "Impulsive SEP Events (and Flares)." In: *Solar Energetic Particles: A Modern Primer on Understanding Sources, Acceleration and Propagation*. Cham: Springer International Publishing, pp. 71–95. ISBN: 978-3-030-66402-2. DOI: 10.1007/978-3-030-66402-2_4. URL: https://doi.org/10.1007/978-3-030-66402-2_4.

Reid, H. A. S. and H. Ratcliffe (July 2014). "A review of solar type III radio bursts." In: *Research in Astronomy and Astrophysics* 14.7, pp. 773–804. DOI: 10.1088/1674-4527/14/7/003. arXiv: 1404.6117 [astro-ph.SR].

Reid, H. A. S., N. Vilmer, and E. P. Kontar (July 2014). "The low-high-low trend of type III radio burst starting frequencies and solar flare hard X-rays." In: *Astronomy and Astrophysics* 567, A85, A85. DOI: 10.1051/0004-6361/201321973. arXiv: 1403.1839 [astro-ph.SR].

Ribas, I., G. F. P. de Mello, L. D. Ferreira, et al. (May 2010). "Evolution of the Solar Activity Over Time and Effects on Planetary Atmospheres. II. κ^1 Ceti, an Analog of the Sun when Life Arose on Earth." In: *The Astrophysical Journal* 714.1, pp. 384–395. DOI: 10.1088/0004-637X/714/1/384. arXiv: 1003.3561 [astro-ph.SR].

Ribas, I., E. F. Guinan, M. Güdel, et al. (Mar. 2005). "Evolution of the Solar Activity over Time and Effects on Planetary Atmospheres. I. High-Energy Irradiances (1-1700 Å)." In: *The Astrophysical Journal* 622.1, pp. 680–694. DOI: 10.1086/427977. arXiv: astro-ph/0412253 [astro-ph].

Richards, M. T. (Jan. 1992). "Magnetic Activity in Algol-Type Binaries." In: *Cool Stars, Stellar Systems, and the Sun*. Ed. by M. S. Giampapa and J. A. Bookbinder. Vol. 26. Astronomical Society of the Pacific Conference Series, p. 367.

Ricker, G. R., J. N. Winn, R. Vanderspek, et al. (Aug. 2014). "Transiting Exoplanet Survey Satellite (TESS)." In: *Space Telescopes and Instrumentation 2014: Optical, Infrared, and Millimeter Wave*. Ed. by J. Oschmann Jacobus M., M. Clampin, G. G. Fazio, et al. Vol. 9143. Society of Photo-Optical Instrumentation Engineers (SPIE) Conference Series, 914320, p. 914320. DOI: 10.1117/12.2063489. arXiv: 1406.0151 [astro-ph.EP].

Rigney, J., G. Ramsay, E. P. Carley, et al. (Oct. 2022). "Searching for stellar flares from low-mass stars using ASKAP and TESS." In: *Monthly Notices of the Royal Astronomical Society* 516.1, pp. 540–549. DOI: 10.1093/mnras/stac2143. arXiv: 2207.00405 [astro-ph.SR].

Robinson, C. R. and B. W. Bopp (1987). "A "Helium Flarl" on the active G5 Dwarf Kappa ceti." In: *Cool Stars, Stellar Systems, and the Sun*. Ed. by J. L. Linsky and R. E. Stencel. Berlin, Heidelberg: Springer Berlin Heidelberg, pp. 509–511. ISBN: 978-3-540-48041-9.

Robitaille, T. and E. Bressert (Aug. 2012). *APLpy: Astronomical Plotting Library in Python*. Astrophysics Source Code Library, record ascl:1208.017. ascl: 1208.017.

Rose, K., J. Pritchard, T. Murphy, et al. (July 2023). "Periodic Radio Emission from the T8 Dwarf WISE J062309.94-045624.6." In: *The Astrophysical Journal* 951.2, L43, p. L43. DOI: 10.3847/2041-8213/ace188. arXiv: 2306.15219 [astro-ph.SR].

Rosén, L., O. Kochukhov, T. Hackman, et al. (Sept. 2016). "Magnetic fields of young solar twins." In: *Astronomy and Astrophysics* 593, A35, A35. DOI: 10.1051/0004-6361/201628443. arXiv: 1605.03026 [astro-ph.SR].

Röser, S., E. Schilbach, B. Goldman, et al. (June 2018). "A new compact young moving group around V1062 Scorpii." In: *Astronomy and Astrophysics* 614, A81, A81. DOI: 10.1051/0004-6361/201732213. arXiv: 1712.10143 [astro-ph.SR].

Rubenzahl, R. A., S. Halverson, J. Walawender, et al. (Dec. 2023). "Staring at the Sun with the Keck Planet Finder: An Autonomous Solar Calibrator for High Signal-to-noise Sun-as-a-star Spectra." In: *Publications of the Astronomical Society of the Pacific* 135.1054, 125002, p. 125002. DOI: 10.1088/1538-3873/ad0b30. arXiv: 2311.05129 [astro-ph.IM].

Sadykov, V. M., J. T. Stefan, A. G. Kosovichev, et al. (Jan. 2024). "Can Proton Beam Heating Flare Models Explain Sunquakes?" In: *The Astrophysical Journal* 960.1, 80, p. 80. DOI: 10.3847/1538-4357/ad0cf3. arXiv: 2306.13162 [astro-ph.SR].

Saikia, S. B., T. Lüftinger, C. P. Folsom, et al. (Feb. 2022). "Time evolution of magnetic activity cycles in young suns: The curious case of κ Ceti." In: *Astronomy and Astrophysics* 658, A16, A16. DOI: 10.1051/0004-6361/202141525. arXiv: 2110.06000 [astro-ph.SR].

Saint-Hilaire, P., N. Vilmer, and A. Kerdraon (Jan. 2013). "A Decade of Solar Type III Radio Bursts Observed by the Nançay Radioheliograph 1998-2008." In: *The Astrophysical Journal* 762.1, 60, p. 60. DOI: 10.1088/0004-637X/762/1/60. arXiv: 1211.3474 [astro-ph.SR].

Salvini, S. and S. J. Wijnholds (Nov. 2014). "Fast gain calibration in radio astronomy using alternating direction implicit methods: Analysis and applications." In: *Astronomy and Astrophysics* 571, A97, A97. DOI: 10.1051/0004-6361/201424487. arXiv: 1410.2101 [astro-ph.IM].

Sazonov, V. N. (Nov. 1972). "The Circular Polarization of Sources of Synchrotron Radiation." In: *Astrophysics and Space Science* 19.1, pp. 25–45. DOI: 10.1007/BF00643165.

Schaefer, B. E., J. R. King, and C. P. Deliyannis (Feb. 2000). "Superflares on Ordinary Solar-Type Stars." In: *The Astrophysical Journal* 529.2, pp. 1026–1030. DOI: 10.1086/308325. arXiv: astro-ph/9909188 [astro-ph].

Schmitt, J. H. M. M. (Feb. 1997). "Coronae on solar-like stars." In: *Astronomy and Astrophysics* 318, pp. 215–230.

Schmitt, J. H. M. M., T. A. Fleming, and M. S. Giampapa (Sept. 1995). "The X-Ray View of the Low-Mass Stars in the Solar Neighborhood." In: *The Astrophysical Journal* 450, p. 392. DOI: 10.1086/176149.

Shibata, K., H. Isobe, A. Hillier, et al. (June 2013). "Can Superflares Occur on Our Sun?" In: *Publications of the Astronomical Society of Japan* 65, 49, p. 49. DOI: 10.1093/pasj/65.3.49. arXiv: 1212.1361 [astro-ph.SR].

Shibayama, T., H. Maehara, S. Notsu, et al. (Nov. 2013). "Superflares on Solar-type Stars Observed with Kepler. I. Statistical Properties of Superflares." In: *The Astrophysical Journal Supplement Series* 209.1, 5, p. 5. DOI: 10.1088/0067-0049/209/1/5. arXiv: 1308.1480 [astro-ph.SR].

Shimwell, T. W., H. J. A. Röttgering, P. N. Best, et al. (Feb. 2017). "The LOFAR Two-metre Sky Survey. I. Survey description and preliminary data release." In: *Astronomy and Astrophysics* 598, A104, A104. DOI: 10.1051/0004-6361/201629313. arXiv: 1611.02700 [astro-ph.IM].

Shimwell, T. W., C. Tasse, M. J. Hardcastle, et al. (Feb. 2019). "The LOFAR Two-metre Sky Survey. II. First data release." In: *Astronomy and Astrophysics* 622, A1, A1. DOI: 10.1051/0004-6361/201833559. arXiv: 1811.07926 [astro-ph.GA].

Skinner, S. L. and A. Brown (Apr. 1994). "The Enigmatic T Tauri Radio Source." In: *The Astronomical Journal* 107, p. 1461. DOI: 10.1086/116959.

Skumanich, A. (Feb. 1972). "Time Scales for Ca II Emission Decay, Rotational Braking, and Lithium Depletion." In: *The Astrophysical Journal* 171, p. 565. DOI: 10.1086/151310.

Smith, K., M. Pestalozzi, M. Güdel, et al. (Aug. 2003). "VLBI observations of T Tauri South." In: *Astronomy and Astrophysics* 406, pp. 957–967. DOI: 10.1051/0004-6361:20030764. arXiv: astro-ph/0305543 [astro-ph].

Somalwar, J. J., V. Ravi, D. Z. Dong, et al. (Apr. 2025). "VLASS Tidal Disruption Events with Optical Flares. I. The Sample and a Comparison to Optically Selected TDEs." In: *The Astrophysical Journal* 982.2, 163, p. 163. DOI: 10.3847/1538-4357/adba4f. arXiv: 2310.03791 [astro-ph.HE].

Song, Y. L., H. Tian, M. Zhang, et al. (June 2018). "Observations of white-light flares in NOAA active region 11515: high occurrence rate and relationship with magnetic transients." In: *Astronomy and Astrophysics* 613, A69, A69. DOI: 10.1051/0004-6361/201731817. arXiv: 1801.04371 [astro-ph.SR].

Southworth, J., T. C. Hinse, U. G. Jørgensen, et al. (June 2009). "High-precision photometry by telescope defocusing - I. The transiting planetary system WASP-5." In: *Monthly Notices of the Royal Astronomical Society* 396.2, pp. 1023–1031. DOI: 10.1111/j.1365-2966.2009.14767.x. arXiv: 0903.2139 [astro-ph.EP].

Spangler, S. R. and T. J. Moffett (Jan. 1976). "Simultaneous radio and optical observations of UV Ceti-type flare stars." In: *The Astrophysical Journal* 203, pp. 497–508. DOI: 10.1086/154105.

Stefansson, G., S. Mahadevan, L. Hebb, et al. (Oct. 2017). "Toward Space-like Photometric Precision from the Ground with Beam-shaping Diffusers." In: *The Astrophysical Journal* 848.1, 9, p. 9. DOI: 10.3847/1538-4357/aa88aa. arXiv: 1710.01790 [astro-ph.IM].

Stovall, K., P. S. Ray, J. Blythe, et al. (Aug. 2015). "Pulsar Observations Using the First Station of the Long Wavelength Array and the LWA Pulsar Data Archive." In: *The Astrophysical Journal* 808.2, 156, p. 156. DOI: 10.1088/0004-637X/808/2/156. arXiv: 1410.7422 [astro-ph.IM].

Strassmeier, K. G., T. Pichler, M. Weber, et al. (Dec. 2003). "Doppler imaging of stellar surface structure. XXI. The rapidly-rotating solar-type star HD 171488 = V889 Hercules." In: *Astronomy and Astrophysics* 411, pp. 595–604. DOI: 10.1051/0004-6361:20031538.

Struminsky, A. B., I. Y. Grigorieva, Y. I. Logachev, et al. (Sept. 2020). "Two Phases of Solar Flares and a Stochastic Mechanism for Acceleration of Electrons and Protons." In: *Astrophysics* 63.3, pp. 388–398. DOI: 10.1007/s10511-020-09643-2.

Suresh, A., S. Chatterjee, J. M. Cordes, et al. (Dec. 2020). "Detection of 2-4 GHz Continuum Emission from Eridani." In: *The Astrophysical Journal* 904.2, 138, p. 138. DOI: 10.3847/1538-4357/abc004. arXiv: 2010.05929 [astro-ph.SR].

Swift, J. J., M. Bottom, J. A. Johnson, et al. (Apr. 2015). "Miniature Exoplanet Radial Velocity Array (MINERVA) I. Design, Commissioning, and First Science Results." In: *Journal of Astronomical Telescopes, Instruments, and Systems* 1, 027002, p. 027002. DOI: 10.1117/1.JATIS.1.2.027002. arXiv: 1411.3724 [astro-ph.IM].

Taylor, G. B., C. L. Carilli, and R. A. Perley, eds. (Jan. 1999). *Synthesis Imaging in Radio Astronomy II*. Vol. 180. Astronomical Society of the Pacific Conference Series.

Tristan, I. I., Y. Notsu, A. F. Kowalski, et al. (July 2023). "A 7 Day Multiwavelength Flare Campaign on AU Mic. I. High-time-resolution Light Curves and the Thermal Empirical Neupert Effect." In: *The Astrophysical Journal* 951.1, 33, p. 33. DOI: 10.3847/1538-4357/acc94f. arXiv: 2304.05692 [astro-ph.SR].

Tu, Z.-L., M. Yang, Z. J. Zhang, et al. (Feb. 2020). "Superflares on Solar-type Stars from the First Year Observation of TESS." In: *The Astrophysical Journal* 890.1, 46, p. 46. DOI: 10.3847/1538-4357/ab6606. arXiv: 1912.11572 [astro-ph.SR].

Vasilyev, V., T. Reinhold, A. I. Shapiro, et al. (Dec. 2024). "Sun-like stars produce superflares roughly once per century." In: *Science* 386.6727, pp. 1301–1305. DOI: 10.1126/science.adl5441. arXiv: 2412.12265 [astro-ph.SR].

Vedantham, H. K. (July 2020). "Prospects for radio detection of stellar plasma beams." In: *Astronomy and Astrophysics* 639, L7, p. L7. DOI: 10.1051/0004-6361/202038576. arXiv: 2006.11882 [astro-ph.SR].

Vedantham, H. K., J. R. Callingham, T. W. Shimwell, et al. (Feb. 2022). "Peculiar Radio-X-Ray Relationship in Active Stars." In: *The Astrophysical Journal Letters* 926.2, L30, p. L30. DOI: 10.3847/2041-8213/ac5115. arXiv: 2201.12203 [astro-ph.SR].

Véron-Cetty, M. .-. and P. Véron (Aug. 2006). "A catalogue of quasars and active nuclei: 12th edition." In: *Astronomy and Astrophysics* 455.2, pp. 773–777. DOI: 10.1051/0004-6361:20065177.

Veronig, A. M., P. Odert, M. Leitzinger, et al. (Jan. 2021). "Indications of stellar coronal mass ejections through coronal dimmings." In: *Nature Astronomy* 5, pp. 697–706. DOI: 10.1038/s41550-021-01345-9. arXiv: 2110.12029 [astro-ph.SR].

Vida, K., M. Leitzinger, L. Kriskovics, et al. (Mar. 2019). "The quest for stellar coronal mass ejections in late-type stars. I. Investigating Balmer-line asymmetries of single stars in Virtual Observatory data." In: *Astronomy and Astrophysics* 623, A49, A49. DOI: 10.1051/0004-6361/201834264. arXiv: 1901.04229 [astro-ph.SR].

Vidotto, A. A., S. G. Gregory, M. Jardine, et al. (July 2014). "Stellar magnetism: empirical trends with age and rotation." In: *Monthly Notices of the Royal Astronomical Society* 441.3, pp. 2361–2374. DOI: 10.1093/mnras/stu728. arXiv: 1404.2733 [astro-ph.SR].

Vidotto, A. A., M. Opher, V. Jatenco-Pereira, et al. (Sept. 2010). "Simulations of Winds of Weak-lined T Tauri Stars. II. The Effects of a Tilted Magnetosphere and Planetary Interactions." In: *The Astrophysical Journal* 720.2, pp. 1262–1280. DOI: 10.1088/0004-637X/720/2/1262. arXiv: 1007.3874 [astro-ph.SR].

Vilhu, O. (Apr. 1984). "The nature of magnetic activity in lower main sequence stars." In: *Astronomy and Astrophysics* 133, pp. 117–126.

Villadsen, J. and G. Hallinan (Feb. 2019). "Ultra-wideband Detection of 22 Coherent Radio Bursts on M Dwarfs." In: *The Astrophysical Journal* 871.2, 214, p. 214. DOI: 10.3847/1538-4357/aaf88e. arXiv: 1810.00855 [astro-ph.SR].

Villadsen, J., G. Hallinan, S. Bourke, et al. (June 2014). "First Detection of Thermal Radio Emission from Solar-type Stars with the Karl G. Jansky Very Large Array." In: *The Astrophysical Journal* 788.2, 112, p. 112. DOI: 10.1088/0004-637X/788/2/112. arXiv: 1405.2341 [astro-ph.SR].

Villanueva Jr., S., B. S. Gaudi, R. W. Pogge, et al. (Jan. 2018). "DEdicated MONitor of EXotransits and Transients (DEMONEXT): System Overview and Year One Results from a Low-cost Robotic Telescope for Followup of Exoplanetary Transits and Transients." In: *Publications of the Astronomical Society of the Pacific* 130.983, p. 015001. DOI: 10.1088/1538-3873/aa9603. arXiv: 1709.05353 [astro-ph.IM].

Virtanen, P., R. Gommers, T. E. Oliphant, et al. (2020a). "SciPy 1.0: Fundamental Algorithms for Scientific Computing in Python." In: *Nature Methods* 17, pp. 261–272. DOI: 10.1038/s41592-019-0686-2.

– (2020b). "SciPy 1.0: Fundamental Algorithms for Scientific Computing in Python." In: *Nature Methods* 17, pp. 261–272. DOI: 10.1038/s41592-019-0686-2.

Voges, W., B. Aschenbach, T. Boller, et al. (Sept. 1999). "The ROSAT all-sky survey bright source catalogue." In: *Astronomy and Astrophysics* 349, pp. 389–405. DOI: 10.48550/arXiv.astro-ph/9909315. arXiv: astro-ph/9909315 [astro-ph].

Waite, I. A., S. C. Marsden, B. D. Carter, et al. (Feb. 2017). "Magnetic fields on young, moderately rotating Sun-like stars - II. EK Draconis (HD 129333)." In: *Monthly Notices of the Royal Astronomical Society* 465.2, pp. 2076–2091. DOI: 10.1093/mnras/stw2731. arXiv: 1611.07751 [astro-ph.SR].

Wang, Y., L. Zhang, T. Su, et al. (June 2024). "Magnetic activity of radio stars based on TESS and LAMOST surveys." In: *Astronomy and Astrophysics* 686, A164, A164. DOI: 10.1051/0004-6361/202348342.

Watanabe, K., T. Shimizu, S. Masuda, et al. (Oct. 2013). "Emission Height and Temperature Distribution of White-light Emission Observed by Hinode/SOT from the 2012 January 27 X-class Solar Flare." In: *The Astrophysical Journal* 776.2, 123, p. 123. DOI: 10.1088/0004-637X/776/2/123. arXiv: 1308.5059 [astro-ph.SR].

Wenger, M., F. Ochsenbein, D. Egret, et al. (Apr. 2000). "The SIMBAD astronomical database. The CDS reference database for astronomical objects." In: *Astronomy and Astrophysics Supplement Series* 143, pp. 9–22. DOI: 10.1051/aas:2000332. arXiv: astro-ph/0002110 [astro-ph].

White, S. M., M. Shimojo, K. Iwai, et al. (July 2024). "Electron Cyclotron Maser Emission and the Brightest Solar Radio Bursts." In: *The Astrophysical Journal* 969.1, 3, p. 3. DOI: 10.3847/1538-4357/ad4640. arXiv: 2405.01755 [astro-ph.SR].

Williams, P. K. G., K. N. Allers, B. A. Biller, et al. (July 2019). "A Tool and Workflow for Radio Astronomical "Peeling" in CASA." In: *Research Notes of the American Astronomical Society* 3.7, p. 110. DOI: 10.3847/2515-5172/ab35d5. URL: https://dx.doi.org/10.3847/2515-5172/ab35d5.

Wood, B. E., H. .-. Müller, G. P. Zank, et al. (Aug. 2005). "New Mass-Loss Measurements from Astrospheric Lyα Absorption." In: *The Astrophysical Journal Letters* 628.2, pp. L143–L146. DOI: 10.1086/432716. arXiv: astro-ph/0506401 [astro-ph].

Wood, B. E., H.-R. Müller, S. Redfield, et al. (Feb. 2014). "Evidence for a Weak Wind from the Young Sun." In: *The Astrophysical Journal Letters* 781.2, L33, p. L33. DOI: 10.1088/2041-8205/781/2/L33.

Woods, T. N., G. Kopp, and P. C. Chamberlin (Oct. 2006). "Contributions of the solar ultraviolet irradiance to the total solar irradiance during large flares." In: *Journal of Geophysical Research (Space Physics)* 111.A10, A10S14, A10S14. DOI: 10.1029/2005JA011507.

Wright, N. J., J. J. Drake, E. E. Mamajek, et al. (Dec. 2011). "The Stellar-activity-Rotation Relationship and the Evolution of Stellar Dynamos." In: *The Astrophysical Journal* 743.1, 48, p. 48. DOI: 10.1088/0004-637X/743/1/48. arXiv: 1109.4634 [astro-ph.SR].

Wu, C. S. and L. C. Lee (June 1979). "A theory of the terrestrial kilometric radiation." In: *The Astrophysical Journal* 230, pp. 621–626. DOI: 10.1086/157120.

Xu, Y., J. D. Alvarado-Gómez, H. Tian, et al. (Aug. 2024a). "Simulated Coronal Mass Ejections on a Young Solar-type Star and the Associated Instantaneous Angular Momentum Loss." In: *The Astrophysical Journal* 971.2, 153, p. 153. DOI: 10.3847/1538-4357/ad5845. arXiv: 2406.08194 [astro-ph.SR].

Xu, Y., H. Tian, A. M. Veronig, et al. (July 2024b). "Sun-as-a-star Observations of Obscuration Dimmings Caused by Filament Eruptions." In: *The Astrophysical Journal* 970.1, 60, p. 60. DOI: 10.3847/1538-4357/ad500b. arXiv: 2405.13671 [astro-ph.SR].

Yang, H., C. M. Johns-Krull, and J. A. Valenti (Dec. 2005). "Measuring the Magnetic Field of the Classical T Tauri Star TW Hydrae." In: *The Astrophysical Journal* 635.1, pp. 466–475. DOI: 10.1086/497070. arXiv: astro-ph/0509549 [astro-ph].

Yang, H., J. Liu, Q. Gao, et al. (Nov. 2017). "The Flaring Activity of M Dwarfs in the Kepler Field." In: *The Astrophysical Journal* 849.1, 36, p. 36. DOI: 10.3847/1538-4357/aa8ea2.

Yashiro, S., S. Akiyama, N. Gopalswamy, et al. (Oct. 2006). "Different Power-Law Indices in the Frequency Distributions of Flares with and without Coronal Mass Ejections." In: *The Astrophysical Journal Letters* 650.2, pp. L143–L146. DOI: 10.1086/508876. arXiv: astro-ph/0609197 [astro-ph].

Yashiro, S. and N. Gopalswamy (Mar. 2009). "Statistical relationship between solar flares and coronal mass ejections." In: *Universal Heliophysical Processes*. Ed. by N. Gopalswamy and D. F. Webb. Vol. 257, pp. 233–243. DOI: 10.1017/S1743921309029342.

Yiu, T. W. H., H. K. Vedantham, J. R. Callingham, et al. (Apr. 2024). "Radio emission as a stellar activity indicator." In: *Astronomy and Astrophysics* 684, A3, A3. DOI: 10.1051/0004-6361/202347657. arXiv: 2312.07162 [astro-ph.SR].

Zahn, J. .-. (May 1977). "Tidal friction in close binary systems." In: *Astronomy and Astrophysics* 57, pp. 383–394.

Zarka, P., F. P. Magalhães, M. S. Marques, et al. (Oct. 2021). "Jupiter's Auroral Radio Emissions Observed by Cassini: Rotational Versus Solar Wind Control, and Components Identification." In: *Journal of Geophysical Research (Space Physics)* 126.10, e29780, e29780. DOI: 10.1029/2021JA02978010.1002/essoar.10507542.1.

Zhang, J., H. Tian, P. Zarka, et al. (Aug. 2023). "Fine Structures of Radio Bursts from Flare Star AD Leo with FAST Observations." In: *The Astrophysical Journal* 953.1, 65, p. 65. DOI: 10.3847/1538-4357/acdb77. arXiv: 2306.00895 [astro-ph.SR].

Zic, A., T. Murphy, C. Lynch, et al. (Dec. 2020). "A Flare-type IV Burst Event from Proxima Centauri and Implications for Space Weather." In: *The Astrophysical Journal* 905.1, 23, p. 23. DOI: 10.3847/1538-4357/abca90. arXiv: 2012.04642 [astro-ph.SR].

Appendix A

AUTOMATED FLARE IDENTIFICATION AND EVALUATION

A.1 Effects of Color Correction On Flare Energy

In equations 2-4 of Tu et al. (2020), they report the bolometric flare flux as being:

$$F_{\rm flare} = (F - F_{\rm q}) 4\pi R_\star^2 \sigma_{\rm SB} T_\star^4 \tag{A.1}$$

where F is the normalized light curve flux, $F_{\rm q}$ is the normalized quiescent flux of the light curve, $\sigma_{\rm SB}$ is the Stefan-Boltzmann constant, and $R_\star$ and $T_\star$ are the effective radius and temperature of the quiescent star, respectively. However, this does not account for the fact that flares peak much more in the blue than the quiescent stellar surface, which is an important consideration for *TESS*, which has a preferentially red band.

To account for this temperature and color difference, the bolometric flare flux should instead be:

$$F_{\rm flare} = (F - F_{\rm q}) 4\pi R_\star^2 \sigma_{\rm SB} T_{\rm fl}^4 \frac{\int_{\rm I} B(\lambda, T_{\rm q})\, {\rm d}\lambda}{\int_{\rm I} B(\lambda, T_{\rm fl})\, {\rm d}\lambda} \tag{A.2}$$

where $T_{\rm fl}$ is the temperature of the flare and $B(\lambda, T)$ is the Planck function for a blackbody. $B(\lambda, T)$ is integrated over the wavelengths of the *TESS* band (I), between 600 nm and 1000 nm. Similar or equivalent expressions have been utilized by Shibayama et al. (2013), Yang et al. (2017), and Jackman et al. (2021).

Using the median quiescent stellar temperature from their sample (5,500 K) and assuming a flare temperature of 10,000 K (*e.g.*, Hawley et al. (2003), Kowalski et al. (2010), and Kretzschmar (2011)), this then suggests that Tu et al. (2020) might have been underestimating the flare energies by about at least a factor of 2. It has been shown more recently by (Berger et al., 2024) that flares may be significantly hotter than the $\sim 10,000$ K that is regularly assumed, and so this underestimate in flare energy may be even more severe.

Doyle et al. (2020) use a different method: they assume the luminosity of the flare is the same luminosity as the quiescent star. The energy would then be calculated by multiplying the luminosity by an effective duration, determined by the area under the light curve of the flare. Even though they do account for the *TESS* bandpass effect on the quiescent flux, because they also do not account for the temperature difference

between the quiescent star and the flare this would suggest an underestimate of the flare energy. Indeed, for each star that is common between Doyle et al. (2020) and Tu et al. (2020)'s work, Doyle et al. (2020) reports a lower maximum flare energy than the already underestimated flare energy of Tu et al. (2020).

A.2 Identifying and Characterizing Flares

As mentioned in Section 2.4, my method for identifying flares closely follows Jackman et al. (2021)'s method used for *Kepler* data. The full method is described here.

I used the `lightkurve` package (Lightkurve Collaboration et al., 2018) to access light curves from the Science Processing Operations Center (SPOC) pipeline for the 153 stars. We used this package's box-least-squares method to produce a periodogram for each star. The period at maximum power from the periodogram was taken to be the star's rotational period P. This period was used to determine the median-filter window size—the window was taken to be $P/15$. If the window size was less than 100 minutes, then the window size was set to 100 minutes.

Like Jackman et al. (2021), I split the full light curve into separate continuous segments before smoothing to avoid jumps in measured flux between gaps and entire sectors. Gaps in data were required to be at least 30 minutes for the two sections to be considered separate segments. Segments that were less than the window size were excluded from the flare search.

After splitting the light curve, each light curve segment was iteratively smoothed. At each iteration, we used `scipy`'s (Virtanen et al., 2020b) `medfilt` function to produce a median filter of the light curve segment. The segment was then divided by this smoothed curve to produce a normalized curve. Points in the normalized curve that were greater than 3σ from the median value were masked in the original segment. This was repeated 20 times, or until there were no outlying points. I repeated this process using a window twice the size of the original window to mask points *less* than 3σ from the median value to remove eclipses.

A final median filter was produced using the final, masked light curve segment. The original, non-masked light curve is then divided by this median light curve. I clipped points within $P/45$ of the edges of the light curve segments. This was done to prevent the code from mistakenly identifying increased flux at the edges (an effect of the median light curve quotient) as a flare. Points greater than 2σ were flagged as a preliminary flare candidate. I then required that segments: 1.)

contain at least three 3σ points, 2.) contain at least an additional two 2.5σ points, and 3.) that consecutive points be separated by no more than 8 minutes to allow for some flexibility regarding erroneously-masked points. After flares were identified, I consolidated flares where the end of one flare was within 2.4 hr of the start of the preceding flare so that complex flare events were not treated as multiple individual flares, which would skew the flare rate to be anomalously high.

After the flares were identified and consolidated, I checked all flare candidates to make sure they had the correct morphology (steep rise, exponential decay) to be considered a flare. For exceptional cases—*e.g.*, extremely short rotation periods—I went back and manually assigned window sizes and re-ran the procedure in order to appropriately de-trend the rotational modulation. When this happened, it often meant also identifying when the derived period was not the actual rotation period. These periods were then also manually updated.

The bolometric flux of the flares were calculated using equation A.2 for each of the points in the flare light curve and assuming a flare temperature of 10,000 K. The bolometric energy is then determined by multiplying each of these fluxes by the surface area of the star and the *TESS* exposure time (120 s). The flare rate was calculated by dividing the number of flares found by the duration of light curve was searched for flares (*i.e.*, the edges of light curves that were clipped were not included in the flare rate calculation). All derived data for the 153 stars and their flares will be on the flare_id github repository along with the code and examples on how to use it. An example of how this flare-finding method performs is shown for HD 295290 in Figure A.1.

A.3 Ruling out M-dwarf Contamination

The concern of an M-dwarf contaminating the *TESS* PSF can be addressed on an energetic basis by assuming the *TESS* light curve for the solar-type star includes the quiescent flux of the star $F_\star$, the quiescent flux of an M-dwarf $F_{\rm M}$, and the flux of a flare originating from the M-dwarf $F_{\rm fl} = x\,F_{\rm M}$. The relationship between the fractional increase in the *TESS*-band flux of the M-dwarf due to a flare and the factor x by which the M-dwarf's flux increases from the flare is then:

$$x = \frac{F_{\rm N}(F_\star + F_{\rm M}) - F_\star}{F_{\rm M}} - 1 \tag{A.3}$$

where $F_{\rm N}$ is the normalized flux of the light curve (*e.g.*, if $F_{\rm N} = 1$, the flux is simply from the quiescent star and M-dwarf and $x = 0$). The flux in the *TESS* band from a

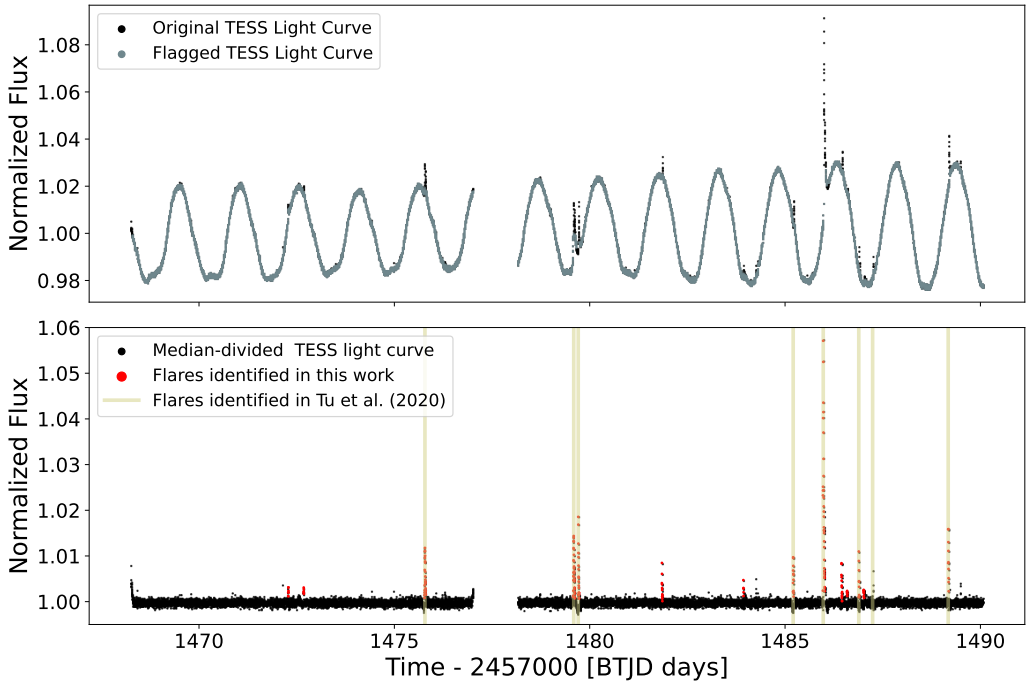

Figure A.1: The original SPOC light curve and the light curve with masked outlying points for HD 295290 (top) and the corresponding detrended light curve with the identified flares (bottom). Because Tu et al. (2020) provided the times for the flares they identified, the peak times of their flares are also included in the bottom plot. The flare-identification framework identified 14 flares for HD 295290 compared to Tu et al. (2020)'s 8 flares and Doyle et al. (2020)'s 16 flares. It is possible that many of the flares that we detected that Tu et al. (2020) did not report is because they did not qualify as superflares from their energy calculations and so would be excluded in their analysis.

given star is estimated as:

$$F = \frac{R^2}{d^2} \int_{600\text{nm}}^{1000\text{nm}} B(\lambda, T)\, \mathrm{d}\lambda \tag{A.4}$$

where R is the radius of the star, d is the distance to the star, T is the temperature of the star, and $B(\lambda, T)$ is the Planck function for a blackbody. The bolometric luminosity of the flare on the M-dwarf, $L_{\text{fl,bol}}$ can then be estimated as:

$$L_{\text{flare}} = x 4\pi R_\star^2 \sigma_{\text{SB}} T_{\text{fl}}^4 \frac{\int_{\text{I}} B(\lambda, T_{\text{q}})\, \mathrm{d}\lambda}{\int_{\text{I}} B(\lambda, T_{\text{fl}})\, \mathrm{d}\lambda} \tag{A.5}$$

I use the Gaia DR3 catalog to look for stars within 42" (two pixels on the *TESS* detector) of HD 156097 and HD 321958. The most nearby star within HD 156097's

	$T_\star$ K	$R_\star$ $R_\odot$	$d_\star$ pc	T_M K	R_M $R_\odot$	d_M pc	$F_{N,min}$	x_{min}	f_{min}	$F_{N,max}$	x_{max}	f_{max}
HD 156097	5,844	1.44	116	3943	1	358	1.003	0.29	0.56	1.023	2.23	4.27
HD 321958	5,626	1.26	172	3775	1	910	1.005	1.34	2.47	1.129	34.53	63.69

Table A.1: Details on HD 156097, HD 321958, and the M-dwarfs contaminating their *TESS* PSF. x_{min} and x_{max} are the fractional change in flux in the *TESS* light curve for the dimmest and brightest flare, respectively. f_{min} and f_{max} are the required change in the M-dwarf's bolometric luminosity for x_{min} and x_{max}, respectively.

TESS PSF with a reported temperature is Gaia DR3 5980482341853888384 at a distance of 358.1 pc and a temperature of 3943 K. For HD 321958, the most nearby star within its PSF with a reported temperature is the 3775 K star Gaia DR3 5971100445300717440 at 910 pc. Both of these contaminating stars have $\log(g) > 4$, suggesting they are dwarf stars. For this argument, I favor the contaminants by assuming they have radii $R = 1\mathrm{R}_{\odot}$ despite their low temperatures and $\log(g)$ values that imply smaller radii. As in Appendix A.1, I take the flare temperature to be 10,000 K. Using these values in equations A.3 and A.5, I find that the M-dwarfs contaminating HD 156097 and HD 321958 would need to reach bolometric luminosities $\sim 4\times$ and $\sim 64\times$ the quiescent bolometric luminosities of their respective stars in order to replicate the brightest flares observed for these stars. M-dwarf bolometric flare luminosities only exceed the quiescent bolometric luminosity in extreme circumstances (Chang et al., 2018), and have never been reported to reach as high as $64\times$ their quiescent luminosity. Because of this, I find it unlikely that M-dwarf contaminators are responsible for the flares in these light curves. A summary of the stellar values that were used in equations A.3 and A.5 as well as the results of the calculations are given in table A.1.

Appendix B

BEAMFORMER BACKGROUND IDENTIFICATION AND SUBTRACTION

I consider four different methods for identifying the time-invariant emission (the beam's "background" flux): 1.) low-pass filtering, 2.) high-pass filtering and subtracting from the data, 3.) median filtering, and 4.) a rolling window median. Each method is applied on a per-channel basis. I discuss the details and performance of these methods here to justify my use of the rolling median method for background subtraction.

B.1 Method 1: Low-pass Filtering

For low-pass filtering, I use the second-order sections (SOS) functionality of the `butter` function in `scipy`'s `signal` module. I specify the sampling frequency as 4 Hz (corresponding to the 0.256 s native integration time) and use a critical frequency of 0.04 Hz and first-order filtering. Using higher-order filtering or a much lower critical frequency results in extreme artifacts. This is partially related to the fact that this method ignores flags and just heeds the raw data—bright, impulsive RFI ends up getting smeared in time. The trade-off for using a higher-frequency critical frequency for cut off is that much of this impulsive RFI does not get effectively filtered, leading to over-subtraction when the background is subtracted from the raw data. The one boon of this method is its rapidity—it filters 14000 time intervals 2216 times in ≈ 0.5 s.

B.2 Method 2: High-pass Filtering

The high-pass filtering is performed with the same function inputs as as the low-pass method with the exception of using the 'highpass' bandpass type. This produces the same effect as running the low-pass filtering method and then subtracting the result from the raw data. This means that this method is susceptible to the same artifacts related to low-frequency cut-offs as the low-pass filtering. It has the benefit of performing at the same speed as the low-pass filtering method without needing to actually identify a background to produce a "background subtracted" dynamic spectrum. As such, this high-pass filtering would be the preferred method between the two band-pass filtering methods.

B.3 Method 3: Median Filtering

Median filtering was performed using the `medfilt` function, also apart of `scipy`'s `signal` module. This method's performance only varies with the kernel size and effectively accounts for flagged data unlike the bandpass filtering techniques. As such, it does not suffer from the impulsive-signal smearing effect of those methods. However, this method suffers substantially from the processing time required and how this processing time scales with window size—it took 42 seconds for a 39 interval (10 s of data) window, 323 seconds for a 235 interval (1 min of data) window, and 753 s for the 469 interval (2 min of data) window. Although the quality of the background extracted through this method is much better than the bandpass filtering methods (see Table B.1 for statistical details on background-subtraction performance), a full night of observing ($\approx$ 8 hr) with this method would require more than 1.5 hr without parallelization dedicated just for filtering the background flux. While manageable, this is far from ideal.

B.4 Method 4: Rolling-window Median

The final method I considered was the `rolling` median functionality apart of `pandas` data frames. Like median filtering, this method accounts for flagged data. However, it performs its calculations much faster- a window size of 469 intervals takes 10.3 s for this method compared to the 753 s for the median filtering method. The downside of this method is related to how the rolling window handles the first $n - 1$ values of a channel's light curve, where n is the size of the window. These values are calculated as not a number (NaNs), regardless of whether there are NaNs in the original light curve. This can be remedied by having the minimum number of viable points for median calculation be set to one, but this then produces an effect of the light curves being shift relative to the actual time interval of the flux by $n/2 + 1$ intervals. This is easily fixed by shifting the light curves by the same number of intervals in the opposite direction, but then the data for the $n/2+1$ intervals at the end of every light curve is lost. Accounting for all this, the dynamic spectrum produced is nearly identical to what is produced through the median filter method, with the median difference between flux extracted by the two different methods being 0, and the mean difference between two pixels being 0.47, or a difference in flux by a factor of $\approx 6 \times 10^{-5}$.

The loss of the last $\approx$ 200 time intervals ($\approx$ 1 min of data) from this method is easily justified when comparing the background-subtracted dynamic spectra to that of the bandpass-filtering methods. The light curves produced by summing over the

background-subtracted dynamic spectra are shown in Figure B.1. This plot makes the effects of over-subtraction from the low-pass method immediately obvious—a significant fraction of the data are negative with exceptionally high magnitudes. This is reflected in the statistics of the background-subtracted dynamic spectra, reported in table B.1.

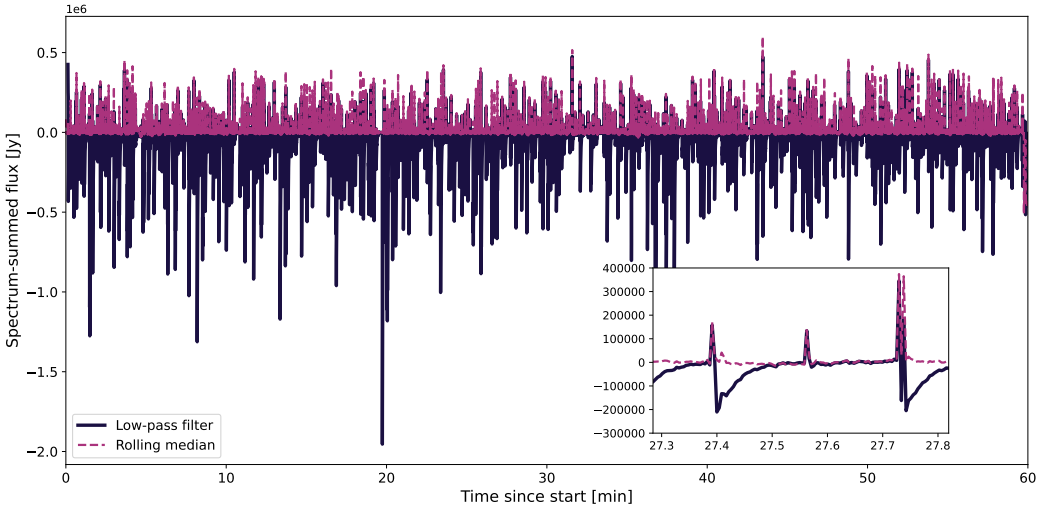

Figure B.1: The light curves from the background-subtracted data produced from the low-pass-filter method and the rolling-median method. Summing, rather than averaging, in frequency makes the severity of over-subtraction from the low-pass filtering more apparent. A $\approx$ 30 s inset in the bottom right corner is provided to demonstrate the failure of the low-pass method around strong, brief signals.

	Processing time	**Mean**	**Median**	**STD**	**Min**	**Max**
Bandpass filtering	$\approx$ 0.5 s	-30.3	-1.85	496.10	-1.15×10^5	1.08×10^4
Median filtering	$\approx$ 753 s	6.24	3.91	143.70	-3.83×10^3	6.54×10^3
Rolling median	$\approx$ 10 s	4.99	2.89	143.15	-1.42×10^3	6.54×10^3

Table B.1: Summary of the performance for the various background-retrieval methods. The bandpass-filtering method leads to over-subtraction as evidenced from its mean and median values being negative and its lowest value (Min) being a higher magnitude than the maximum value (Max). The rolling-median method produced the best results—the statistics were comparable to if not better than the median-filtering method and ran 75× faster.

Appendix C

FLARESCOPE AUTOMATION SCHEMA

Flarescope's automation protocol includes 1.) carrying out the observations, 2.) troubleshooting problems and executing potential solutions, and 3.) halting setup/ executing emergency shutdown if a terminal error or bad weather is encountered. Our custom automation code is written in python and manages all of the equipment summarized in table C.1. The only "manual" input it requires is the provision of a session definition file (SDF) which outlines the names and coordinates of the targets to look at, the filter and diffuser needed for each target, and the exposure time and number of frames for each target. I provide an overview of the automated-observing management here.

A large swath of potential errors are solved by either power-cycling the equipment or the connection to the equipment. To take advantage of this, the majority of the equipment is powered through a remotely-accessible power-distribution unit (PDU) from Synaccess Networks Incorporated. The PDU itself is powered by a 120 V power uninterruptible power supply (UPS) which is managed by Palomar staff. Additionally, I use the Pegasus Astro USB Control Hub (USB Hub hereafter), which allows for power-cycling the connection of devices that use USB. Although the USB Hub and the PDU have their own GUI for manual interfacing, for the sake of automation I manage power cycling the relevant positions by sending commands through python's `serial` package. Although the communication and power supply to the dome *controller* can be power cycled, the connectivity for the dome itself (as well as the camera) is not USB and so cannot benefit from the USB Hub. Instead, the dome connection can be reset through serial command. The camera is communicated with through a peripheral component interconnect (PCI) cable which cannot be remotely reset except by restarting the entire observatory-control computer. The dome itself is powered by a 220 V supply which cannot be remotely power cycled, and the weather station is managed by the WINTER observatory and therefore I do not control its power.

The automated observing protocol begins by checking that all of the equipment can be connected to. If any equipment connected to the USB Hub fails this check, then its USB connection is power cycled and connection is attempted again. If

this solution fails or is not applicable, then equipment that is powered by the PDU has their PDU position power cycled; the USB Hub position is power cycled again if available. Because communication with the dome is managed by two different methods (serial connection with the dome itself and USB Hub connection with the Astrometrics controller) it has a different protocol: a reset command is sent through the dome serial connection first and then the USB Hub position for the Astrometrics controller is power-cycled. If any of these solutions fail, then observatory set up does not continue and equipment connections are released.

If the software is able to connect to all of the equipment, then the observatory begins preparing for observing. This begins with launching the PWI softwares which are needed for interfacing with the mount, EFA, and dew heater. This is followed by cooling down the camera, which takes $\approx 10 - 20$ min, and the filter wheel is set to the appropriate position for the first target of the night. The observatory checks that the weather is conducive to observing (dewpoint depression $> 2^{\circ}$ C, humidity less than 85%, and wind speed less than 3.5 m/s). If the weather conditions are not satisfied or if communication to the weather station cannot be established then the observatory waits 10 min before checking again. This is checked every 10 min for an hour. If communication with the weather station cannot be established or if the weather quality is dangerous after an hour, then the filterwheel is homed, the camera cooler is turned off, the PWI softwares are closed, and the equipment connections are released and observing does not proceed.

If the weather conditions are suitable for observing then threads are initiated for 1.) checking the weather every three minutes and 2.) updating a JavaScript Object Notation (JSON) file with the status of the observatory. This JSON is interpreted by a simultaneously-running program that updates a webpage accessible from Palomar intranet that makes it easy to check the status of the observatory alongside a web camera that is hosted inside the dome. Finally, the dome opens and the mount slews to the first target and waits until the observing time as designated in the SDF, which contains all of the information that the mount, camera, and filterwheel need to conduct observations.

If the weather is registered to be unsafe for observing during the middle of an observing run or if an shutdown signal is received from the Flarescope webpage, then the emergency shutdown protocol is run. This begins with closing the dome, then homing and parking the mount, turning off the camera cooler, and homing the filter wheel before disconnecting from all equipment. If the observatory is running

normal shutdown procedures at the end of an observing run, then it runs this same protocol with the exception that the mount is homed and parked before the dome is closed. If by the end of either of these protocols the dome is not interpreted as closed, or if connection was lost and cannot be re-established, then the dome light and alarm are turned on to alert Palomar staff. This is done by simply toggling on the power to the PDU position associated with the alarm.

C.1 Dome Safety

Because the dome poses the most immediate and severe threat to staff in the case of a failure, is so critical for maintaining the safety of the other equipment, and has demonstrated the most persistent failures, I have taken extra care to manage its automation. The dome's shutters are held by tension in belts. There is currently no infrastructure to indicate the exact shutter positions or degree of slack in the belt—the dome can only tell whether it is CLOSED, OPENED, or MIDWAY depending on the shutters' positions relative to the limit switches. If the dome is mechanically prevented from opening by, *e.g.*, the shutters being stuck together, then the belts will still unspool when the drives receive the open command but the shutters themselves will not move. This produces slack in the belt that can be exceptionally dangerous if the shutters should, *e.g.*, spontaneously un-stick. To avoid this, I do a pulsed-opening technique—the open command is given to the South-facing shutters for two seconds, corresponding to 12 inches of belt slack if the shutters are not moving. At two seconds, the South shutter status is checked to see if they are registering as MIDWAY. If they are not, then the open command is halted and the dome alarm system is triggered to alert staff to a problem and to indicate that caution is necessary. If the South shutters *do* register as MIDWAY, then the opening command is continued until the South side of the dome is open. There is an additional, alarm-triggering timeout after 15 s for reaching the final OPENED status. This process is repeated for the North shutters. This same protocol is followed with the close command, closing the North shutters first and then the South shutters.

Although this protocol addresses the failure modes that we have observed thus far with the dome, the ideal measure of the state of the dome would involve measuring the slack in the belts and having an exact measure of the shutter positions and inclinations. This would require custom engineering for the dome and the introduction of additional signal paths between the dome, the controller, and the observatory-control computer. Although this solution is of major interest, the implementation is non-trivial. While I will be considering paths forward for implementing these solu-

tions so that we may have a more robust record of the dome status, the observatory is essentially prepared for fully-automated observing.

Table C.1: Hardware incorporated in the Flarescope automation protocol and how the power and communication are managed for each. Those that are ASCOM compatible allow for easy access to the device drivers for commanding via Python, while those without ASCOM compatibility require serial commands.

Hardware	**Power Management**	**Communication Management**	**ASCOM Compatible**
Mount	PDU	USB Hub	Yes
EFA	PDU	USB Hub	Yes
Dew heater	PDU	USB Hub	Yes
Astrohaven Dome	220V UPS	Serial	No
Astrometrics Dome Controller	N/A	USB Hub	Yes
Camera	PDU	PCI	Yes
Filter wheel	PDU	USB Hub	Yes
USB Hub	PDU	USB COM	No
Dome light/alarm	PDU	–	No
PDU	120V UPS	Intranet	No
Weather	N/A	Intranet	No

Appendix D

FLARE FIELD STRENGTH ESTIMATES

The energy available to a flare is limited by the magnetic energy contained within the magnetic loop E_B. Thus, we can use the energy of the flare presented in Chapter 5 to estimate the magnetic field strength using:

$$E_{\text{flare}} \sim E_B = \frac{(B/\text{G})^2}{8\pi} \frac{V}{\text{cm}^3} \text{ erg}, \tag{D.1}$$

where B is the field strength of the loop and V is the volume that the loop fills. To approximate the volume of the loop, we can take the area heated (which is the signal Flarescope measures) to be the area of the loop footpoints and then use the loop scale height l expression from Namekata et al. (2022a):

$$l \sim 1.64 \times 10^9 \left(\frac{\tau_{\text{decay}}}{100\,\text{s}}\right)^{2/5} \left(\frac{E_{\text{flare}}}{10^{30}\,\text{erg}}\right)^{1/5} [\text{cm}]. \tag{D.2}$$

Using the values I have estimated in Chapter 5, I find that the length of the flare loop should be $\approx 2.6 \times 10^{10}$ cm (about 0.37 $R_\star$, and similar to loop lengths derived for EK Dra previously). I take the maximum foot point size to be $L_{\text{peak, bol}}\,(\sigma_{\text{SB}}\,T_{\text{flare}}^4)^{-1}$ where $L_{\text{peak, bol}}$ is the peak bolometric luminosity assuming the flare temperature T_{flare} of 10,000 K. A peak flare luminosity of 7.9×10^{31} erg/s then implies an overall volume of $\approx 7.3 \times 10^{30}\,\text{cm}^3$. Taking this volume with the overall flare energy in equation D.1 implies a field strength of 370 G.

An alternative way to estimate the field strength is by determining the Alfvén speed, estimated from the rise time of the flare luminosity and the loop length. It took ≈ 2 min for the flare to reach its peak luminosity; paired with the loop length, this suggests an Alfvén speed of 2,170 km/s. Assuming an electron number density of $10^{11-12}\,\text{cm}^{-3}$ estimated from X-ray observations of EK Dra's flares (Guedel et al., 1995) and assuming the loop is purely ionized hydrogen such that the mass density is the electron density multiplied by the proton mass, then we get that the field strength is 89–280 G depending on the density. That these two estimation methods agree with each other within an order of magnitude suggests that the field responsible for the flare was on average $\gtrsim 200$ G. This is consistent with field strengths determined through Zeeman Doppler imaging.